Alma Mater Studiorum · University of Bologna

School of Science
Department of Physics and Astronomy
Master Degree in Physics

Quality Controls for the Mu2e Electromagnetic Calorimeter and R&D studies for the Muon Capture Rate determination

Supervisor:
Prof. Andrea Castro

Co-supervisor:
Dr. Stefano Miscetti

Submitted by:
Elisa Sanzani

Academic Year 2021/2022

Abstract

The Standard Model (SM) is a very precise theory which has proven its effectiveness, but as measurements become more and more precise it has begun to show its limits. According to the SM, while Lepton Flavour Violation is allowed in the neutral sector, Charged Lepton Flavour Violation (CLFV) processes are forbidden.

The Mu2e experiment at Fermilab will search for the CLFV process of neutrinoless conversion of a μ^- into an e^- within the field of an Al nucleus. The Mu2e detectors and its state-of-the-art superconducting magnetic system are presented, with special focus put to the electromagnetic crystal calorimeter. The calorimeter is composed by two annular disks, each one hosting pure CsI crystals read-out by custom silicon photomultipliers (SiPMs). The SiPMs are amplified by custom electronics (FEE) and are glued to copper holders in group of 2 SiPMs and 2 FEE boards thus forming a crystal Readout Unit. These Readout Units are being tested at the Quality Control (QC) Station, whose design, realization and operations are presented in this work. The QC Station allows to determine the gain, the response and the photon detection efficiency of each unit and to evaluate the dependence of these parameters from the supply voltage and temperature. The results for the first ~ 900 units are shown and summarized. The station is powered by two remotely-controlled power supplies and monitored thanks to a Slow Control system which is also illustrated in this work.

In this thesis, we also demonstrated that the calorimeter can perform its own measurement of the Mu2e normalization factor, i.e. the counting of the 1.8 MeV photon line produced in nuclear muon captures. A specific calorimeter sub-system called CAPHRI, composed by four LYSO crystals with SiPM readout, has been designed and tested. We simulated the capability of this system on performing this task showing that it can get a faster and more reliable measurement of the muon capture rates with respect to the current Mu2e detector dedicated to this measurement. The characterization of energy resolution and response uniformity of the four procured LYSO crystals are also illustrated.

Contents

Introduction

In this thesis, the design, construction and test of the read-out sensors for the Mu2e electromagnetic calorimeter are discussed, together with the proposal of a calorimetry based method to perform the normalization of Mu2e measurement.

Mu2e is an innovative experiment to search for the Standard Model forbidden μ^- to e^- conversion and it is currently under construction at the Muon Campus of the Fermi National Accelerator Laboratory (Fermilab) in Batavia, United States.
The Standard Model (SM) is a very precise theory which has proven its effectiveness, but as measurements become more and more precise it has begun to show its limits. According to the SM, while Lepton Flavour Violation is allowed in the neutral sector, Charged Lepton Flavour Violation (CLFV) processes, such as μ^- to e^-, are forbidden. The nature of flavour is one of the most challenging open questions and it can be investigated through CLFV processes. These processes, especially in some Beyond the Standard Model scenarios, acquire a rate which is within reach of the next generation experiments. Moreover, many precision searches would yield a sensitivity to New Physics energy scales which are out-of-reach for the accelerators. Many CLFV processes have been investigated, but no direct violation has so far been observed. A very clean channel uses muons, since there is no need of hadronic corrections and they can be produced copiously in high-energy proton-target interactions, allowing high-intensity beams.
Mu2e goal is to measure the ratio between the rate of the neutrinoless conversion of muons into electrons recoiling against an Al nucleus, relative to the rate of muon capture in the nucleus:

$$R_{\mu e} = \frac{\mu^- + {}^{27}_{13}\mathrm{Al} \rightarrow e^- + {}^{27}_{13}\mathrm{Al}}{\mu^- + {}^{27}_{13}\mathrm{Al} \rightarrow \text{all } \mu \text{ captures}}. \tag{1}$$

The signature of this process is a mono-energetic electron with an energy nearly equivalent to the muon rest mass. At the moment of writing, Mu2e has reached the CD3 stage of approval by the United States Department of Energy and is under construction, with expected data-taking beginning at the end of 2025. In order to meet its aims, Mu2e plans to collect $\mathcal{O}(10^{18})$ stopped muons in 3 years of running, thus planning to improve the result of previous generation experiments (SINDRUM II) by a factor of 10^4.

This thesis is organized in six chapters:

1. In the first Chapter, CLFV processes and past searches are illustrated, together with the theoretical motivations for CLFV searches.

2. In the second Chapter, Mu2e is presented in its main components and detectors. Focus is also put on the signal and background characteristics and on the explanation of the experimental technique. The current status of the experiment is presented.

3. In the third Chapter, the design, construction and tests of the Mu2e calorimeter are discussed. This is an innovative crystal based calorimeter with solid state photosensor read-out that has to operate in a very challenging environment, i.e. in vacuum, in a radiation hard environment and in B-field. The Mu2e calorimeter is composed by two annular disks, each one filled with a matrix of 674 pure CsI crystals. Each crystal is read-out by a custom silicon photomultiplier (SiPM) matrix, coupled to custom electronic boards. The status of the calorimeter commissioning is summarised here.

4. In the fourth Chapter, the Quality Control Station for the calorimeter Readout Units (ROUs) is described. This Station allows to measure the main SiPM characteristics, like gain, collected charge and photon detection efficiency, providing a baseline for the ROUs performance.

5. In the fifth Chapter, the Mu2e Detector Control System (DCS) is described, with focus put to the implementation of the calorimeter power supplies DCS and of the related software tools.

6. In the sixth Chapter, the measurement of the normalization factor in the $R_{\mu e}$ ratio is presented. We propose to perform an independent measurement with respect to the experiment Stopping Target Monitor (STM) by relying on a calorimeter sub-system: CAPHRI (Calorimeter Precise High-Resolution Intensity detector). CAPHRI is composed by four LYSO crystals with SiPM readout that could provide a much faster and performing measurement of the muon capture rates with respect to the STM. The performed simulation and the characterization of the four procured LYSO crystals are illustrated in this Chapter.

I was personally involved in the work regarding the Mu2e Readout Units Quality Control station, which I have helped developing in its software and analysis parts, at the Laboratori Nazionali di Frascati (LNF). Always at LNF, I have also contributed to the

Front-End Electronics (FEE) calibration and monitored the performance of both the ROUs and the FEEs over the span of 9 months. I have then developed a first DCS interface for the Station power supplies, which I was able to improve and expand to the full calorimeter racks, while at Fermilab in May 2022. During this time, I was also able to analyse the response and resolution of the LYSO crystals readout with Mu2e SiPMs to fully characterize the procured CAPHRI components. I had the opportunity to personally perform those measurements and present the results to the Collaboration and at dedicated instrumentation/HEP conferences.

Chapter 1

Charged Lepton Flavour Violation in the Muon Sector

As high-energy subnuclear physics theories are being probed, their limits are becoming undeniable. The New Physics (NP) frontier has to look past the Standard Model (SM) for processes that were so far thought forbidden. Collider based searches are continuing with projects like the High-Luminosity Large Hadron Collider (HL-LHC) or even the Future Circular Collider (FCC), but it is the precision searches that offer the opportunity to probe physics up to a mass scale of $\mathcal{O}(10^4)$ TeV that will not be easily accessible by colliders. A very interesting prospect for precision searches is to detect SM-forbidden Charged Lepton Flavour Violation (CLFV) processes.

1.1 The Standard Model

The Standard Model is a non-abelian gauge theory which currently provides the best description of the fundamental constituents of matter and their interactions. The SM accounts for the strong, electromagnetic and weak forces, while the gravitational force has so far appeared negligible at the energies we have been able to investigate. Its relative weakness with respect to the other three forces can be appreciated in the comparative strength of the force between two protons when just in contact which, normalised at the strong force, is merely of the order of 10^{-39} [1]. The SM has three underlying theories which are quantum electrodynamics, the theory of electroweak processes developed by Glashow, Weinberg and Salam, and quantum chromodynamics. The associated gauge symmetry group is then $SU(3)_C \times SU(2)_L \times U(1)_Y$, where C stands for colour charge, L refers to the fact that only the left-handed components of the fields are involved in the interactions and Y refers to the hypercharge.

Quarks and leptons are the first constituents of ordinary matter and both can be

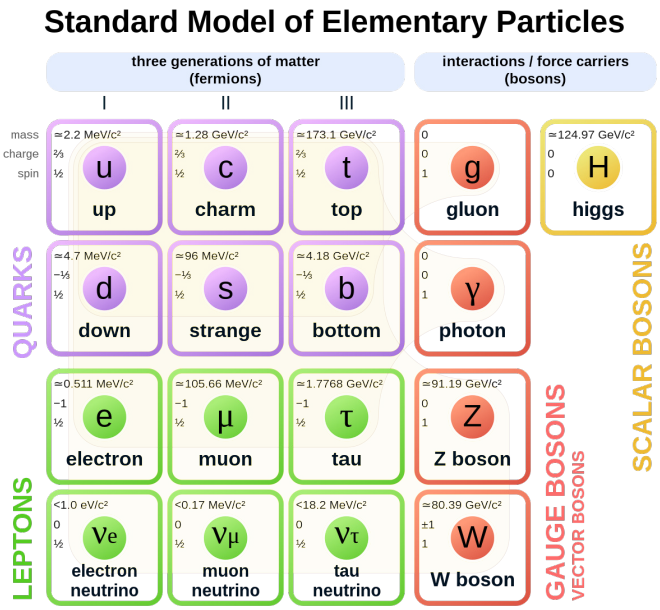

Figure 1.1: Fundamental constituents of matter according to the Standard Model.

arranged into three families, as depicted in Fig. 1.1. They are fermions, as they follow the Fermi–Dirac statistics and have spin 1/2 [2]. Each family of quarks has three color charges (r, g, b), originally introduced from both statistical and dynamical arguments, and a fractional charge of +2/3 for up-type quarks (up, charm and top) and −1/3 for down-type quarks (down, strange, bottom). Same-family quarks form a weakly charged doublet, as it occurs for a neutrino and its charged lepton partner. Also included in the list of elementary particles are the force particles that convey the interaction. These are particles with integer spin, called bosons as they obey the Bose–Einstein statistics. The photons mediate the electromagnetic interaction, the Z^0, W^+ and W^- vector bosons the weak interaction, eight gluons the strong interaction and the hypothetical graviton the gravitational interaction. Latest addition to the fundamental particles is the Higgs boson, a scalar spin 0 boson theorised in 1964 and observed in 2012 by independent experiments operating at LHC. This particle was predicted in the context of the Higgs mechanism, which is the process through which particles acquire mass via spontaneous symmetry breaking in the electroweak sector, i.e. $SU(2)_L \times U(1)_Y$. In addition to these fundamental constituents, for every fermion exists an anti-fermion, that is an antiparticle having the same mass, lifetime and spin of the corresponding particle, though with opposite electric charge and magnetic dipole moment.

The theories which constitute the SM as formulated today describe the interactions among these *building blocks* of matter and how the quarks compose heavier mass states, namely mesons and baryons, deeply studied since the beginning of this theory itself in

the 60s.

As accelerator energies increase and technological advancements allow more and more precise measurements, the Standard Model fails to describe the observed phenomena and has to be regarded as an effective theory. There are many points where it fails, as it does not explain the particle quantum numbers, such as the electric charge, weak isospin, hypercharge and colour, and contains at least 19 arbitrary parameters [3]. The number of free parameters increases even more as the neutrino oscillation and masses are taken into account.

In this scenario it becomes mandatory to look beyond the SM and to keep testing its limits with precision measurements and search for forbidden processes.

1.2 Charged Lepton Flavour Violation in muons

Considering the initial naive hypothesis of massless neutrinos, the the SM Lagrangian is invariant under global $U(1)_e \times U(1)_\mu \times U(1)_\tau$ rotations of the lepton fields [4]. With this assumption, individual lepton flavour numbers - electron, muon and tau - must be conserved. These quantum numbers are L_e, L_μ, L_τ and have the values of $+1$ for leptons and -1 for antileptons. In the last decades there has been extensive proof of neutrino oscillation, from the 1998 Super Kamiokande result with atmospheric neutrinos [5], to the recent conclusive data from the Opera experiment which utilised neutrinos produced at CERN [6]. The quantum-mechanical phenomenon of neutrino oscillation has been established for atmospheric, accelerator, solar and reactor neutrinos, proving that in the neutral leptons sector, flavour mixing is not forbidden and that neutrinos have actually non-zero mass [7]. The weakly-interacting flavour neutrinos (ν_μ, ν_e, ν_τ) are then superpositions of the mass eigenstate neutrinos (ν_1, ν_2, ν_3) which have a defined mass (m_1, m_2, m_3, respectively). These weak and mass eigenstates are related via the Pontecorvo–Maki–Nakagawa–Sakata (PMNS) unitary matrix:

$$\begin{pmatrix} \nu_\mu \\ \nu_e \\ \nu_\tau \end{pmatrix}_L = U_{PMNS} \begin{pmatrix} \nu_1 \\ \nu_2 \\ \nu_3 \end{pmatrix}_L = \begin{pmatrix} U_{e1} & U_{e2} & U_{e3} \\ U_{\mu 1} & U_{\mu 2} & U_{\mu 3} \\ U_{\tau 1} & U_{\tau 2} & U_{\tau 3} \end{pmatrix} \begin{pmatrix} \nu_1 \\ \nu_2 \\ \nu_3 \end{pmatrix}_L \tag{1.1}$$

where the subscript L indicates that the left-handed components of the field is considered. Alternatively, Eq. 1.1 can be written in compact notation as

$$\nu_{\alpha L} = \sum_i U_{\alpha i} \nu_{iL} \tag{1.2}$$

with $\alpha = e, \mu, \tau$ and $i = 1, 2, 3$.

The PMNS matrix can be written as the product of three rotations through angles θ_{23}, θ_{13}, θ_{12}, with the second rotation depending on a phase δ_{CP}, and of a diagonal matrix of phases P. The PMNS matrix can then be expressed as in Eq. 1.3:

$$U_{PMNS} = \begin{pmatrix} 1 & 0 & 0 \\ 0 & c_{23} & s_{23} \\ 0 & -s_{23} & c_{23} \end{pmatrix} \begin{pmatrix} c_{13} & 0 & s_{13}e^{-i\delta_{CP}} \\ 0 & 1 & 0 \\ -s_{13}e^{i\delta_{CP}} & 0 & c_{13} \end{pmatrix} \begin{pmatrix} c_{12} & s_{12} & 0 \\ -s_{12} & c_{12} & 0 \\ 0 & 0 & 1 \end{pmatrix} P \qquad (1.3)$$

with $c_{ij} \equiv cos\theta_{ij}$ and $s_{ij} \equiv sin\theta_{ij}$ and P which can either be a unit matrix in case of Dirac neutrinos, or a diagonal matrix containing two required phases in the Majorana neutrinos case.
In the weak charged current interaction of a neutrino with a lepton of a given flavour, the neutrino is then not going to be a mass eigenstate, but a coherent superposition of mass eigenstates. This coherence makes neutrino oscillation possible and this phenomenon is the clear proof of Lepton Flavour Violation (LFV).

LFV has been observed only in the neutrino sector and the charged lepton partners - muon, electron and tau - do not seem to act in a symmetric way. CLFV processes have been searched since the discovery of the muon, but no evidence has yet been found. In Fig.1.2 are shown two Feynman diagrams for CLFV processes concerning muon conversion into an electron.

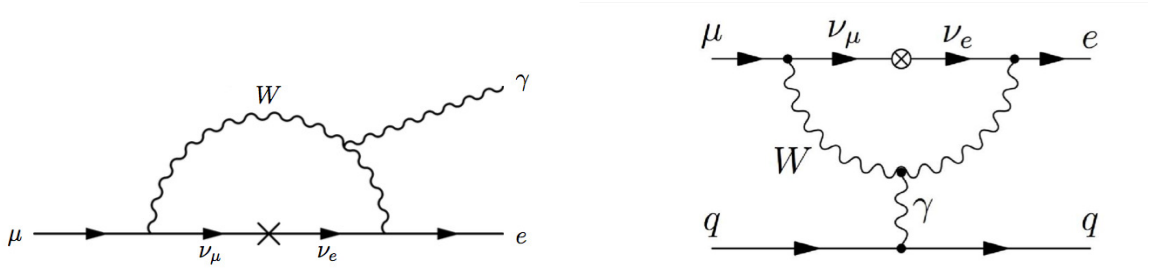

(a) $\mu \to e\gamma$ (b) $\mu^- N \to e^- N$

Figure 1.2: Feynman diagrams with two examples of muon to electron conversion.

1.2.1 CLFV process

Charged-lepton flavour violation comprehends all charged-lepton processes that violate lepton-flavour number. These include $\ell \to \ell'\gamma$, $\ell \to \ell'\ell''\bar{\ell}'''$, $\ell + X \to \ell' + X$ and $X \to \ell\ell$ where ℓ, $\ell', \ldots \in \{e, \mu, \tau\}$ and X are states that have no lepton-flavour number. The rates for the various CLFV processes depend on the mechanism behind neutrino masses and lepton mixing, so different Lagrangians which describe neutrinos mass generation

lead to very different CLFV rates. For instance, since the rate of ordinary muon decay can be expressed as $\Gamma(\mu \to e\nu\bar{\nu}) = m_\mu^2 G_F^2/192\pi^3$ with $G_F/\sqrt{2} = g^2/8M_W^2$, the branching ratio for $\mu \to e\gamma$ can be expressed as

$$BR(\mu \to e\gamma) \simeq \frac{\Gamma(\mu \to e\gamma)}{\Gamma(\mu \to e\nu\bar{\nu})} = \frac{3\alpha}{32\pi} \left| \sum_{i=2,3} U_{\mu i}^* U_{ei} \frac{\Delta m_{1i}^2}{M_W^2} \right|^2 < 10^{-54} \tag{1.4}$$

with $U_{\alpha i}$ elements of the PMNS matrix, Δm_{1i}^2 the neutrino mass-squared differences and M_W the W boson mass. This limit applies to some neutrino mass models and if neutrinos get their masses through renormalizable Yukawa interactions with the Higgs boson, there is the suppression of flavour-changing neutral currents due to the GIM mechanism. Rates with an analogous order of magnitude are expected also for $\mu \to eee$, $\mu \to e$ conversion and also rare processes which involve tau leptons. Nevertheless, for instance, in another scenario involving one sterile neutrino (ν_4 with a mass $m_4 \gtrsim 10\,\text{GeV}$) these ratios go within or slight below the reach of experimental resolution [8]. Different models hint to a reachable value of the BR and an experimental observation of CLFV would be a clear sign of new dynamics associated to an extension of the lepton sector of the SM.

CLFV can be investigated through many channels: μ and τ decays, meson decays (J/ψ, π^0, K_L^0, K^+, B^0), Z^0 and Higgs decays. The experiments involving muon decays have two advantages with respect to other CLFV searches: (i) it is simple to obtain high intensity muon beams and (ii) the final states are always leptons, allowing reliable theoretical calculation and avoiding hadronic corrections. Due to these aspects, the CLFV searches in the muon sector were carried out since the discovery of the muon and have been progressed enormously along time reaching extremely high sensitivity. In Table 1.1 the current sensitivity for processes involving muon CLFV is shown [9] and the evolution of the ratio for three golden channels for muon CLFV searches is depicted in Fig. 1.3, together with the prospected values. Given their availability and importance in the current physics programs, focus will be put on this line of research.

Other searches not involving muon CLFV can be pursued [10]. For the remaining cases, except for kaons since it is not possible to produce a dedicated beam, general multipurpose detectors have been used (ATLAS, CMS, LHCb and others). For instance, the tau lepton could be a very promising source of CLFV decays and many channels could be investigated ($\tau \to 3\ell, \ell\ell'\ell', \ell\gamma$ with $\ell = \mu, e$). These searches are affected by the τ very short lifetime, so can be performed only in high energy environments. Also top quark decays, Z boson decays and meson decays offer important channels to investigate CLFV processes in high energy accelerator environments.

It is possible to work in an independent framework to consider CLFV mechanism

Process	Experiment	Limit
$\mu^+ \to e^+\gamma$	MEG	4.2×10^{-13}
$\mu^\pm \to e^\pm e^- e^+$	SINDRUM	1.0×10^{-12}
$\mu^- N \to e^- N$	SINDRUM-II	$6.1(7.1) \times 10^{-13}$ Ti(Au)
$\mu^- N \to e^+ N'$	SINDRUM-II	5.7×10^{-13}

Table 1.1: Current experimental upper limits on the branching ratios of CLFV processes for muons at 90% CL.

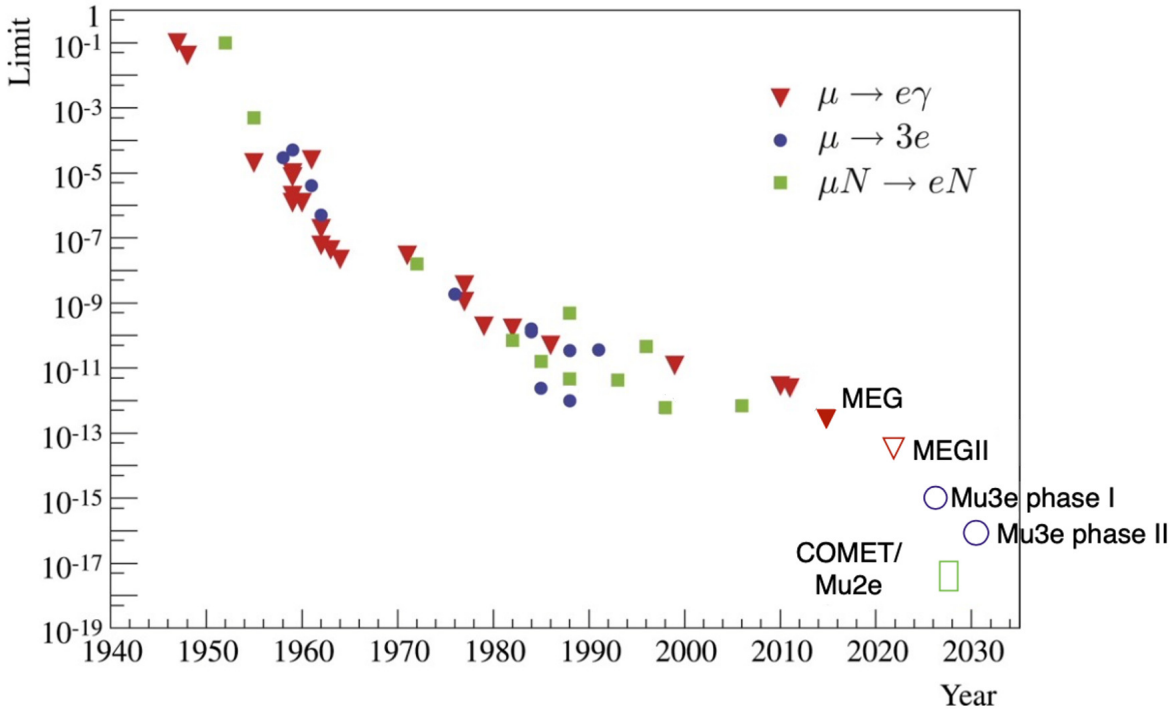

Figure 1.3: The history of limits for branching ratios of three CLFV processes from muons. Empty markers indicate expected measurements [11].

behind neutrino masses and related oscillation. There is reason to believe that there are several degrees of freedom beyond those in the Standard Model. Lepton-flavour numbers in the neutral sector have proved they do not represent reliable quantum numbers. So, it is expected that these new degrees of freedom are involved in virtual processes and will mediate CLFV at some higher order of perturbation theory. It is then possible to add to the SM Lagrangian the following effective Lagrangian [4]:

$$\mathcal{L}_{CLFV} = \frac{m_\mu}{(1+\kappa)\Lambda^2}\bar{\mu}_R\sigma_{\mu\nu}e_L F^{\mu\nu} + \frac{\kappa}{(1+\kappa)\Lambda^2}\bar{\mu}_L\gamma_\mu e_L\left(\sum_{q=u,d}\bar{q}_L\gamma^\mu q_L\right) \tag{1.5}$$

The subscripts L and R indicate the chirality of the SM fermion fields, $F_{\mu\nu}$ is the

photon field strength, m_μ the mass of the muon. The coefficients of the two types of operators are parametrized by two contants, Λ and κ, which are independent between themselves: Λ is a dimensionful (mass) parameter which represents the effective mass scale of the new degrees of freedom previously mentioned, κ is dimensionless and governs the relative weight of the two operators. Depending on the value of κ we can then determine whether the dominant NP contribution to CLFV is expressed by a magnetic moment-type operator ($\kappa << 1$) or by a four-fermion interaction ($\kappa >> 1$). The two terms of this Lagrangian can be identified as a *loop* and a *contact* term. The former mediates directly processes like $\mu \to e\gamma$ and, at an order α due to the electromagnetic photon interaction, $\mu \to eee$ and $\mu N \to eN$ (Fig. 1.4). This implies that if a $\mu \to e\gamma$ signal is found, then also a signal from conversion process is expected. Instead, if no $\mu \to e\gamma$ is seen, there is still a possibility to see a conversion CLFV event because of the non-photonic contribution to this process, since it is related to the *contact* term which does not give rise to a on-shell photon. The different regions which these processes allow to probe, can be also appreciated in Fig. 1.5 where the sensitivity limits for NP are shown. For $\kappa << 1$, a limit on $\mathrm{BR}(\mu \to e\gamma) < 10^{-14}$ would allow to study a region of Λ of almost 4×10^3 TeV, while the searches for muon to electron conversion would probe up to 8×10^3 TeV. Assuming that new physics will predominantly induce flavour-violating effective interactions such that $\kappa << 1$, at one-loop level, then the relation between Λ and the masses of new states which could be found, M_{new}, is

$$\frac{1}{\Lambda^2} \sim \frac{eg^2}{16\pi^2}\frac{\theta_{e\mu}}{M_{new}^2} \tag{1.6}$$

with g the coupling of these states to SM fields and $\theta_{e\mu}$ a flavour violating factor, likely inaccessible at the LHC energies. Assumptions can be made on g and given M_{new} known, important constraints can be put on $\theta_{e\mu}$. Even if $\theta_{e\mu}$ value is model dependent, already strong constraints can be put thanks to $\mu \to e$ conversion limits or measurements of the muon anomalous magnetic moment. Other new physics scenarios will lead to different values of κ, including $\kappa \sim 1$ and $\kappa >> 1$ and from Eq. 1.5, in the limit $\kappa >> 1$, one obtains

$$\frac{1}{\Lambda^2} \sim \frac{\lambda'^2}{M_{new}^2} \tag{1.7}$$

where λ'^2 is the coupling with the potential term in a SUSY scenario [12] where the branching ratio for $\mu \to e$ conversion is much larger than that of $\mu \to e\gamma$ and $\mu \to eee$.

One characteristic of this type of measurements is that the observation of a signal would give very light information about NP. For instance, a CLFV signal as a $\mu \to e$ conversion event does not allow to measure separately Λ and κ, but only a function of

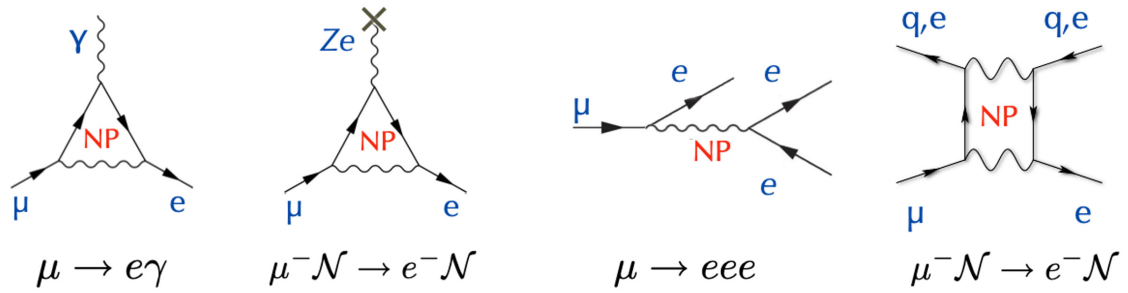

Figure 1.4: Representation of some CLFV processes where New Physics could be measurable. The two diagrams on the left are mostly relevant to investigate $\kappa << 1$, the other two are related to the *contact* term of the Lagrangian ($\kappa >> 1$).

both. To learn more about new physics, it is needed to combine the measured rates of more than one CLFV process, like $\mu \rightarrow eee$, $\mu \rightarrow e\gamma$, or to consider also recent studies of the electromagnetic properties of the charged leptons, neutrinos properties and also direct high energy searches as the ones that can carried out at Tevatron or LHC. Nevertheless, the lack of observation of CLFV can constrain many models, including some Super-Symmetric extensions, and provide critical information about our understanding of what lies beyond the SM.

1.2.2 Experimental Searches for CLFV in the muon sector

Searches for CLFV processes in the muon decay started almost as soon at the muon was discovered from cosmic rays in 1937. The nature of this "mesotron" was unclear because while it was thought to be the Yukawa meson, Conversi, Pancini and Piccioni stopped it in carbon. Yukawa's predicted meson should be absorbed by the carbon nuclei, and no decay should be observed, in contrast with the results obtained by the three Italian physicists. The question of the decay of the muon continued with the measurement by Pontecorvo and Hincks [14] as they assumed the μ as an excited state of the electron and looked, without success, for $\mu \rightarrow e\gamma$. In the following years also muon conversion processes in nuclei started to be searched and not too much later also $\mu \rightarrow eee$. In the following paragraphs, the main characteristics of these three processes are illustrated, together with the latest associated experimental results.

$\mu^+ \rightarrow e^+\gamma$

The signal from $\mu^+ \rightarrow e^+\gamma$ is a positron and a photon emitted back-to-back with the energy in the rest frame of the muon equal to half the muon mass, namely $E_{e^+} = E_\gamma =$

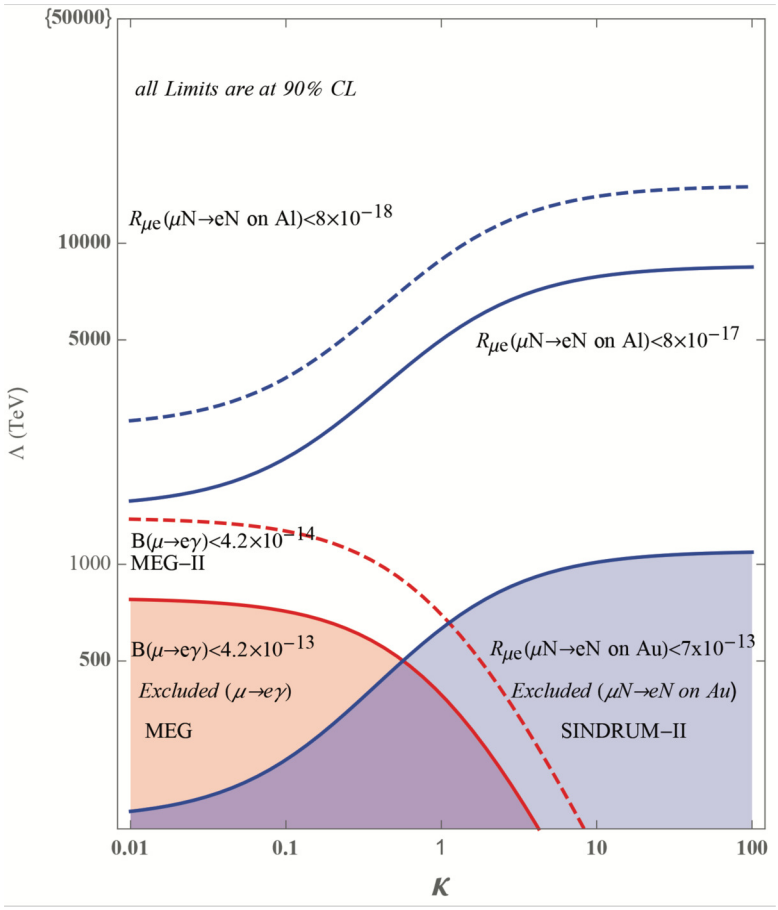

Figure 1.5: Sensitivity limits for New Physics scale Λ as a function of κ for $\mu \to e$ conversion in ^{27}Al and for $\mu \to e\gamma$. The coloured areas show the excluded regions and upper limits expected for future experiments are also shown. Plot from [13].

$m_{\mu^+}/2 = 52.8\,\text{MeV}$. For this search, positive muons are used to avoid the formation of muonic atoms in the muon stopping target. Since extremely small branching ratios have to be explored ($\sim 10^{-13}$), a very large number of muons is required (more than $10^7\,\mu$/sec) [15]. Experiments who work in this channel have to cope with two main sources of background: a radiative muon decay (RMD) or an accidental overlap of a Michel positron and a photon. The first is the $\mu^+ \to e^+\nu_\mu\nu_e\gamma$ decay that can be misinterpreted as a signal event when the two neutrinos carry away a small fraction of the energy. The second can be the accidental coincidence of a SM μ^+ decay and a photon from a RMD or the annihilation of a positron in flight. To improve the signal to background ratio and data collection efficiency, a direct-current beam is used, since the rate of accidental coincidences is proportional to the square of the μ^+ decay rate [16]. In this respect, when increasing the beam rate, the sensitivity is limited by this quadratic increase so that the solution is to improve resolution to define both the photon and electron energies as well as their relative timing and opening angles. So far, the best upper limit for this process

is 4.2×10^{-13}, measured by the MEG experiment at PSI. The MEG II experiment, a sophisticated detector upgrade of MEG with improved calorimetry, tracking and timing counter systems, aims to look for this CLFV decay with higher beam intensity achieving a factor of 10 increase in sensitivity, up to 6×10^{-14} at 90% CL, in three years of data taking [17].

$\mu^- N(A,Z) \to e^- N(A,Z)$

In this channel, the measurement performed is the ratio $R_{\mu e}$ between the neutrinoless conversion of the muon into electron, in the field of a nucleus, and the nuclear capture process. The relative rates of capture and decay are nucleus dependent, for instance, in aluminum the capture rate is 61% and the decay rate is 39%, whereas in carbon the capture rate is just 8%. The conversion signal is a monoenergetic electron at an energy $E_e = E_\mu - BE(1S) - E_{recoil}$, with its value nuclear dependent. The current best limit has been set by the SINDRUM II experiment, which used different targets, and obtained $R_{\mu e} = 7 \times 10^{-13}$ in Au at 90% CL. The Mu2e experiment, under construction at Fermilab, aims to reach a 90% CL on $R_{\mu e}$ of 8×10^{-17}. The concurrent experiment, COMET, is preparing their apparatus at J-PARC, Japan, with a planned sensitivity of $\mathcal{O}(10^{-15})$ in the first phase of the experiment. Both experiments will use an Al target. In the same period, again at J-PARC but with a carbon target, there will be the DeeMe experiment which has an expected sensitivity of $\mathcal{O}(10^{-13})$. There are three main sources of background in this channel: radiative pion capture, electrons from decay of muons in atomic orbit, and cosmic rays. The first channel is difficult to eliminate in the beamline, since muons are obtained from pion decay. However it is much prompter than the muon decay to that, to address this issue, both Mu2e and COMET will use pulsed muon beams, delaying the data-taking window until the pion stopping rate decreases sufficiently to be negligible.

$\mu^+ \to e^+ e^+ e^-$

In the $\mu \to eee$ decay, the experimental signature is three charged particles in the final state, with an invariant mass that is consistent with the mass of a muon. The current best experimental upper limit for the rate of this process is set by the SINDRUM experiment at 1.0×10^{-12} with a 90% CL. The backgrounds come from $\mu \to e\nu\nu\gamma$ with two low-energy neutrinos and the further conversion of the photon into an e^+e^- pair and from a radiative muon decay with the conversion of the photon, accidentally overlapped with a SM decay of a muon. At PSI, the Mu3e collaboration aims for a 10^{-16} single event sensitivity in the $\mu^\pm \to e^\pm e^+ e^-$ search, improving by four orders of magnitude the

current limit.

Other physics channels at Mu2e

In addition to the primary search channel, searches for $\mu \to e$ conversion can also have sensitivity to other CLFV processes Beyond the Standard Model (BSM) such as

- $\mu^- N \to e^+ N'$
  This search can be conducted in parallel to the main channel search in Mu2e since the detector is symmetric for the electron/positron charges. COMET could do this only on its first phase. The relevance of such a process is that not only it would violate lepton flavour conservation, but also lepton number conservation ($\Delta L = 2$), thus offering a complementary search for the neutrinoless double beta decay channel. The experimental signature is a monochromatic positron with a momentum of $\sim 100\,\text{MeV}$ from the $\mu^- N(A, Z) \to e^+ N(A, Z-2)$ transition, with the final nucleus in the ground state.

- $\mu^- \to e^- X$
  In this process X denotes a light neutral invisible particle. There are a series of BSM candidates, including axion-like particles.

1.2.3 CLFV for Beyond of the Standard Model physics

CLFV processes offer unique discovery potential for many BSM scenarios. Observation of a CLFV transition would be an undeniable sign of new physics, which goes beyond that induced by non-zero neutrino masses. Here are listed some BSM physics scenarios and their relationship with CLFV searches.

SUSY scenarios

The minimal required extension of the SM is called Minimal Supersymmetric Standard Model (MSSM) where each SM particle has its superpartner. After electroweak symmetry breaking, the superpartners of the SM gauge bosons and the Higgs boson mix forming two charged Dirac fermions (charginos, $\tilde{\chi}^{\pm}_{1,2}$) and four Majorana fermions called neutralinos ($\tilde{\chi}^{0}_{1,2,3,4}$). The MSSM Lagrangian consists of two parts: the SUSY-invariant and the soft SUSY-breaking terms. The ordinary Yukawa coupling constants are included in a scalar function called the superpotential ($W(\phi)$). In the MSSM, generally the soft SUSY-breaking mass terms become a new source of flavour mixing: in the basis where the lepton mass matrix is diagonal, nonzero off-diagonal matrix elements in the slepton mass matrix introduce LFV. Fig. 1.6 depicts the Feynman diagram of the

$\mu^+ \to e^+\gamma$ process in this scenario. Measuring the branching ratio of that process would help constraining the off-diagonal elements of the slepton mass matrix.

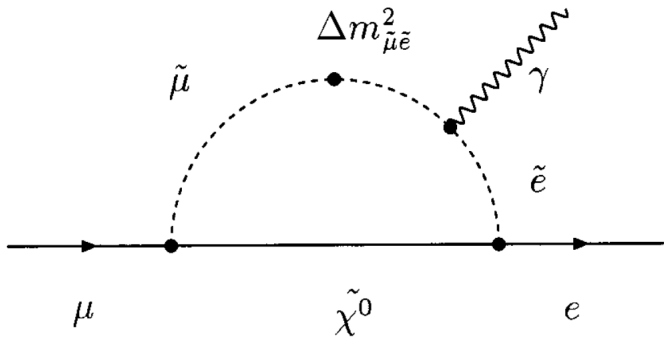

Figure 1.6: Feynman diagram for $\mu^+ \to e^+\gamma$ taking into account slepton flavour mixing, $\Delta m^2_{\tilde{\mu}\tilde{e}}$.

SUSY GUT (Grand Unified Theories) with the SU(5) group are well motivated extensions of the SM and the source of LFV comes from the off-diagonal elements of the right-handed slepton mass matrix [18]. Large LFV effects are also expected in SO(10) SUSY GUT where both left and right-handed receive LFV effects. With respect to SU(5) there is an enhancement of the branching ratio for $\mu \to e\gamma$ of the order of $(m_\tau/m_\mu)^2$, yielding branching ratios for muon LFV processes within reach of the experiments. The expected magnitudes of the LFV effects depend on the Yukawa couplings and the flavour mixing in the lepton sector. For example, $\mu \to e$ conversion rate in Ti can be computed in this context, as a function of SUSY breaking parameters, assuming very massive right-handed neutrinos and experimental constraints from LHC and on θ_{13} [19].

Muon LFV may be observable through renormalization effects in the slepton mass matrix if the mixing between fields of gauge mediators and the ordinary matter fields is allowed or a similar effect can appear in a supersymmetric model with vector-like leptons.

Scalar leptoquarks

Leptoquarks (LQ) are particles predicted in GUTs which pose an interaction vertex connecting leptons with quarks. Leptoquarks are classified into 10 representations, 5 scalar and 5 vector particles. In this scenario, the effective hamiltonian for muon to electron conversion has its source in the dipole transition operator that comes from the loop diagrams responsible for $\mu \to e\gamma$. In Fig. 1.7 is shown the λ parameter, combination of the couplings between quarks and leptons, and the scalar leptoquark mass. As can be seen from that plot, according to calculations performed in [20], Mu2e will be able to constrain LQ couplings with different strength, depending on the parameters region of

space.

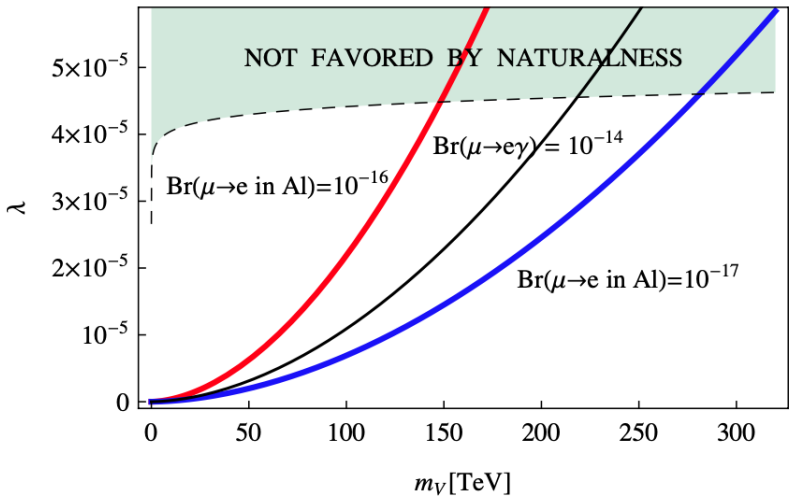

Figure 1.7: The coupling parameters combination λ as a function of the scalar leptoquark mass for two values of the branching ratio of $\mu \to e$ conversion in Al, relevant for the Mu2e experiment.

Higgs and LFV

Flavour violating decays of the Higgs boson ($h \to e\mu, e\tau, \mu\tau$) arise at tree level, having assumed flavour violating Yukawa interactions, and muon CLFV searches can constrain the couplings of the Higgs boson with e and μ. Particularly, strong constraints on the flavour violating Yukawa coupling, $Y_{\mu e}$ and $Y_{e\mu}$, come from $\mu \to e$ conversion in nuclei. In Fig. 1.8, the relevant tree-level and one-loop diagram are shown. There are also two-loops contributions which are actually numerically comparable to tree-level ones. Even if with more difficulties, through muon conversion, one could also infer on the Yukawa couplings involving taus [21].

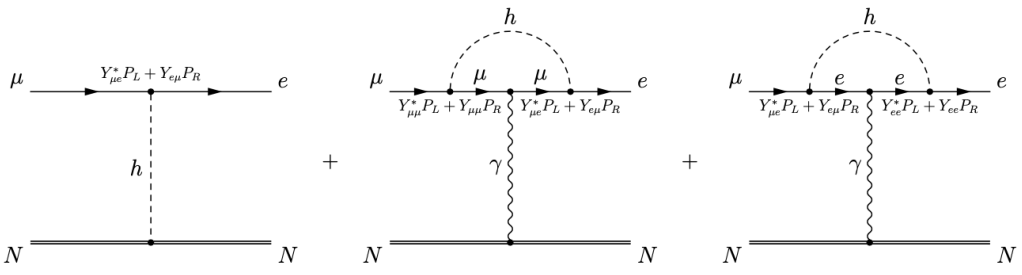

Figure 1.8: Tree-level and one-loop diagrams contributing to $\mu \to e$ conversion in nuclei via the flavour violating Higgs Yukawa couplings $Y_{\mu e}$ and $Y_{e\mu}$.

Little Higgs models

The SM does not provide a microscopic explanation for electroweak symmetry breaking or an explanation for the generation of its scalar potential. Little Higgs models offer a way to solve the little hierarchy problem [22]. In these models the Higgs boson is considered as a pseudo-Goldstone boson. The original construction of Little Higgs models suffered severely from electroweak precision tests which led to the introduction of a discrete symmetry called T-parity. Under this new symmetry the particles have distinct transformation properties, that is, they are either T-even or T-odd. One of the most attractive models of this class is the Littlest Higgs model with T-parity (LHT), where the discrete symmetry forbids tree-level corrections to electroweak observables, so weakening the electroweak precision constraints. In this context, the T-even fermion sector contains, in addition to the SM fermions, a heavy top quark partner and the T-odd fermion sector consists of three generations of mirror quarks and leptons. One of the important ingredients of the mirror sector is the existence of four CKM-like unitary mixing matrices, two for mirror quarks (V_{Hu}, V_{Hd}) and two for mirror leptons ($V_{H\nu}$, $V_{H\ell}$), that are related via $V_{Hu}^{\dagger}V_{Hd} = V_{CKM}$ and $V_{Hu}^{\dagger}V_{H\ell} = V_{PMNS}^{\dagger}$. Here the relevant parameters are the mixing angles θ_{ij}^{ℓ} and complex phases δ_{ij}^{ℓ} of $V_{H\ell}$, which can be determined from limits on the rates of CLFV processes.

Left-right symmetric models

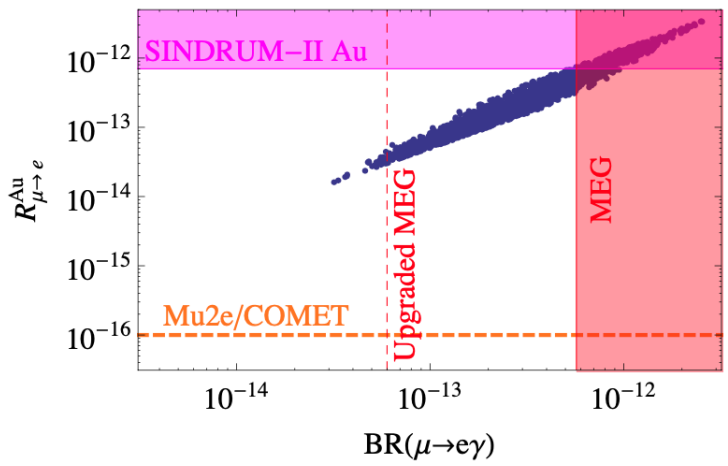

Figure 1.9: Correlation between the branching ratio for $\mu \to e\gamma$ and the muon to electron conversion rate in Au in a left-right symmetric model.

Left-right symmetric models are extensions of the Standard Model that restore parity at short-distances and which allow one to build neutrinos mass models which can be

experimentally probed. In [23] is argued that a simple paradigm for understanding the small neutrino masses is the type-I seesaw mechanism and in the left-right symmetric theory of weak interactions the needed ingredients appear naturally. This L-R symmetric model is based on the gauge group $SU(2)_L \times SU(2)_R \times U(1)_{B-L}$ and the right-handed neutrino field arises as the necessary counterpart of the left-handed field, while the see-saw scale is identified as the one where the $SU(2)_R$ symmetry is broken. Assuming the new breaking scale to be at 5 TeV, the consequent rates for $\mu \to e$ conversion and $\mu \to e\gamma$ are within reach of the future experiments like Mu2e and MEG II (Fig. 1.9)

CLFV and neutrino masses

Even if neutrinos oscillations are deeply intertwined with CLFV processes, one cannot accurately infer on CLFV parameters from neutrino oscillations measurements, given the dependence of CLFV processes on the mechanism behind neutrino masses. This implies that different Lagrangians describing neutrino mass generation give very different rates for lepton flavour violating generation, but also that information on CLFV processes could disclose important characteristics of the neutrino mass model. The relationship between neutrino mixing parameters and CLFV can be direct or indirect. In Fig. 1.10 is reported the rate of different muon CLFV processes, directly associated to $|U_{e3}| \simeq sin\theta_{13}$ for the normal (left) and inverted (right) neutrino mass hierarchy.

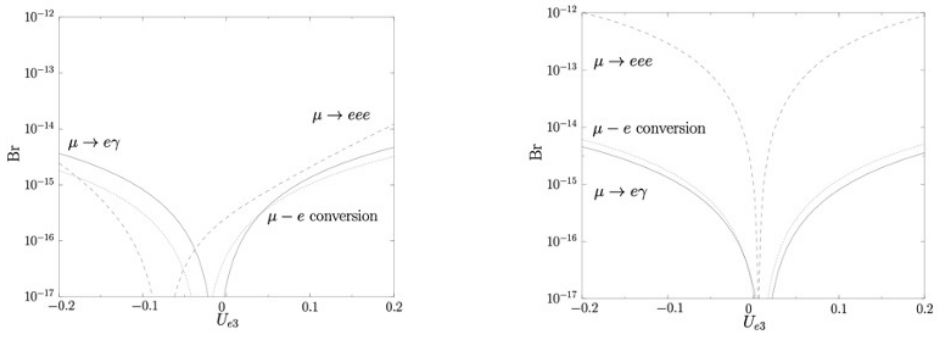

Figure 1.10: The branching ratios of the processes $\mu \to e\gamma$ (solid line), $\mu \to 3e$ (dashed line), $\mu \to e$ conversion in Ti (dotted line) for the normal (left) and inverted (right) neutrino mass hierarchy. The ratios are plotted as a function of $|U_{e3}|$ in a framework where neutrino masses arise from the presence of a triplet Higgs field [24].

1.3 Lepton Number Violation

Lepton number and baryon number are, at the classical level, accidental global symmetries of the renormalizable Standard Model Lagrangian. At the quantum level these

symmetries are anomalous, i.e. they are violated by non-perturbative effects [25]. If one adds new degrees of freedom to the SM there is then violation of both lepton and baryon number conservation, having considered operators of order five or higher. Regardless of the efforts so far made for this search, yet no Lepton Number Violating (LNV) process has been found. A possible explanation is that the degree of this violation in unknown and there is the possibility that only a subset of LNV phenomena are within reach of current particle physics experiments [26]. The evidence that neutrinos have small, but yet non-zero masses, is often seen as an indirect evidence of LNV new physics. Searches for the nature of neutrinos - Dirac or Majorana fermions - are often searches for LNV processes. The observation of those would confirm the Majorana nature of neutrinos. The most used channel is neutrinoless double-beta decay ($0\nu\beta\beta$), $N(A,Z) \rightarrow N'(A,Z+2) + 2e^-$, and several experiments searching for $0\nu\beta\beta$ are ongoing or a being built ([27], [28], [29], [30]). The most stringent limit on $0\nu\beta\beta$ has been set by the GERDA experiment which measured the half life for this process in ^{76}Ge to be $T_{1/2}^{0\nu\beta\beta} > 1.8 \times 10^{26}$ years at 90% CL. [28]. This channel is the most sensitive for LNV, but another way to investigate processes with a change of lepton number $\Delta L = 2$ is through $\mu^- \rightarrow e^+$ conversion ($\mu^- + N(A,Z) \rightarrow e^+ + N'(A,Z-2)$). This is a channel which can be studied by many experiments under development: COMET [31] and DeeMe [32] at J-PARC and Mu2e [33] at Fermilab. The Feynman diagrams for these two processes are shown in Fig. 1.11.

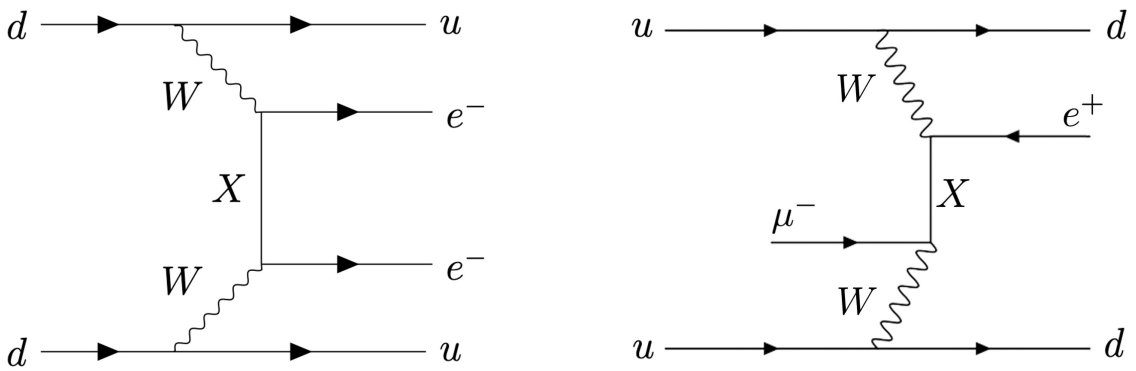

Figure 1.11: Feynman diagrams of $0\nu\beta\beta$ (left) and $\mu^- \rightarrow e^+$ conversion (right). The particle X represents a known neutrino.

The best bounds on the $\mu^- \rightarrow e^+$ conversion rate relative to the capture rate on titanium were obtained by the SINDRUM II experiment [34]:

$$R^{Ti}_{\mu^- e^+} \equiv \frac{\Gamma(\mu^- + Ti \rightarrow e^+ + Ca)}{\Gamma(\mu^- + Ti \rightarrow \nu_\mu + Sc)} < \begin{cases} 1.7 \times 10^{-12}\ (GS,\ 90\%\,\mathrm{CL}) \\ 3.6 \times 10^{-11}\ (GDR,\ 90\%\,\mathrm{CL}) \end{cases} \tag{1.8}$$

where GS considers scattering off titanium to the ground state of calcium and GDR considers the transition to a giant dipole resonance state. Since the nucleus changes from initial to final state, there is no coherent enhancement of the ground state transition, as it is instead for $\mu^- \to e^-$ conversion. Usually is then assumed a GDR for the daughter nucleus, with both a mean energy and a width of 20 MeV, resulting in a broad momentum distribution for the emitted positron. Looking at future experiments, in particular at Mu2e, the expected reaction is ${}^{27}Al + \mu^- \to e^+ + {}^{27}Na$. With the Al stopping target present in Mu2e, the expected positron energy is 83.9 MeV for GDR transitions, where the search would be blinded by the intense radiative muon capture (RMC) background. Fortunately, calculations [35] indicate that around 60% of the transitions will go to the GS in the final state, yielding a positron with a momentum $p_e \simeq 94.5$ MeV, allowing Mu2e to look for this process. Both COMET and Mu2e will search for $\mu^- \to e^+$ conversion with an experimental sensitivity down to 10^{-17} [36]. Any interaction which involves a $\Delta L = 2$ other than the tree level shown in Fig 1.11 could lead to a muon to positron conversion, as studied in [37]. There it is used an effective operator description and the estimation of the Majorana neutrino exchange case, including the one and two loop corrections, is normalized with the tree level case. The conversion rate $R_{\mu^- e^+}$ is estimated according to the new physics energy scale Λ and their dependence is show in Fig. 1.12. Taking into consideration the expected sensitivity of Mu2e, the new physics scale accessible is around 40 GeV, low in comparison to the $\mathcal{O}(10^4)$ TeV when looking for $\mu^- \to e^-$ conversion events.

1.3.1 Past $\mu^- \to e^+$ experiments

The results from past experiments are listed in Table 1.2. Most of these experiments employed similar setups in which a muon beam would interact with a target. The muons would then rapidly fall to a 1s orbit in an atom of the target material. A tracker is used to measure the outgoing positron energy. As mentioned, the final state nucleus can either be in a ground state or in an excited state. If the transition occurs to the ground state, the signal positron is monoenergetic

$$E_{e^+} = m_\mu + M(A, Z) - M(A, Z-2) - BE_\mu - E_{recoil} \tag{1.9}$$

where m_μ is the muon mass, $M(A, Z)$ is the mass of the nucleus, BE_μ is the binding energy of the muonic atom, and E_{recoil} is the recoil energy of the outgoing nucleus. Similarly to photo-nuclear reactions, the $\mu^- \to e^+$ process may leave the target nuclei in an excited state, a giant dipole resonance, which is a collective vibration of protons against neutrons with a dipole spatial pattern. For example, a GDR with a 20 MeV

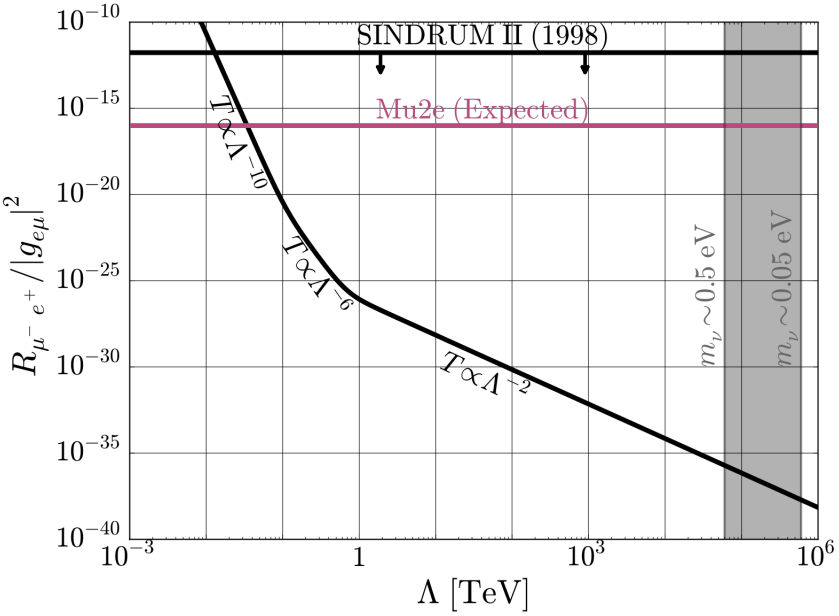

Figure 1.12: The $\mu^- \to e^+$ conversion rate as a function of the scale of new physics, Λ. The black line shows the current bound by the SINDRUM II Collaboration, while the pink line indicates the estimate of the reach of the Mu2e experiment, both assuming $|g_{e\mu}|^2 = 1$. The g coefficients characterise the operator distinct flavour components. The grey region highlights the range of Λ necessary to generate neutrino masses between 0.05 eV and 0.5 eV.

width was assumed in [34], resulting in a much wider energy distribution for the signal positron.

Target	Upper limit	Experiment	Year	Detector type	GS/GDR
Ti	3.6×10^{-11}	SINDRUM II	1998	Drift Chamber	GDR
	1.7×10^{-12}	SINDRUM II	1998	Drift Chamber	GS
^{32}S	9×10^{-10}	SIN	1980	Streamer Chamber	GDR
Cu	2.6×10^{-8}	\	1972	Spark Chamber	GS/GDR

Table 1.2: Table which sums up all the last results performed on the upper limit for $\mu^- \to e^+$ conversion, for different target nuclei [36].

SINDRUM II

The SINDRUM II spectrometer consists of a set of concentric cylindrical detectors inside a superconducting solenoid [38]. A muon beam, produced from 590 MeV protons, hits a target made of titanium foils (Fig. 1.13). Before the target, two moderators are able to stop 99% of the spurious pions. Two plastic scintillator hodoscopes and a lucite Cherenkov hodoscope provide timing and triggering information. The conversion particle

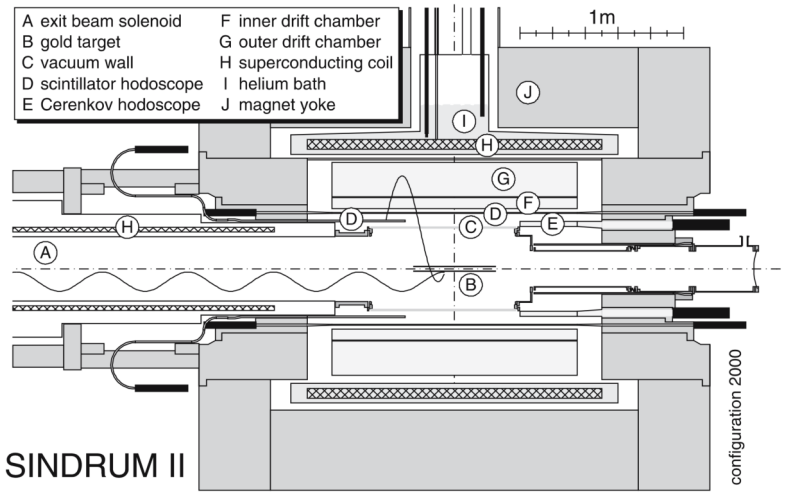

Figure 1.13: Cross-section view of SINDRUM II. Typical trajectories of a beam muon and a hypothetical conversion electron are indicated.

follows a helical trajectory, allowing particles with a momentum less than 100 MeV to be fully contained in the detection region. Tracking of the final state particles is performed with two drift chambers. The final positron sample has a linear momentum distribution with an endpoint around 92.3 MeV with an isolated candidate event at 95.7 MeV (see Fig. 1.14). From the momentum distributions built during beam-off periods, it was possible to explain the isolated event as cosmic ray background, confirming that no conversion event had been observed. Nevertheless, the expected branching ratios were efficiently measured and are reported in Table 1.2.

TRIUMPH

The TRIUMPH TPC (Time Projection Chamber) has been developed to search for both the muon to electron CLFV process, as well as the LNV process of conversion of a muon into a positron. The experiment used 73 MeV μ^- beam hitting on a Ti target. Scintillation counters were used to detect the incoming particle beam and to define a muon stop. The interaction products would then enter the TPC, shown in Fig. 1.15, placed in a uniform 0.9 T magnetic field. At each side of the hexagonal TPC there are six sectors with proportional wires to detect the ionisation electrons. Coordinates on the transverse plane were obtained by the anode wires positions and the induced charge on cathode pads, placed along the wires length. The axial coordinate was instead obtained from the drift time, allowing to have a full 3D reconstruction of the event. The system trigger was based on multiwire proportional chambers and scintillators signals which would give information about the entering and exiting of the particles in the TPC. Muon-electron and muon-positron conversion data were taken simultaneously. In Fig. 1.16 are

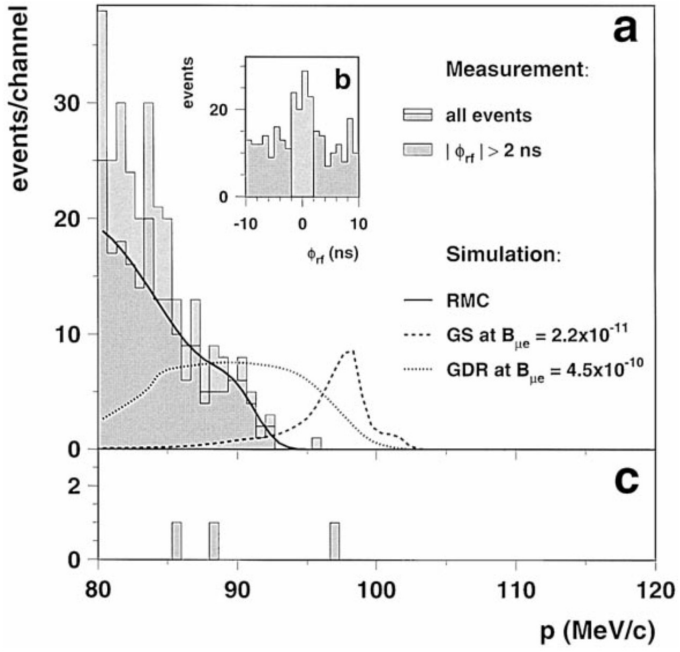

Figure 1.14: Positron momentum distributions for measuring periods with (a,b) and without (c) muon beam. The events from the grey region outside the peak have been interpreted as RMC events. Their momentum distribution is compared with the results from the RMC simulation performed by the SINDRUM II collaboration.

shown both these spectra in the momentum range $75 - 130\,\mathrm{MeV}$. No positron events were observed with momentum greater than 92 MeV, given the expected positron energy in Ti of 96.4 MeV. To obtain the total branching ratio, a model dependent analysis is needed. Having assumed an average excitation energy of 20 MeV with a 20 MeV width, it is found

$$BR(Ti) = \frac{\Gamma(\mu^- + Ti \rightarrow e^+ + Ca)}{\Gamma(\mu^- - Ti\ capture))} < 1.7 \times 10^{-10} \tag{1.10}$$

at 90% CL.

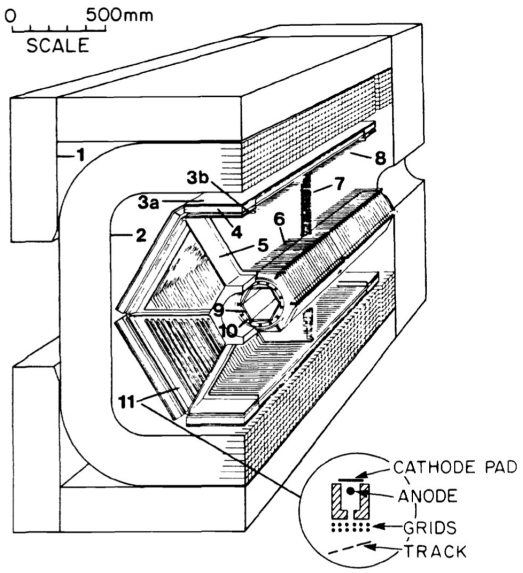

Figure 1.15: Cross-section view of the TRIUMPH TPC. The numbered parts are: 1, magnet iron; 2, magnet coil; 3, exterior trigger scintillators; 4, exterior trigger wire chambers; 5, TPC end-cap support frame; 6, central electric-field cage wires; 7, central high-voltage plane; 8, outer electric-field cage wires; 9, interior trigger scintillators; 10, interior cylindrical wire chamber; 11, TPC end-cap proportional wire modules for track detection. In the zoomed part is highlited the way anode wires and cathode pads are arranged.

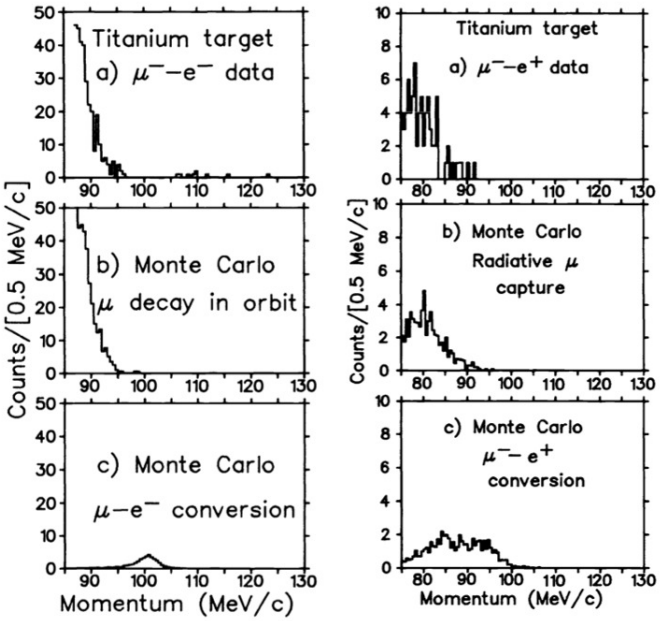

Figure 1.16: Left: The electron momentum spectrum from the Ti target momentum region $85 - 130\,\text{MeV}$ for (a) data, (b) Monte Carlo simulation of decay in orbit background, and (c) Monte Carlo simulation of muon-electron conversion process. Right: The positron momentum spectrum from the Ti target in the momentum region $75 - 130\,\text{MeV}$ for (a) data, (b) Monte Carlo simulation of the radiative muon capture, (c) Monte Carlo simulation of the muon-positron conversion process [39].

Chapter 2

The Mu2e Experiment at Fermilab

The Mu2e experiment is being built at Fermilab (Batavia, IL) and it will search for the coherent, neutrinoless conversion of muons into electrons in the field of a nucleus. It will measure the ratio, $R_{\mu e}$, between the conversion events and all the capture events, defined as:

$$R_{\mu e} = \frac{\Gamma(\mu^- + N(A,Z) \to e^- + N(A,Z))}{\Gamma(\mu^- + N(A,Z) \to \nu_\mu + N(A,Z-1))}, \tag{2.1}$$

improving by four orders of magnitude the current limit set by SINDRUM II at 7×10^{-13} at 90% CL on a Au target [40]. Mu2e goal is to reach on $R_{\mu e}$: (i) a single event sensitivity of 3×10^{-17}, (ii) a 5σ discovery of 2×10^{-16} and (iii) a 90% CL upper limit of 8×10^{-17}. As already mentioned, the CLFV interaction investigated by Mu2e probes new physics scenarios, constraining important parameter for BSM physics, looking at effective energy scales which are out of reach for the current collider technologies. Furthermore, this measurement will complement the search for the $\mu \to e\gamma$ decay performed by MEG [16] and MEG II [17] and other searches performed at LHC. The concept behind the Mu2e experiment has its origin in the 1980s with two experiment which, in the end, were never built: the MELC experiment at the Moscow Meson Factory [41] and MECO experiment at BNL [42]. The design and R&D phase for Mu2e started in 2009. In 2016, the experiment received the DOE approval of full Critical Decision 3, allowing the collaboration to start construction on the experiment hall, the solenoids, the accelerator system and the detector components. To achieve its goal, Mu2e has specific needs:

- A high intensity pulsed proton beam from which an intense secondary muon beam can be produced. It has to have a pulsed structure to allow most of the stopped muons to decay before the next pulse arrives while making negligible the contribution of prompt background.
- A pion and muon transport system which can capture the pions generated at the production target and transport them, and the muons from their decay, on the

aluminum Stopping Target. The momentum spectrum has to be low enough to allow most of the muons stop in a thin target.

- A detector system which can efficiently and accurately identify the conversion electrons (CE) while rejecting backgrounds.
- A detector hall to host the experimental apparatus.

In the following sections, the physics environment and the components of Mu2e will be presented.

2.1 Experimental Setup Overview

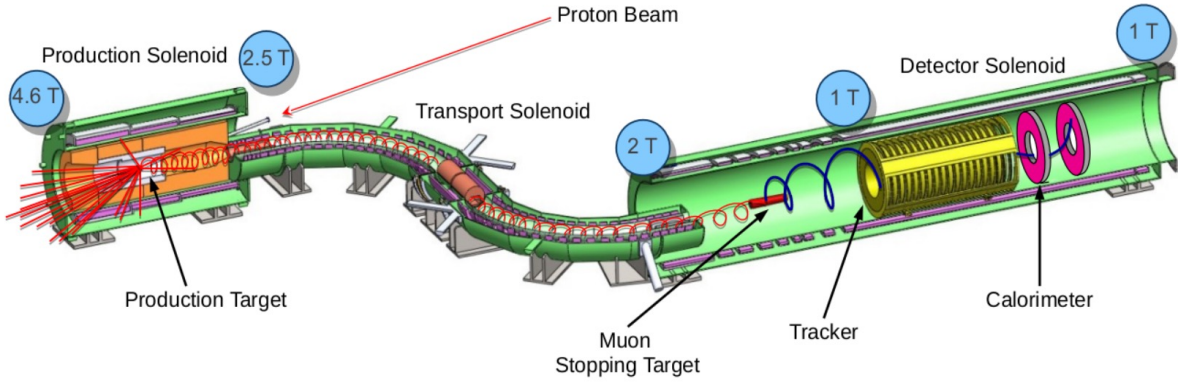

Figure 2.1: Schematic representation of the Mu2e experimental apparatus.

The Mu2e experimental apparatus is composed of three large, state of the art, superconducting magnet sections (the Production, Transport and Detector solenoids) which are assembled in an S-shaped layout, whose schematic representation can be seen in Fig. 2.1. To provide a sense of the technical difficulties for such a system we recall that the total length is around 25 m. In the Production Solenoid (PS), the 8 GeV pulsed proton beam coming from the Fermilab Accelerator System impinges on a tungsten target (Production Target). The beam enters at 17° to the axis of the solenoid system, which defines the "forward" direction. The reason behind this scheme is to avoid that the overwhelming flux of particles, especially neutrons, photons and leftover protons, reaches the detectors. The main products of the interaction are pions which are collected, focused and sent inside the Transport Solenoid (TS) by means of a graded field that act as a magnetic lens for low momentum pions. A large fraction of the charged pions decay to muons ($\tau_{\pi^\pm} = 2.6 \times 10^{-8}$ s) in the TS and the produced low momentum negative muons are charged selected by means of a collimator in the TS middle section. The shape of the TS and its length are designed to allow the hadrons to decay and to suppress the

background coming from neutral particles. The selected muons then reach an Al target (Stopping Target), located within the Detector Solenoid (DS), where around 50% of them are stopped. In the volume covered by the DS and behind the Stopping Target (ST), the Mu2e detectors are located: a straw tube tracker and a crystal electromagnetic calorimeter. In order to reduce muon capture on residual gas, minimize multiple scattering and deter any possible high voltage discharge from the detectors and their electronics, the inner volumes of all three solenoids are evacuated (10^{-5} Torr in the PS and 10^{-4} Torr in the detectors region). Extensive documentation about Mu2e can be found in its Technical Design Report [33]. A detailed description of the accelerator and of the solenoidal and detector systems will be reported in a later part of this chapter, after having described the expected signal and backgrounds.

2.1.1 Signal

As previously mentioned, the $\mu^- \to e^-$ conversion process has the characteristic signature of a monoenergetic electron, CE or conversion electron, with an energy given by

$$E_e = m_\mu - B_\mu - E_{recoil} \simeq m_\mu - B_\mu = 104.973\,\text{MeV} \tag{2.2}$$

where m_μ is the muon rest mass (105.658 MeV), $B_\mu \simeq Z^2\alpha^2 m_\mu/2$ is the binding energy of the muonic atom (~ 0.46 MeV [43]) and $E_{recoil} = m_\mu^2/(2m_N) = (m_\mu - B_\mu)^2/(2m_N)$ is the nuclear recoil energy (with α the fine structure constant and $m_N = 25.133$ GeV, the nucleus mass).

The mass of a nucleus is large compared to the electron mass, so that the recoil terms are small and the electron energy is just slightly below the muon rest mass. Since the conversion of a muon to an electron in the field of a nucleus is coherent, the muon recoils off the entire nucleus and the kinematics are those of a two-body decay.

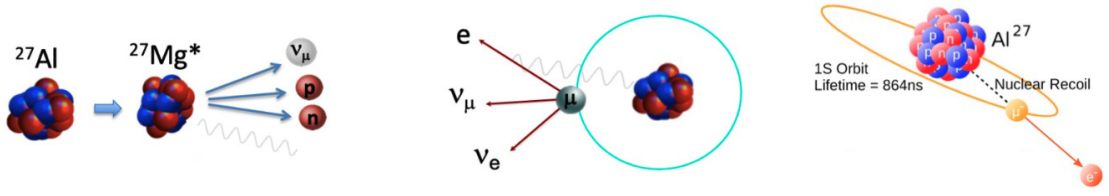

Figure 2.2: Processes consequent the creation of a muonic atom. Left: Muon capture. Centre: Muon decay in orbit. Right: Neutrinoless conversion of a muon into an electron.

In the Mu2e experiment muons are stopped in ^{27}Al where they form muonic atoms with a muon lifetime of 864 ns [44]. They then quickly decay to the 1S state emitting

photons. At this point, the muon either undergoes a nuclear capture (in 61% of the cases) or decays in orbit (39% of the cases), as depicted in Fig. 2.2-left and centre. In few cases, depending on BSM, it can undergo the conversion process (Fig. 2.2-right). The nuclear capture process mostly create neutrons, photons and protons that constitute a sort of radiation source for the detector, while the DIO (Decay In Orbit) of muons is the irreducibile background processes for the conversion search. Both of them scale with the beam intensity. A complete description of these and other backgrounds is reported in the next section.

2.2 Conversion Electron Backgrounds in Mu2e

There are a variety of processes which could mimic the signal of the monochromatic electron. All those physics processes have very different timing dependencies. The rates of the Radiative Pion Captures (RPC) beam electrons and decays in flight are strongly correlated with the arrival time of the proton pulse at the production target. The lifetime of the muonic Al atom instead determines the time dependence of the conversion signal, DIO and Radiative Muon Capture (RMC) while the cosmic background is distributed uniformly in time.

2.2.1 Intrinsic backgrounds

Decay in orbit

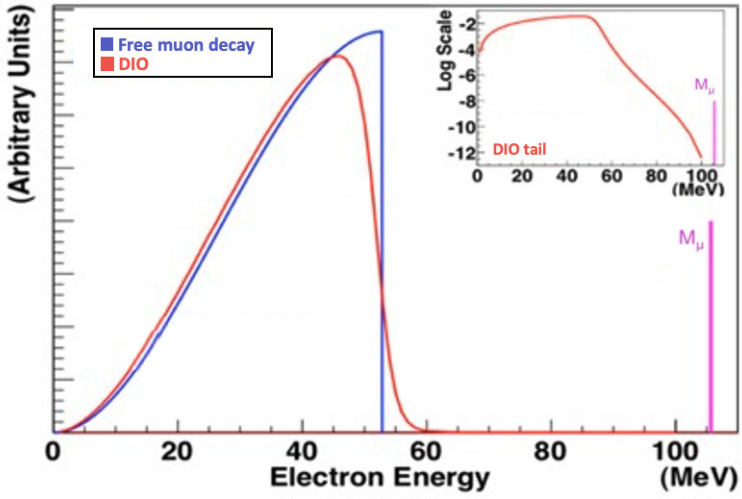

Figure 2.3: Free muon decays spectrum superimposed with the DIO spectrum. A line highlights the muon mass value. The high energy tail of the DIO spectrum is plotted in log scale.

A free muon decays following the Michel spectrum ($\mu^- \to e^- + \nu_\mu + \overline{\nu_e}$) with a peak probability at $E_{max} = (m_\mu^2 + m_e^2)/(2m_\mu) = 52.8\,\text{MeV}$, as can be seen in the blue line of Fig. 2.3, with the electron and the two neutrinos emitted in opposite directions. In a DIO process, i.e. in a decay in a bound system, the outgoing electron can exchange momentum with the nucleus, resulting in an electron with a maximum possible energy (ignoring the neutrino mass) equal to that of a CE [43]. This process has a very small probability, $\mathcal{O}(10^{-17})$, but represents the most important irreducible/intrinsic background source in the muon to electron conversion search. The DIO spectrum is better shown in Fig. 2.4. The differential energy spectrum of DIO electrons falls rapidly after the peak, approximately as $(E_{endpoint} - E_e)^5$, following Sargent's rule. Considering this feature, it is possible to resolve this background from the CE line thanks to a good momentum resolution with a FWHM (Full Width at Half Maximum) of the order of 0.5 MeV. Given the high muon rate required there are no precise measurements of the last part of the DIO tail, thus affecting the background uncertainty estimate. From the latest measurement [43], the rate uncertainty in the energy region near the endpoint has been estimated to be smaller than 20%.

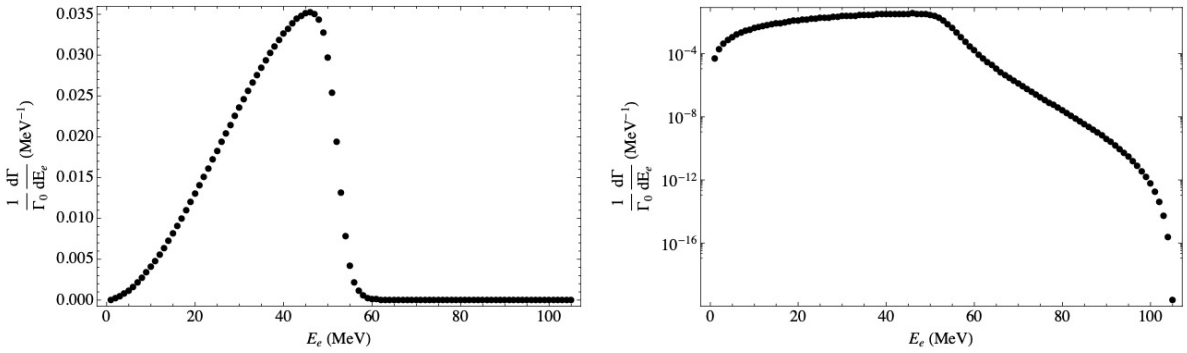

Figure 2.4: Electron spectrum for aluminum. Left plot: linear scale; right plot: logarithmic scale.

Radiative muon capture

Another background is provided by the RMC, during which a muon is absorbed by an Al nucleus and a photon is emitted: $\mu^- + N(A, Z) \to \gamma + \nu_\mu + N(A, Z-1)$. In Mu2e, since the target is made of Al(27, 13), the produced atom is Mg(27, 12). The produced RMC photons can then internally or externally convert and produce an e^+e^- pair in the Stopping Target or in the surrounding material, yielding an electron with an energy that can get close to the conversion energy. A shift in the value of the pair-produced electron can be given by the mass difference between the initial and final nuclear states, so that the final value is influenced by the chosen target material. The latest information on the

RMC spectrum comes from the TRIUMPH experiment [45] which measured the electron spectrum for different materials, Al included.

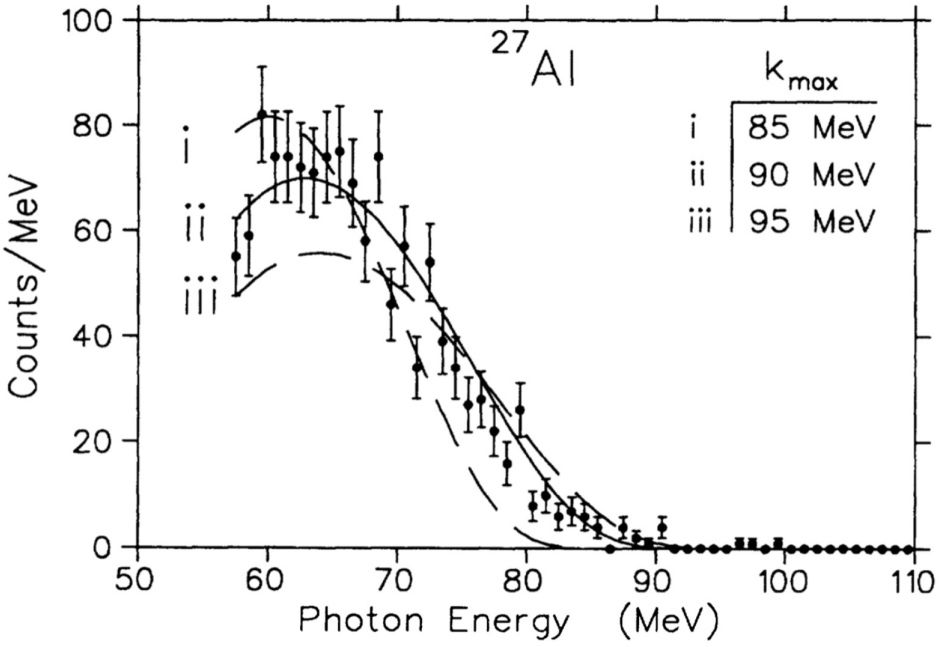

Figure 2.5: Photon energy spectra from RMC on Al with the spectral shapes given by Eq. 2.3 (convoluted by the detector response function). The solid line is the spectral shape for the best-fit value of k_{max} and the dashed lines are for other values of k_{max}.

The RMC photon spectrum can be parameterised, using the closure approximation, as a polynomial:

$$\frac{d\Lambda_\gamma(E_\gamma)}{dE_\gamma} = \mathcal{N}(1 - 2x + 2x^2)x(1 - x)^2, \tag{2.3}$$

where $\mathcal{N}$ is the normalization factor and $x = E_\gamma/k_{max}$ is a dimensionless quantity with k_{max} the kinematic endpoint of the process. As show in Fig. 2.5, the best fit value of the endpoint energy is $k_{max} = (90.1 \pm 1.8)\,\text{MeV}$. However, the maximal kinematically allowed energy of a photon emitted in RMC on Al is

$$k^{kin}_{max} = m^2_\mu - |B_\mu| - E_{recoil} - \Delta M \simeq k^{DIO}_{max} - \Delta M = 101.85\,\text{MeV} \tag{2.4}$$

where $\Delta M = M(A, Z-1) - M(A, Z)$ and k^{DIO}_{max} is the kinematic endpoint of a DIO electron. The RMC background therefore overlaps with the DIO in the $80 \div 100\,\text{MeV}$ region. As for DIO, this background can be reduced thanks to a high detector resolution since there is actually negligible background exactly at the conversion energy, according to the above estimate.

However, this background can be problematic since Mu2e plans to use the low mo-

menta DIO electrons to validate the theory needed to estimate the endpoint data, that is less known. Mu2e will have to perform a dedicated measurement to constrain the RMC background using both photons measured in the calorimeter and positron tracks above 100 MeV [46].

2.2.2 Beam related backgrounds

These background sources are associated with the production and transport of the beam along the solenoids toward the Stopping Target. These processes can yield an electron with energy close to the electron conversion energy in $\mu^- \to e^-$.

Prompt background

Associated to these background processes there is an electron that is almost coincident in time with the arrival of a beam particle at the ST.

This occurs in Radiative Pion Capture (RPC) events, when pions manage to arrive to the Stopping Target initiate the process $\pi^- + Al \to \gamma^{(*)} + N'$, where N' is an excited nuclear state. For an Al target, RPC occurs for 2.1% of the pion captures. The photon can convert and produce an electron-positron pair, both radiatively with an on-shell photon and internally with a virtual photon $\gamma^{(*)}$. By numerical coincidence, in Mu2e given its target and geometry, the probabilities for internal conversion and conversion in the Stopping Target as the photon propagates through it, are basically equal [47]. All in all, the number of electrons is going to be larger than the number of positrons because the photons produced will also undergo some Compton scattering, yielding additional e^-. The RPC photon spectrum endpoint is quite near the pion rest mass (~ 135 MeV) and the RPC distribution is peaked at around 110 MeV, so that e^+ and e^- from pair production can get an energy that can cover the conversion signal region, for both $\mu^- \to e^{\pm}$. Since the pion lifetime in Al is short (~ 26 ns) this process occurs promptly after the pion stop inside the target.

Another source of background is due to the pion and muon decay in flight. Indeed, a small fraction of pions, $\mathcal{O}(10^{-4})$, can decay in flight into high energy electrons ($\pi^- \to e^- + \overline{\nu_e}$) while in the DS volume. If the pions have a momentum greater than 77 MeV, these electrons will be boosted and can have momenta greater than 100 MeV. An analogous process exist for the muons which themselves decay in flight in the DS volume and produce electrons with a momentum close to 100 MeV. While the kinematic endpoint of the electron spectrum from free muon decay is well below the 105 MeV expected for conversion electrons, in-flight muon decays are more similar to in-flight pion decays and can boost the energy of the resulting electron into the signal region. Both these

backgrounds can be considered negligible since it can be shown by relativistic kinematics that these boosted electrons will arrive no later than 500 ns after the proton burst.

Beam electrons are instead produced upstream, in the TS and PS, from decaying π^0 and the subsequent conversion of the decay photons. These can have an energy close to the conversion energy, enter the DS and scatter on the Stopping Target.

Suppressing these backgrounds requires the measurement to be delayed by several hundreds of nanoseconds with respect to the proton pulse arrival at the production target. In the experiment this corresponds to place the start of the TDAQ (Trigger and Data Acquisition) acquisition window [47] at around 700 ns. This delayed observation window allows the prompt background to become negligible. See Section 2.3.1 for further details.

Delayed background

Antiprotons produced by the incoming proton beam can be delayed in the transport lines and, due to their low speed, can arrive later to the detector region. The 8 GeV protons of the beam are above threshold for production of antiprotons (the threshold for $p + p \rightarrow p + p + (p + \bar{p})$ is calculated at 5.2 GeV). The antiprotons do not decay and are negatively charged, so the ones with a momentum smaller than 100 MeV can be transported through the Transport Solenoid and reach the ST. There are two main ways that antiprotons can induce background: they interact in the TS and produce pions or they reach the DS and annihilate in the Stopping Target, producing π^0 and π^-. This pion "regeneration" contributes to the RPC background and the resulting electrons would enter the signal window. Since $\bar{p}$ travel slowly toward the DS, the delayed acquisition window is sufficiently not effective in suppressing this background and absorption elements in the TS are needed. Since these have a small kinetic energy, the dE/dx is higher than for muons, so even a thin absorber is sufficient to reduce this background. The time-delayed acquisition window can still tame this background, together with the construction of a long muon beam line.

In occasion of the 2020 sensitivity update (see Sect. 2.7.1), a through study has been done on the antiprotons background modelling and prediction [48]. Close to the $\bar{p}$ production threshold of ~ 5.6 GeV, the antiproton production process cannot be described by QCD and requires the use of phenomenological effective theories. While plenty of data and reliable parameterizations exist for the high-energy regime ($p > 100$ GeV), in the region of interest for Mu2e at $E_{proton} \sim 9$ GeV and for backward production, very few data are available. Within the Mu2e collaboration, the first attempt to reproduce the experimental data was done in 2011 by S. Striganov [49]. Taking into consideration the flaws of this approach, an alternative parametrisation has been developed [50].

A full simulation of the antiprotons propagation along the Mu2e solenoids has been produced with Geant4 and the new model calculates the invariant cross section in the centre-of-mass system, shown in Fig. 2.6.

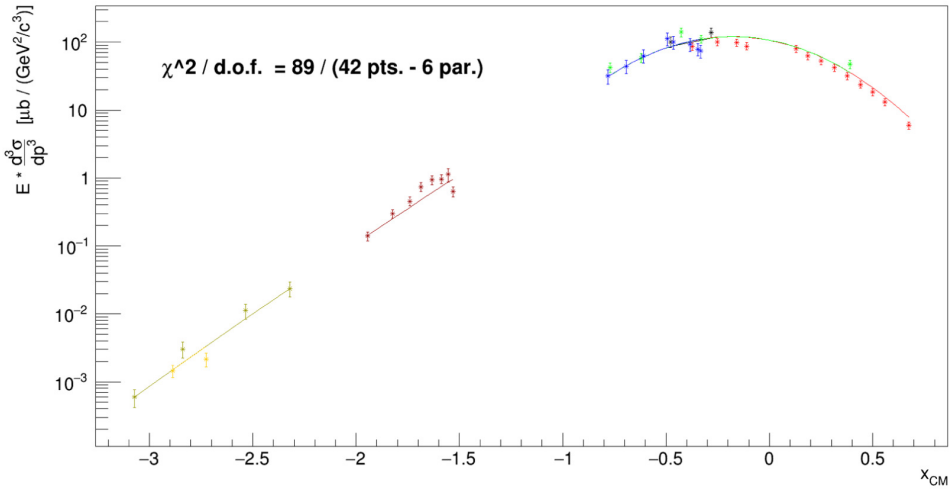

Figure 2.6: Invariant cross-section as a function of x_{CM} for all data points. The fit with the alternative model is showed. x_{CM} is the ratio between the antiproton momentum and the maximum antiproton momentum allowed in case of $p + p$ collision, both in the centre-of-mass.

The dominant contribution to the systematic error associated to this background comes from the poor knowledge of the antiprotons production cross-section at the Mu2e energies and this alternative cross-section model allows an estimate of a systematic uncertainty when compared to the previous one. A proposal has been made to operate an in-situ measurement of the number of antiprotons stopped in the Stopping Target to reduce significantly the systematic uncertainty on the production and back-scattering theoretical models.

2.2.3 Other backgrounds

Cosmic Rays induced

Cosmic Rays interacting and decaying in the detector volume are a source of particles, mainly muons and electrons, whose momentum spectrum can cover the region around 100 MeV, creating at least one candidate electron/day. The majority of these events must be vetoed using detectors that cover a large solid angle around the DS and a portion of the TS with an efficiency for identifying a Cosmic Ray track of around $\sim$ 99.99%. The Cosmic Ray Veto (CRV), described in Section 2.6.3, serves this purpose. Most of this background comes from cosmic muons which can decay in the DS or interact in

the nearby material and produce electrons or muons which could be misidentified as electrons. A muon to electron particle identification is needed to eliminate all muons produced by CRs.

Event reconstruction errors

When spurious signals are present in the detectors, tracks may not be optimally reconstructed and this could result in low energy DIO electrons inside the energy region of the CE. This has to be considered when evaluating the detector systematic uncertainty. The detector tracking capabilities could also be compromised by low energy protons ejected from the nucleus after muon capture. Instead, ejected neutrons can undergo capture and emit photons. To contrast these backgrounds and to ensure the correct particle identification, high resolution detectors are needed.

2.3 Accelerator system and proton beam

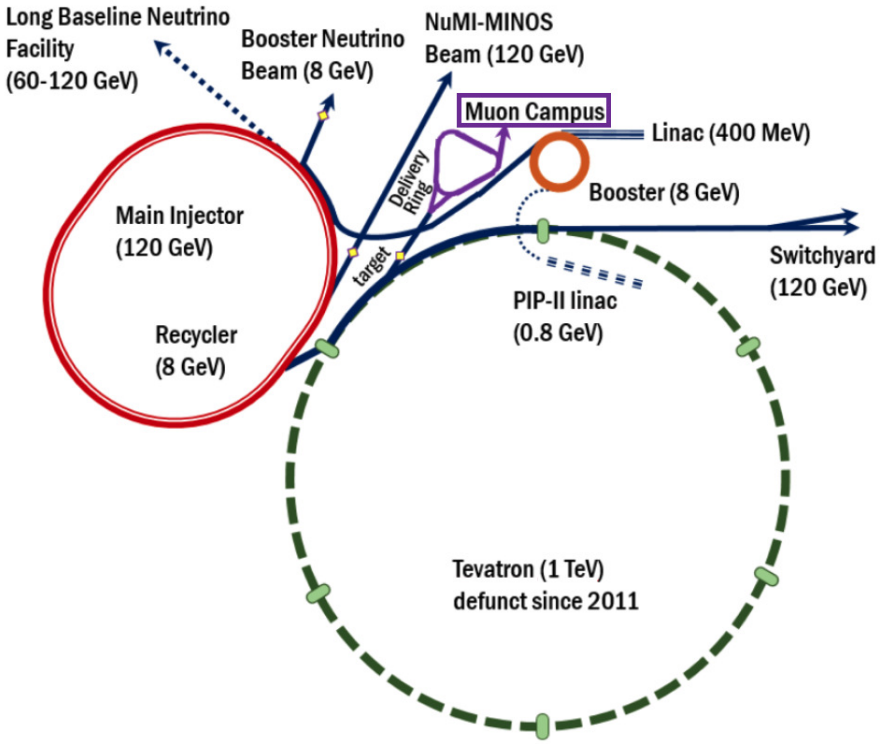

Figure 2.7: The Fermilab accelerator complex.

The Fermilab accelerators are expected to deliver 3.6×10^{20} protons on the Mu2e Production Target, over its lifetime. The Fermilab accelerator complex is shown in Fig. 2.7, while a closer look at the Delivery Ring can be seen in Fig. 2.8. As explained

in the previous sections, Mu2e will require a pulsed proton beam to keep backgrounds to a manageable level. The beam will then consist of narrow pulses, 250 ns wide, which have to be separated by a time interval greater than the lifetime of a muon captured in Al (864 ns). For the Fermilab machine, this interval is chosen to be 1695 ns. In order to exclude delayed protons, the beam has to be extinguished soon outside the 250 ns wide proton pulses. An extinction factor (EF), defined as the ratio between the out-of-time beam to in-time beam with respect to the nominal bunch full width, has to be smaller than 10^{-10} in order to make negligible the delayed background contributions. The requirements of the beam structure are shown in Fig. 2.9.

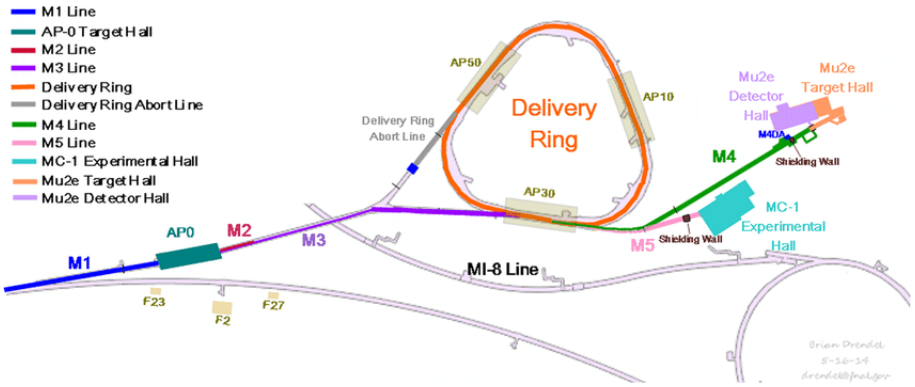

Figure 2.8: Close-up view of the beam lines that lead the protons to the muon campus and the Mu2e detector hall.

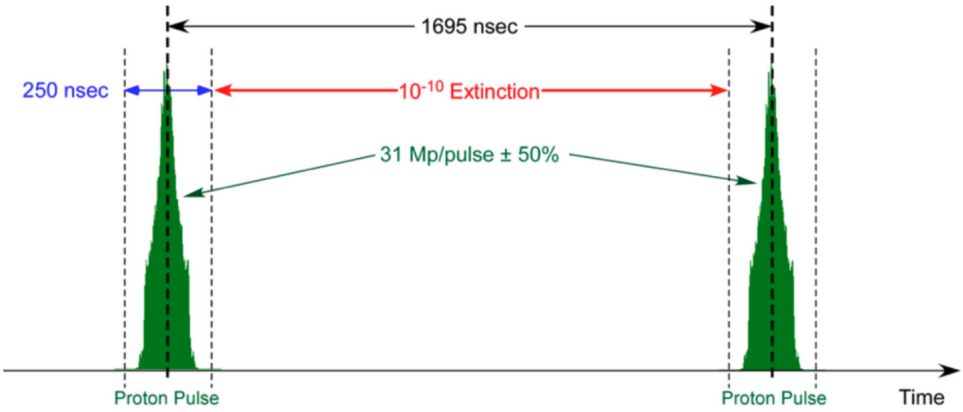

Figure 2.9: Longitudinal structure of the proton beam delivered to the Mu2e production target. In green is shown the time profile of a beam pulse. The extinction and beam pulse intensity (an intermediate intensity value is 3.1×10^7 protons/pulse) requirements are written.

The accelerator process starts with hydrogen gas. This is ionised and the protons then start their acceleration in a series of steps:

- A LINAC accelerates the protons up to 400 MeV.
- The protons are injected in a Booster Ring, where they circulate until they reach an energy of 8 GeV. These are also divided in bunches with 4×10^{12} protons each.
- The protons are extracted into the Main Injector beamline and then injected into the Recycler Ring.
- The beam is re-bunched, with a rate of 15 Hz, into 20 protons batches. Two of those are reserved for Mu2e, while 14 are delivered to the NOνA experiment [51], as shown in Fig. 2.10.
- Batches are extracted and go into the Delivery Ring (formerly the Antiproton Debuncher). A resonant extraction system injects a micro-bunch of $\sim 10^7$ protons into the Mu2e beam line. This is known as "slow extraction" because the single bunch circulating in the Delivery Ring is fully extracted over a relatively long duration (i.e. spill) of 54 ms. The Delivery Ring has a period of 1.7 μs, thus producing the bunch structure needed by Mu2e.
- After the resonant extraction is completed, a clean-up kicker is fired to remove any remaining beam in the line.

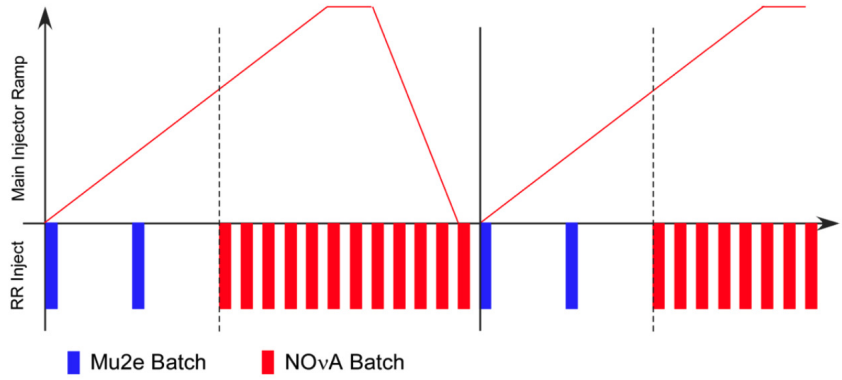

Figure 2.10: Structure of the batches that are obtained in the Recycler Ring. One Main Injector cycle lasts 1.333 s.

2.3.1 Mu2e proton beam

In Fig. 2.11, the timing structure of the Mu2e proton beam is shown. It shows the effectiveness of a delayed live time window for the experiment, which is free from the prompt background. Mu2e will acquire data starting from $\sim$ 700 ns after the proton pulse until right before the arrival of the successive injected bunch.

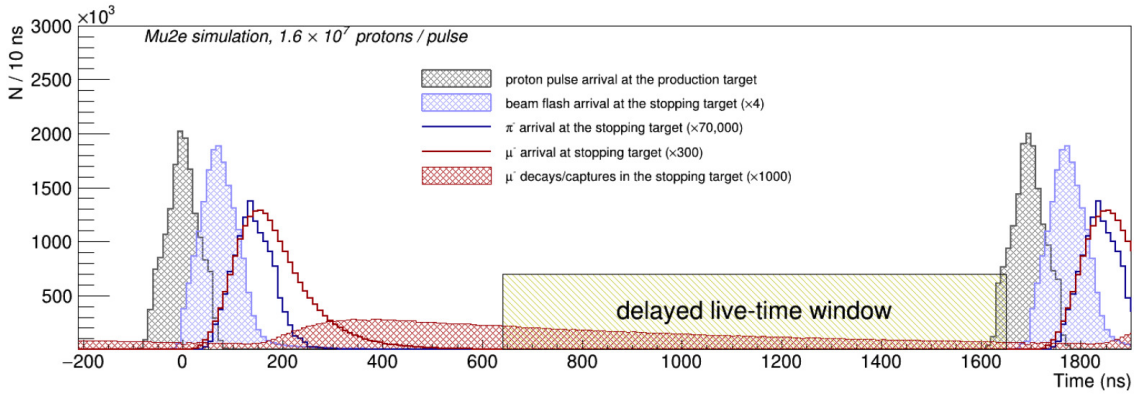

Figure 2.11: Timing structure of the Mu2e proton beam.

In Fig. 2.11, the beam flash is also shown. This is a burst of low-momentum electrons and positrons, pair-produced from photons from the $\pi^0 \rightarrow \gamma\gamma$ process, which then undergo bremsstrahlung in the target Al foils. These particles would blind the detector, saturating the channels increasing the occupancy. Muons that stop in the target and undergo capture also produce protons, neutrons, and photons ($\mu^- +^{27} Al \rightarrow \nu_\mu + X + kp + k'n + k''\gamma$) which can increase the radiation damage to the detectors. Thanks to the delayed live window, the flash can be avoided, since the radiation damage from it would lead to shorter lifetimes for the detector elements. Furthermore, it limits the possibility to explore different Z materials for the Stopping Target, since it forces the data taking window to be at least ~ 200 ns after the proton pulse, which may be longer than the muon lifetime in certain materials (see Section 2.5 for more information about the ST characteristics).

Much of the instrumentation needed to monitor the proton beam is already present along the beam lines, but it has to be modified in order to be used with the faster cycle times and the pulsed beam structure. Beam monitoring will be performed by different systems. Toroids, which produce a signal proportional to the beam intensity, and Beam Loss Monitors will check the beam intensity and the transmission efficiency along the beam lines while Beam Position Monitors will provide real-time information about the orbit with a sub-millimeter resolution and will keep the beam on the desired trajectory.

As vital as the proton bunches, it is the beam extinction. To reach a EF of $\mathcal{O}(10^{-10})$ two steps are required [52]. The first is in the formation of the micro-bunches where an EF of $\mathcal{O}(10^{-5})$ can be reached. A further factor of 10^{-7} is provided by a system of AC resonant dipole magnets and collimators in the beam line. This will induce in the beam line a high frequency field, such that the beam passes when the field is basically null while the beam outliers will find an increasing field which will direct them toward the collimators. This system allows for two orders of magnitude safety margin with respect

to the EF requirement. Monitoring of the EF is done by the beam extinction monitor. It is located in the forward direction with respect to the incoming proton beam, before the beam dump (Fig. 2.12-left). It is a system made of a spectrometer with eight detector planes of pixels, half up-stream and half down-stream (Fig. 2.12-right). The spectrometer can detect a small fraction of the out-of-time particles, so that over many bunches an accurate time profile of the beam can be built with increasing precision. Another EF monitoring system is located upstream, before the AC dipole, and consists of a thin foil which will scatter protons into Cherenkov radiators.

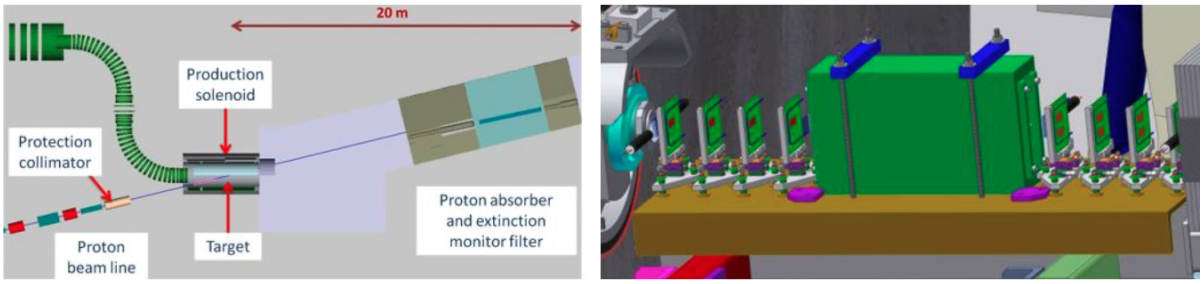

Figure 2.12: Left: Extinction monitor placement within Mu2e. Right: The beam extinction monitor spectrometer and tracking planes.

2.4 Superconductive Solenoids and the Muon Beam

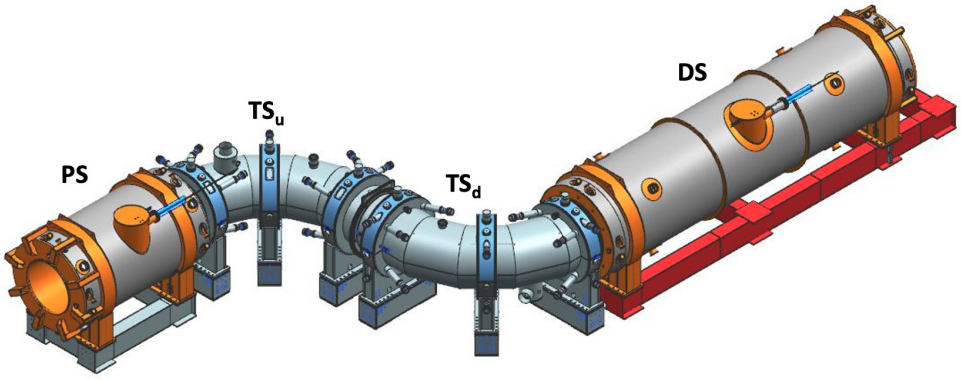

Figure 2.13: The Mu2e Superconductive Solenoids system.

The most ambitious and innovative component in Mu2e is represented by the Superconductive Solenoids that form the so called muon beam line and have the main goal of increasing the rate of muons on target with respect to traditional muon beam generation. The basic idea is to focus and transport toward the detectors most of the pions produced by the reaction of protons on target and to let them decay into muons in the transport channel, moving the muon beam up to the Stopping Target. All other

particles contribution have to be minimised and this is done with the magnetic fields obtained from three Superconductive Solenoids elements: the Production Solenoid, the Transport Solenoid (upstream and downstream) and the Detector Solenoid. A graphical representation of these is shown in Fig. 2.13.

Because of the high magnetic field and large amount of stored energy, the solenoids are made of superconducting NbTi coils, stabilised with Al, and indirectly cooled with liquid helium. The inner volumes of all three solenoids are kept at a vacuum of 10^{-5} Torr in the PS, to prevent the tungsten target oxidation, and 10^{-4} Torr in the DS volume. A vacuum environment is pivotal to optimise transport efficiency and to suppress possible background interactions with the residual material.

At the end of the transport line, the overall muon-stop efficiency is very high, with ~ 0.005 muons/proton-on-target reaching the Al Stopping Target. These muons have a peak momentum of 50 MeV, and the effective stopped fraction is ~ 0.0016 muons/proton-on-target which corresponds to a muon stopping rate of 10^7 kHz at full beam intensity.

2.4.1 Production Solenoid

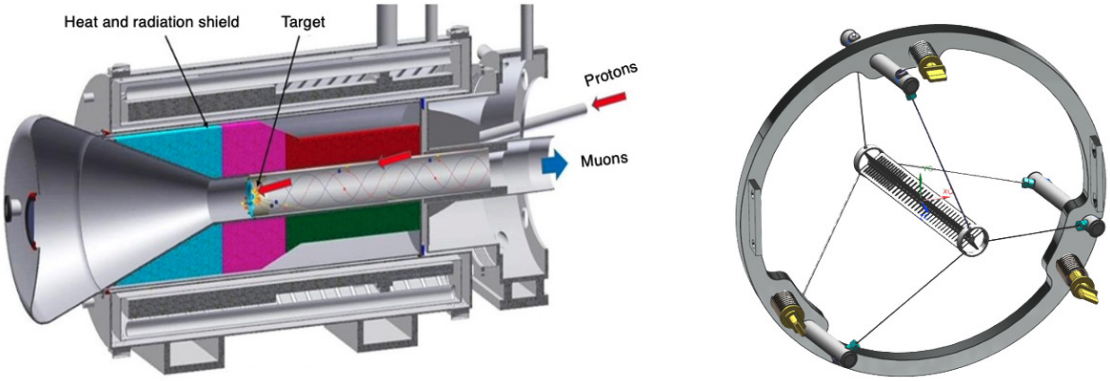

Figure 2.14: Left: Schematic representation of the Production Solenoid. Right: Production Target 3D rendering.

The Production Solenoid (Fig. 2.14-left) is placed around the production target (Fig. 2.14-right) and it has the role of focusing the muons and pions produced from the proton interaction. This solenoid has an axially graded field, from 4.6 T to 2.5 T with a gradient of ~ 1 T/m. This "magnetic bottle" can reflect the particles emitted in the opposite part with respect to the TS position, since the p_t/p ratio decreases as the magnetic field decreases, guiding the particles toward the TS. The PS is located in a particularly challenging environment due to the high radiation, so it will be equipped with a Heat and Radiation shield made of bronze.

2.4.2 Transport Solenoid

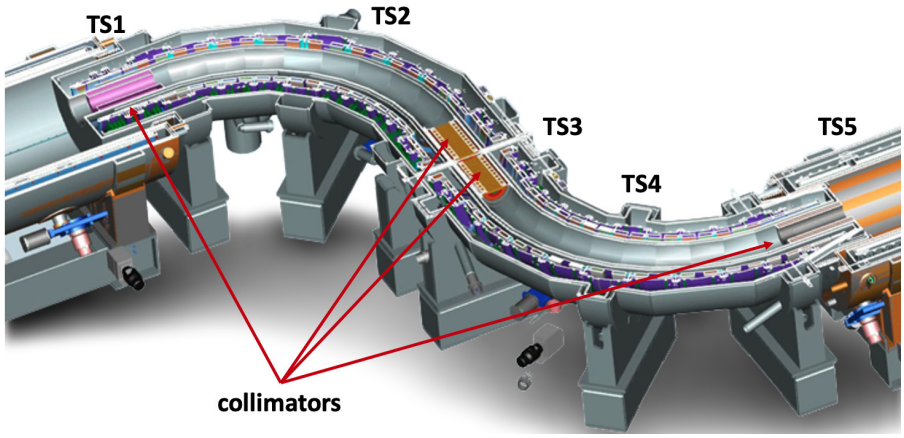

Figure 2.15: Transport Solenoid with the most important components identified.

The Transport Solenoid (Fig. 2.15) consists of 27 sections and it is designed to select and transport to the detector region low momentum μ^- ($p < 80\,\text{MeV}$). Five main sections can be identified. Two straight sections, TS1 and TS5, which interface with the PS and DS respectively and have one collimator each (COL1 and COL5) for momentum selection. Two toroid sections, TS2 and TS4, which are bent at 90° to reduce the high energy negatively charged particles, positively charged particles and line-of-sight neutral particles which reach the detectors region. One central straight section, TS3, about 2 m long which contains two collimators (COL3u and COL3d) which filter particles exploiting the fact that the helical motion of charged particles in a magnetic field depends both on the particle charge and its momentum.

The calculations carried out in order to maximise the the stopped muon yield and minimise the antiproton induced backgrounds lead to a specific configuration of antiproton absorbers in the TS [53]. A first antiproton absorber foil is placed 1 mm upstream of the collimator in TS1 and consists of a 250 μm thick aluminum window, with a diameter of 30 cm. A 20 cm long half-moon collar made of graphite is positioned inside COL1. It has a inner radius of 120 mm and extends for 90 degrees. This collar suppresses antiprotons by a factor of 6 while reducing the stopped muon rate by $\sim 4\%$. The other absorber window is located between COL3u and COL3d. It consists of a 150 μm thick titanium window followed by 2 suspended aluminum foils of 127 μm. These foils allow to increase the absorber thickness going outward with respect to the TS axis, where higher momentum particles arrive.

2.4.3 Detector Solenoid

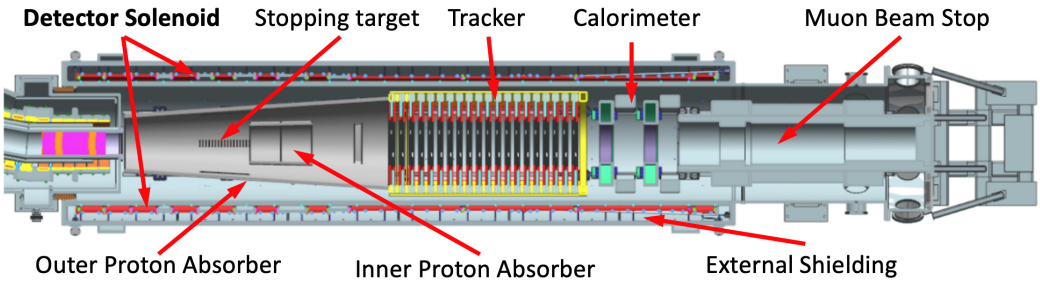

Figure 2.16: Top view of the Detector Solenoid area.

The Detector Solenoid is a ∼11 meters long straight section, with a bore diameter of 2 m and with a field gradient from 2 T to 1 T. In the detector region, after the Stopping Target, the field is kept constant at 1 T to allow tracking reconstruction. The muon beam has a peak momentum of ∼ 45 MeV as it enters the DS. The field configuration allows to bring back toward the detectors any CE that may have been emitted in the opposite direction. Another important consequence of this field structure is that any spurious high energy electron that reaches the DS, is going to be accelerated toward the detectors and their helix angle will not match the one expected for a conversion electron, allowing the tracker system to easily reject it. It is interesting to notice the pros and cons that come with a straight DS. The detector is going to be exposed to the remnant of the beam flash or muon beam, but thanks to its symmetry, Mu2e is going to be able to simultaneously search for $\mu^- \to e^-$ and $\mu^- \to e^+$ processes.

Within the bore of the DS there is also the Muon Beam Stop, designed to absorb the particles that reach the end of the solenoid while minimising the possible background sent back upstream. It is made of alternating cylindrical structures of high-density polyethylene and stainless steel.

Shown in Fig 2.16 is also the outer proton absorber, a conical polyethylene absorber, which surrounds the inner proton absorber. These structures have to reduce the outgoing flux of neutrons and especially protons which could generate spurious hits in the detectors.

2.5 Stopping target

The Mu2e Stopping Target is made of ∼ 160 g of aluminum with a purity > 99.99%. It is made of 37 foils, 100 μm thick and with a hole in the centre. Each foil is kept suspended

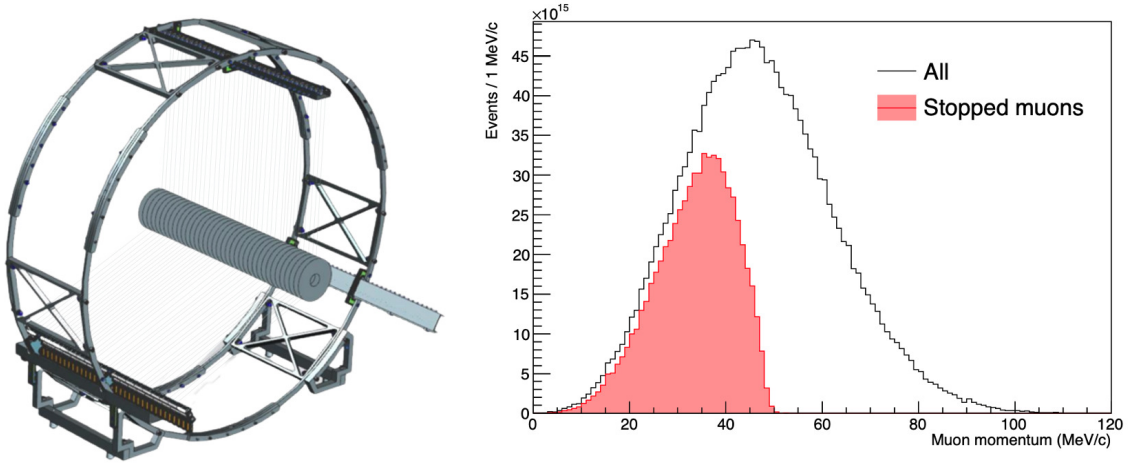

Figure 2.17: Left: Stopping target 3D rendering. Stopping target foils are supported by thin wires, tensioned by bronze weights visible on the lower left-hand side of this image. Right: Momentum distribution of muons delivered to the Stopping Target superimposed with the distribution of the stopped muons.

by three thin wires, so that the target is aligned with the DS magnetic field axis and at its centre. The target and the support system are shown in Fig. 2.17-left. The target is further surrounded by polyethylene absorbers to reduce the flux of neutrons and protons ejected as muons stop, which could damage the detector elements or increase the CRV dead-time. The choice of the target design had to be a compromise between two opposite requirements. On one hand, the muon stop probability has to be maximised, so a thicker target would be needed. On the other one, the energy loss of the conversion electron has to be minimised, by reducing the material it has to cross. The number and thickness of the foils were therefore optimized and a 40% stopping efficiency can be reached.

Another consideration to make is about the foils shape. Beam electrons traversing the target, as well as other interactions like due to cosmics, would yield a spray of particles which could damage the first layers of the tracker. To reduce this effect an annular geometry has been chosen, similar to the one of the detectors.

Another important choice is the target material. The muon-to-electron conversion rate depends on the Z of the target nucleus from the photonic contributions to the conversion [54], while non-photonic contributions depend on A rather than Z. The coherent rate, normalised to the total capture rate, goes like Z^4 [55]. There are several requirements on the target material:

- The material has to be stable, pure and malleable enough that it can be made into thin sheets.

- The target material has to be such that the endpoint energy for RMC is below the

conversion energy, or the produced photons present a strong background in the CE energy window.

- The muon conversion rate, which has to be maximised, increases with Z and reaches a maximum at Sb and Se (Fig. 2.18-left). For high Z targets there is also a dependence of the conversion rate on the nature of the interaction.

- The lifetime of the muonic target atom has to be long enough to fit in the time structure of the Mu2e beam. The lifetime will decrease with Z, as can be seen in Fig. 2.18-right, since there are more nucleons to interact with and the Bohr radius decreases, increasing the overlap with the nucleus. If the lifetime is too short, there is not enough time for the backgrounds to subside, making the measurement not feasible.

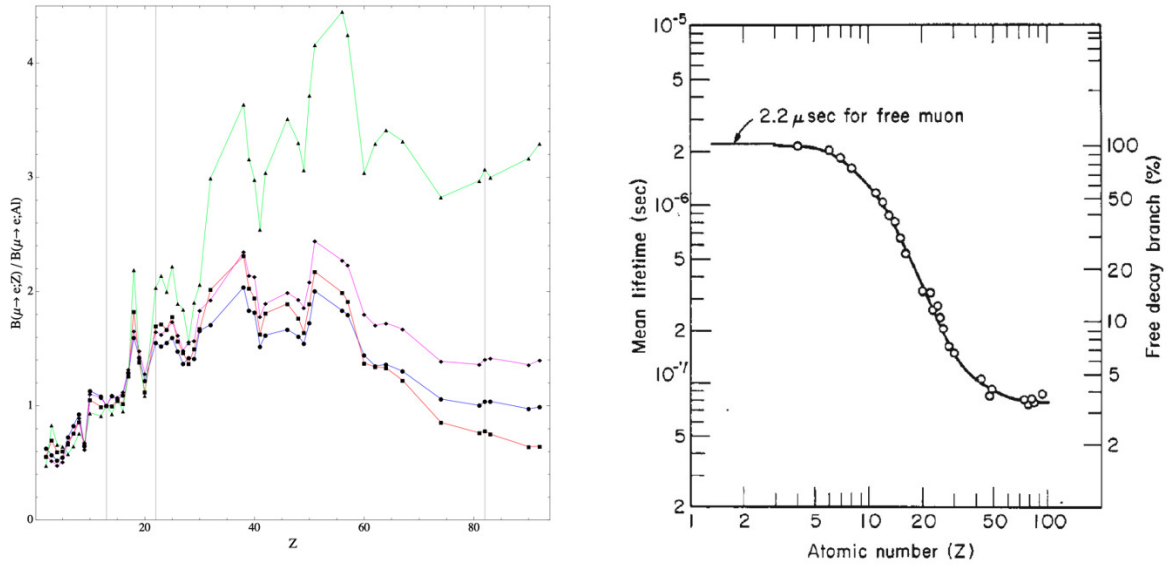

Figure 2.18: Left: Target Z dependence of $R_{\mu e}$ in different single-operator dominance models, normalised to the rate in aluminum (Z = 13). The vertical lines correspond to Z = 13 (Al), Z = 22 (Ti), and Z = 83 (Pb) [56]. Right: Mean lifetime of muonic atoms vs Z [57].

Having made all these considerations, aluminum is the material best fitting the beam period and it has been chosen for producing a Stopping Target with the described shape. Titanium has also been considered and it remains a viable option for future measurements since its conversion energy is practically the same as for Al albeit its shorter lifetime.

2.5.1 Stopping Target Monitor

The Stopping Target Monitor (STM) is a high purity germanium detector which has to measure the normalization factor of $R_{\mu e}$. To this purpose, Mu2e will detect the 357 keV X-rays produced as a muon cascades down from the $2p \rightarrow 1s$ state (other lines can be also observed, like $3p \rightarrow 1s$ or $4p \rightarrow 1s$) to measure the stopping rate and a so called "golden line" at 1.809 MeV related to the nuclear capture that instead follows the muon atom decay time. The STM has a very high resolution so that it will be possible to identify muons captured by impurity atoms thanks to their specific X-ray spectra. Further details about the STM are illustrated in Section 6.1.

2.6 Detectors

The Mu2e detectors are constituted by a very high precision tracker followed by a calorimeter system located within the volume of the Detector Solenoid, inside its evacuated warm bore. They are complemented by a Cosmic Ray Veto that surrounds the Detector Solenoid and part of the Transport Solenoid and has the duty to reduce the Cosmic Ray originated backgrounds. The detectors inside the DS are designed to operate in a 1 T magnetic field, where they have to accurately and precisely reconstruct conversion electron tracks. After the Stopping Target, the interaction products first meet the straw tube tracker, which suppresses the irreducible decay in orbit background and performs a high-precision momentum and position measurement of the incoming particles. Then the crystal electromagnetic calorimeter complements the tracker information, ensures redundancy and provides excellent energy and time measurements resolution. Both these detectors are annular in shape. This design allows the passage of the products of muon capture, remnant beam, and electrons produced in the initial proton collision, which would overwhelm and rapidly damage the detectors. Also, most of the low momentum electrons from muon decays ($p < 70$ MeV) will have their helical trajectory radius too small to reach the sensitive parts of the detectors, thus reducing the total amount of background sources.

2.6.1 Tracker

The straw tube tracker principal task is to accurately measure the particles' momentum and to reconstruct their curved trajectories. In order to achieve this it is essential to minimise the detector material budget to minimise multiple scattering which would degrade the momentum measurement and to avoid increasing the background rate from spurious hits. DIO electrons represent an important background and since the spectrum

falls like $\sim E^5$, as the resolution degrades the background increases quickly. Positive high momentum tail, in particular, has to be accurately reduced in the tracking reconstruction to avoid pushing the DIO spectrum in the CE energy region. On the other hand, energy loss is problematic since it could smear the CE energy and thus increase the signal/background overlap in the high-end region of the DIO spectrum.

The chosen tracker design is composed by 20736 straw tubes, arranged in planes perpendicular to the solenoid axis. These straws have a 5 mm diameter, with a central 25 μm gold plated tungsten sense wire [58]. Each straw is made of two layers of $\sim 6\,\mu$m mylar, wound spirally together, with a $\sim 3\,\mu$m layer of adhesive between them, for a total wall thickness of 15 μm. As the sense wire acts as anode, the inner surface has 500Å aluminum overlaid with 200 Å gold as the cathode layer. The outer surface has 500 Å of aluminum to act as additional electrostatic shielding and reduce the leak rate. The straws have a length ranging from 334 to 1174 mm and are supported only at the ends, since a 1.251 mm gap has to be guaranteed between straws to allow for manufacturing tolerance and expansion due to gas pressure. Inside the straw there is a gas mixture of Ar (80%) and CO_2 (20%), which would provide an estimated gain of $3 \div 5 \times 10^4$ at a voltage $\lesssim 1.5$ kV.

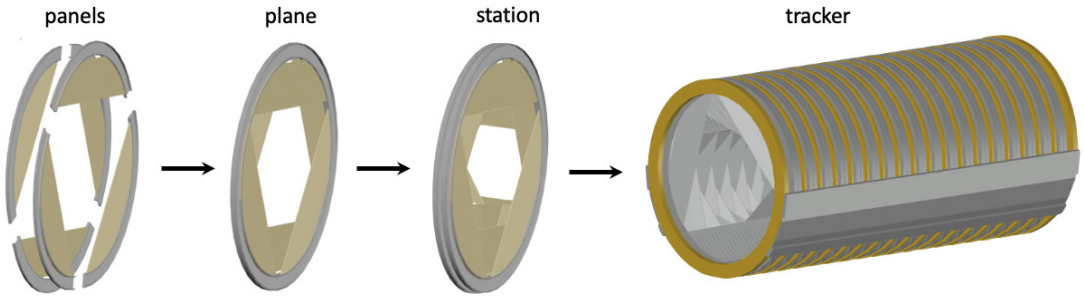

Figure 2.19: Scheme of the parts that make up the Mu2e tracker. From the left: 6 panels form a plane, two planes form a station and 18 stations form the entire tracker.

The structure of the tracker is shown in Fig. 2.19. Groups of 96 straws are assembled into a panel, which covers 120° with two layers of straws which help resolve the left-right ambiguity. Six panels are assembled into a plane: three panels complete the ring of one face and the other three, rotated by 30°, complete another ring on the opposing face. A pair of planes forms a station, where the two planes are identical, only rotated by 120° one respect to the other. The entire tracker is made of 18 stations, for a total length of 3.27 meters. Signals from the straws are read at both ends, amplified by custom preamplifier and the amplified signal is sent to digitizer electronics. A time division technique is employed to get the hit position information along the straw, as it enables better track reconstruction and momentum measurement. A Time-to-Digital Converter

(TDC) with resolution < 35 ps is required to get a hit position resolution of the order of few centimeters. The pulse height information is also collected, thanks to an ADC, to provide dE/dx for particle identification, particularly to discriminate electron and proton hits. No good muons to electron discrimination is performed by the tracker. Thanks to this design, low momentum electrons ($p < 53$ MeV) will leave no hits in the tracker, as shown in Fig. 2.20-left. Electrons with a momentum up to ~ 90 MeV will leave some hits but the full track is not reconstructable, so only high momentum electrons leave a full, well-identifiable track.

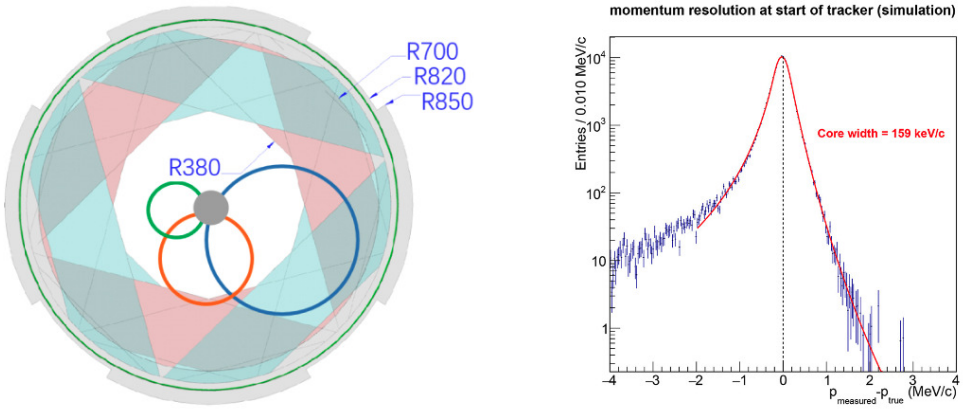

Figure 2.20: Left: Beam eye view of the tracker with the view of the trajectory of low momentum electrons (green), mid-momentum (orange) and high momentum (blue). Right: Resolution of the Mu2e tracker for electrons at the conversion energy. The simulation uses measured properties of the tracker, charge cluster formation, processing by the electronics, and passage through simulated DAQ, which is then passed to a reconstruction program that includes accidental activity from the beam and stopped muons.

The tracker is required to have a high-side resolution of $\sigma < 180$ keV, to avoid smearing background signal, like DIO, into the CE energy region. As shown in Fig. 2.20-right, the simulated momentum resolution has a core width of 159 keV, well within requirements, and a small high-side tail. "Core resolution" refers to a fit to the central part of the resolution that can be thought of as the Gaussian σ. The asymmetric low side tail is because of the stochastic nature of energy loss in the tracker. The high side tail is mostly due to wrong pattern recognition. A small panel prototype with 8 straws was built at Lawrence Berkeley Laboratories to measure the tracking performance using Cosmic Rays and radioactive sources [59]. Lately the just assembled panels have been used to perform a vertical slice test of the electronics and compare the results found with simulation and with the small size prototype.

2.6.2 Calorimeter

The Mu2e calorimeter serves the main purpose to provide additional and complementary information to the tracker for the CE reconstruction. It has particle identification capabilities and a rejection factor > 200 for e/μ separation, needed to exclude muons with momentum in the CE region. It helps the tracker in track reconstruction since it can provide a "seed" for the reconstruction algorithms allowing consistency checks on the tracker information. Moreover, the calorimeter has standalone trigger capabilities based on the total energy deposit and pattern of the hits. To perform these tasks, a calorimeter with a high acceptance for conversion electrons and with good energy and time resolution is needed. The physics and technical requirements it has to satisfy for 100 MeV electrons are:

- An energy resolution $\sigma_E/E < 10\%$.
- A timing resolution $\sigma_t < 500\,\text{ps}$.
- A position resolution better than 1 cm.
- To work in a 10^{-4} Torr vacuum and 1 T magnetic field.
- To withstand high radiation doses.

The chosen design for the calorimeter is of two annular disks, each loaded with 674 pure CsI crystals with each crystal read out on one side by two UV-extended custom Hamamatsu Silicon photomultipliers (SiPMs).

A detailed description of the Mu2e calorimeter is reported in Chapter 3.

2.6.3 Cosmic Ray Veto

Cosmic Ray (CR) muons will reach Mu2e detector area with a rate of around 15000/s, yielding one conversion-like event per day, whether it is a mis-identified muon, an electron from a decay or an electron knocked out of the material surrounding the detectors. Since CRs are not associated to the muon beam, the associated background scales only with the live time of the experiment. CR background has to be suppressed to achieve the Mu2e requirement sensitivity. This can be achieved with passive shielding above and on the sides of the detector hall but, most importantly, with an active veto detector whose purpose is to detect penetrating Cosmic Ray muons. The Cosmic Ray veto consists of 83 modules, each one made of four layers of extruded polystyrene scintillator strips with aluminum absorbers between each layer. The scintillator counters are coated with TiO_2 and have embedded wavelength shifting fibers which are read-out by SiPMs. The

scintillator surrounds the top and sides of the DS and the downstream end of the TS, as shown in Fig. 2.21.

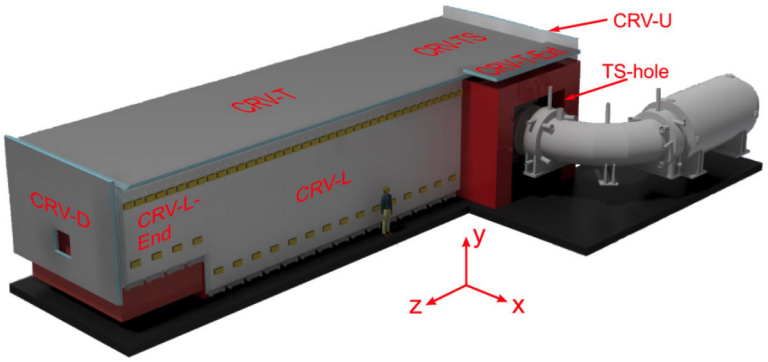

Figure 2.21: 3D representation of the Cosmic Ray Veto modules.

Considering that three out of the four layers have to be hit successfully in order to count as a CR event, the evaluated efficiency of the CRV modules is of $\sim 99.99\%$ [60]. The evaluation of CRV performance over time and aging of its components have been carefully analysed after the decision to perform two Mu2e runs, increasing the live time for the experiment. It was found that the light yield decrease and the increase in dead time would reach levels not acceptable by the CRV requirements, so different strategies are being evaluated to contrast these effects [61].

2.7 Mu2e current status

Important progress has been done in the last years, and Mu2e is steadily moving toward its commissioning phase. Nevertheless, delays were accumulated due to COVID-related reduction of field work and performance issues of the PS and DS magnet vendors. For these reasons, the Collaboration chose to divide the data-taking into a Run I (up to the Fermilab accelerator complex shutdown in 2026) and a Run II (starting in 2029).

Concerning the proton beamline, the transport of the 8 GeV proton beam to the start of Mu2e beamline diagnostic absorber was demonstrated, the fabrication of electrostatic septa for the protons extraction and extinction AC dipoles was started and the first production target was completed (as shown on the left of Fig. 2.22). The Stopping Target is also ready (Fig. 2.22-right). About the muon beamline, the coils for the TS and DS have been fabricated and can be seen in Fig. 2.23, but DS coils and the cold masses for PS and DS are still under construction.

The tracker has produced all the straws and 167 out of 216 panels, with 16 out of 36 planes assembled. This is an ongoing process while Cosmic Ray tests are being

Figure 2.22: The Production Target (left) and the Stopping Target (right) assembled.

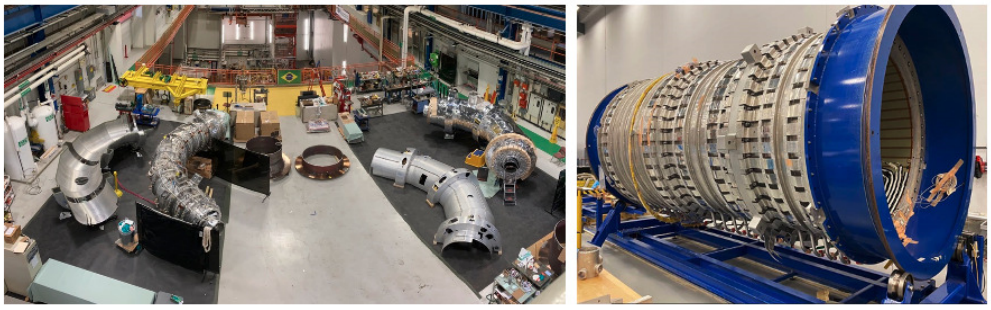

Figure 2.23: The TS being assembled at Fermilab, left, and the PS coils, right.

performed on a single plane. Fig. 2.24 shows a few planes of the tracker which are being assembled. The Cosmic Ray Veto construction is in an advanced stage (4400 out of 5500 scintillators produced). The calorimeter construction is also at a good stage and proceeding steadily: all crystals, SiPMs, and Front-End Electronics (FEE) boards were produced and all mechanical parts are available. The first disk was partially assembled, including most mechanical parts and the crystals are stacked (as shown in Fig. 2.24). Meanwhile, Cosmic Rays test are underway on a large prototype of the calorimeter at LNF. The assembly and commissioning status of the calorimeter is discussed more in detail in Section 3.7.

2.7.1 Run I sensitivity

Given time constraints due to the beam availability at Fermilab, Mu2e has opted for a run plan divided in two different phases. Run I will take place in 2025–2026, before a 2 years shutdown due to the planned accelerator upgrade for the long baseline neutrino program. A dedicated simulation work, called SU2020 (2020 Sensitivity Update), has been performed to evaluate the expected limit and discovery sensitivity for Run I. At

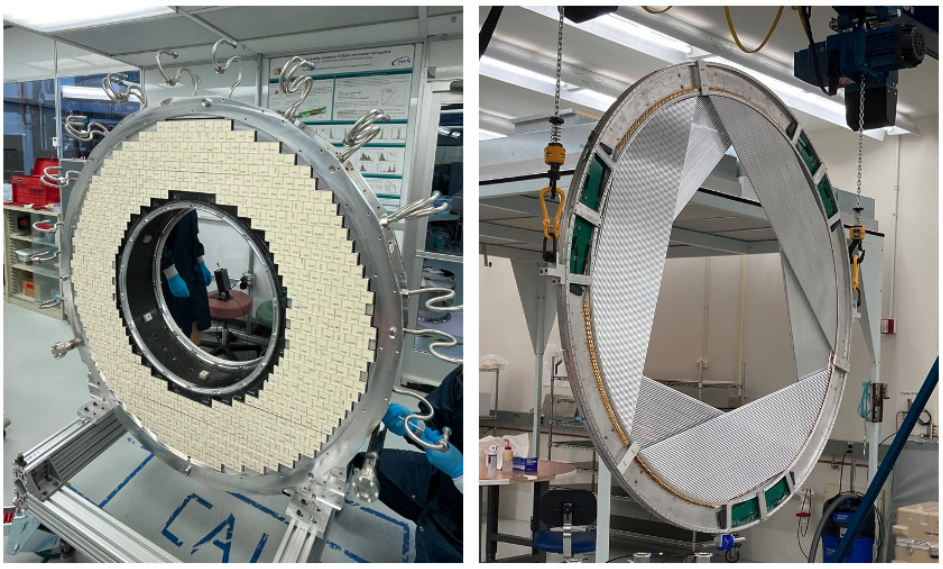

Figure 2.24: The first disk of the calorimeter being assembled (left), with the crystals already stacked, and a station of the tracker (right).

the beginning of this first run, a low intensity proton beam, 1.6×10^7 protons/pulse, will be used. During the second part, the mean intensity will be increased to reach 3.9×10^7 protons/pulse. The total number of stopped muons will be 5.99×10^{16}, corresponding to the 10% of the number required to satisfy the Mu2e goals in the complete data-taking. The Mu2e single-event sensitivity (SES) is defined as the $R_{\mu e}$ corresponding to one expected signal event with negligible background. The events selection for the searched CLFV process, is carried out using two different series of cuts optimised for discovery or limit, chosen based on the number of CE candidates observed. In the discovery-optimised case, considering ϵ as the product of acceptance and efficiency on signal events, the SES can be then evaluated as:

$$SES = \frac{1}{BR(\text{all}\,\mu\,\text{captures}) \cdot N_\mu \cdot \epsilon} = (3.01 \pm 0.03\,(\text{stat}) \pm 0.41\,(\text{syst})) \times 10^{-17}. \quad (2.5)$$

The expected total background is of 0.41 ± 0.13 events, with different contributions as reported in Table 2.1, given 3.6×10^{20} protons on target (POT), i.e. the full Mu2e statistics (Run I + Run II). The expected electron momentum spectrum, with a hypothetical $R_{\mu e} = 2 \times 10^{16}$, is shown in Fig. 2.25.

Considering instead the results of SU2020 for Run I, the expected SES is 2.5×10^{-16}, with a background of 0.017 ± 0.032 events. The number of events needed to declare a 5σ discovery is 5.8 at $R_{\mu e} = 1.4 \times 10^{-15}$ and the expected 90% CL upper limit is 4.8×10^{-16}, reached when the observed events are less than 2.4 [63]. Considering an hypothetical $R_{\mu e}$ of 10^{-15}, the expected distribution of conversion electron candidates in momentum

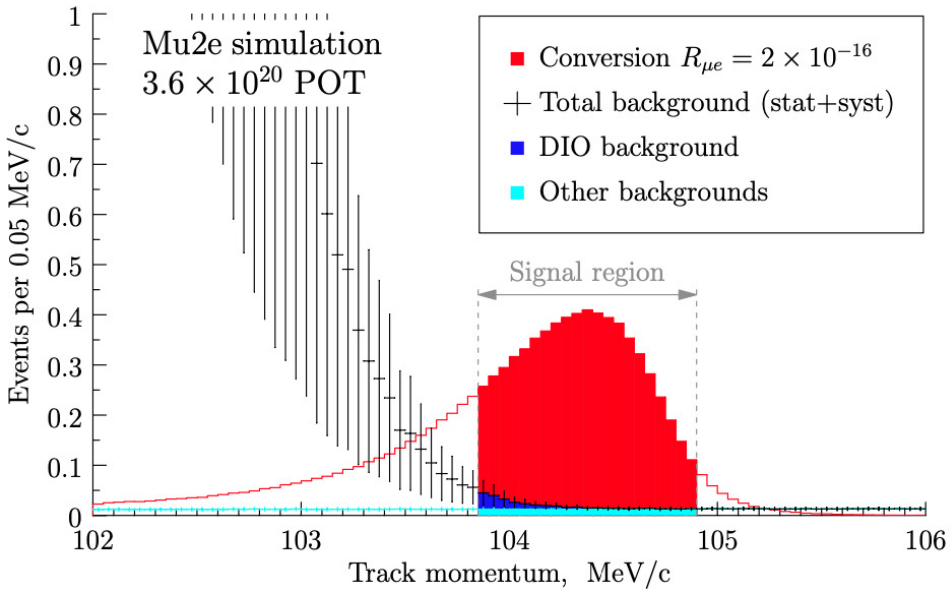

Figure 2.25: Expected background contributions and possible conversion signal in Mu2e for 3.6×10^{20} POT.

and time is shown in Fig. 2.26.

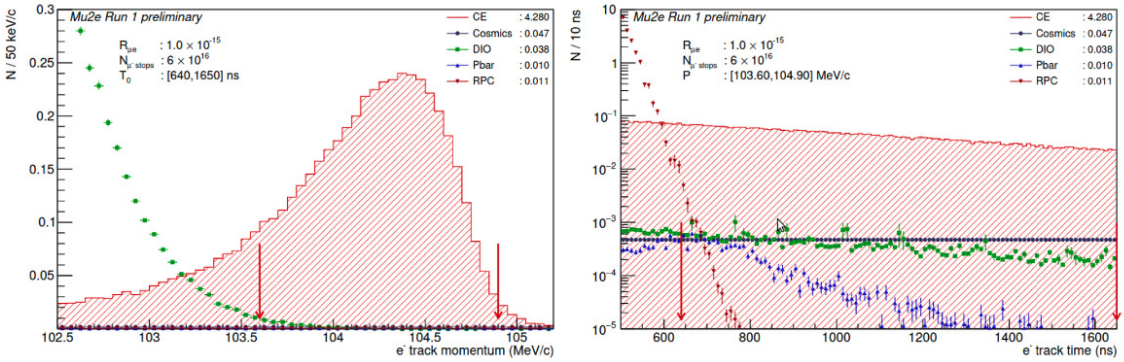

Figure 2.26: Electron momentum (left) and time (right) distributions. The background estimate numbers are the integrals over the optimized signal windows indicated by the red arrows.

Bkg type	Process	Event yield
Intrinsic	Decay in orbit (DIO)	$0.144 \pm 0.028\,(\text{stat}) \pm 0.11\,(\text{syst})$
	Radiative Muon Capture (RMC)	0.000 ± 0.004
Late arriving	Radiative Pion Capture (RPC)	$0.021 \pm 0.001\,(\text{stat}) \pm 0.002\,(\text{syst})$
	Muon decay in flight	< 0.003
	Pion decay in flight	$0.001\pm < 0.001$
	Beam electrons	$(2.1 \pm 1.0) \times 10^{-4}$
Others	Cosmic rays	$0.209 \pm 0.0022\,(\text{stat}) \pm 0.055\,(\text{syst})$
	Antiprotons	$0.040 \pm 0.001,\,(\text{stat}) \pm 0.020\,(\text{syst})$
	Total	$0.41 \pm 0.13\,(\text{stat+syst})$

Table 2.1: Summary of backgrounds for the discovery-optimized momentum window $[103.85, 104.90]$ MeV and a live window from 700 ns after the proton pulse. The pion capture and beam electron lines assume 10^{-10} beam extinction [62].

Chapter 3

The Mu2e Electromagnetic Calorimeter

The Mu2e experiment has to perform a search for a very rare process which requires high precision and excellent background rejection. To ensure that the goal set for single event sensitivity (3×10^{-17}) is met, there is the need to introduce a detector which can complement the CRV and tracker information. Non-vetoed cosmic ray muons could produce signal-like tracks while bad reconstructed tracks in the tracker could increase the background. To help on the CE identification task, a crystal calorimeter has been chosen and designed to provide excellent time resolution, together with energy and position information, and achieve good Particle Identification (PID) capabilities. In the following, the calorimeter is described in its active components as well as in its mechanical and electrical aspects.

3.1 Requirements

The calorimeter physics requirements have been set by the Mu2e collaboration to satisfy the tasks it has to perform. The calorimeter has to support the tracking reconstruction, providing a seed to improve the pattern recognition and reconstruction efficiency. To do so, the hits of the tracker are down-selected in a 50 ns window centered on the cluster timing, taking into consideration only tracking hit-level information. The calorimeter also needs to have a large acceptance for signal electrons and provide shower shape, energy, and timing information to reject background pions and muons and improve the tracker PID reconstruction. Simulation guided us to require a μ/e rejection factor of 200 for muons and electrons with momentum in the signal region. The calorimeter has also the capability to provide a tracking independent trigger, based on the energy deposit characteristics, that could be useful for saving data on disk in the first running phase, if

needed, as well as allowing an unbiased set for the measurement of the tracking based trigger efficiency.

Starting from those needs, it has been evaluated that the calorimeter technical requirements, for 105 MeV electrons, are [64]:

- An energy resolution $\sigma_E/E < 10\%$, to confirm the most precise tracker momentum measurement while having a sufficient E/p resolution to achieve the required muon rejection factor, considering that 105 MeV muons create calorimeter clusters with a deposited energy of ~ 40 MeV.
- A timing resolution $\sigma_t < 500$ ps, to achieve our PID requirement and to match calorimeter and tracker hits.
- A cluster position resolution of the order of $\sigma_{x,y} \sim 1$ cm, to allow a good correlation between the cluster position and the electron trajectories extrapolated by the tracker on the calorimeter surface.
- A fast response time (< 40 ns) to avoid pile-up and cope with the high experimental rates (50 kHz/cm^2 in the live window, in the innermost region).
- A temperature (gain) stability within ± 0.5°C ($\pm 0.5\%$) to avoid deteriorating the energy resolution.

Finally, the environment in which the calorimeter will operate has to be carefully taken into consideration. In the hottest region, the calorimeter will be exposed to $\sim$ 90 krad and to an equivalent neutron fluency of the order of 1.2×10^{12} $n_{1MeV\,eq.}$/cm^2 [65]. The calorimeter will also have to operate in a 10^{-4} Torr vacuum and in presence of an axial 1 T magnetic field of the Detector Solenoid.

3.2 General Design

On basic grounds, a homogeneous crystal calorimeter would satisfy the energy resolution requirements. However, the final design and the choice of the major calorimeter characteristics have undergone a long research and development phase, with different materials and layouts being considered. The final design is illustrated in the Mu2e Calorimeter Final Technical Design Report [66].

Scintillating crystals were chosen over scintillating noble gases, as employed for instance by the MEG experiment, due to the much tighter temperature restraints and to avoid the insertion of a separated cryostat inside the DS, which would have caused a

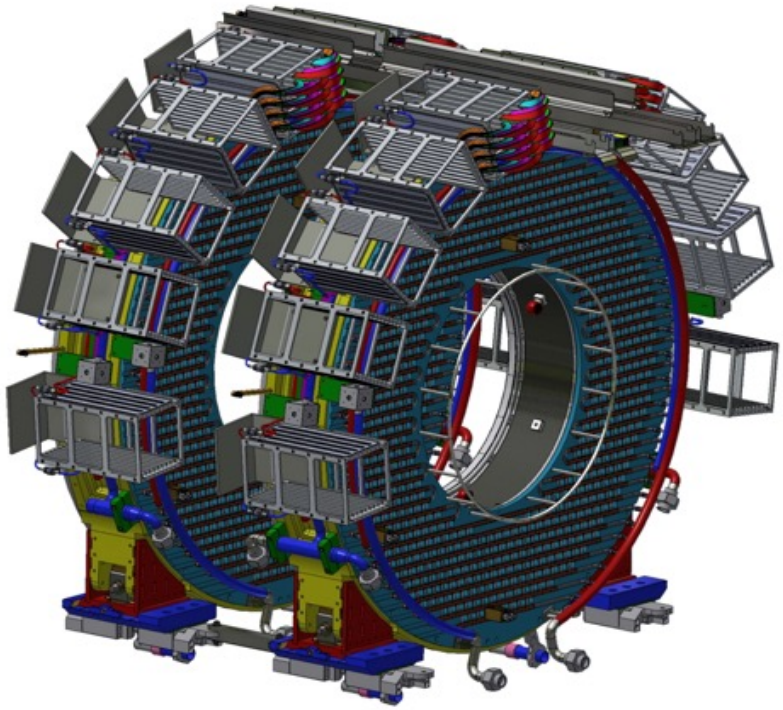

Figure 3.1: The two Mu2e calorimeter disks. The Readout Units assembled on the back of the second disk are also depicted. Mounted on top of each disk are the 10 crates that host the data acquisition and digitisation boards.

higher energy loss for the candidate electrons and it generally would have been difficult to achieve.

The calorimeter has an annular shape like the tracker and is composed by two disks, with an inner radius of 37 cm and an outer radius of 66 cm, allowing for a cross-section area of $\mathcal{O}(1\,\mathrm{m}^2)$. A 3D rendering of the calorimeter is shown in Fig. 3.1. The distance between the two disks has been set to 70 cm, based on the expected pitch of the helical trajectory of signal electrons and the best expected efficiency (Fig. 3.2).

Each disks is made by 674 pure CsI parallelepipedal crystals of $3.4 \times 3.4 \times 20$ cm^3, stacked one on top of the other. Each crystal is wrapped with a layer of 150 μm thick Tyvek foils and with 50 μm thick Tedlar foils, to eliminate the optical cross-talk between adjacent crystals. Working in magnetic field, silicon photosensors have been chosen. Each crystal will be read out by two custom-made Hamamatsu SiPMs, whose signal is digitized by boards housed in the crates on top of the disks. A cooling system runs through the crates to ensure temperature control and stabilization.

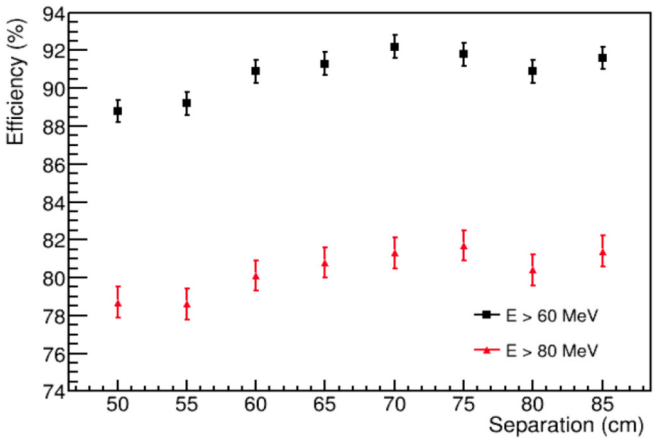

Figure 3.2: Calorimeter acceptance for electrons and positrons as a function of the disk separation distance [67].

3.2.1 Crystals

In the Mu2e CDR [68], it was reported that the chosen crystals for the calorimeter were LYSO (lutetium-yttrium oxy-ortho-silicate) crystals, which were already substituting the first hypothesis of $PbWO_4$ crystals to get an improved light yield. LYSO was considered an optimal solution for the calorimeter requirements, given its high light output, its excellent radiation hardness, its fast signals, and the fact that its scintillation spectrum, centered at 420 nm, well matched with the available avalanche photodiodes (APDs). Due to the strong increase in the cost of lutetium salt, that made this option impossible to afford and other crystals had to be taken into consideration. BaF_2 and CsI characteristics were evaluated to make the final down-select. In Table 3.1, the main characteristics of the four mentioned crystals are reported. BaF_2 was an excellent alternative since it has the fastest emission time among all the scintillating crystals. The main issue here was that its emission spectrum, peaked at 220 nm, showed also the presence of a slow component at higher wavelength with a 650 ns decay time, which would have introduced a concerning pile-up risk. The initial R&D plan was to develop solar-blind photosensors (APDs or SiPMs) or to dope the crystals with rare earths to suppress the slow component. Unfortunately, due to time constraints and difficulty in developing these new options this choice was then discarded. The pure CsI crystal was finally offering a viable solution due to the fact that the light yield was acceptable and newly developed SiPMs from Hamamatsu had a sensitivity that could match its emission wavelenght at 310 nm.

The dimensions of the crystals were chosen to satisfy the technical requirements of position and energy resolution. A crystal length of 20 cm (11 X_0 of CsI) was considered sufficient to reduce longitudinal leakage since the average arrival angle of the CE signal ($\sim 55\,^\circ$) corresponded to and effective length of around 17 X_0.

Crystal	**$PbWO_4$**	**BaF_2**	**LYSO**	**CsI**
Density [g/cm^3]	8.28	4.89	7.28	4.51
Radiation length X_0 [cm]	0.9	2.03	1.14	1.86
Molière radius R_M [cm]	2.0	3.10	2.07	3.57
Interaction length λ_{int} [cm]	20.7	30.7	20.9	39.3
dE/dx [MeV/cm]	13.0	6.5	10.0	5.56
Peak luminescence [nm]	420	220, 300	402	310
Decay time τ [ns]	30, 10	0.9, 650	40	26
LY (w.r.t. Na(Tl)) [%]	0.3, 0.1	4.1, 36	85	3.6
LY change with temp. [%/°C]	-2.5	0.1, -1.9	-0.2	-1.4
Hygroscopicity	None	None	None	Slight

Table 3.1: Comparison of crystal properties for the four crystals considered for the Mu2e calormeter: $PbWO_4$, BaF_2, LYSO and CsI.

The CsI emission spectrum has a dominant fast component ($\tau \sim 20$ ns) at 310 nm and a slow component with $\tau \sim 1000$ ns at ~ 500 nm, as shown in Figure 3.3-left. The latter one can represent up to 30% of the total light output and it is mainly due to crystal impurities.

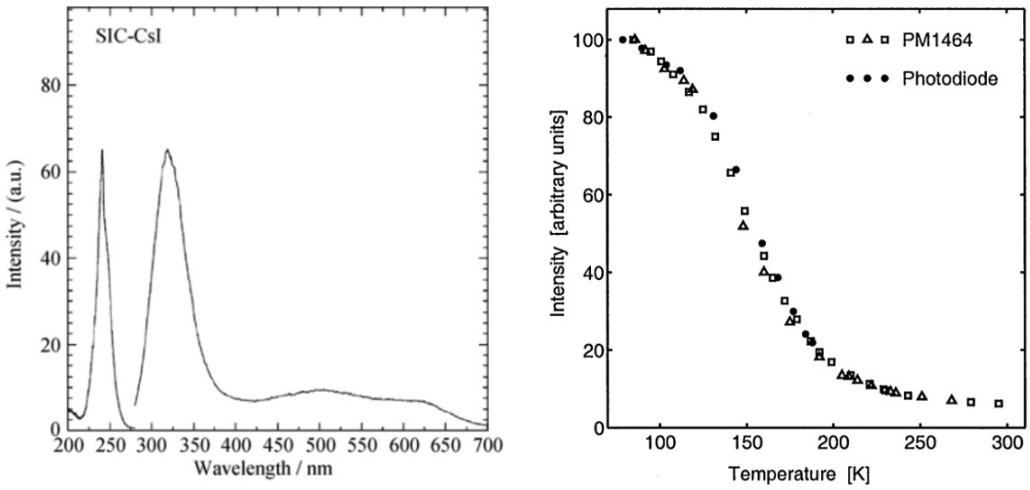

Figure 3.3: Left: Photoluminescence spectra of pure Shanghai Institute of Ceramics (SIC) CsI crystal with the emission peak at 318 nm and the excitation peak at 241 nm [69]. Right: Light yield of pure CsI crystals as a function temperature. Both measurements, one with a photomultiplier (Hamamatsu R1464), and the other with a photodiode (SINTEF) and wavelength shifter, are normalised independently to the maximum [70].

Each crystal is coupled to two Mu2e SiPMs, each one a large area (12 mm^2 active surface) array of Hamamatsu UV extended SiPMs (see Section 4.1.1), via a 2 mm gap without any optical grease or glue in order to reduce the thermal coupling between the two elements. This is a very important technical choice, since the CsI output quickly

increases at low temperatures, as shown in Fig. 3.3-right, while the photosensors should work at low temperatures to ensure their best performance. Leaving an empty gap, given also the vacuum environment in which Mu2e will operate, minimised the risk of harmful temperature gradients along the crystal axis that could deteriorate the achievable energy resolution. A 150μm Tyvek foil is wrapped around each crystal and it is sustained at the sides edges by 3D printed plastic frames which prevent it from folding forward and keep the 2mm-gap between crystals and SiPMs. On the crystal open end, i.e. the one without the SiPM, a cap covered by Tyvek is placed to grant reflection on that side as well. Dedicated studies evaluated that Tyvek is approximately 90% reflective for the CsI emission wavelength, making it an optimal reflector choice to improve the collected light. During the data analysis of the large size prototype of the Mu2e Calorimeter (see Sect. 3.6), an optical cross-talk between adjacent crystals of $\mathcal{O}(2\%)$ was observed, so that a black Tedlar foil was added over the external wrapping to address this problem.

Crystals characterisation and quality controls

A Quality Control (QC) test on all the production crystals has been performed at the Silicon Detector Facility (SiDet) at Fermilab, using the finally wrapped crystals and reading them out with a 2" diameter UV-extended PMT (ET Enterprise 9202QB), coupled through a 2 mm air gap. Several characteristics of the crystals have been evaluated in this way.

The Light Yield (LY) is the most relevant property of a scintillator and is defined as the number of photoelectrons $\mathrm{N_{p.e.}}$ in the photosensor for MeV of energy deposited in the crystal. It can be expressed as

$$LY = LY_{abs} \times \epsilon_L \times \epsilon_A \times \epsilon_{QE}\ [\mathrm{N_{p.e.}/MeV}] \tag{3.1}$$

with LY_{abs} the crystal absolute light yield, dependent on the material, the energy bands and the band gap. The other three parameters are: ϵ_L the optical transmission efficiency of the scintillating photons from their generation point through the crystal end where the photosensor is located, ϵ_A a geometrical coupling factor between the crystal and the photodetector active area, and ϵ_{QE} the quantum efficiency of the photodetector coupled to the crystal.

The Longitudinal Response Uniformity (LRU) is a parameter which allows to evaluate the crystal response along its longitudinal axis. This quantity can be evaluated from the normalised RMS of the LY value for different impact positions of the incident particle/calibration source.

The relative contribution of the fast component is evaluated by calculating the Fast-

over-Total (FT) ratio, $FT = Q_{fast}/Q_{tot}$, where Q_{fast} and Q_{tot} are, respectively, the charge integrated in a time window of 200 ns and 3000 ns after the peak. This ratio allows to evaluate the quality of the crystals and the weight of the slow component in the total emission.

The energy resolution of a scintillating crystal/photosensor system can be parametrized by three terms summed in quadrature:

$$\frac{\sigma_E}{E} = a \oplus \frac{b}{\sqrt{E}} \oplus \frac{c}{E}. \tag{3.2}$$

The term a is constant with energy and depends on the photosensor qualities, on its efficiency, the presence of non-uniformities in the light response and leakage which generally is the dominant contribution. This term sometimes is also related to the LRU. The statistical component b is $\propto 1/\sqrt{E}$ and is derived from the photoelectrons statistics (Poisson), so b decreases for higher LY. The component c, which is $\propto 1/E$, is determined by the electronic noise.

Pre-production CsI crystals were tested, starting at the end of 2016, using the 511 keV annihilation photons from a collimated ^{22}Na source to identify the selection criteria satisfying the detector requirements, such as:

- a Light Yield $LY > 100$ photoelectrons/MeV
- a fractional energy resolution $\sigma_E/E < 20\%$
- a Longitudinal Response Uniformity $LRU < 5\%$
- a Fast-over-Total ratio $FT > 75\%$

Furthermore, strict tolerances on the dimensions of the crystals were set: 100 μm for the transversal dimension, 200 μm for the longitudinal dimension, and a flatness below 100 μm in lateral and longitudinal faces [71]. These mechanical requirements have been controlled for each production crystal with a CMM present at SiDet. Three pre-production vendors were selected (Amcrys [72], Shanghai Institute of Ceramics (SIC or SICCAS) [73] and Saint–Gobain Corporation [74]) and a sample of pre-production crystals (see Figure 3.4) was required from each vendor.

To measure the physical properties of the production crystals, a QC Station was developed, allowing to perform LRU measurements by placing a collimated ^{22}Na source in 8 positions along the crystal axis. Further details about the SiDet crystals QC station are given in Section 6.3.1. Thanks to these tests, SIC and Saint–Gobain were chosen as best producers. SIC has supplied most of the crystals while Saint–Gobain delivered a small fraction. In Fig. 3.5 is shown the LY and resolution of the production crystals.

Figure 3.4: Picture of the pre-production crystal provided by three vendors: Amcrys, Saint–Gobain and SIC.

The quality assurance of optical (LY, LRU, FT, RIN) and mechanical (thickness, shape) properties lead to the decision to give the final production back SICCAS since Saint–Gobain failed to match our specifications.

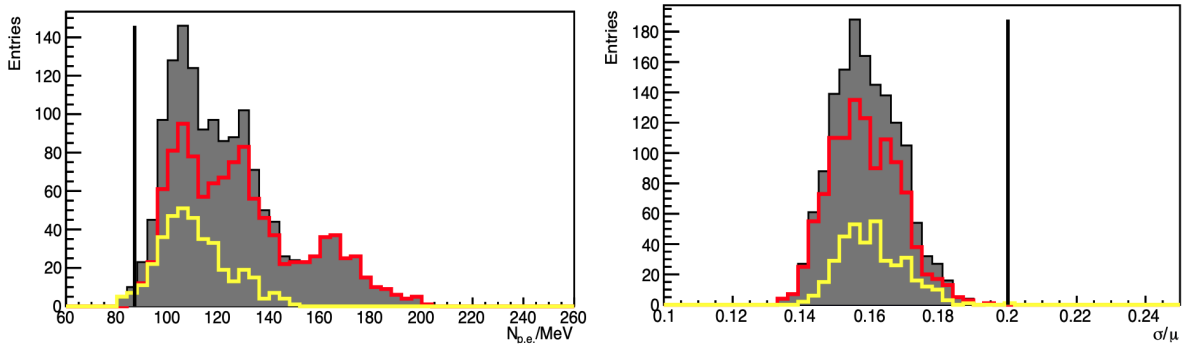

Figure 3.5: Distribution of the LY (left) and resolution (right) for the production crystals received from SICCAS (red) and Saint–Gobain (yellow). The gray distribution is the cumulative of the two. The black lines indicate the cut-off that was set for acceptance or rejection of the crystal.

3.2.2 SiPMs, Front End Electronics and Readout Units

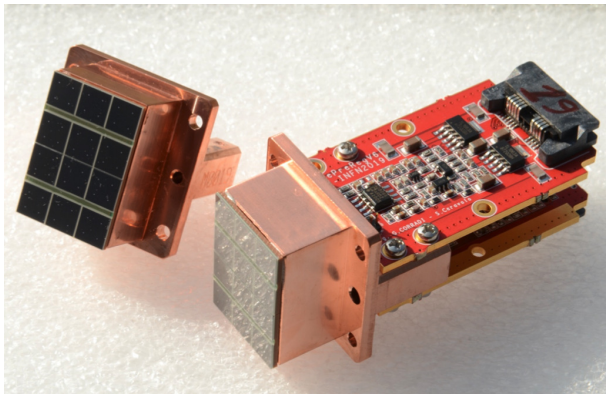

Figure 3.6: Picture of the Mu2e SiPM and the Front End Electronics boards.

In order to improve redundancy and reliability, each of the 674 crystals is coupled to two large area SiPM arrays, glued to a copper holder, and two FEE boards. This assembly is named Readout Unit (or ROU). Each SiPM array consists of two series of 3 monolithic $6 \times 6\,\mathrm{mm}^2$ UV extended Hamamatsu SiPMs connected in parallel, with $50\,\mu$m pixel size. Each SiPM array is entirely independent from the other array in the same ROU. The two SiPMs and the two connected FEE boards per ROU are shown in Fig 3.6. Maintenance and repairs to the detector are limited to once a year, so that the SiPM radiation hardness and their mean time to failure must be excellent, in order to have sensors which remain reliable over time. The final requirements for the production SiPMs are summarized as follows [75]:

- The 6 cells in a single SiPM matrix should have a RMS spread of the breakdown voltages, V_{bd}, within $\pm 0.5\%$.
- Similarly, the dark current (I_{dark}) RMS over the same 6 cells must remain within $\pm 15\%$.
- The Photon Detection Efficiency (PDE) per cell has to be greater than 20% at 315 nm.
- The dead time for each cell, relative to a load impedance of $15\,\Omega$ or greater, has to be $< 100\,\mathrm{ns}$.
- The gain at the operating voltage, $V_{op} = V_{bd} + 3\mathrm{V}$, must be higher than 10^6.
- When the SiPMs are irradiated up to $3 \times 10^{11}\,\mathrm{n_{1MeV\,eq.}/cm^2}$ at 20°C, the leakage current must be smaller than 10 mA at V_{op}.

- the Mean Time To Failure (MTTF) at 0°C has to be better than 10^6 hours. The MTTF test is performed by setting the SiPMs voltage at their operational voltage and heating them at 65°C for 18 days, allowing to extrapolate their reliability after running 10^6 hours at 0°C.

The analog FEE boards are connected directly to four pins of the photosensor and drive and process the signal from the SiPMs. They provide amplification and shaping of the signals, and a local high voltage (HV) regulation for independent control of the bias voltages (through high-voltage ADCs and DACs). Readout of current and temperature sensors are also provided.

Further details about the Readout Units are given in Chapter 4

3.2.3 Data Acquisition and Digitization Boards

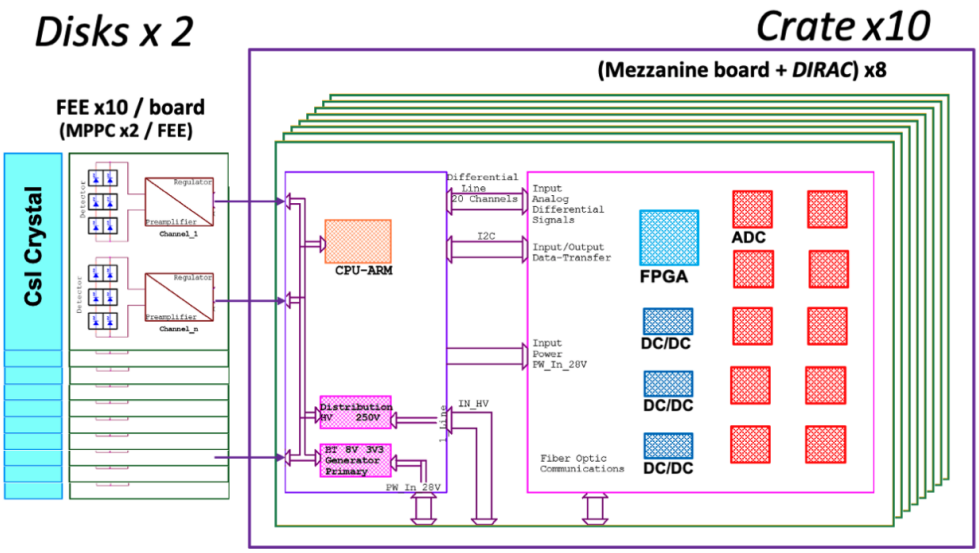

Figure 3.7: FEE, MZB and DIRAC architecture.

The FEE boards are gathered in groups of 20, so that each group is controlled by one Mezzanine Board (MZB) which handles 200 V HV distribution and the regulated low voltages (LV) needed by the FEE circuitry. The bias voltages are controlled individually per each SiPM, allowing to set individual operational voltages. An ARM controller handles the distribution of the HV and LV, by storing on its flash memory all the individual SiPM and FEE calibration parameters, such as board and SiPM IDs, HV 2-point calibration (slope and intercept) and SiPM bias setpoints. The DAQ system has to handle 2696 fast analogue channels, which start at the FEE boards and go through the MZB,

as depicted in Figure 3.7. These signals consist in the SiPM pulses, which have a 200 ns maximum width, a minimum rise time of 25 ns and a 2 V dynamic range.

From each MZB, sets of 20 analog signals are sent to a DIRAC (Digitiser Readout Controller) custom board for digitization, zero-suppression and hits building. This board digitizes the waveforms with a speed of 200 Msps, i.e. 10^6 samples/second, yielding 5 points on the rising part of the signal. The heart of the DIRAC is a FPGA which controls 10 12-bit ADCs and carries out online operations like zero suppression, baseline calculation, mean charge and timing reconstruction. The digitized data are then sent via optic fibers to the event builder. The digitizing system contains a total of 140 DIRAC boards arranged in 10 crates per disk, with each crate that can house up to 4 MZB/DIRAC pairs. Each DIRAC board is cooled through a copper cold plate that is kept in thermal contact with the highest dissipation components. The cold plate is then thermally connected to the crate custom aluminum structure where the coolant is circulated. A schematic view of the FEE-MZB-DIRAC chain is shown in Figure 3.8.

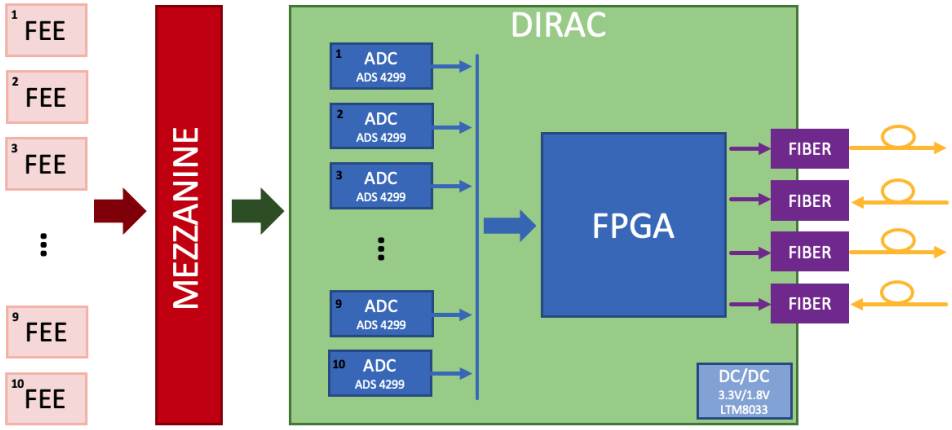

Figure 3.8: Block diagram for the Calorimeter Waveform Digitizer board, including also the MZB and the Amp-HV chips. The main components used are shown.

3.2.4 Radiation hardness tests

The calorimeter will be exposed to heavy doses of ionizing radiation and high neutron fluences (Sect. 3.1). It is then mandatory to test how all the components of the calorimeter, crystals, SiPMs, FEE, MZB and DIRAC boards, react when irradiated.

To perform ionizing irradiation tests, the ENEA CALLIOPE facility was used [76]. There, a ^{60}Co source (Fig. 3.9) generates γ-rays at 1.25 MeV. At the moment of the test, the source activity was 0.35×10^{15} Bq, allowing to reach 5 Gy/h at about 5 m distance from the source [65]. Neutron irradiation were mainly performed at the ENEA Frascati Neutron Generator Facility (FNG) [77]. FNG uses a deuteron beam accelerated up to

300 keV impinging on a tritiated target, to produce a nearly isotropic 14 MeV neutron flux via the $T(d,n)\alpha$ fusion reaction. The maximum neutron intensity is 0.5×10^{11} neutrons per second, in close proximity to the target, with a 4π uniform production.

The crystals and the FEEs, given their position inside the calorimeter disk, are going to be exposed to a higher particle flux, with respect to the larger electronic boards, MZB and DIRAC, that are mounted in the shielded crates on top of the disks. The boards have successfully passed tests with both neutrons and ionizing radiation, while measurements with high-energy hadrons are still ongoing.

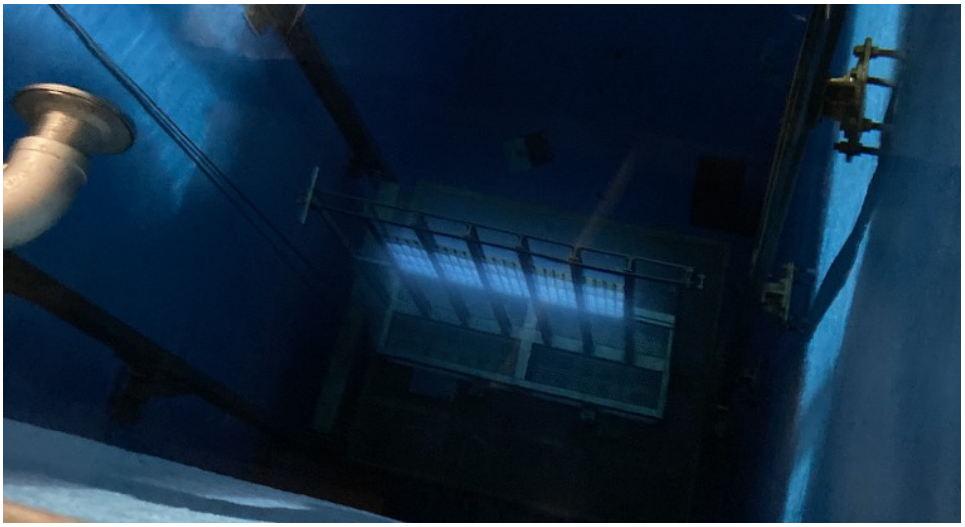

Figure 3.9: ^{60}Co source pool at ENEA CALLIOPE facility. The blue luminescence mainly due to the Cherenkov effect of Compton-scattered electrons can be seen.

Crystal irradiation tests

Tests performed at Calliope [65] showed that a Total Ionizing Dose (TID) of up to 200 Gy (20 krad) does not modify LY and LRU for unwrapped pure CsI crystals produced by SIC. Instead, after a total dose of 900 Gy (90 krad), a 20% LY reduction is observed. The same crystals, 22 days after the first measurements, were also irradiated with a neutron flux of $9 \times 10^{11} n_{1MeV\,eq.}/cm^2$, corresponding to about 2 times the total flux expected for the hottest calorimeter regions in three years of running. At the end of the neutron irradiation, an acceptable LY deterioration ($\lesssim$ 10%) was observed with a LRU that remained well below 10%.

As a thumb rule, neutrons deteriorated CsI properties much less than a comparable TID exposure which yielded a reduction in light output at $70\% \div 80\%$ after a TID of 100 krad.

Another important test to perform is the measurement of the Radiation Induced Noise (RIN), since during exposure of pure CsI crystals to high instantaneous radiation

levels an increase in the RIN value can be observed. RIN is due to the production of phosphorescent light emission that quickly disappears at the end of irradiation. Since during the experiment lifetime the exposure is going to be continuous, the crystals will constantly emit, increasing the noise associated to the performed measurement.

RIN was evaluated using a ^{137}Cs source, at the Caltech Irradiation Facility, which mainly emits γ-rays at 0.66 MeV. Crystals were readout using two Mu2e SiPMs and the respective dark currents were recorded using a picoammeter. The dark current was sampled for 5 minutes without exposure, then the RIN induced photocurrent (I_{RIN}) was measured for 15 minutes. Lastly, the measurement was kept going for further 15 minutes to evaluate the RIN decay over time, as seen in Fig. 3.10-left. At the center of the holder, a 1.5 mm diameter collimator reduces the dose and restricts the photon emission direction. The number of photoelectrons induced by radiation per unit dose rate is given by the relation:

$$F = \frac{I_{RIN}}{G \times q_e \times \phi_s} \tag{3.3}$$

where G is the SiPM gain, q_e the electron charge in pC and $\phi_s = 42$ mrad/h is the source rate.

To evaluate the number of background photoelectrons due to RIN (N_{RIN}), F has to be re-scaled to the dose rate expected in the Mu2e operating environment, $\phi_{Mu2e} \sim 1.8$ rad/h in the innermost region, and it has to be integrated over the 200 ns gate of a typical calorimeter signal: $N_{RIN} = F \times \phi_{Mu2e} \times 200$ ns. The value of the RIN in MeV can then be obtained normalizing N_{RIN} with respect to the crystal LY: $RIN = \sqrt{N_{RIN}}/LY$. The results of the RIN for SIC and Saint–Gobain crystals is shown in Figure 3.10-right, with the mean value at ~ 400 keV and tails close to 1 MeV.

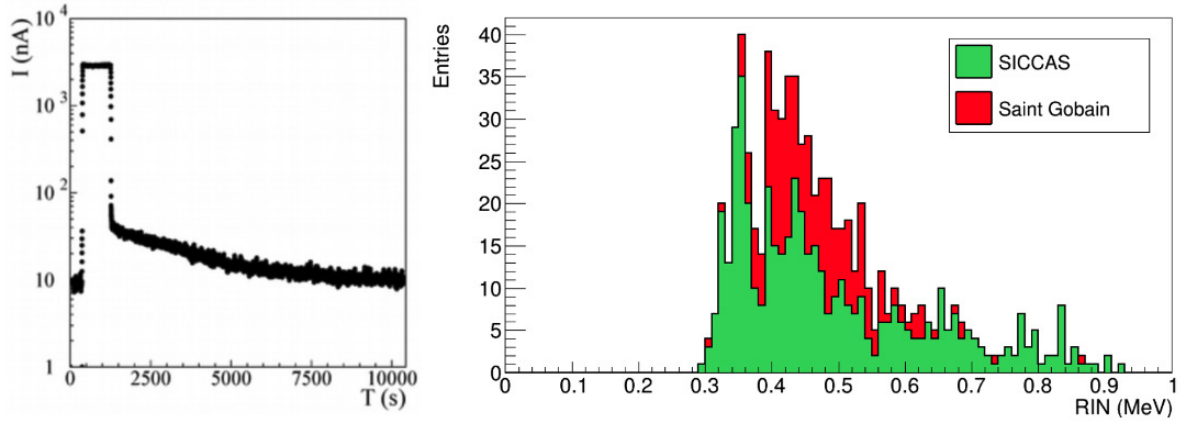

Figure 3.10: Left: Example of the photocurrent output during RIN tests. Right: Summary RIN results for Saint–Gobain and SICCAS (SIC) crystals.

RIN measurements were also performed with low energy neutrons at the HOTNES

facility of ENEA (Frascati), following an analogous data taking scheme [78]. A single crystal, coupled to a photomultiplier, was inserted inside a hollow AmB neutron source and irradiated with a uniform flux of 700 n/cm^{2}s at thermal energies. It was observed that the RIN due to ionization is much larger than the one induced by neutrons, allowing to carry out the final control on radiation hardness using only ionisation dose tests. Considering a safety factor on the dose rate, evaluated via simulations, the final requirements on the crystals radiation hardness are:

- $RIN < 0.6$ MeV for a dose rate of 1.8 rad/h;
- $LY > 85\%$ (60%) of the initial value, after exposure to a TID of 10 (100) krad.

Electronics and SiPMs irradiation tests

Different irradiation campaigns have been carried out on the SiPMs and the FEE boards. The TID tested for the SiPMs (FEE) is of 450 Gy (900 Gy) and a maximum neutron fluence of $\mathcal{O}(10^{12})$. The SiPMs were irradiated at CALLIOPE with a total dose of 200 Gy in 3 days. The dose effect on the SiPM performance is negligible both in terms of leakage current and signal amplitude, being the effect related to surface and not bulk currents. Instead, the neutron irradiation affects the bulk, yielding an increase of the leakage current that is proportional to the neutron fluence.

The latest tests were performed at FNG on a total of 35 SiPMs at 4 different fluences: 5×10^{10}, 1×10^{11}, 5×10^{11} and 1×10^{12} $n_{1Mev\,eq.}/cm^2$ [79]. The breakdown voltage was studied through the I-V curves. When the bias voltage starts to increase, the current increases more and more rapidly until the breakdown voltage (V_{bd}). At that point the curve behavior changes from a convex function to a concave one. V_{bd} can then be evaluated by finding the maximum of the Logarithmic Derivative $d(logI)/dV$ [80]. Figure 3.11 reports an example of two I-V curves for SiPMs irradiated with a fluence of 5×10^{10} (left) and 1×10^{12} (right), for different operational temperatures. As can be seen from these plots, the dark current shows a clear reduction with decreasing temperature.

For every fluence, the mean current was evaluated at 4 voltage points: V_{bd}^{cell}, $V_{bd}^{cell} + 3\,V$, $V_{bd}^{cell} + 6\,V$, $V_{bd}^{cell} + 9\,V$ (V_{bd}^{cell} is the the breakdown voltage of a single SiPM cell and six cells constitute one Mu2e SiPM). The results for the mean current are shown in Fig. 3.12 for fluences of 5×10^{11} and 1×10^{12} $n_{1Mev\,eq.}/cm^2$. These measurements were performed at $-5\,°C$. The mean value we obtained at the temperature at $V_{op} = V_{bd}^{cell} + 9\,V$ is ~ 7 mA. To reduce this, the temperature can be lowered up to $-10\,°C$ and also the bias voltage can be reduced and a lower V_{op} can be chosen, also exploiting the results obtained at the ROUs QC Station in Frascati, described in Chapter 4.

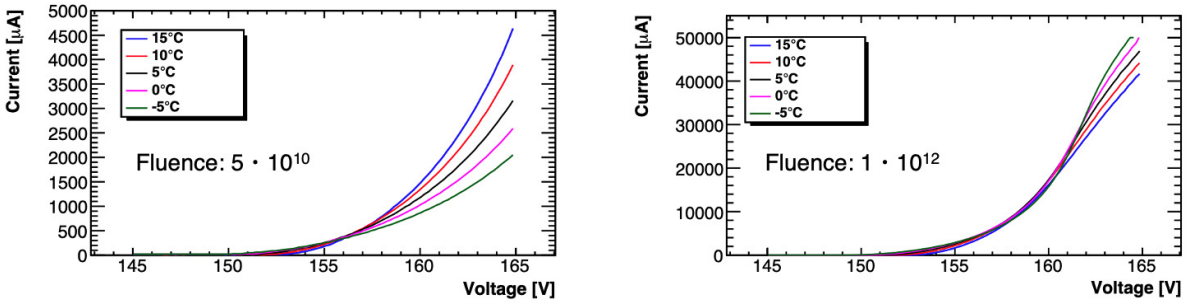

Figure 3.11: Example of two I-V curves for two SiPMs irradiated with fluences of 5×10^{10} (left) and $1 \times 10^{12}\,\mathrm{n_{1Mev\,eq.}/cm^2}$ (right). The curves for different working temperatures are shown.

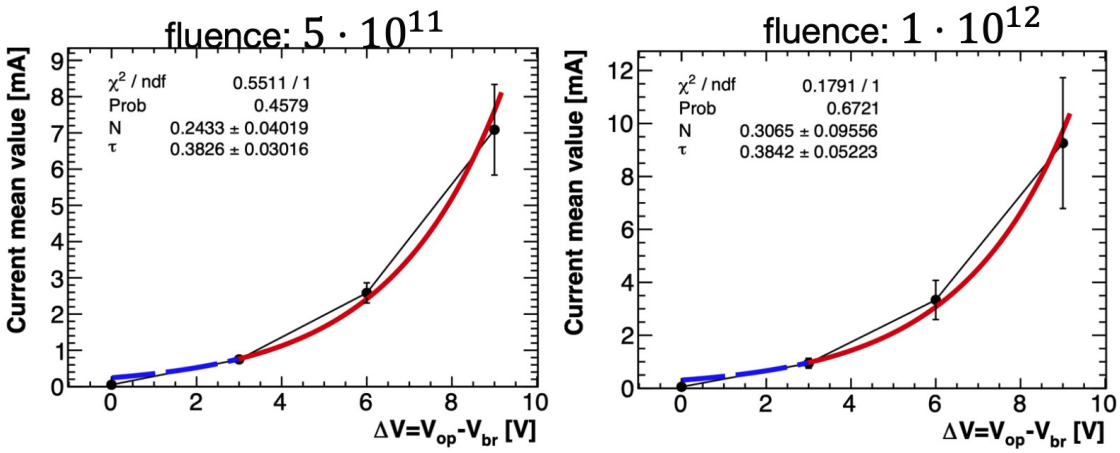

Figure 3.12: Mean current values as a function of the overvoltage for a fluence of $5 \times 10^{11}\mathrm{n_{1Mev\,eq.}/cm^2}$ (left) and $1 \times 10^{12}\mathrm{n_{1Mev\,eq.}/cm^2}$ (right).

The first version of the calorimeter FEE boards suffered a lot the exposition to ionizing doses, so that some board components were replaced with radiation harder parts. The final version of the FEE boards was tested up to 1030 Gy at Calliope and $10^{12}\,\mathrm{n_{1Mev\,eq.}/cm^2}$ at FNG without showing problematic behaviour.

3.3 Calorimeter Mechanics

The calorimeter mechanics is designed to ensure structural rigidity and support for the 674 crystals per disk which are piled-up in a self-standing array, organized in staggered rows, for a total weight of 700 kg. Furthermore, each crystals has to be aligned with its readout unit, the calorimeter has to be aligned within the DS and the electronic components have to be sustained and cooled. In each disk, the crystals are supported by an inner and an outer cylinder, as can be seen in Fig. 3.13. The inner disk is made of a carbon fiber and aluminum honeycomb to minimise the amount of material that has to

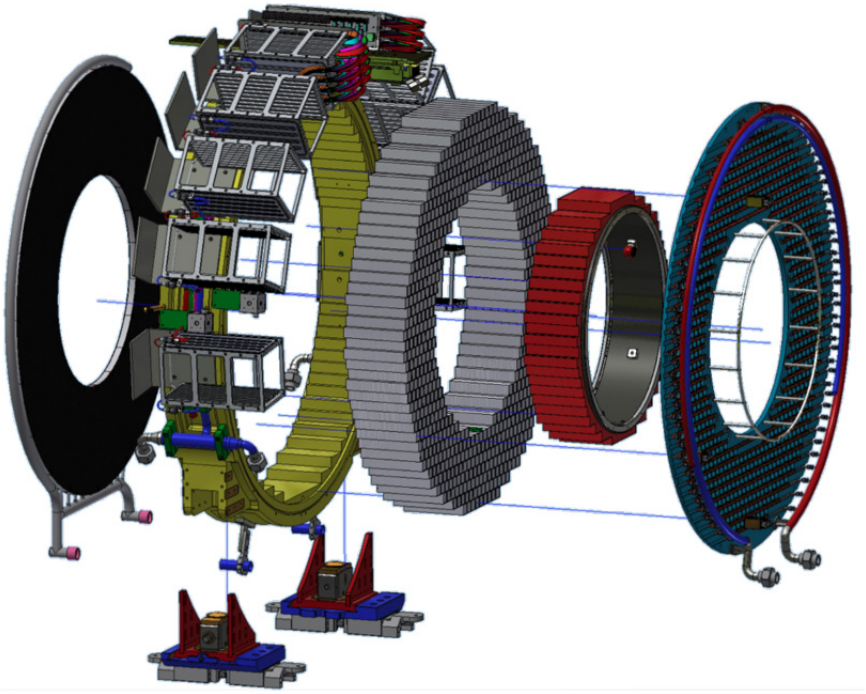

Figure 3.13: Exploded view of one calorimeter disk.

be crossed by the particles. The outer cylinder, coaxial to the inner, was machined from a solid block of aluminum. Each disk has two cover plates. The back plane is made of a plastic material with good outgassing properties, polyether-ether-ketone (PEEK). It provides support for the readout units and hosts the cooling pipes to dissipate the heat from the electronics and cool down the sensors. The plate facing the beam is made of carbon fiber to minimize the degradation of the electron energy and it hosts the thin aluminum tubing to distribute the source calibration fluid. As previously mentioned, all the muon beam-line is in vacuum, with 10^{-4} Torr inside the DS. In order to obtain this value, the limit on the outgassing rate is 8×10^{-3} Torr $\times$ liter/s, negligible with respect to the tracker contribution. A cooling system surrounds the electronic components and runs back-and-forth the back plate to maintain the temperature of all SiPMs at $\sim -10\,^{\circ}$C. The chosen fluid is a mixture of 35% MPG (Monopropylene glycol) aqueous solution.

3.4 Calibration Systems

The high sensitivity for discovery of a CLFV event of the Mu2e experiment, implies a special care in detector calibration to avoid any systematic effect. The different independent calibration methods which will be followed employ:

- A radioactive source for absolute energy calibration.

- A laser pulsing system to monitor and correct variations of the SiPMs gains associated to small temperature variations or to radiation damage in the long-term, as well as to perform a fast equalisation of time offsets.
- Cosmic-ray muons.
- Decays of stopped muons and pions by exploiting the very precise measurement of the track momenta carried out by the tracker. This calibration requires a reduction of the magnetic field and beam intensity to 1/2 in order to get hits in all the crystals without degrading the tracker performances.
- An alternative solution to the calibration with electrons from pions and muons, is to look at electrons and positrons coming from internal conversions of RMC photons. This could be used as a calibration signal in the calorimeter by relying on the very precise measurement of the track momenta carried out by the tracker, without requiring runs at reduced magnetic field.

Furthermore, prior to the installation in the final hall, the two calorimeter disks will be scanned with cosmic rays, so as to calibrate energy response and to align time offsets of all calorimeter channels using a Cosmic Ray Tagger (CRT).

3.4.1 Pre-calibration with the Cosmic Ray Tagger

After completing their assembly at the Fermilab Silicon Detector facility (SiDet) and prior to the installation in the detector solenoid, each calorimeter disk will be individually tested. Performance validation and reference calibration of the detector will be carried out using Minimum Ionizing Particles (MIPs) traced in 3D by means of the CRT. The 3D MIP tracking performed by the CRT will be used for the calibration of the calorimeter absolute energy response, equalisation of the channel responses, time offset alignment, crystals *LRU* check and study of timing resolution dependence on crystals z-axis. With the CRT both 2D and 3D path length reconstruction can be achieved. The CRT system is composed of two independent planar modules to be installed above and below the calorimeter disk under test, each composed of a single layer of 8 parallel scintillating bars, with a length of 1600 mm and a $15 \times 25\,\mathrm{mm}^2$ transversal cross-section. The scintillating material emission is peaked at 425 nm with a high light output of $\sim 10^4$ photons/MeV. Each bar is wrapped in Tyvek and read on each side by a single Mu2e SiPM, with its FEE board, coupled via optical grease. Each module is enclosed in a PVC box to ensure light tightness. One module is shown in Figure 3.14.

Considering a SiPM gain of 3.6×10^6, a MIP peak is visible at $\sim 480\,\mathrm{pC}$. The timing of each SiPM is reconstructed using a template fit procedure, in order to evaluate the

(a) One side of the module **(b)** Complete CRT module

Figure 3.14: Pictures of one CRT module with the PVC light-tight box removed.

time difference ΔT between the two sides. The longitudinal position of the hit (Z) is reconstructed from ΔT using the effective light speed in the bars $v_p = (14.29 \pm 0.05)\,\text{cm/ns}$, evaluated scanning the bar with a β source. Reconstructing Z allows also to estimate the light attenuation along the bars. The attenuation is well modelled by a double exponential function that considers both the bulk attenuation length (BAL = 380 cm), which corresponds to light propagating directly and depends only on material properties, and the technical attenuation length (TAL), which depends on the wrapping configuration of the scintillator. The obtained distribution is shown in Figure 3.15.

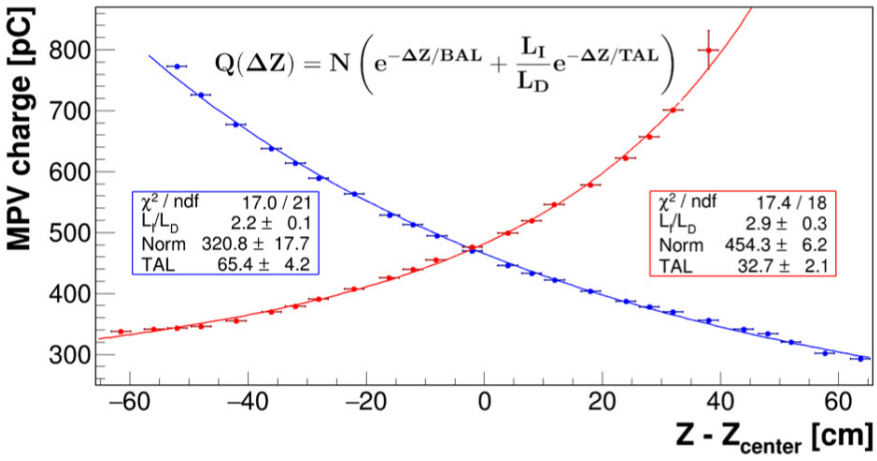

Figure 3.15: Most probable values of the Landau distributions fitted to the MIP charges for different slices in Z.

The hit position in the two CRT planes (placed above and below the disks) can be reconstructed on the transversal direction and on the Z axis with $\sigma_Z = 1.6\,\text{cm}$ at the center and $\sigma_Z = 2.3\,\text{cm}$ at the bar edges. The CRT has been completely assembled and

characterised, showing good performances and 3D tracking capabilities. It will be then used to study its tagging performance on the large scale prototype of the calorimeter in order to validate all the calibration procedures.

3.4.2 Radioactive source

The low-energy equalisation is carried out by means of a liquid radioactive γ source (Fluorinert, FC-77), circulated through aluminium pipes, shown on the left of Figure 3.16, placed in between the carbon fiber skins of each disk frontal cover plate.

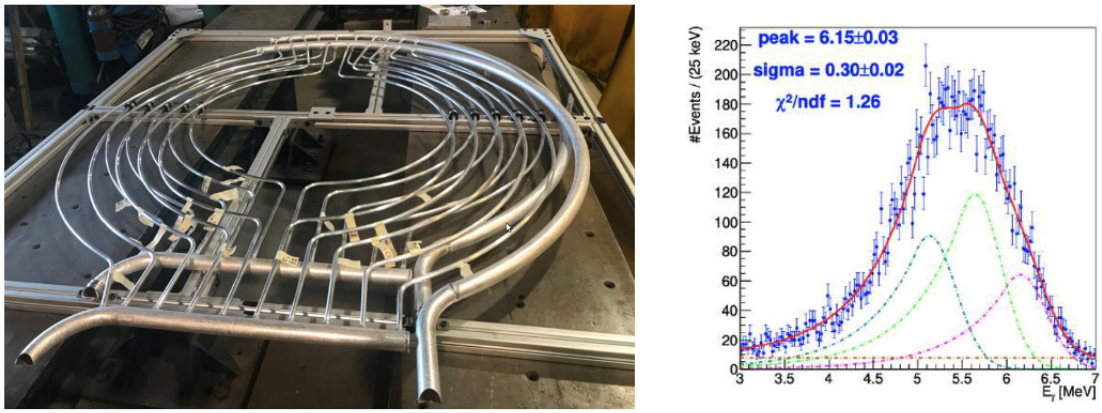

Figure 3.16: Left: Picture of one aluminium pipe for the circulation of the source. Right: Energy spectrum for a crystal irradiated with 6.13 MeV photons from an $^{16}O^*$ source. The different contributions are shown: the full absorption peak at 6.13 MeV and the two e^+e^- annihilation escape peaks at 5.62 MeV and at 5.11 MeV [33]. These peaks are then superimposed to the Compton spectrum.

The Fluorinert will be irradiated with 14.2 MeV neutrons produced by an external deuteron-tritium generator, with a flux of 10^8 n/s, which will trigger the decay chain:

$$\begin{aligned} {}^{19}\mathrm{F} + n &\rightarrow {}^{16}\mathrm{N} + \alpha \\ {}^{16}\mathrm{N} &\rightarrow {}^{16}\mathrm{O}^* + \beta^- + \bar{\nu}_e \; (\tau_{1/2} = 7.13\,\mathrm{s}) \\ {}^{16}\mathrm{O}^* &\rightarrow {}^{16}\mathrm{O} + \gamma\,(6.129\,\mathrm{MeV}) \end{aligned} \tag{3.4}$$

The dominant photon line in the oxygen daughter is at 6.129 MeV, occurring in a fraction 0.670 of the ^{16}N decays followed by the line with one or two escape photons.

The liquid source circuit consists of 12 Al pipes, 0.5 mm thick, with a diameter of 3/8 inches and a length which ranges from 1.5 to 1.7 m. The selected geometry allows to have an uniform illumination of the disk with a variation in the intensity smaller than 5% [67]. The 6.13 MeV photons can be seen by the calorimeter and the overall energy distribution can be reconstructed (Fig. 3.16-right). This method of calibration takes 10

minutes to be performed and it will be done once a week to check the absolute energy scale of the calorimeter at low energy. A sample of 10^4 photons can be collected and a 1.5% equalisation among the crystals can be obtained.

3.4.3 Cosmic rays

Cosmic Rays (CRs) are a great tool to perform in-situ calibration runs on the Mu2e calorimeter, as the specific energy loss of MIPs is uniform throughout the whole calorimeter active area, allowing a precise energy scale equalisation for each channel. The energy calibration is performed by reconstructing the cosmic muon path length and measuring the energy deposit released on the calorimeter crystals. The distribution of deposited energy in a single crystal is shown in Figure 3.17-left. Preliminary simulations indicate that an equalisation of $\mathcal{O}(1 \div 2\%)$ can be obtained, as seen in Figure 3.17-right, having fitted the energy loss with a Landau and extracted the peak.

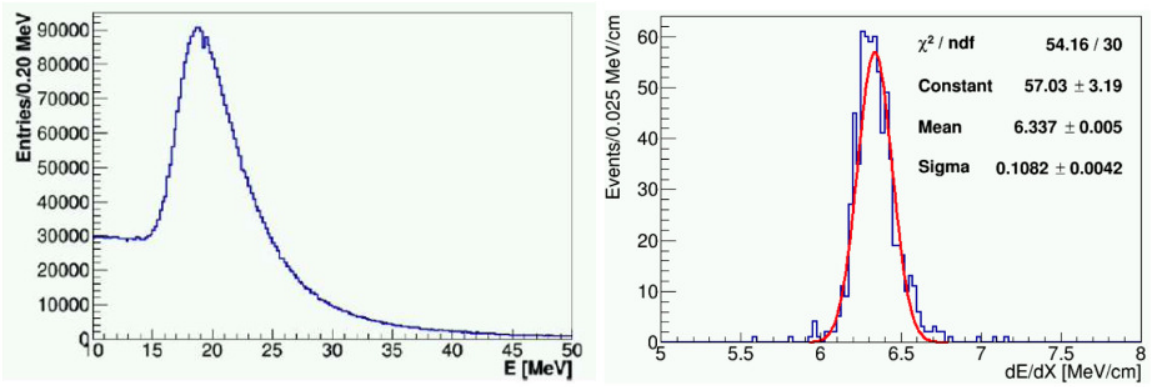

Figure 3.17: Left: Distribution of the energy released by a cosmic muons in a single crystal. the MIP peak for the Mu2e CsI crystals corresponds to a 20 MeV energy deposition. Right: Distribution of the specific energy loss calibrated.

3.4.4 DIO muons and pions decays

To perform a calibration at energies closer to the conversion energy, so $\sim$ 100 MeV, muons and pions decays can be used, specifically the channels: $\pi^+ \to e^+\nu_e$ with $E(e^+) =$ 69.8 MeV and $\mu^- \to e^-\nu_\mu\bar{\nu}_e$ which has a characteristic spectrum edge at 52.8 MeV. With the help of the tracker, the expected accuracy is $\sim$ 0.5%. Unfortunately, at nominal field, both particles decay illuminate only a reduced part of the detector, due to the relation between the particle momentum and the radial coordinate, so dedicated runs with reduced magnetic field are needed to cover all the calorimeter crystals. Problems arise since the reduction of the B field, causes a deterioration in the tracker resolution due to the higher particle rate. A reduction of the beam intensity would then be required.

3.4.5 Laser system

The laser monitor system allows to perform a fast equalisation of the ROUs time offset, as well as to control the photosensors gains, charge and timing resolution. A green laser has been chosen because its wavelengths is far away from the CsI emission peak at 310 nm and the changes in transmittance caused by radiation are expected to be small. In Figure 3.18 is shown a schematic representation of the distribution layout of the laser.

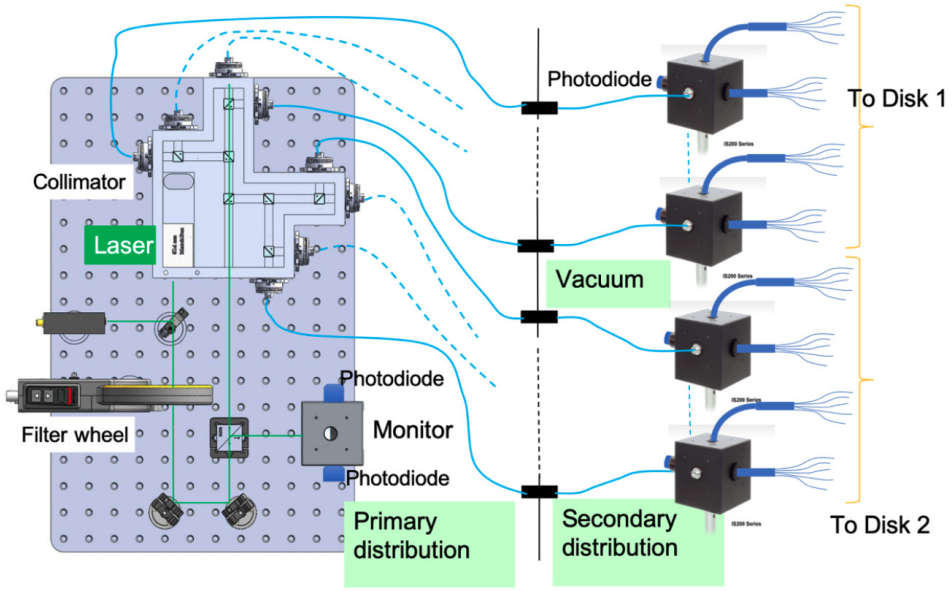

Figure 3.18: Block scheme of the laser calibration system.

The pulsed laser sends light through collimating optics and then to a optical splitting system to divide the laser initial output into 8 equal beams and 1 primary monitor system. Via eight 1 mm diameter, 60 m long quartz fibers, the light then reaches the DS region. On each calorimeter disk there are four integrating spheres with one input for the incoming fiber and three outputs: two for secondary fiber bundles and one for a photodiode employed for monitoring of the secondary distribution. Each bundle is made of 110 SiO_2 fibers with the cladding doped with fluorine. In total 880 laser lines per disk are available. Each fiber ending is inserted into a dedicated needle, part of the ROUs, which allows to illuminate directly the crystal and be readout by the photosensors. One laser pulse, corresponding to an energy deposit of 50 MeV is sent at each spill-off period, so once every $\sim$ 1.4 s. This system is expected to provide a 0.5% equalisation on all channels in 25 minutes.

3.5 Calorimeter simulation

In order to evaluate the expected performance of the detector, it is pivotal to perform a preliminary simulation of the entire experimental setup and environment. A full event is simulated using the GEANT4 toolkit. The energy deposited into the crystals is converted into optical photons and the SiPMs collecting this light are simulated considering a Poissonian photostatistic fluctuation for each energy deposit and a Gaussian distributed electronic noise, equivalent to 150 keV.

3.5.1 Event reconstruction

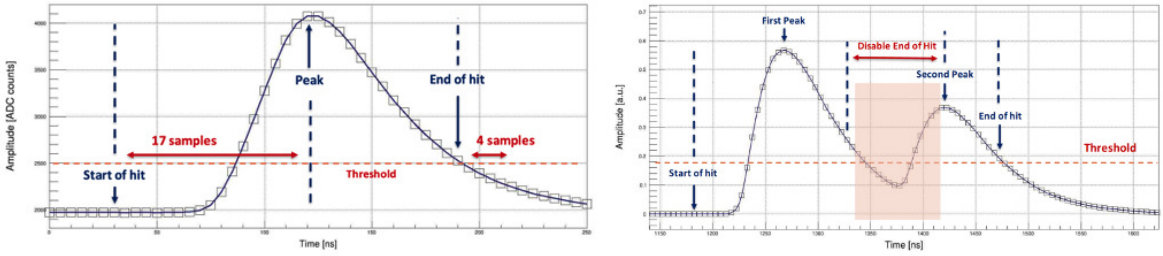

Figure 3.19: Scheme of the DIRAC firmware zero-suppression (left) and pile-up (right) handling.

The waveform, i.e. the pulse in mV, from the photoelectrons collected by a SiPM/FEE pair is acquired and reconstructed by the DIRAC board with 5 ns sampling. When a threshold in mV is surpassed, the acquisition of a wave is triggered and its local maximum is found. The acquisition is interrupted when the signal is below threshold for at least 20 ns. The DIRAC firmware features a circular buffer, so the signal is stored from 17 samples (85 ns) before the first peak, up to the stop of the acquisition. In order to handle pile-up, if after the first peak over threshold other pulses arrive within 17 samples from the moment the waveform goes under threshold, the hits are merged (Fig. 3.19). The individual hits are extracted via fits to the waveforms and the two SiPM hits connected to the fired crystal are averaged to form a crystal hit. The association of reconstructed hits to the incoming particles is performed through clustering algorithm. It starts by taking the crystal hit with the largest energy as a "seed" and adds all simply connected hits within a time window of ± 10 ns and a threshold in energy of 3 times the electronic noise. Hits are defined "simply connected" if they can be reached through a series of adjacent hits. The procedure is repeated until all crystals hits are assigned to clusters. Dedicated algorithms then have the job to recover low-energy deposits disconnected from the main cluster, significantly improving the energy resolution [66]. With this method,

an efficiency on CE candidates of around 95% is achieved for cluster energies above 60 MeV.

3.5.2 Energy, time and position resolution

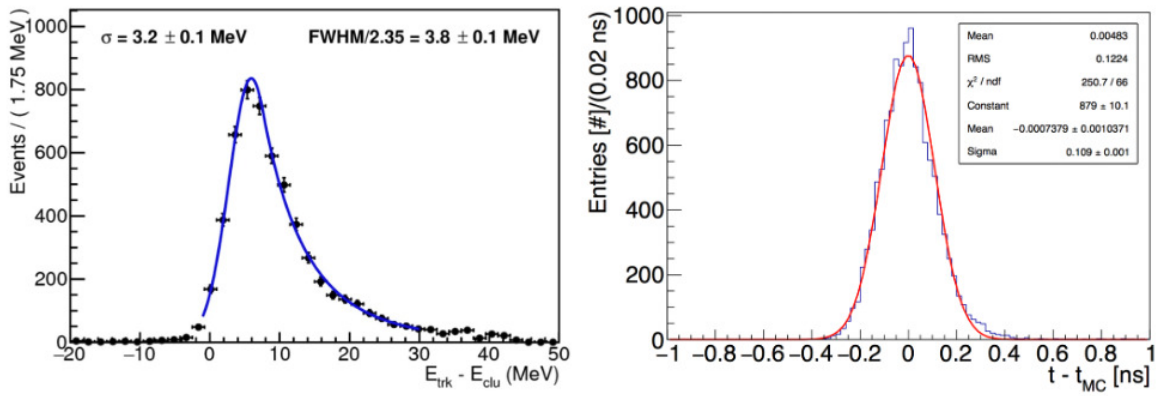

Figure 3.20: Left: Energy resolution fit with a double-sided Crystal Ball function, quoting both core resolution (σ) and FHWM/2.35. Right: Distribution of the time residuals between the reconstructed cluster time (t) and the Monte Carlo truth (t_{MC}).

To obtain the energy resolution, CE were simulated together with the Mu2e expected background. The distribution of the difference between the true signal electron energy obtained by simulation and the reconstructed cluster energy (Fig. 3.20-left) is used to estimate the energy resolution. This variable accounts for the energy lost by the electron before hitting the calorimeter. The distribution is fit with a Crystal Ball function to extract the resolution which can be estimated from the FWHM as (3.8 ± 0.1) MeV. Since it is dependent on the crystal quality, a *LRU* below 5% and a light yield above 30 photoelectrons/MeV are required.

The cluster time is defined as the linear energy weighted time of all the crystals belonging to the cluster, employing a constant fraction of the pulse height as threshold. Figure 3.20-right shows the time residuals between the reconstructed cluster time and the Monte Carlo true time. A Gaussian fit to this distribution shows that the expected time resolution is ~ 110 ps.

The cluster position is also important to match the reconstructed tracks with the calorimeter hits. Using a linear energy weighted mean, hit coordinates were extracted from the simulation: the distribution of the difference between the predicted and effective position of the track at the calorimeter surface showed that it is possible to achieve a transverse coordinate resolution of ~ 6 mm [33].

3.5.3 Particle identification

Although the tracker momentum resolution allows to discriminate a CE from background better than the calorimeter, its information is not enough to identify, for instance, an electron from a muon. For a muon rejection factor of 200, the efficiency of the electron identification based on the tracker-only information could be too low [33]. The energy and timing measurements from the Mu2e calorimeter become then critical for efficient separation of electrons and muons in the detector and to improve pattern recognition in the tracker. The aid of the calorimeter to the tracker can be appreciated by looking at Figure 3.21 where the tracker hits are shown before and after the addition of the calorimeter information. Thus, to keep the total background from cosmic rays at a level

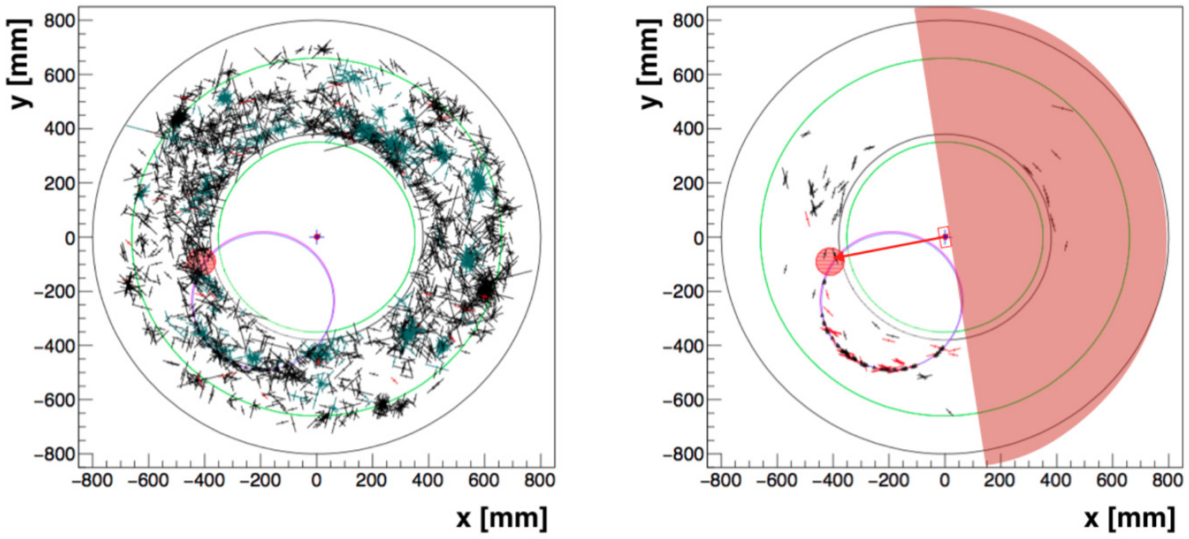

Figure 3.21: Distribution of the hits in the tracker before (left) and after (right) the application of a timing window based on timing information in the calorimeter. The tracking efficiency is improved by 9%.

below 0.01 events, a muon rejection factor > 200 is required, given the expected ~ 1 CR event per year that will escape the CRV cuts.

3.6 Calorimeter Module0

The calorimeter performances were also estimated from a large-scale calorimeter prototype, called Module0, assembled at LNF-INFN. The Module0 is composed of 51 staggered crystals, wrapped in 150 μm Tyvek foils, each one readout by two custom Mu2e SiPMs with (prototype) FEE boards, as shown in Figure 3.22. Tests were performed at the Frascati Beam Test Facility where the Module0 was exposed to slow-rate electrons from

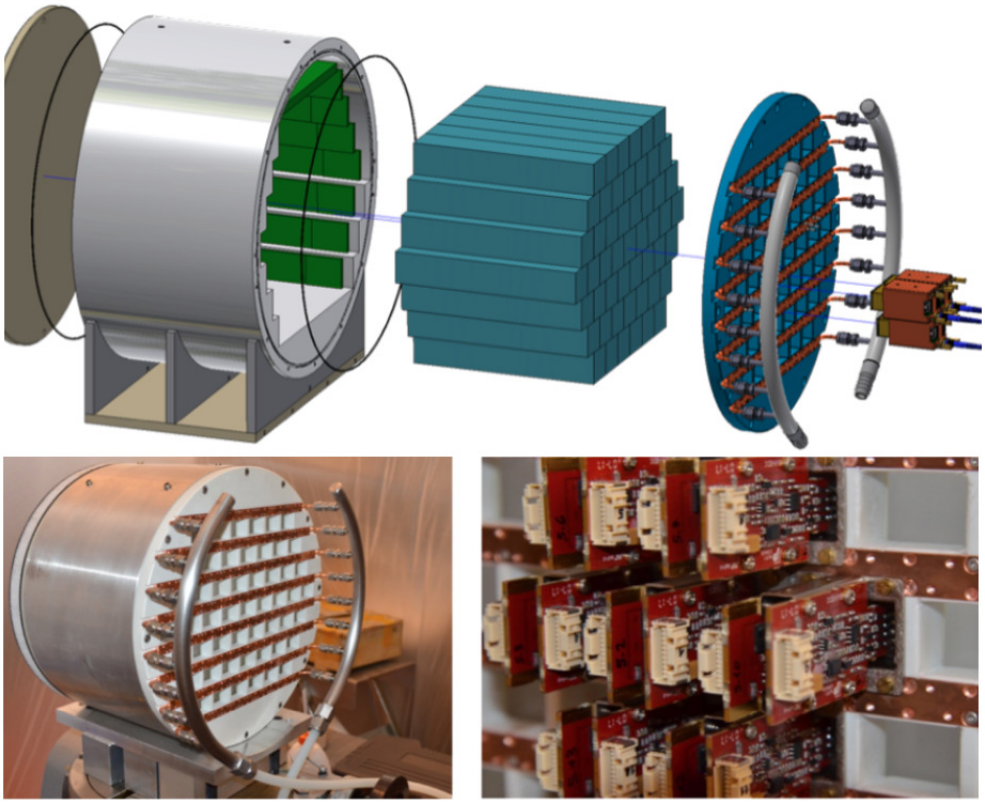

Figure 3.22: Top: Module0 exploded view showing the chassis, the crystals, the back plate with cooling lines and some SiPM/FEE modules. Bottom: Module0 assembled and detail of the FEEs on the back plate.

60 to 120 MeV. The beam energy spread was evaluated as $\mathcal{O}(2\%)$ at 100 MeV. The output signals were acquired with two CAEN V1742 boards, where a 12-bit ADC performed the digital conversion. The waveforms were resampled offline at 5 ns to verify the performances achievable with the 200 Msps Mu2e acquisition rate. In order to better reproduce a CE, tests were performed with an electron impinging on the prototype center at 0° and 50°, i.e. the expected CE incidence angle. The energy resolution was estimated by fitting a log-normal function over the energy distributions observed at different beam energies, as shown in Figure 3.23 at 100 MeV.

The energy resolution dependence over the beam energy can be parametrised as:

$$\frac{\sigma_E}{E} = a \oplus \frac{b}{\sqrt{E[\text{GeV}]}} \oplus \frac{c}{E[\text{GeV}]} \tag{3.5}$$

with the standard contributions given by: a for the stochastic contribution related to fluctuations in shower development, b the noise term due to the signal chain and electronic noise, c the constant term related to instrumental effects associated with non-uniformities in the calorimeter response. The obtained σ_E/E is shown in Figure 3.25-left and it can

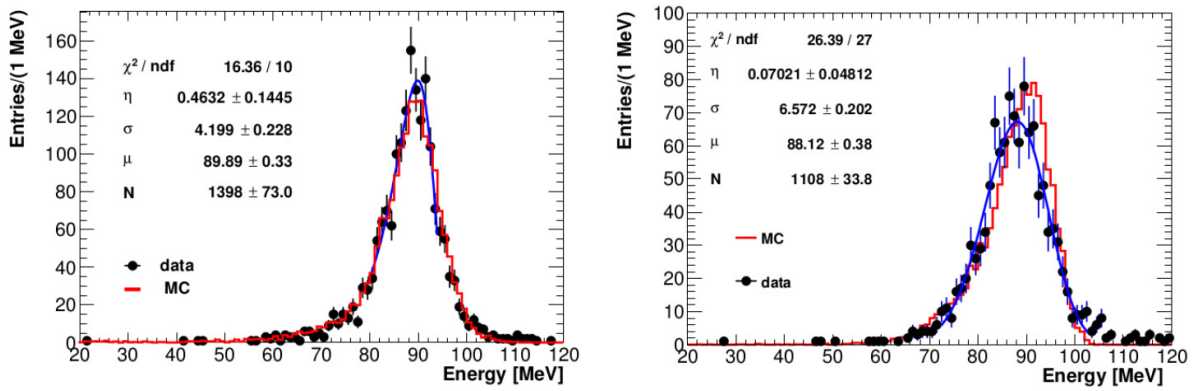

Figure 3.23: Reconstructed energy distribution for 100 MeV electron beam at 0° (left) and 50°(right). Both the data and Monte Carlo results are shown.

be seen that the obtained energy resolution is better than 10% at 100 MeV, so within the requirements.

The time resolution was evaluated with the time difference between the signals relative to the two SiPMs reading the same crystal. Both data from cosmic rays and electrons were used for the analysis. From plot in Figure 3.24, σ_t was estimated by dividing the σ from the gaussian fit by $\sqrt{2}$, where 2 is the number of photosensors involved. The time resolution dependence on energy for a single channel, shown in Figure 3.25-right, is then:

$$\sigma_t = \frac{a}{E[\text{GeV}]} \oplus b \tag{3.6}$$

with a proportional to the optical emission time constant of pure CsI and b related to additional contributions due to jitter in the readout electronics.

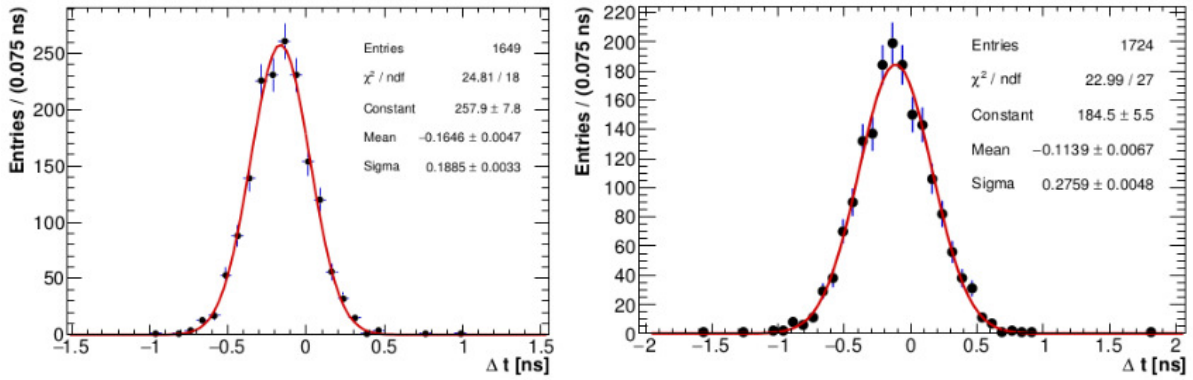

Figure 3.24: Time resolution of the central crystal sampled with two different rates: 1 GHz (left) and 200 MHz (right).

In the case of an orthogonal beam at 100 MeV, the resulting time resolution values were of 132 ps and 195 ps, respectively for the 1 GHz acquisition frequency and for the

200 MHz resampling.

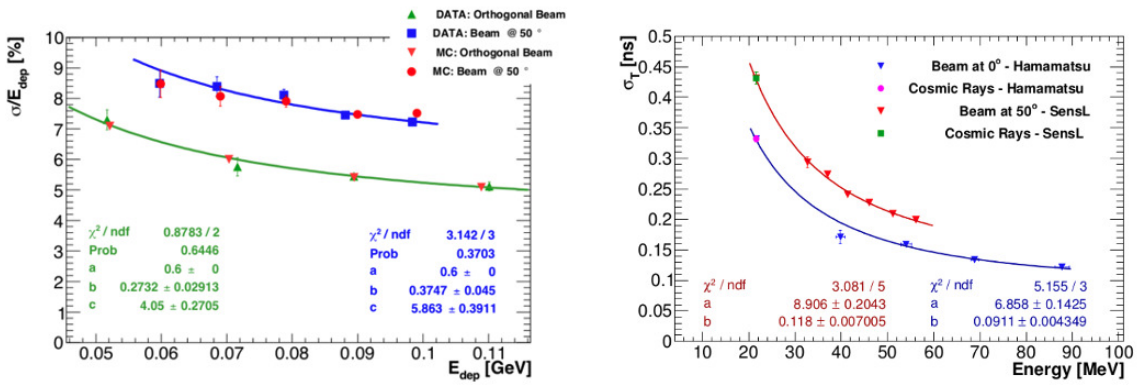

Figure 3.25: Left: Energy resolution as a function of the energy deposited in the Module0 for the 0° orthogonal and 50° tilted runs. The Monte Carlo expectation is also shown. Right: Time resolution as a function of the highest energy deposit in a single crystal considering two incidence angles (0° and 50°).

3.7 Construction and commissioning status

Following the current schedule, the calorimeter is going to be brought to the experimental hall by spring 2024 and all the service lines will be completed by the autumn of that same year. At that point, a commissioning data-taking with cosmic rays will start, while waiting for the tracker to be installed. Following this schedule, the disks are expected to be assembled by 2023. Currently, the down-stream disk (Disk1) is being assembled at the Silicon Detector facility (SiDet) at Fermilab in a clean room (ISO 7).

Furthermore: all cables for power supplies and for FEE-MZB were procured, 5+5 MZB-DIRAC boards prototype pairs were produced and tested, production of the Mezzanine Boards is underway even if slightly delayed, all Low and High voltage power supplies were procured and installed in the Mu2e building TDAQ room and the DT neutron generator for calibration was procured.

Of the 1450 crystals (all wrapped in Tyvek and tested), 674 were selected to be stacked in the Disk1. The positioning of the crystals on the disk was carefully optimised, taking into account physical (LY, LRU, FT, RIN) and technical (thickness) properties. Three areas have been identified as a function of the expected level of Total Ionizing Dose (TID), occupancy and resolution, considering that TID and occupancy decrease going toward the outermost part of the disk. The chosen crystal distribution is shown in Figure 3.26.

Another property that needs to be well controlled before stacking is the maximum outgassing level allowed to each component (8×10^3 Torr $\times$ l/sec). To comply to that

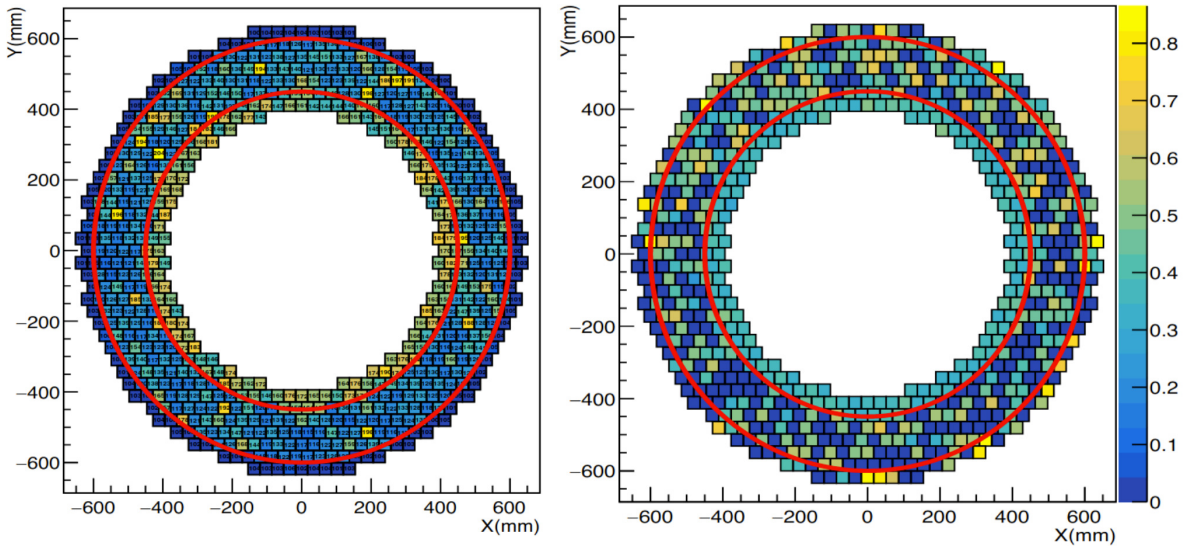

Figure 3.26: Distributions of the LY in photoelectrons/MeV (left) and the radiation induced noise in MeV (right) for the upstream disk, after optimisation. Red circles represent the three regions chosen for three levels of expected occupancy and TID.

limit, each component has to be treated with proper care (gloves and nitrogen storage) and before assembly it has either to be outgassed or "baked" and outgassed. For this reason, we have designed and assembled a large outgassing vessel (70 cm in diameter for a volume of 0.5 m^3) to perform this operation.

All 4000 Mu2e-SiPMs were produced by Hamamatsu, shipped at Fermilab and tested at SiDet, but due to the pandemic the gluing of them to the copper holders took place at LNF. The glue used was the two-component epoxy-hardened EP30AN glue, which has good thermal contact quality and is well performing in vacuum. 2800 SiPMs were glued and integrated in 1400 SiPM holders, while other 200 SiPMs will act as spares. Assembling of the full ROUs (two Mu2e-SiPMs, two FEE boards, a Faraday Cage and a copper holder) is ongoing and expected to finish in the coming months.

The FEE boards after production have been tested, checking both the amplification and rise time values, and have been calibrated for the HV setting in a facility setup in JINR Institute in Dubna (Russia), under the supervision of LNF engineers. Each unit has also undergone a burn-in at 65°C for 6 hours to determine the so-called infant mortality, and only few tens of boards were discarded.

The testing of the FEE-SiPM pairs is ongoing at the QC Station and expected to finish before the end of 2022.

All the large mechanical parts of the calorimeter were produced in Italy: 2 aluminium outer cylinders, 2 carbon-fibre inner cylinders, 2 PEEK back plates, 2 carbon-fibre front plates with the aluminium source tubing embedded and 20 aluminium crates with related

cooling manifolds. Among these, 1 outer cylinder, 1 inner cylinder and 1 back plate were shipped to Fermilab and assembled to realise the downstream disk. The inner cylinders have successfully undergone a 400 kg load test.

Two disk assembly positions will be available in the assembly clean room at SiDet, to test the first assembled disk while building the second one. Another assembly station was realised at the INFN National Laboratory of Frascati to test the mechanical components received from the vendors before shipping them to Fermilab. Tests of the cooling system and electronic components will be performed during and after the detector assembly and disk stability and alignment of the crystal matrix will be continuously monitored during detector assembly using a laser tracker. A dry fit of the calorimeter mechanics was successfully performed at LNF-INFN, after assembling an outer cylinder, a back plate, all the electronic crates and some readout units, as shown in Fig. 3.27.

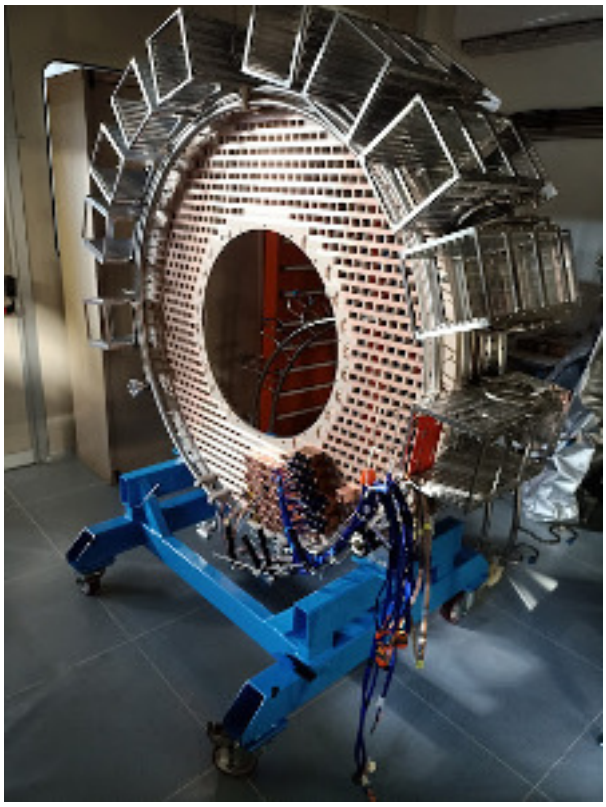

Figure 3.27: Calorimeter disk partially assembled during the dry-run test at LNF.

After this successful test, the components for the downstream disk were shipped to Fermilab and, after outgassing, the crystals stacking began. The crystals were stacked in rows, and a 50 μm Tedlar layer was placed between any two rows. The crystal rows were compressed using spring screws coupled with plastic shims on both sides. The crystals stacking for the downstream disk proceeded steadily in less than a month, having started in advance the outgassing of the crystals. Different stacking steps can be seen in

Figure 3.28. Stacking of the Disk1 was completed in July 2022 and in August 2022 the two front plates were received in Frascati and tested. They are now ready to be shipped to Fermilab to complete the assembly of the first disk.

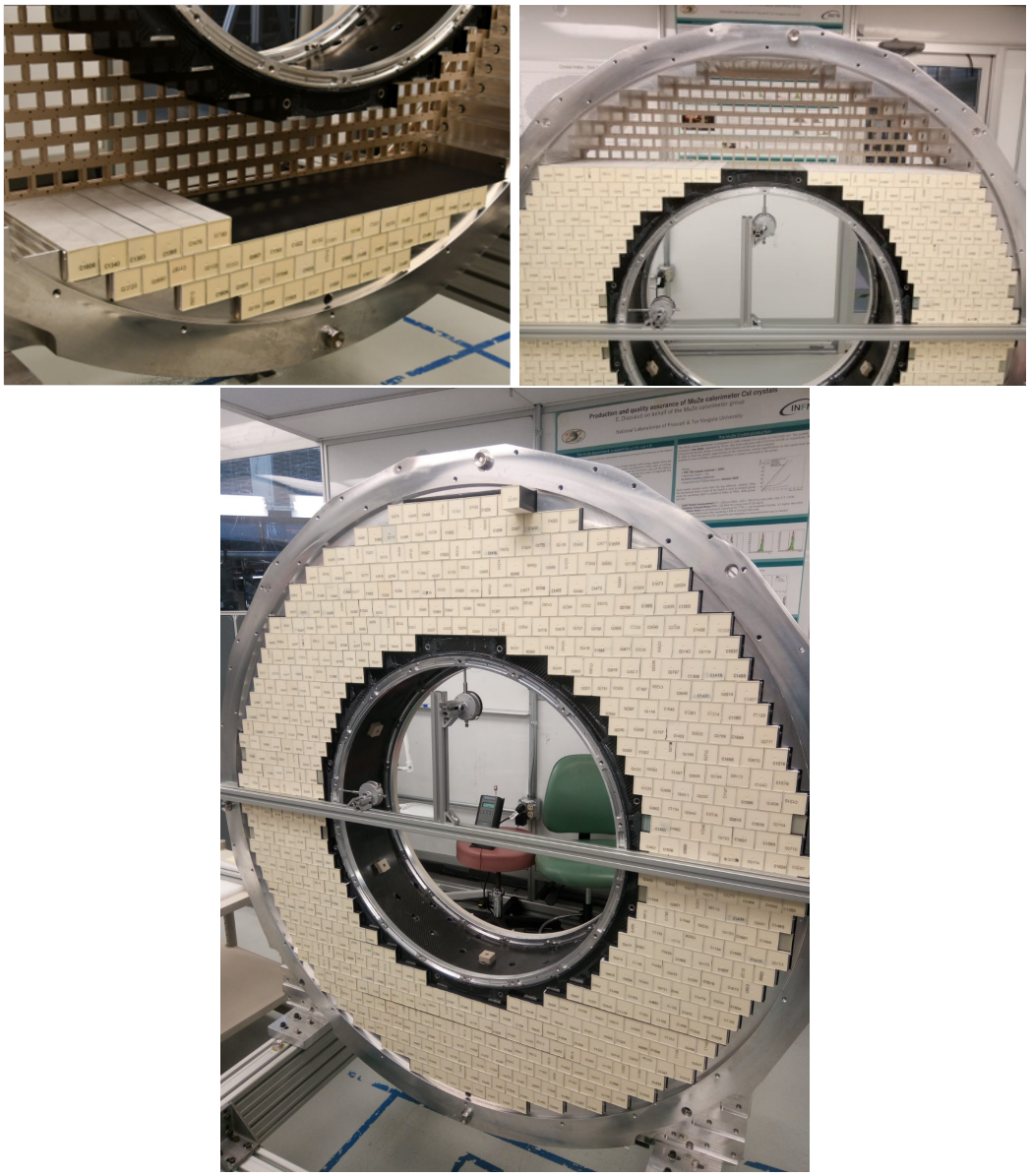

Figure 3.28: Progress in the stacking of the crystal in the Disk1. The picture on the top left shows the Tedlar layer inserted to reduce cross-talk.

Chapter 4

Characterisation of the Readout Units at LNF

The Mu2e calorimeter has strict requirements for what concerns its performance and resolutions on energy, time and momentum, as illustrated in Chapter 3. These have to be satisfied when operating inside the DS harsh environment, i.e. in presence of high doses of ionizing radiation and neutron fluence, while being immersed in 1 T axial magnetic field. These premises imply the mandatory use of solid state photodetectors, guiding the choice toward our Mu2e custom SiPMs, and reliable analog FEE.

The access to the Mu2e detector hall is going to be restricted to roughly once a year, so maintenance of the detector parts has to be reduced to a minimum. The components which are assembled have to be tested for reliability and fully characterised on their response to ensure that the detector will be ready for Run I. To follow the planned schedule, it is also important to optimise the workflow during assembly and test of the single components to provide fully working parts and avoid any delay on the calorimeter realization. In this way, faulty components will be discarded or repaired beforehand.

Mu2e will perform a precision measurement, so it is mandatory to understand in advance any possible variation in performance due to changing working conditions in order to keep the expected detector resolutions within requirements up to the end of the data-taking periods. As an example, due to neutron irradiation (see Sect. 3.1) the SiPM leakage current will increase during running, up to a level (2 mA) where the signal will be really deteriorated. Our mitigation is to reduce SiPM working temperature during running to reduce the leakage current. To handle this, the SiPM gain has to be properly adjusted so that the relation between gain and supplied voltage as well as gain and working temperature have to be fully characterised.

In this chapter, we explain the work done to characterise the FEE boards and the assembled SiPM/FEE/holder units, named Readout Units or simply ROUs. To ensure

consistency and reliability of the assembled ROUs, we have designed, assembled and put in operation an automated Quality Control (QC) Station to test them. In this station, we perform a direct measurement of the ROUs properties, such as gain, collected charge and PDE, in a controlled and known environment for different supply voltage (HV) values. This allows us to build a statistically significant distribution of these properties and to fully characterise each single unit, while providing the dependence on temperature and HV. Reproducibility studies on the parameter determination have also been carried out.

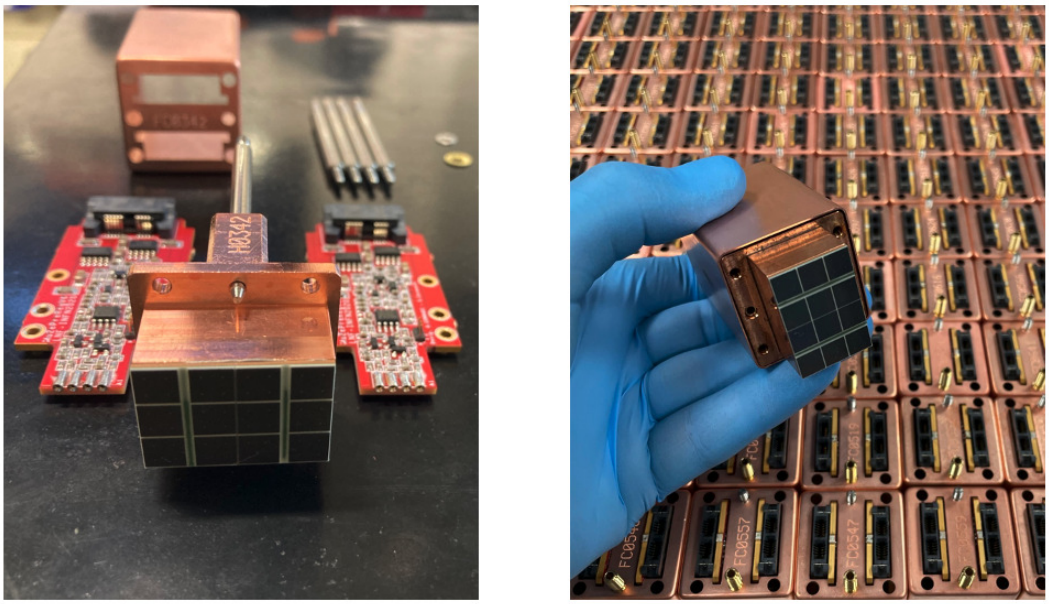

Figure 4.1: A disassembled calorimeter ROU and some assembled units ready to be tested

4.1 The Calorimeter Readout Units

One Mu2e calorimeter Readout Unit, shown in Figs. 4.1 and 4.2, is composed of:

- Two custom Mu2e SiPMs, each one made of the parallel of two series of 3 UV extended monolithic $6 \times 6\,\mathrm{mm}^2$ SiPMs.
- One copper holder on which the two Mu2e SiPMs are glued.
- Two custom Front End Electronics (FEE) boards, one per Mu2e SiPM, connected via 4 pins directly to the SiPMs.
- One copper Faraday cage for shielding.

- One needle guide for the optic fiber that will carry the laser light needed for the laser calibrating system (see Sect. 3.4.5).
- One reference guide to ensure the correct placement of the ROU on the PEEK back plane.
- Four screws to secure the ROU to the calorimeter back plane.

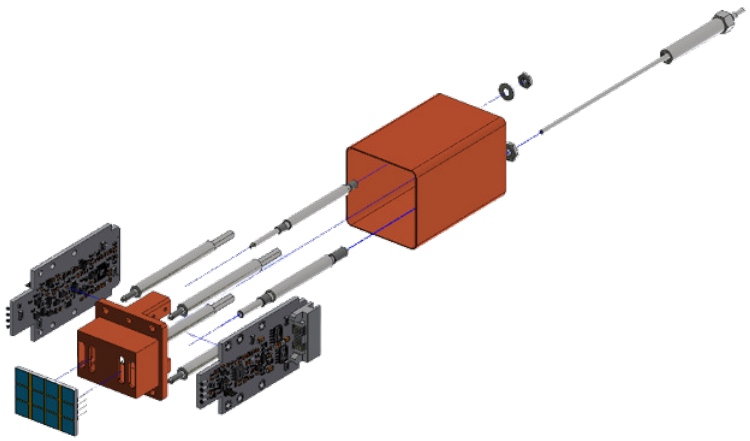

Figure 4.2: Exploded view of the components of a ROU.

One Readout Unit is going to be coupled to one CsI crystal. The readout is going to be performed only on the back side of the crystal in order to protect the electronics from the high radiation doses and to avoid spoiling the calorimeter resolution due to energy losses in the ROU material. The bias supply of the FEE requires the current of each channel to be smaller than 2 mA. To achieve that, it is convenient to cool down the SiPMs up to a temperature T$\sim -10°$C.

4.1.1 Silicon Photomultipliers

SiPMs are solid state detectors sensible to light pulses down to the single photon level. One SiPM is composed by a planar matrix of pixels, which are Single Photon Avalanche Diodes (SPADs) (Fig. 4.3-left). Each SPAD is an inversely polarized p-n junction operating in Geiger mode, i.e. with a bias voltage above the breakdown value. In presence of a reverse bias, a depletion region free of mobile carriers is formed at the interface of the two inversely doped semiconductors. In presence of high electric fields, $\mathcal{O}(10^2)$ kV/m, a charge carrier injected or generated in the depletion region has enough kinetic energy to initiate an avalanche process. This allows to amplify the initial event, like the arrival of one single photon, and obtain a detectable photocurrent. This Geiger discharge

is then generally quenched via resistors in series to the diode, allowing to restore the initial conditions and recharge the diode. This operating mode allows to produce output pulses independently on from initial number of absorbed photons in a single SPAD, also called pixel, thus the output pulse is not proportional to the instantaneous photon flux magnitude, with the SPAD working like a photon triggered switch. To obtain a proportionality between the photon flux and the output current, dense arrays of $10^{2\div3}$ pixels/mm^2 are implemented. In this way, the sum of the single contributions yields a "digital" information about the photon flux, i.e the number of fired pixels. This number remains linearly proportional to the incoming flux only when the number of fired pixels is few % of the maximum number of pixels in the array. The overall response reaches a saturation for increasing flux, up to the point it remains flat for a flux greater than the number of pixels, since, as explained before, two photons arriving at the same time in the same SPAD are not distinguishable, producing a single Geiger discharge.

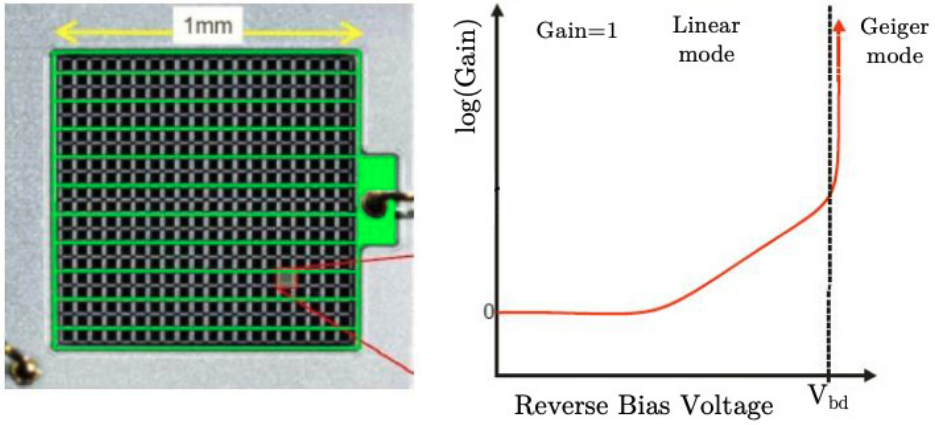

Figure 4.3: Left: Photo of the individual SPAD microcells which compose a SiPM sensor. Right: Multiplication factor (gain) behaviour of an ideal SPAD for the different bias voltages.

The breakdown voltage V_{bd} is defined as the minimum bias needed to initiate a Geiger discharge, so it is the voltage for which the multiplication factor (gain) diverges. The multiplication factor behaviour of an ideal SPAD is shown in Fig. 4.3-right. The breakdown voltage can be obtained through the logarithmic derivative of the I-V curves (Section 3.2.4). In order to improve detection efficiency via a larger avalanche, the SiPM operational voltage V_{op} is typically set few Volts higher with respect to V_{bd} of the pixels. The difference between the two is called overvoltage $\Delta V = V_{op} - V_{bd}$.

If the SiPM working temperature increases, scattering of charge carriers on the crystal lattice becomes more likely and mean free paths are shortened, reducing the average energy of the accelerated carriers. This translates into an increase of the breakdown

voltage for increasing temperature. A higher E-field, so higher bias voltage, is then required in order to compensate this effect and keep constant the SiPM gain.

The SiPM gain, G, is defined as the current pulse (or charge) generated for a single detected photon normalised to a single electron charge, q_e. The gain of a microcell is related to its inverse polarization voltage as follows:

$$G = \frac{Q}{q_e} = \frac{C_{pix} \cdot \Delta V}{q_e}, \tag{4.1}$$

where C_{pix} is the capacitance of a single pixel which presents a dependence on the supplied bias as $\propto (V_{bias})^{-1/2}$.

The Photon Detection Efficiency (PDE) is an important parameter for SiPM and is expressed as the product of three independent factors:

$$PDE(\lambda, V_{bd}) = QE(\lambda) \times \epsilon(V_{bd}) \times FF, \tag{4.2}$$

where $QE(\lambda)$ is the quantum efficiency at a given wavelength λ, $\epsilon(V_{bd})$ is the efficiency to trigger an avalanche process at the breakdown voltage V_{bd} and FF, the Filling factor, is the ratio between the SiPM sensitive area and its overall transverse dimension.

When a pixel is hit by one photon, there is an associated dead time (named recovery or quenching time), due to the presence of the quenching circuit. SiPMs dynamic range upper limit is represented by the totality of the pixels fired during the dead-time. Increasing the number n of incoming photons results in multiple hits on single pixels, thus decreasing the output linearity. The number of fired pixels can be expressed as

$$N_{fired} = N_{max} \cdot \left(1 - exp\left(-\frac{n \cdot PDE}{N_{max}}\right)\right) \tag{4.3}$$

In order to get a linear response it is mandatory to select the N_{max} in a way that the sensors operate with a photon flux that does not saturate the SiPM ($< 5\%$).

The Mu2e SiPMs

The SiPMs for the Mu2e calorimeter have been custom made by Hamamatsu [81]. Hamamatsu refers to each single monolithic SiPM as MPPC, standing for Multi-Pixel Photon Counter. Two adjacent 2×3 MPPCs matrices per ROU are employed as a way to increase redundancy of the readout and reliability over time. Each MPPC has an effective area of $6 \times 6\,\mathrm{mm}^2$ and is made up by 14400 $50\,\mu$m pixels. The total SiPM active area of one matrix covers $\sim 19\%$ of the crystal transversal cross section. The photodetectors are UV-extended to match the 310 nm emission peak of pure CsI. To retain a high ef-

ficiency, Silicone Protection Layer (SPL) and Through-Silicon Vias (TSV) technologies are employed. As shown in Fig. 4.4, in the UV range $250 \div 350\,\text{nm}$, the PDE of this UV-enhanced SiPM with SPL is $\mathcal{O}(30)\%$, a factor six better than a standard Hamamatsu SiPMs. Consistently to these expectations, the Mu2e photosensors PDE has been measured to be of $(28.0 \pm 1.3)\%$ [82].

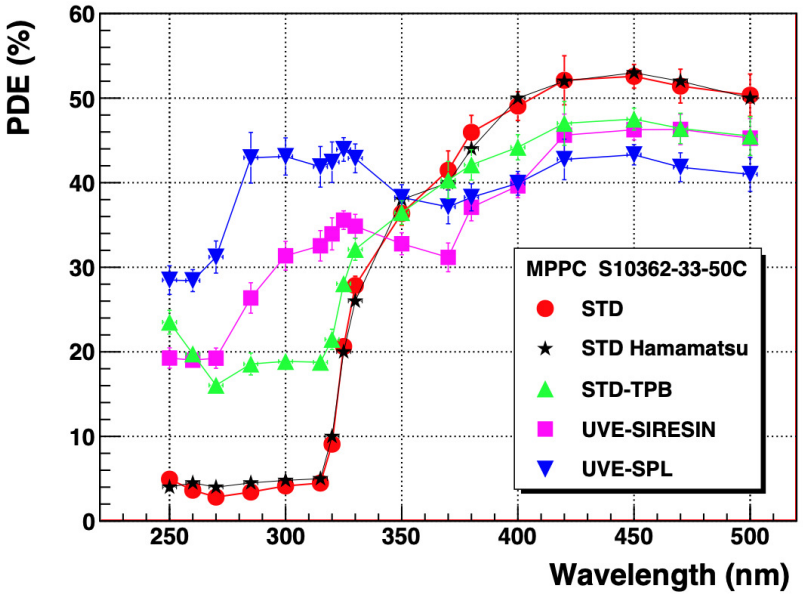

Figure 4.4: PDE as a function of the wavelength for four SiPM prototypes. The typical PDE values of the standard SiPM S10362-33-50C from Hamamatsu are shown for comparison. These measurements were performed at 25°C and include effects of cross-talk and after-pulses [83].

In order to comply to the requested short pulse width (FWHM $\sim 50\,\text{ns}$), needed to prevent pile-up, the 6 cells are connected as the parallel of two series made of 3 MPPCs each. This arrangement allows the total capacitance to be reduced to 2/3 of the value corresponding to the parallel of 6 cells. The value of V_{op}^{cell} is set at $V_{bd} + 3\,\text{V}$, with the breakdown voltage given by the manufacturer from the SiPM I-V curves and, although similar, specific per each cell. Considering this and the parallel connection of the two series of cells, each 2×3 matrix will have an operational voltage given by:

$$V_{op} = \frac{\sum_{cells} V_{op}^{cell}}{2} = \frac{\sum_{cells} (V_{bd} + 3\,\text{V})}{2} \tag{4.4}$$

Since each cell is kept at a quite low voltage of around 55 V, the voltage supplied through the FEE is $\sim 165\,\text{V}$. The variation of V_{bd}^{cell} with temperature has been estimated to be $53\,\text{mV}/°\text{C}$. A front and back picture of the Mu2e SiPM and its scheme are shown in Fig. 4.5.

A total of 4000 Mu2e production SiPMs have been procured from Hamamatsu and supplied to the experiment. The Quality Control (QC) procedure of a single MPPC inside the array, was performed at SiDet where they underwent a visual survey and a control of the mechanical specifications. The sensors passing this first check were fully characterised in a dedicated station and randomised batches were used for the Mean Time To Failures, MTTF, evaluation or for dedicated radiation hardness tests.

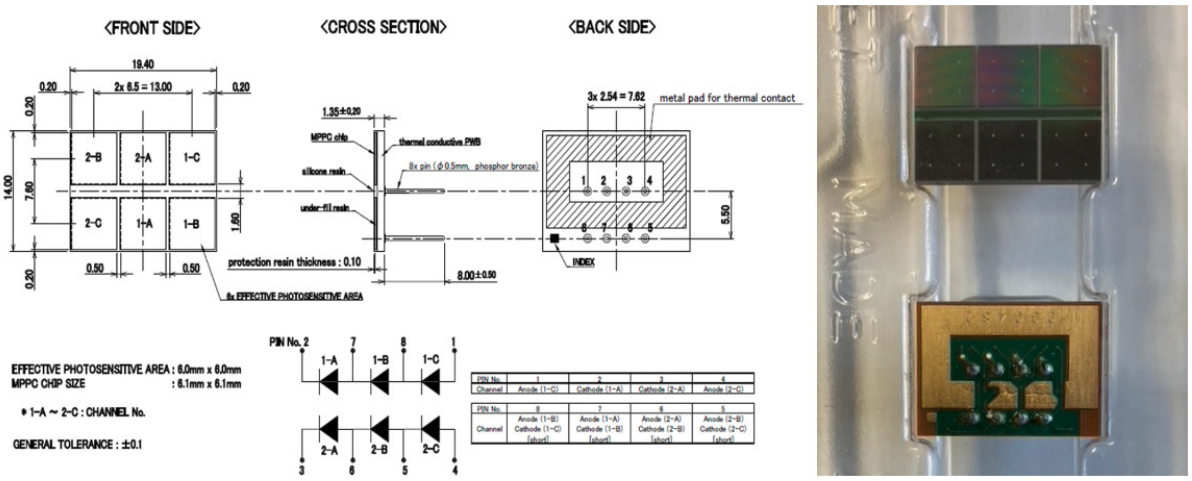

Figure 4.5: Scheme (left) and picture (right) of the Mu2e SiPMs.

4.1.2 Front End Electronics

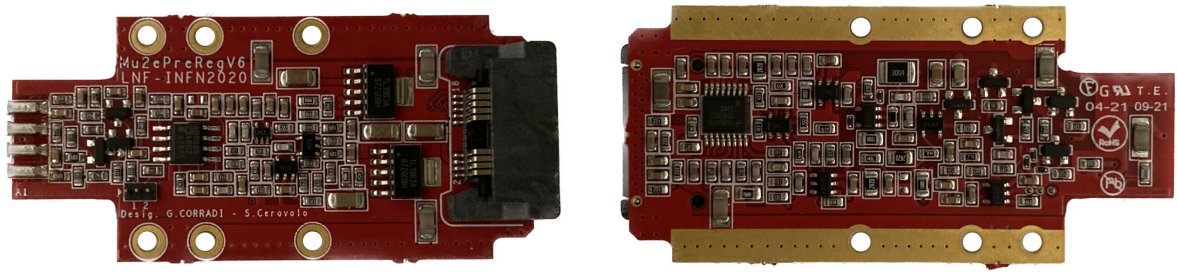

Figure 4.6: Top and bottom view of a Mu2e FEE board.

The design and characterisation of the Front-End Electronics (FEE) has been carried out by the SEA (Servizio Elettronica e Automazione) laboratory at LNF-INFN. A picture of the final FEE design in shown in Fig. 4.6. Two identical and independent FEE boards handle the signals from two SiPMs which read a single CsI crystal. Each board will provide individually programmable bias voltages for each photosensor, perform signal amplification and shaping, while monitoring the current and temperature of each SiPM.

The FEE is made of a double layer Printed Circuit Board (PCB). It incorporates a SiPM preamplifier gain, settable via a jumper at 1 or 2, and a fast pulse shaper with a

25 ns rise time. The chosen rise time is 5 times the digitiser sampling interval and this guarantees at least 5 points on the leading edge to ensure appropriate timing reconstruction. The regulated high voltage supply is distributed at 200 V to the individual FEE boards, which provide the individual bias voltages to each SiPM by means of a linear regulator. The regulator employs 12-bit ADC and DAC which allow a minimum step of 50 mV (corresponding to 1 Least Significant Bit, i.e. LSB).

The thermal management of the board is entrusted to electrically insulating aluminium nitride thermal bridges (Therma-Bridge). These bridges are used to remove the heat generated by the linear regulator circuitry from the analogue ground, towards the thermal ground on the PCB. This ground is in electrical and thermal contact with the SiPM holders, with the calorimeter frame and with the cooling system. The photosensors temperature is checked via a sensor located in close proximity to the SiPM holder and the thermal bridge.

4.2 FEE ADC and DAC calibration

The linear regulator section of each FEE board provides a programmable bias voltage to the SiPM with ±50 mV stability and a maximum current sourcing capability of 2 mA. The regulated high voltage supply is distributed at 200 V to the individual FEE boards, which – by means of a linear regulator – provide the individual bias voltages to each SiPM. Since the handling of the supplied voltage is done by the ADC and DAC, these are calibrated with a 2-points linear calibration to ensure that the voltage set is precisely the voltage provided by the regulator to the SiPMs. Setting these parameters facilitates the analysis of the general performance of the ROUs, normalising the response, since the expected supply voltage is provided to the SiPMs.

4.2.1 The FEE calibration setup

The ROUs electronic slow control is realized by two specialized cards designed to operate in a master-slave configuration: the Mezzanine (MZB) and the Digitizer and Control (DIRAC) boards. The MZB provides the bias of the SiPMs and of the related slow control (voltage regulation, bias, etc.). A flash memory onboard the MZB stores calibration data in order to accurately set and monitor the SiPMs. To facilitate preliminary tests and calibration of the FEEs, an additional board has been designed to operate with a MZB and a DIRAC: the Active Load Board (ALB). The MZB can be connected to the ALB by means of a I2C serial communication bus. The ALB has three main functions:

- Read the High Voltage bias, i.e. the voltage applied to the FEE, as it appears at

the SiPM pin connector.

- Set, change and read the HV source Load Current, i.e. the current sourced by the FEE HV bias regulator flowing through the SiPM pin connections.

- Evaluate the coefficients (offset and slope), in counts per physical unit or volts, of the ADC and DAC linear calibrations.

In this context, the most important task for calibration is to evaluate the slope/offset coefficients of the ADC and DAC on-board of the single FEEs. This can be done since the ALB can simulate any operative condition found when the FEEs will be populated with the SiPMs. These coefficients, which are slightly different for each FEE, can be stored in the MZB non-volatile flash-ROM, so that the MZB can precisely set the HV bias and translate the counts read from the ADC onboard of the FEEs into accurate estimates of the HV bias.

The obtained calibration parameters are then one slope and one offset per DAC

$$N_{counts} = HV_{read} \times slope_{DAC} + offset_{DAC}, \tag{4.5}$$

and an analogous set for the ADC

$$HV_{read} = N_{counts} \times slope_{ADC} + offset_{ADC}. \tag{4.6}$$

In Fig. 4.7, a picture of the setup shown, with also the detail of how the FEE attach to the ALB. A scheme of the ALB-MZB-FEEs connections is shown in Fig. 4.8. Two Power Supplies are employed: one Low Voltage to power the slow control boards and one HV. The ALB card can be connected to up 20 FEEs. Two voltmeters are employed to constantly monitor the calibration results. A well defined and reproducible procedure has been optimised to perform a systematic calibration of all the FEEs. This test also allows to verify any damage from the burn-in test (6 hours at 65°C) or transportation, before the final assembly in a ROU.

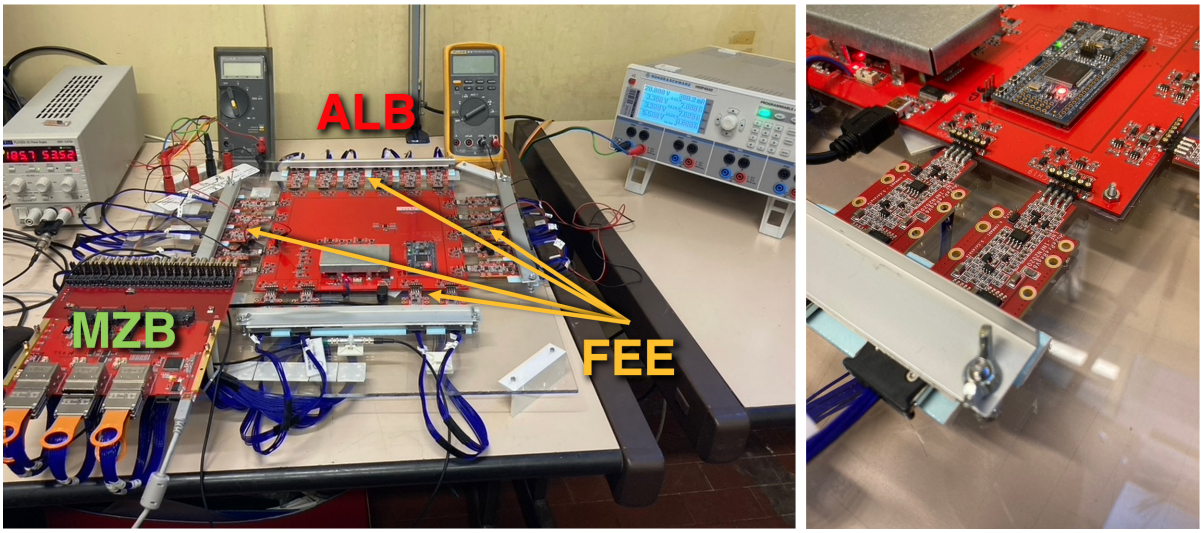

Figure 4.7: Left: Picture of the ALB setup. Right: Detail of the FEE connection to the ALB.

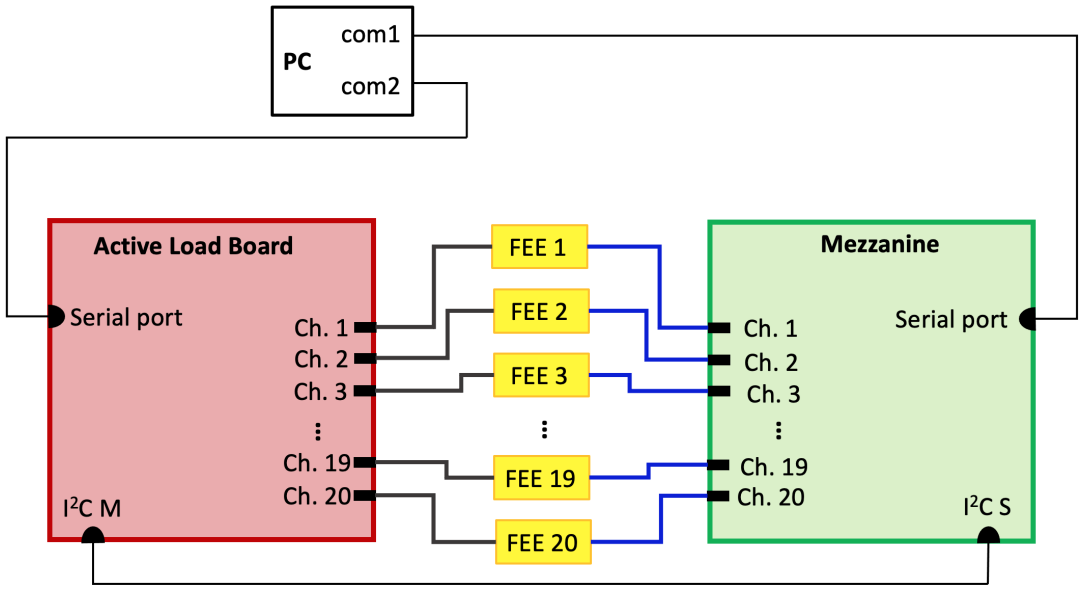

Figure 4.8: Scheme of the connections of the ALB setup.

4.2.2 Software and procedure

A LabView software is implemented to simplify all the operations. The DAC calibration starts by choosing two HV values, taken as "true", and are read-back through the ALB. By setting $slope_{DAC}$ and $offset_{DAC}$, the set and read values are then matched. For the ADC an analogous operation is performed after the DAC calibration simply via a proprietary command of the MZB firmware. The system then saves the calibration values on the MZB flash memory and a test can be done by setting a random voltage

(close to the calibration range) and verify the difference between the set and read values by reading the voltmeters and the results on the LabView interface. The chosen cutoff resolution to label a calibration round as successful is a $|V_{set} - V_{read}| < 100\,\text{mV}$.

Finally, a 5 minutes current stress test is performed by flowing a high current (setting the HV to 20 V) of 2 mA through the FEEs, to verify that there are no issues even with relatively high currents flowing for a longer period of time.

Calibration range choice

Since the calibration is done setting and reading HV on two points, tests have been done to evaluate if any systematics could be associated with the chosen range. Two choices were considered: 160 V and 170 V or 155 V and 165 V.

These different range values were tested on a random batch of 20 FEEs and the difference in counts/volts for the DAC/ADC are calculated at three HV values (V_{in} = 160, 165 and 170 V) following the expressions (4.5) and (4.6). The obtained distributions are shown in Fig. 4.9 where ΔN_{counts} (ΔN_{volts}) is the difference in counts (volts) between the 2 calibrations of the DAC (ADC), given a certain V_{in}. As can be seen from the Gaussian fit, the spread is contained within 1 count (50 mV), excluding a dependence of the calibrations on the range. After this test, the range 155 V and 165 V was chosen.

4.2.3 Performance

In order to closely monitor the ALB performance, it was chosen to manually test the calibration for 4 randomly chosen FEEs for every batch of 20 calibrated at the same time. The ALB creates a database with the information needed to identify the board and the 4 parameters of the calibration. It it possible then, through a MZB, to manually apply the calibration thanks to the board firmware. Two points were tested, at 160 and 165 V, and the values supplied to the SiPM pins were red with high precision multimeters. The result for the tested FEEs is shown in Fig. 4.10, where it can be seen that the vast majority of the read HV values is within the expected 50 mV.

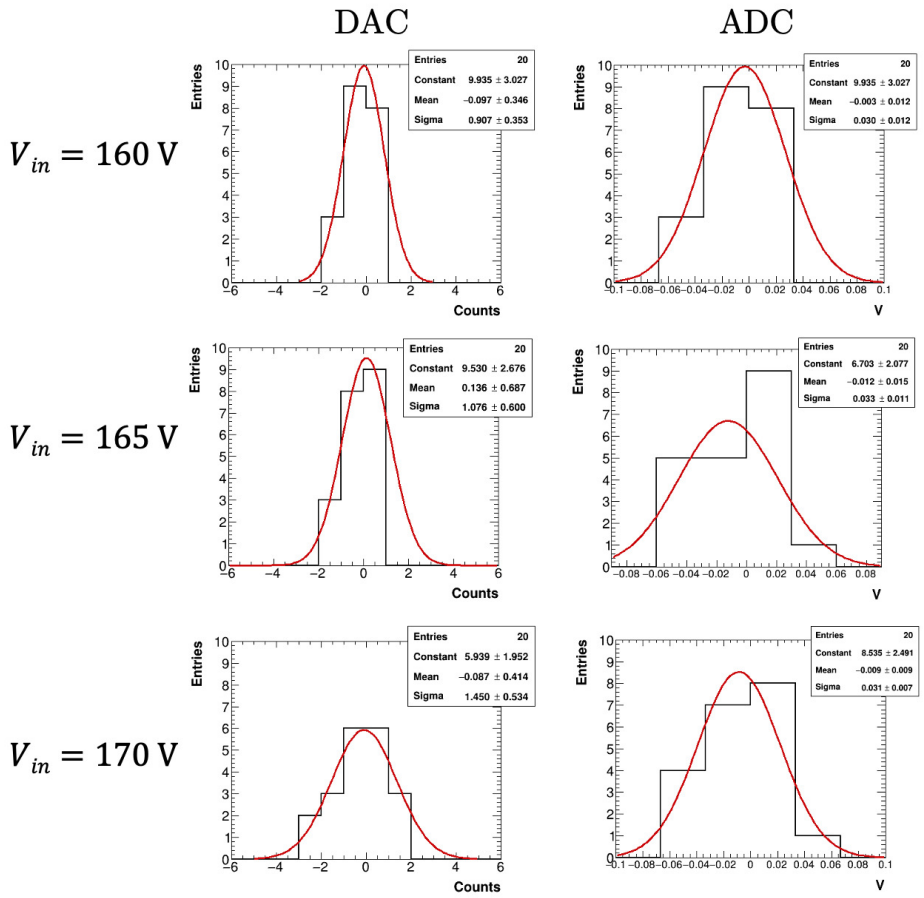

Figure 4.9: Difference in counts/volts between 2 calibration ranges for the DAC (left column) and ADC (right column).

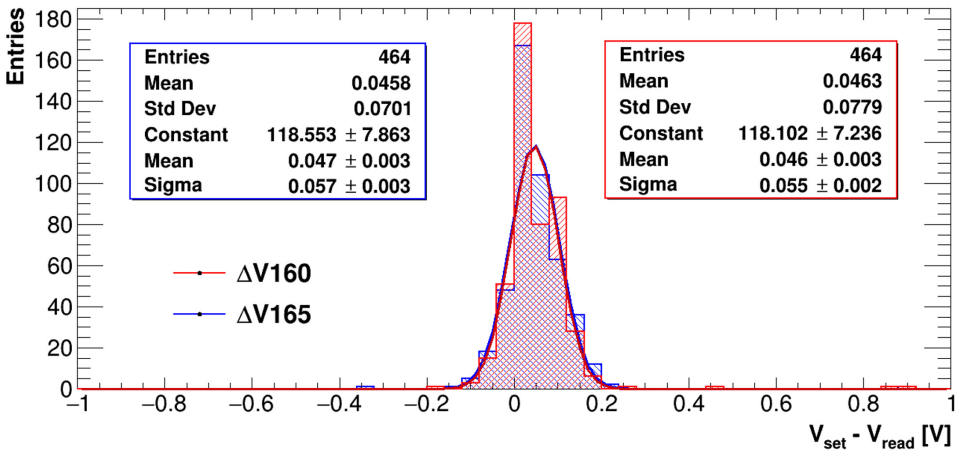

Figure 4.10: Distribution of the difference ΔV between the read and set HV values for V_{set} at 160 and 165 V.

4.3 The Quality Control Station at LNF

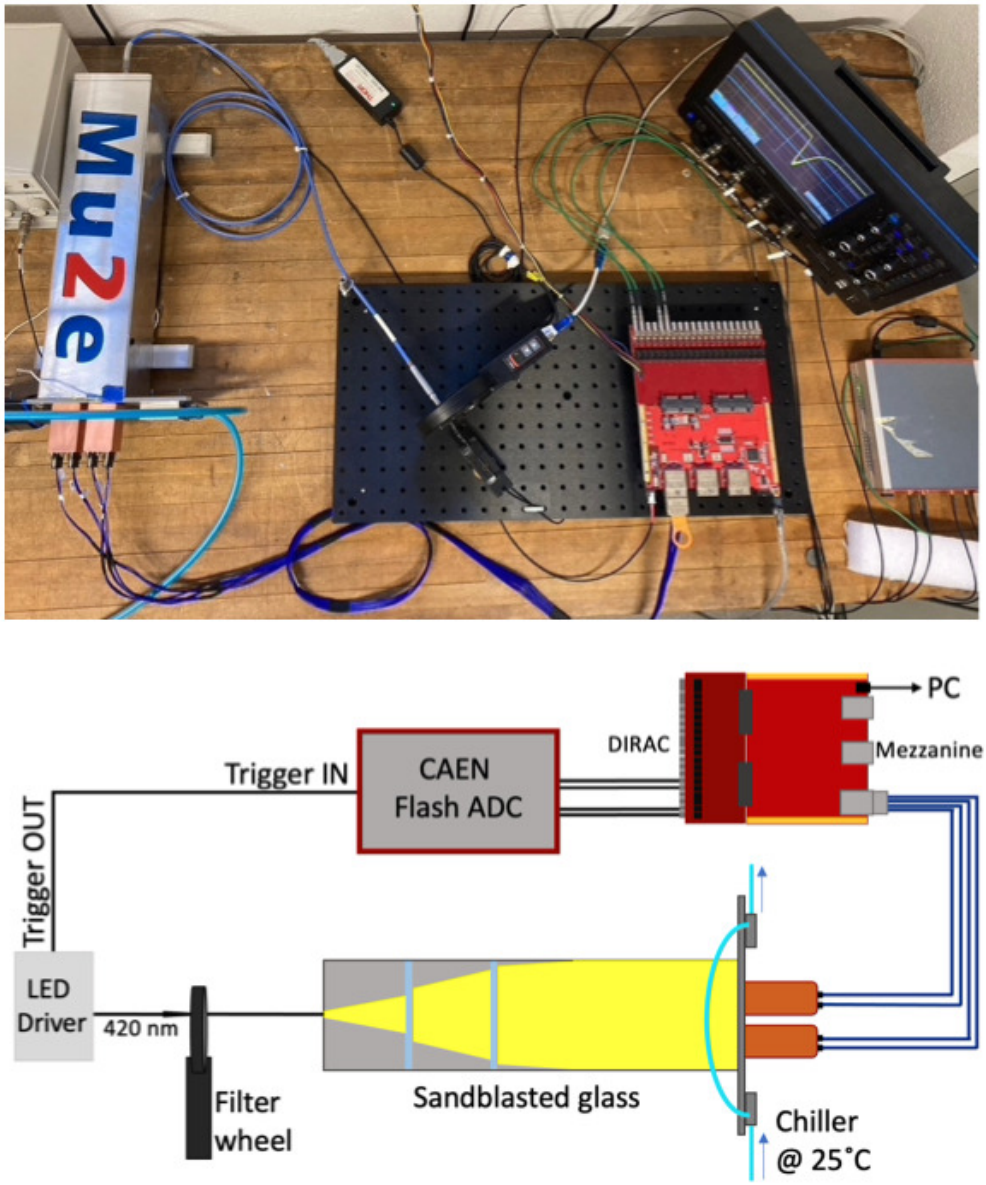

Figure 4.11: Picture and scheme of the QC Station.

In order to perform a quality control on the assembled ROUs, a Quality Control (QC) Station has been set up at LNF, as shown in Fig. 4.11.

This setup can work with two holders at the same time, for a total of 4 SiPMs. To mimic the light source, a 420 nm blue LED at 10 kHz is used. The light goes through an automatic wheel with 9 positions, each one holding a filter that acts as attenuator to decrease the intensity of the transmitted light in a calibrated manner. The transmitted

light is diffused uniformly on the SiPMs surface thanks to a box with sanded glass that also provides light tightness and allows to work in a controlled environment, thus ensuring good reproducibility of the measurements. The copper holders of the ROUs are screwed onto an aluminum plate that serves also as a conductive medium for temperature stabilization. A zoomed picture of the ROUs attached to the Al plate is shown in Fig. 4.12. There, the cap covering the guide of the fiber, further ensuring light-tightness, can also be seen.

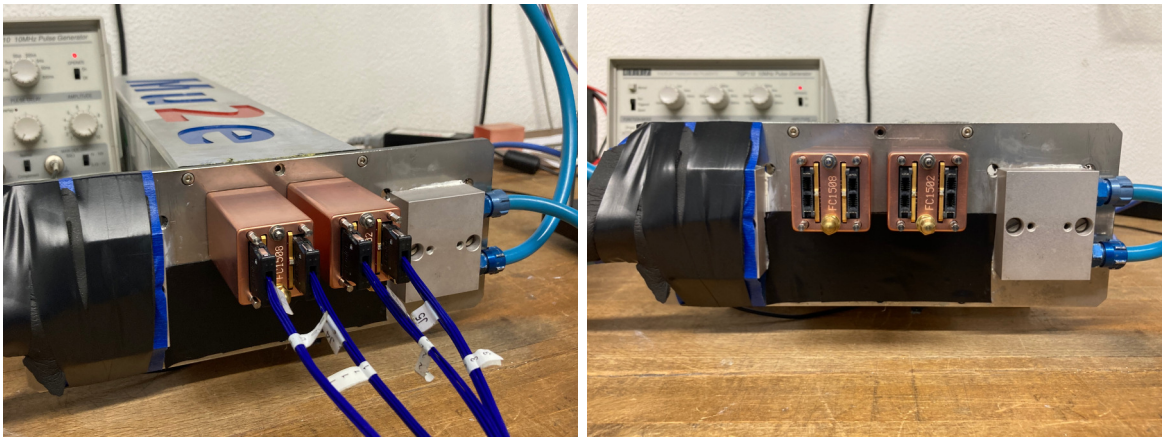

Figure 4.12: Pictures of a pair of Readout Units mounted to the Al plate of the QC Station.

A chiller stabilizes the temperature around $\sim 25°C$, allowing to perform measurements in stable conditions and to have comparable results. Albeit the temperature stabilization, some residual variation of few degrees is still observed on the SiPMs, so we also record their temperature when making the test in order to perform an offline gain correction. A Low Voltage and a High Voltage power supplies are required to power the station. The data acquisition of the FEE signals is handled by a Mezzanine Board and a fake Master Board (Dirac) which sends the signal to a CAEN digitizer. The data acquisition is started by the user thanks to a graphic interface (GUI) which interacts with the setup via USB through Python and C++ programs. SiPM signals are duplicated to be sent also to a digital oscilloscope to perform a live-check in real time.

4.3.1 Data acquisition software and GUI

The data acquisition is controlled via a software implemented in Python and C++ where the Root CERN toolkit is employed to perform the data analysis of the collected information. During assembly of the ROUs, a database has been built, associating the two FEE boards serial numbers to a holder. This database is used by the software to retrieve the FEE ADC and DAC linear calibration parameters. Information about the opera-

tional voltage of the SiPMs that are attached to the holders mounted to the system is also retrieved.

The serial numbers of the holders which are being analyzed is manually set by the worker operating the QC station. For each V_{bias} set, 10^4 events are acquired at each of the 9 filter wheel positions, in around one minute. The acquisition of an event is triggered by the LED driver signal and digitized with a CAEN Flash ADC. The data acquisition has been parallelized for the different steps so that the scan proceeds without interruptions and as soon as the last step is completed, summary results are available to the user within 1 minute.

A graphic interface (Fig. 4.13) is implemented to allow both to configure and control the data acquisition and retrieve any scan result. A power button allows to send the high voltage to the mezzanine board and to power the QC station which is then ready to start a data acquisition run. For safety reasons, the system automatically turns off the HV at the end of the data taking period, independently from the user actions. In order to take care of filling the database with the most relevant information, the GUI presents to the users few fields to be filled. In the first two, the user has to insert his/her name and institution while the second two fields have to be filled with the number of the holders mounted.

Figure 4.13: GUI of the data acquisition software for the QC station.

The HV value is set by default at the operational voltage of the mounted SiPMs, but it is also possible to perform a HV scan (see Section 4.3.3) to determine the SiPM behaviour at different voltages. This allows to determine the gain dependence on the bias voltage, information that will become essential when the supply voltage will need to be adjusted after the SiPMs will be exposed to a strong neutron fluence. In this respect, the scan characteristics – step width, number of steps below and above the operational

voltage – can all be configured via the GUI.

Once all scan parameters have been set, the button *doScan* starts the data acquisition. During the acquisition, a message on the GUI informs the worker of the operation that is being performed. The *MZB OFF* button turns off the power to the mezzanine board. This facilitates the interruption of power to the mezzanine and ensures the safety of the setup, especially if the worker has to act on the cables. When a data taking period is terminated, via the underlying Python program, the HV and the LV are turned off. The button *Quit* closes the GUI and quits the program, fully turning off the QC station.

The *Retrieve Canvas* button opens a pop-up window which allows the user to quickly open a image that summarizes the obtained results. The information to insert are: the couple of the tested holders, the version of the scan and the step in HV. The version is a sequential number (that starts at 0) that differentiates eventual multiple measurements on the same ROUs. The HV step space is used to select the results for a specific value of the bias voltage since HV scans can be performed.

When a multi-step scan, i.e. with with many V_{bias}, is finished, a pop-up window alerts whether the scan results enter within set limits or not. The chosen criteria to determine the online acceptance of a measurement are:

- The gain reduced chi-square $\chi^2/d.o.f < 5$;
- The relative gain error $\Delta G/G < 2.5\%$;
- The SiPM gain at 25°C is $3.4 \cdot 10^6 < G < 4.0 \cdot 10^6$.

If these criteria are not met, the system alerts the user who can check the ROU performance and evaluate if there is a problem with any component (Fig. 4.14). The values of the fit parameters for gain, charge and PDE are also reported to help noticing any anomaly. The difference between the set voltage and the voltage read back by the FEE is also monitored, since this allows to assess if the DAC calibration is working as expected.

4.3.2 Measurements at V_{op}

A scan at the SiPM operational voltage allows to set a baseline for the ROU performance before any damage due to radiation. This allows us to evaluate the SiPM gain and see how the coupling SiPM-FEE is operating before the introduction of any further effects due to the Mu2e operational environment. The SiPM operational voltage is retrieved from the database and set. A nine points scan in light intensity is performed in order to extract the gain (from the fit with Eq. 4.7) and response of the SiPM-FEE pair. The digitizer of the QC station collects the raw data from the FEE boards and using C++

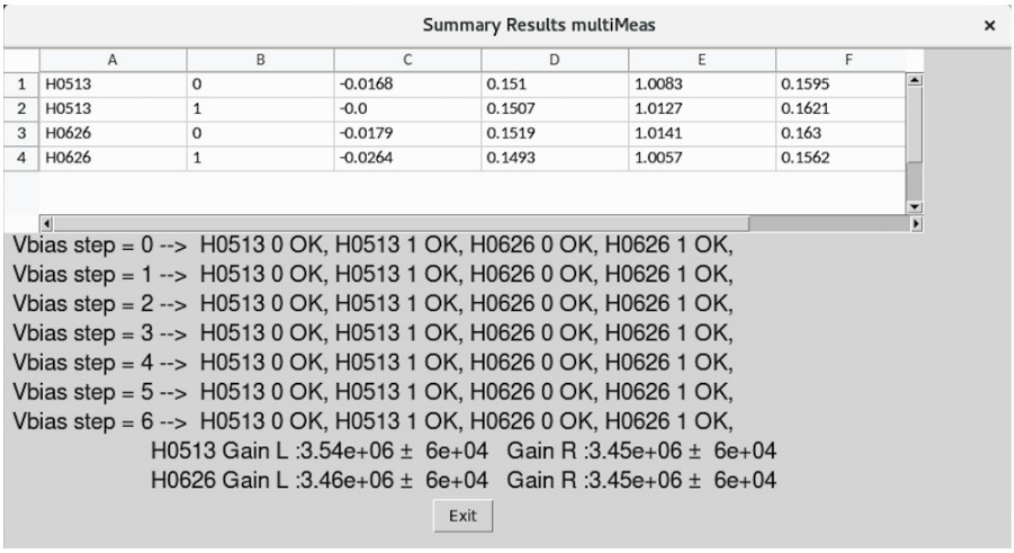

Figure 4.14: GUI displaying the scan results. In the table at the top the fit parameters are shown.

programs and the ROOT toolkit it is possible then to extract the following information: trigger information, events, timing information, signal waveforms. The SIPM waveforms are integrated over a 200 ns gate to obtain the 9 charge peaks reported in Fig. 4.15.

In Fig. 4.16, each column is related to a SiPM-FEE system, joint in pairs in the two holders that are simultaneously tested at the station. In the figure the results for one holder are shown. The gain is extracted from the values of σ_Q/Q for the different filter wheel positions. The function used for the fit is

$$\frac{\sigma_Q}{Q} = \sqrt{\frac{p_0}{Q} + \frac{p_1^2}{Q^2} + p_2^2}. \tag{4.7}$$

The three terms represent: p_0 the Poisson statistics for the photoelectrons, p_1 the electronic noise term and p_2 the constant term related to the source fluctuations. Assuming a small Fano factor, the p_0 term is directly related to photosensor gain via the charge of the electron: $G = p_0/q_e$ with $q_e = 1.6 \cdot 10^{-7}$ pC.

The data points and the fit results are shown in the top row of Fig. 4.16. On the same plot, the extracted gain value is also reported next to the holder ID. The waveforms are shown in the second row of the same plot, while in the bottom part the associated charges are shown. As expected, the charge mean value increases as the light intensity increases. The charge peaks are fitted with a Gaussian to extract their mean and sigma.

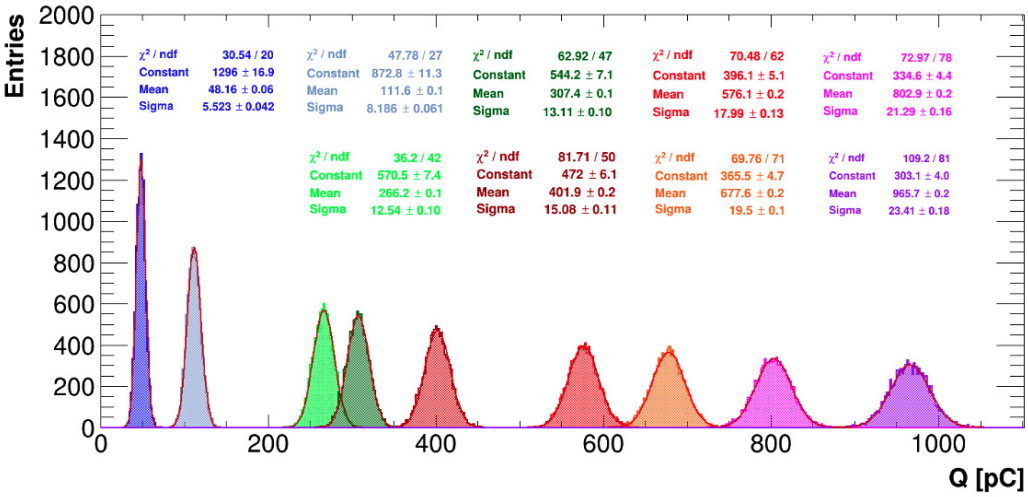

Figure 4.15: Example of the collected charges at V_{op} for the 9 filters, with a Gaussian fit.

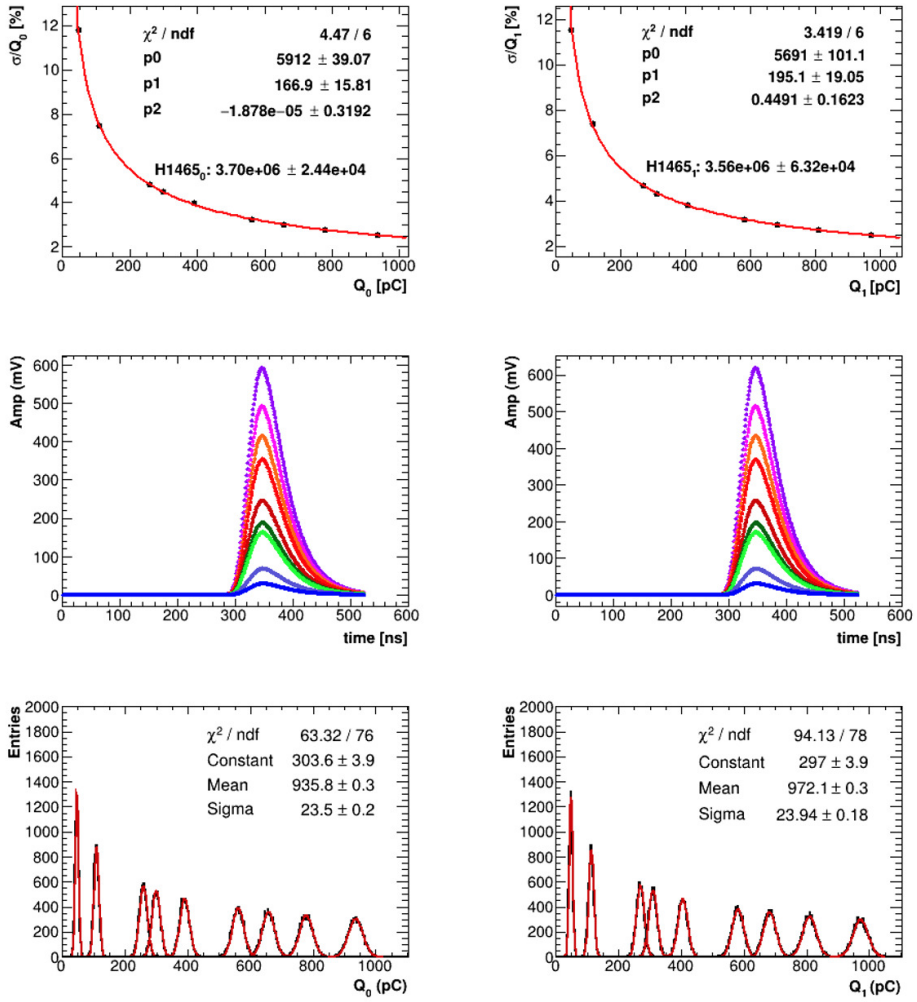

Figure 4.16: Result of a measurement at HV = V_{op}. Each column is associated to a different SiPM-FEE couple. Going down the rows is shown: charge resolution, waves profile, collected charges with the fit stats for the highest one.

Measurements reliability and temperature studies

Before carrying out a systematic study on the production Mu2e ROUs, the setup reproducibility has been tested. The station stability was probed by performing multiple measurements on a pair of holders for a total of 31 scans at V_{op}. The chosen holders were working as expected and for simplicity they will be addressed in the following using their serial ID: H0058 and H0091. The resulting gain distributions are shown in Fig. 4.17, separately for each SiPM.

Looking at the gain distribution over time, no periodic nor cumulative effects can be observed (Fig. 4.18-left)

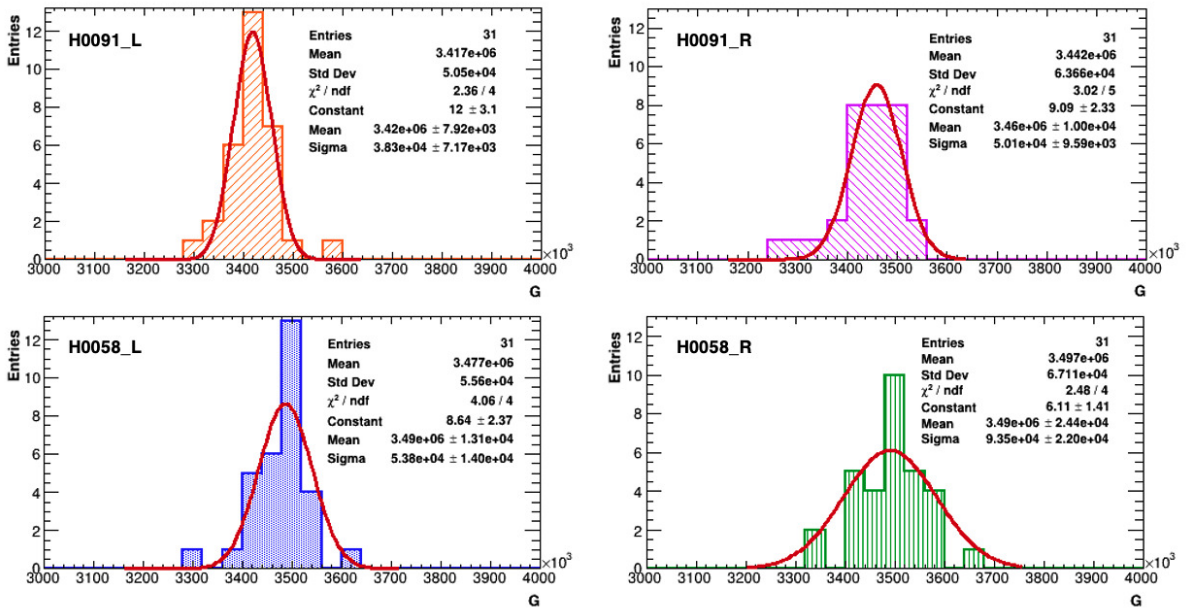

Figure 4.17: Gain distribution for the 4 SiPMs, i.e. 2 holders, over the 31 repeated measurements performed at the station. A Gaussian fit is done in order to evaluate the width of the distributions.

The gain distributions appear to have some outliers, which suggested that there may be effects associated to temperature variations. Thanks to the presence of the temperature sensors on the FEE, it was possible to evaluate the gain dependence on temperature. Two main effects were noticed:

- There is an asymmetry in temperature for the left and right holder at the station.
- Temperature fluctuations have to be taken into consideration since they induce significant effects on the gain value.

By plotting the gain value vs the temperature, as shown in Fig. 4.18 right, can be seen that the distributions lay at two different temperature points due to the directional chiller

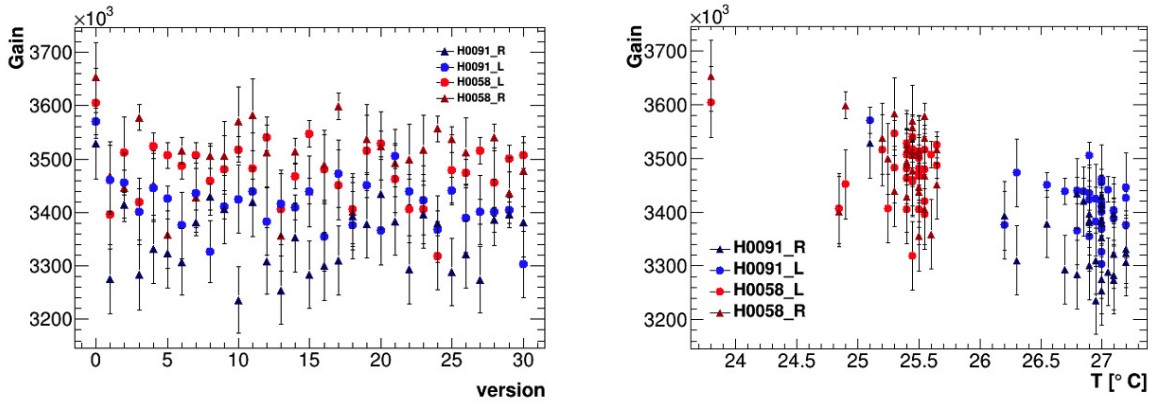

Figure 4.18: Left: Gain distribution vs version. Right: Gain dependence on temperature.

fluid flow from left to right. It can also be noticed that the temperature distribution is quite wide due to cool down periods given by the different time intervals between two measurements. After the first 31 repeated measurements, the holders position at the station was inverted and the histograms in Fig 4.19 show clearly how the mean value of the gain distributions is affected by the position. The chiller allows for a temperature stabilisation at $\sim 25 \pm 2$ °C and efficiently prevents a increase in temperature grater than $\sim 27.5\,°C$, nevertheless it was found to be dependent to fluctuations of the room temperature and to the heating up of the electronic components.

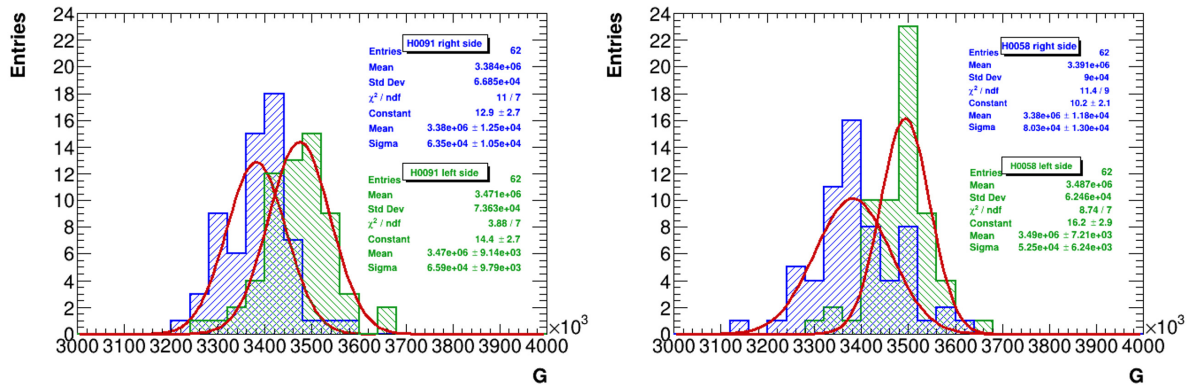

Figure 4.19: Gain distribution for the two holders when they were in the left side of the station (green) or in the right side of the station (blue). The distributions are built with the gains of both the SiPMs of each holder.

To quantify the gain dependence as a function of temperature, the temperature profile of the gain distribution has been constructed. The plot shown in Fig. 4.20 is the result obtained for the full analyzed statistics (916 Holders). A clear linear behaviour is seen that corresponds to a variation of the gain of $G_t = (-1.60 \pm 0.07)\%/\,°C$.

Using this information, it is possible to correct the gain values and to compare the performed measurements even in presence of significant temperature changes. The gain

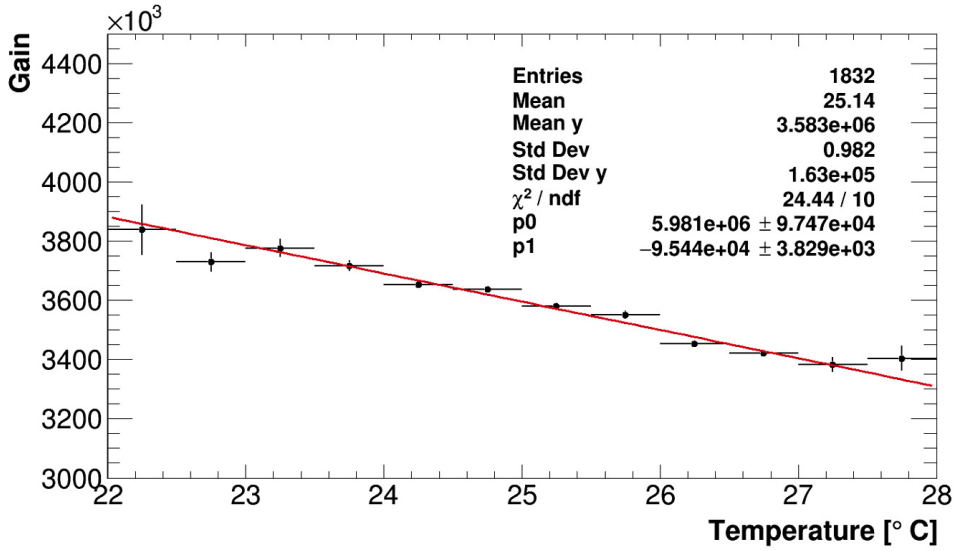

Figure 4.20: Temperature profile of the gain.

is corrected for temperature behaviour to extract its value at 25°C:

$$G(25°\mathrm{C}) = G \cdot (1 - G_t \cdot (T\,[°\mathrm{C}] - 25)). \tag{4.8}$$

The temperature of 25°C was chosen since it is the temperature at which the breakdown voltage was measured as quoted also by the manufacturer. The changes in the gain distribution after this operation can be observed in the gain distribution for all the measurements of the holders H0091 and H0058 in Fig. 4.21. This distribution allows also to evaluate an upper value for the reproducibility of the measurements at the station, which is $\lesssim 1.5\%$.

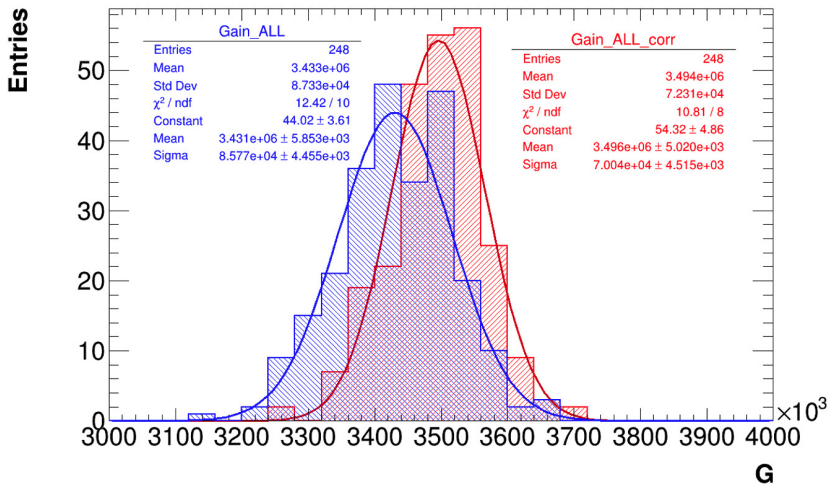

Figure 4.21: Gain distributions of all the repeated measurements for holder H0098 and H0051, both not corrected (blue) and corrected (red) for the temperature with Eq. (4.8).

4.3.3 HV scan

During running, for the worst irradiated SiPMs, we will need to adjust (i.e. decrease) the operational voltage of the SiPMs to keep the leakage currents within the limits supported by the electronics. Therefore, to study the SiPM behaviour at different bias voltages and characterise their response and PDE, scans in HV were performed. Through the GUI it is possible both to set the size of the steps in HV and the number of steps below and above the bias voltage. Studies have been performed in order to determine the step width and the range of voltage values to be studied.

Multi-voltage scan and results presentation

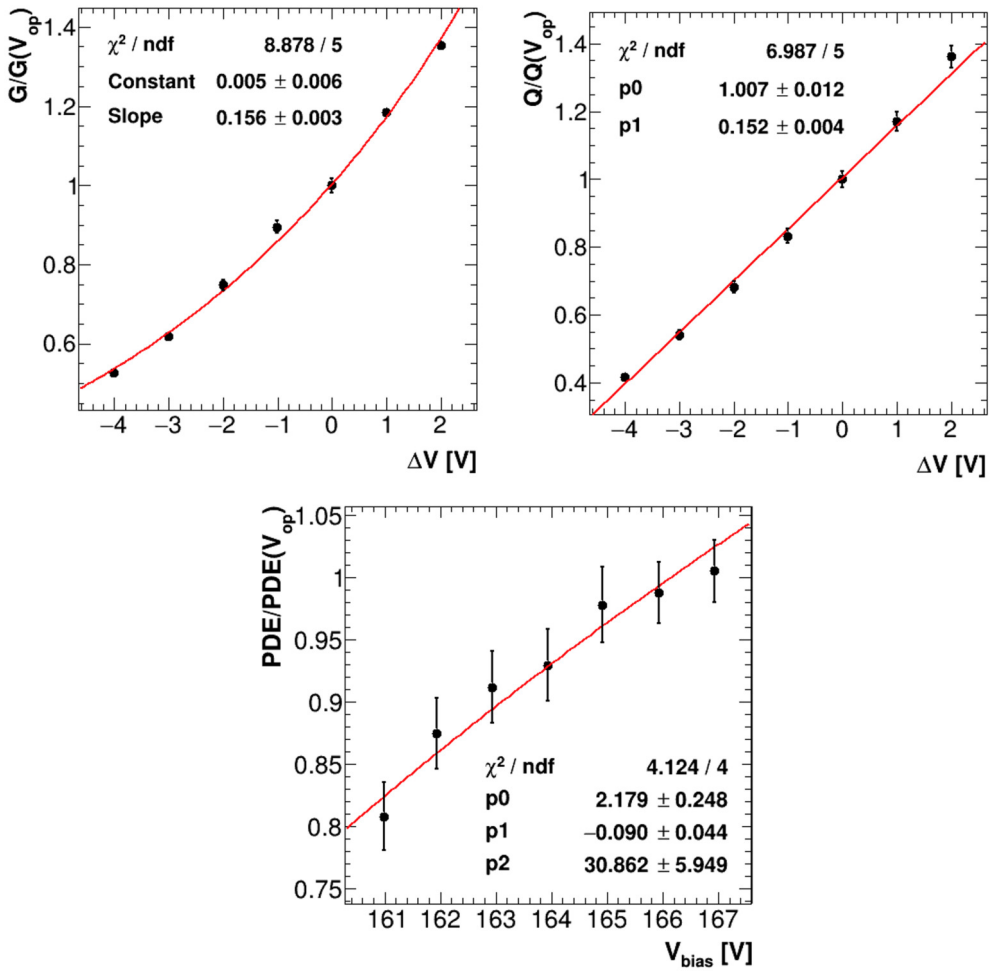

Figure 4.22: Example of the results of a 7 points scan for gain, collected charge and PDE. All values are normalised to the results at V_{op}. G and Q are show as a function of the overvoltage, while the PDE vs V_{bias}.

As mentioned, the chosen analysis for the ROUs is a 7 points scan at 1 V intervals. In Fig. 4.22 is shown a summary plot of the gain, charge and PDE values for a ROU.

The gain behaviour is modelled with an exponential

$$G(V) = exp \cdot [slope \cdot V + const] \tag{4.9}$$

while the charge with a straight line

$$Q(V) = p_0 \cdot V + p_1 \tag{4.10}$$

The PDE is instead fitted with

$$PDE(V) = p_0 \cdot [1 - (p_1 \cdot V \cdot exp(-p_2/\sqrt{V}))^{-2}] \tag{4.11}$$

from [84], where p_0 is related to the maximum value of the PDE, while p_1 and p_2 are two voltage independent parameters used empirically to reproduce the shape of the PDE.

These results and plots analogous to Fig. 4.16 are presented to the user, as these allow to know if some problems were found during the scan (pulse saturation, temperature changes and so on). A database is then filled with the holder ID numbers as these are stored in boxes, while preparing them for shipping to Fermilab.

Scan length choice

Taking into consideration the radiation hardness studies (Sect. 3.2.4), the maximum reduction of the supply voltage expected should be of $4 \div 6$ V.

In order to find the best compromise between the time of the scan and the number of points to acquired, different trials were performed. In Fig. 4.23, the differences of gain and response between a finer scan (with 0.5 V steps) and a coarser scan (1 V steps) are shown. The comparison between the determination of the relative PDE is also shown.

The parameter difference can be included in their error and the station resolution. Since there was no significant advantage in performing a finer scan and in order to optimise the time for the test of production units, it was chosen to perform a 7 points scan with 1.0 V steps, starting 4 V below the operational voltage, up to 2 V above V_{op}.

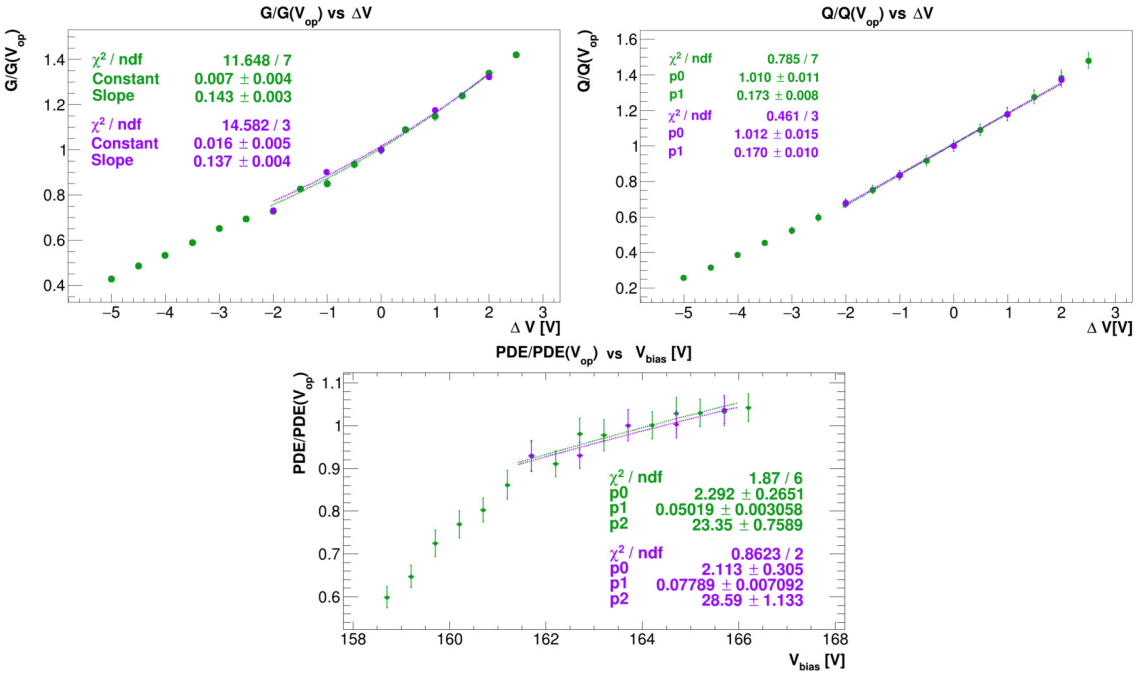

Figure 4.23: Gain, charge and PDE plots for a longer and finer HV scan (green) and one shorter and with less frequent points (purple).

4.4 ROUs performance results

At the moment of writing, the ROUs calibration is reaching its final stage since we have already assembled more than 1200 units, out of which we have already calibrated 916. An additional 50 ROUs were also scanned but did not fit the aforementioned requirements, so will not be considered in the following. They could either have problems at the FEE or a broken SiPM cell, or there could be some discharge due to residues from machining of the copper holder. These ROUs will be addressed after all the units have been scanned in order to avoid influencing the workflow at the station. The last few hundreds ROUs are being tested, planning to complete them in November.

In Fig. 4.24 the gain is shown for the left and right FEE of the scanned holders. As it can be observed, there is a first set of ROUs, corresponding to the lowest holder IDs, which shows a broader distribution as due to the learning curve and of the not perfect control of the FEE calibration factors. As soon as the learning phase was concluded, a steadier setup was achieved and the distribution appears much narrower.

The channel by channel spread during production can be evaluated from the gain distributions shown in Fig. 4.25, both before and after applying the temperature gain correction. As can be seen from the Gaussian fits, the sigma of the Gaussian distribution fit goes from 4% to 3% spread after temperature correction. The average gain at V_{op}

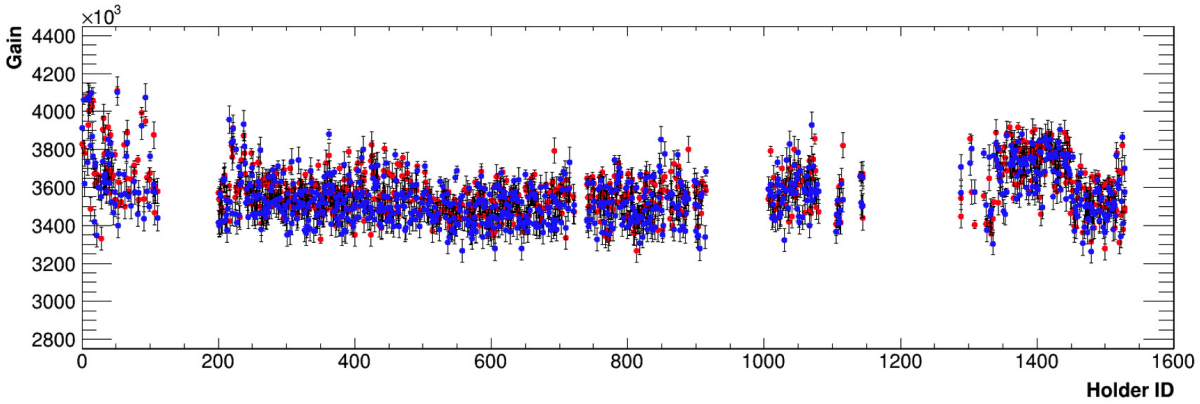

Figure 4.24: Gain distribution with respect to the Holder ID. The gain for the left and right SiPM-FEE couples are plotted separately for each holder.

results to be $(3.541 \pm 0.003) \times 10^6$, in good agreement with Hamamatsu specifications. Few tails are still observed mainly at higher gain values. A study is in progress to control few of these tails and compare channel by channel our determination with the Hamamatsu specified value.

The distributions of the gain, corrected for the temperature, is reported in Fig. 4.26 separately for left and right SiPM of one holder. The two distributions appear consistent and no significant systematic effect can be observed.

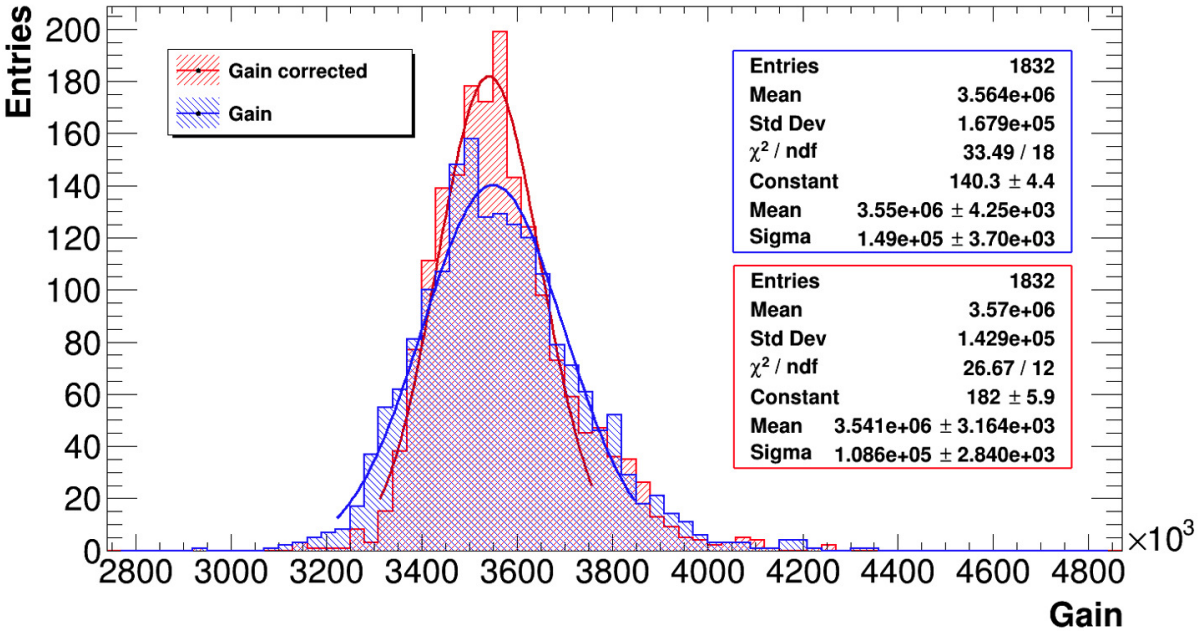

Figure 4.25: Gain distribution corrected (red) and not corrected (blue) for the temperature.

In Fig. 4.27-left the gain difference between the left and right SiPM of one holder, normalised to the mean gain value of that holder is shown. As this distribution appears

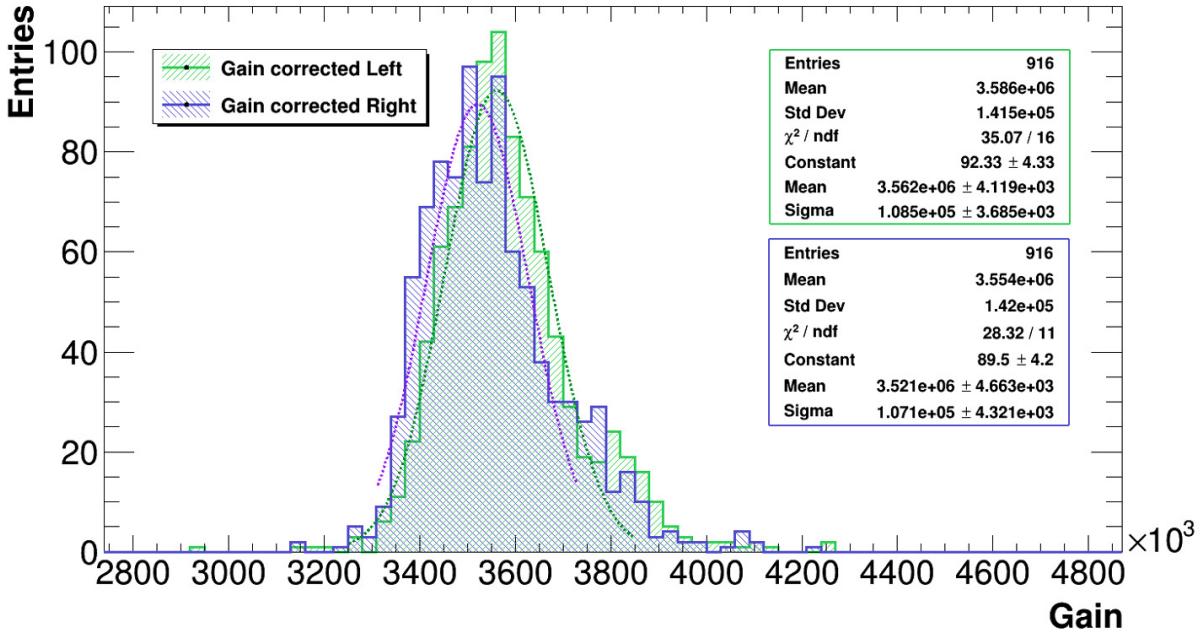

Figure 4.26: Gain distribution corrected for temperature, reported separately for the left and right SiPM in each holder

Gaussian, a cumulative curve (Fig. 4.27-right) indicates that $\sim 97\%$ of the holders have less than 10% difference (while all are below 25%).

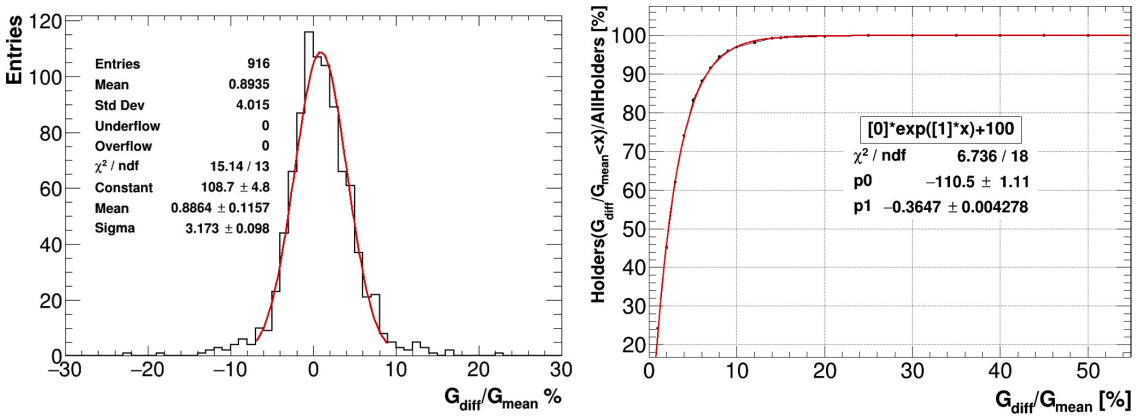

Figure 4.27: Histogram (left) and cumulative curve (right) of the difference in gain between the left and right SiPM of one holder, normalised to the mean value of the gain.

The distribution of the fit parameters of charge and gain dependence on the applied voltage, shown in Fig. 4.28, allows to control if it is possible to derive a global parameterisation for these corrections. In general, except a few tails for the gain fit, that can have a larger channel by channel behaviour, they have a Gaussian core. The central values show very precise numbers for the slope parameters for both the gain and the charge. The RMS gaussian values are at the level of 0.5%, indicating a small residual channel

by channel variation that will correspond to a relative gain/charge change of $< 2\%/\mathrm{V}$ if the mean value will be applied. This could be almost acceptable for the hardware equalization.

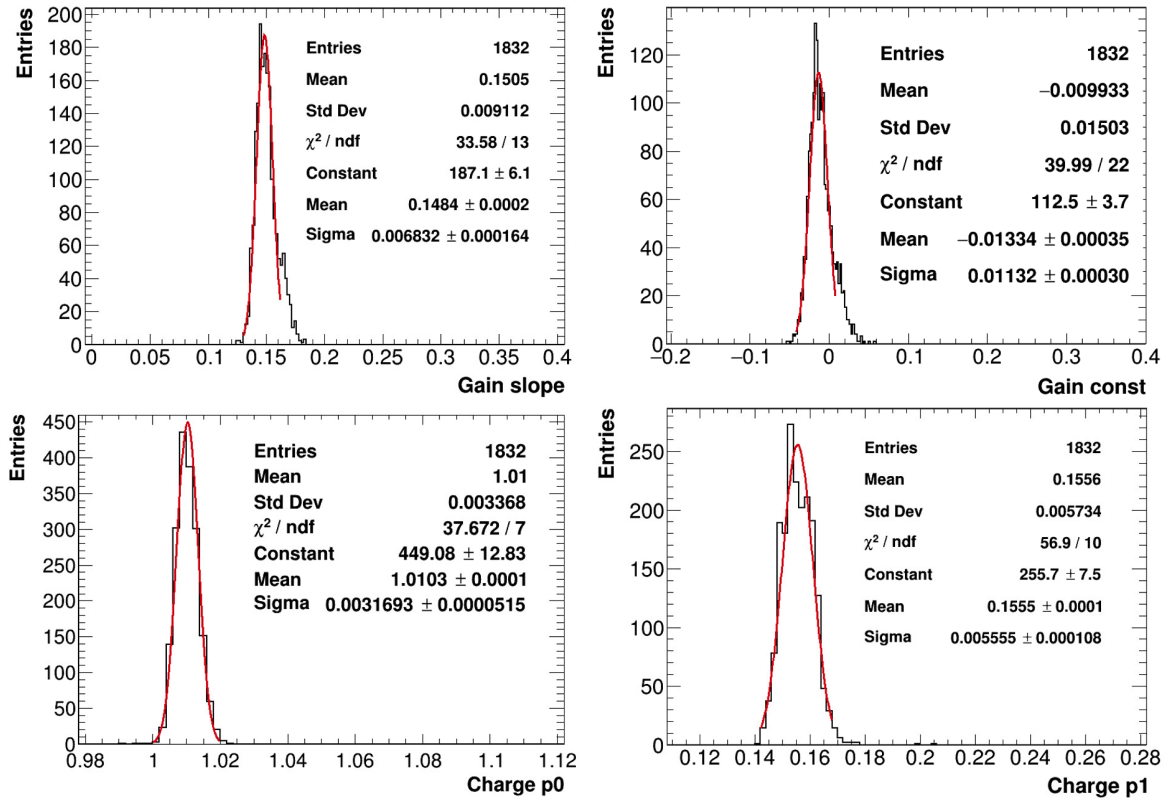

Figure 4.28: Gain fit parameters (top left and top right) and charge fit parameters (bottom left and bottom right) distribution. The plotted parameters are those from Eq. 4.9 and Eq. 4.10. The gain slope is expressed as V^{-1}, p_0 is in pC/V and p_1 in pC.

Chapter 5

A first implementation of the Calorimeter Slow Control

The term "Slow Controls" or Detector Control System (DCS) generally refers to the control and monitoring of the detector, its electronics and its physical environment. It is strictly related to the Data Acquisition System (DAQ), but it needs to be running and to be available independently from the DAQ status. The Trigger and Data Acquisition (TDAQ) subsystem provides the necessary components for the collection of the digitized data from the detectors and Beam Monitoring systems and it also handles the delivery of that data to online and offline processing for analysis and storage. It is also responsible for detector synchronization, control, monitoring, and operator interfaces. The DAQ must also provide a timing and control network for precise synchronization and supervision of the data sources and readout, along with a Detector Control System for operational control and monitoring of all Mu2e subsystems.

5.1 The TDAQ system in Mu2e

The Mu2e TDAQ provides the necessary infrastructure to collect digitized data from the Tracker, Calorimeter, Cosmic Ray Veto and Beam Monitor systems. The TDAQ employs 36 dual-CPU servers to handle a total rate of 192000 proton pulses/second and an average of 5400 events/second/server. According to preliminary estimates, the detectors generate approximately 120 kB of zero-suppressed data per proton pulse, for a resulting average total data rate of about 20 GB/s when the beam is present [33].

The Mu2e TDAQ is a streaming system with a software-only trigger, designed to satisfy the following requirements [85]:

- Provide an efficiency better than 90% for the conversion electron signal.

- Keep the total trigger rate below a few kHz, equivalent to approximately 7 PB/year of total data rate (needed to keep the collected data to less than 21 PB in 3 years of running).
- Keep the processing time below 5 ms/event (which is the spill off time between two spills where the beam is on).

The limits on the data rate are based on the availability given by the Mu2e machines, illustrated for each TDAQ step in Fig. 5.1. The expected data reduction ratio that Mu2e will have to comply to is 150:1.

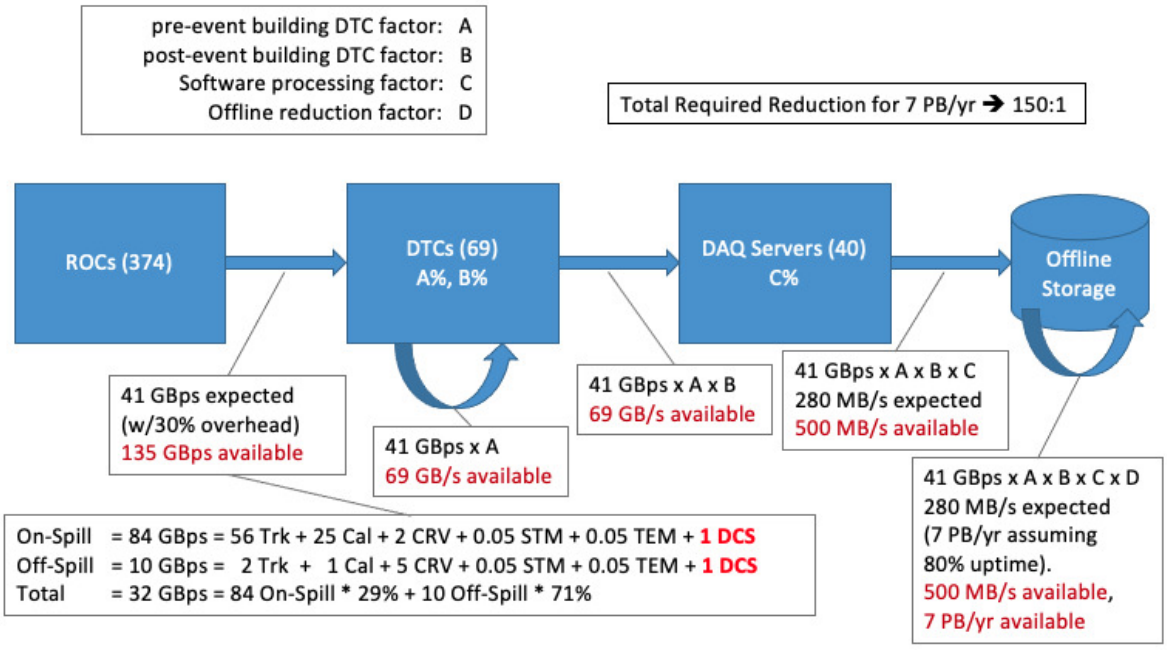

Figure 5.1: Data rate limits for the Mu2e TDAQ chain. Four parameters (A, B, C, D) are factors related to data reduction at the different TDAQ steps [86].

To achieve these goals and allow a higher off-detector data rate, the Mu2e Data Acquisition System is based on a streaming readout. This implies that all detector data are digitized and zero-suppressed in the front-end electronics and then transmitted over bi-directional optical links to the DAQ Servers in the electronics room. The DAQ Servers filter these events and forward a small subset of them to the offline storage. While this approach results in a higher off-detector data rate, it provides greater flexibility in data analysis and filtering, as well as a simplified architecture. Figure 5.2 shows the Mu2e TDAQ architecture.

Each TDAQ process starts from the Run Control Host which receives beam status and timing information from the Accelerator Control network. The Control Fan-Out

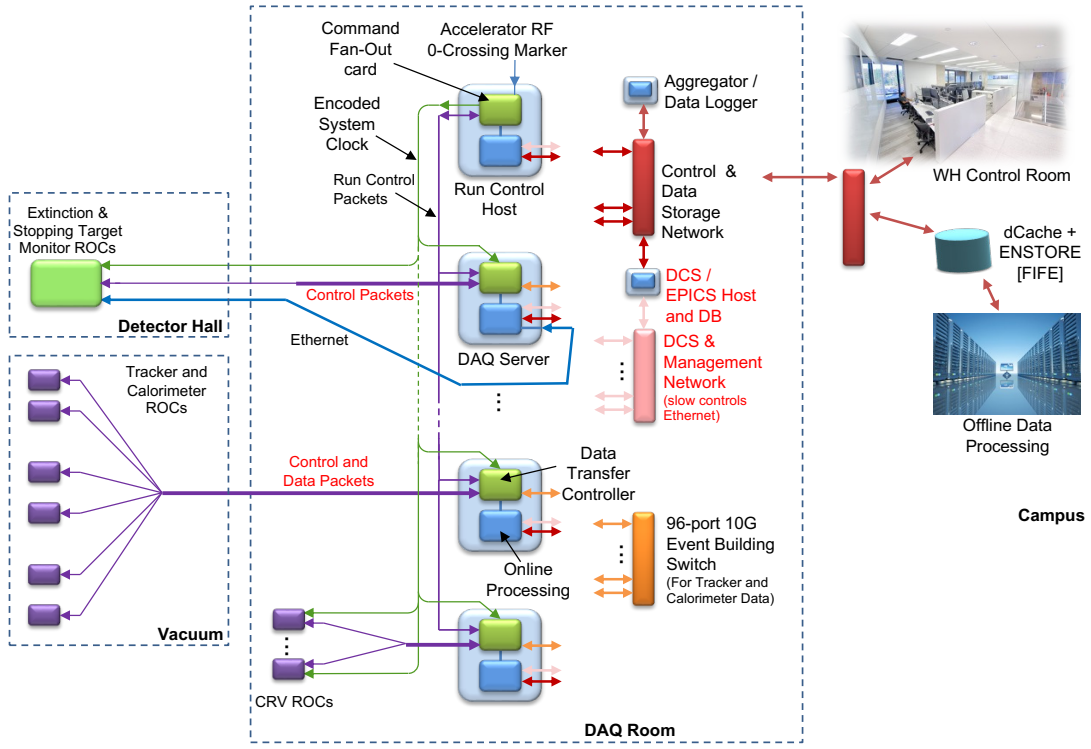

Figure 5.2: Mu2e TDAQ architecture and components diagram [87].

(CFO) module, in the Run Control Host, is responsible for generating and synchronizing Readout Requests. Each Read Out Controller (ROC) has a large front end buffer and its main task it to continuously stream out via optical links, from the detectors to the Data Transfer Controllers (DTCs), the zero-suppressed data collected between two proton pulses. Events are formed and triggered in the Event Builder layer where DTCs are involved in a round-robin process. Readout Controllers have an FPGA for data collection, buffer management and processing. The data acquisition of time-frames are collected in a single server using a 10 GB/s switch. The data stream from the detectors is read by a software filter algorithm that selects events which are combined with the data flux coming from the CRV System. Lastly, the online reconstruction starts and a trigger decision is made. The events are moved via a PCIe bus to the Storage Layer for further filtering and data logging.

Each ROC also has a microcontroller, either integrated into the FPGA or in an external mezzanine board, which handles the DCS operations related to the setting/monitoring of the parameters of the detectors inside DS. To configure the settings of the detectors inside the DS, the DCS configurations are loaded at the Run Control configuration stage. To monitor the detectors inside the DS, the TDAQ reads and stores the DCS information, reading and writing them at a very slow pace, always using the fiber readout. The DCS system also controls and monitors all external power supplies and

the status of the cooling and source systems by means of EPICS (Experimental Physics and Industrial Control System). The reaction to Failure Mode cases (such as loss of vacuum pressure, HV sparking and so on) is controlled by Programmable Logic Controllers (PLCs) integrated in the iFIX software.

5.1.1 TDAQ Software architechture

The software architecture is based on *artdaq* (acronym for "art data acquisition") [88] [89], developed by the Scientific Computing Division at Fermilab for the current and upcoming neutrino and muon experiments, such as DUNE, SBND, ICARUS, MicroBooNE and Mu2e. *artdaq* is a toolkit of C++ libraries and programs for use in the construction of DAQ systems involving data transfer, event building, reconstruction, analysis and writing the event data to disk. This software runs on DAQ servers and on dedicated control and monitoring computers.

By incorporating *art* [90] into the TDAQ toolkit, complex trigger algorithms can be run in real-time and are limited only by the available processing power. *art* is an event-processing framework which works in a variety of contexts: high-level software filters, data monitoring, calibration, event reconstruction, simulation and analysis. Additionally, *art* online monitors can be attached to a running system and provide a subset of the data for control room displays. Data are saved in *art*'s ROOT format by default, reducing the amount of pre-processing necessary for offline analysis. Higher-level tools like *art* and ROOT are involved in the Data Quality Monitor (DQM), which typically runs either online, in parallel to the DAQ seeing only a fraction of all of the events to reprocess them, or purely near-line/offline to fully reconstruct dedicated streams and perform a high level monitoring.

In Mu2e, we use as online DAQ solution a ready-to-use instance of *artdaq* called *otsdaq* (acronym of "off-the-shelf data acquisition"). *otsdaq* makes underlying choices for the users and allows them to get started with a small amount of configuration while providing a multi-user and web-based interface to monitor the online DAQ entities.

5.2 Mu2e Detector Control System

The Detector Control System (DCS) purpose is to monitor the detector status and operational conditions. For each subsystem, the DCS allows to display real-time event and detector data via Graphical User Interfaces (GUIs) and archive the monitoring data to disk. The DCS will handle the subdetectors controlled by the Mu2e DAQ (i.e. Tracker, Calorimeter, Cosmic Ray Veto, Extinction Monitor and Stopping Target Monitor), which

share the notion of a Readout Controller at the front end connected over optical fiber to a DAQ Server. The DCS is the window for experimenters and detector experts onto the status and health of Mu2e. The DCS must archive and present GUIs of high level displays of power supplies (PS), liquid and gas systems operational data, environmental temperatures, magnetic field strength, status and run condition information for the data acquisition of every detector portion. The DCS goal is not only to encapsulate all of this information, but also to present it in a meaningful and easy-to-interpret way, in order to facilitate running and monitoring the experiment, being the pivotal tool for shifters during run periods. For these reasons, the main DCS requirements are [91]:

- Provide live run conditions for all monitored channels, flagging the ones in a problematic state and allowing debugging.
- Provide a standard GUI display accessible through the network, with laptops, and especially accessible in the Mu2e Control Room.
- Associate database contents with the detector geometry, so that information can be easily and promptly extracted for portions of the detector.

Mu2e selected EPICS for the DCS Slow Control and monitoring software [92]. EPICS is an open source framework originally developed at Argonne and Fermilab and now used in numerous experiments.

An Input Output Controller (IOC), running for each subsystem on a central DAQ server, will provide dedicated channels for all the monitored parameters. The IOC is a process that communicates with hardware and maintains Process Variables (PVs). A PV is a named piece of data associated with the detector electronics or hardware like temperature, voltage or current.

The total number of DCS quantities in Mu2e is expected to be of the order of thirty thousand. On average, these quantities will be updated approximately twice per minute, for a resulting generated data rate $\lesssim 10\,\mathrm{kB/s}$. The rate estimates expect $1\,\mathrm{kB/s}$ for the tracker and calorimeter and $0.5\,\mathrm{kB/s}$ for CRV, beam monitoring systems, accelerator and solenoids [91].

As part of the DCS, *otsdaq* delivers slow control data from the DTCs and ROCs to EPICS. To connect *otsdaq* to EPICS, a C++ interface has been developed by the Collaboration and it uses the EPICS Channel Access Client Library functions [93] and PostgreSQL database connections [94] to read/write data. The *otsdaq* interface allows the user to monitor and interact with the DAQ hardware and the other devices managed by EPICS to:

- Observe Process Variables such as settings, alarms, warnings, readouts, time stamps, status.
- Interact through a web interface that is lightweight, user-friendly, ready to use and customisable.
- Implement custom handling of PV alarms integrated with the TDAQ state machine transitions.

The design of *otsdaq* involved C++ and web-app applications to include the Mu2e Slow Control monitoring, alarm handling, TDAQ hardware and online DAQ slow control entities writing in EPICS. From *otsdaq* it is possible to handle alarm propagation from EPICS IOCs to automated plug-in threads or to the web interface and, ultimately, the users.

5.2.1 EPICS and Phoebus

EPICS is a set of software tools and applications which provides an infrastructure to build distributed control systems that can operate devices such as accelerators, large experiments and telescopes. Such distributed control systems typically comprise many computers, networked together to allow communication between them and to provide control and feedback of the various parts of the device from a central control room or even remotely.

EPICS uses Client/Server techniques to communicate between the various computers. Most servers, i.e. the IOCs, perform local control tasks and publish that information to the clients using the Channel Access network protocol. A pivotal point in EPICS performance is the reliability it must ensure since the experiments are run for extended periods of time and information about their status has to be continuously available.

EPICS *base* is the main core of EPICS, comprising the build system and tools, common and OS-interface libraries, Channel Access client and server libraries, database access routines, the database processing code, and standard record, device and driver support. Each IOC in an EPICS-based control system loads one or more databases. A database is a collection of records of various types. A record is an object which can/has to have:

- A unique name.
- A behavior defined by its type.
- Controllable properties, i.e. the fields.

- Optional associated hardware I/O (device support).
- Links to other records.

There are several types of records available and, even if not recommended, it would also be possible to define custom types. Each record comprises a number of fields. Fields can have different functions and typically they are used to configure how the record operates or to store data items. The main tasks a field can have are to: scan parameters, read and convert parameters, display parameters, handle alarms, monitor parameters or monitor run-time parameters. The most commonly used record types are:

- Analog Input and Output (`ai` and `ao`) records can store an analog value and are typically used for things like set-points, temperatures, pressure, flow rates. These records perform number of functions like alarm processing and filtering.
- Binary Input and Output (`bi` and `bo`) records are generally used for commands and statuses to and from equipment and store binary values like ON/OFF.
- `calc` and `calcout` records can access other records and perform a calculation based on their values.

For the Mu2e calorimeter, StreamDevice [95] is employed. It is a generic EPICS support package for devices with a byte-stream based communication interface. These devices can then be controlled by sending and receiving strings. Examples for this type of communication interface are serial line and TCP/IP (Transmission Control Protocol and Internet Protocol). StreamDevice comes with an interface to asynDriver [96], which implements the low-level support for those communication interfaces and can be extended to support other bus drivers.

Upon execution of the IOC, an EPICS prompt is activated and the status of the chosen PVs is updated. These can be monitored thanks to a GUI. The Mu2e Collaboration has chosen to employ CSS Phoebus for that purpose.

Phoebus [97] is a framework born from an update of the Control System Studio (CSS) toolset. It allows to monitor and operate large scale control systems, such as the ones in the accelerator community, by providing a software architecture for a standard graphic interface.

The fundamental Phoebus architecture consists of core modules, user-interface related modules (core-ui) and app modules. The core modules provide the infrastructure, while app modules implement specific application functionality. Everything is based on Java version 9 or higher, using Java FX as a graphics library. The Phoebus architecture is shown in Fig. 5.3.

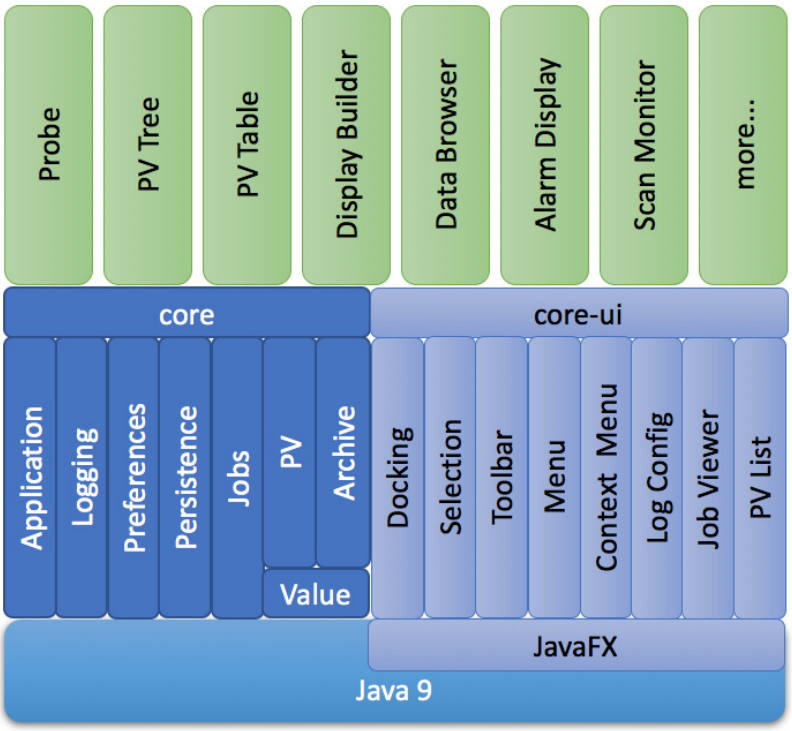

Figure 5.3: Phoebus architecture.

A Phoebus object may contain just one application, for example only one Probe, PV Tree, PV Table, Display Builder, so that there are several Phoebus products and each one has one function. Alternatively, a single Phoebus product can contain all these applications. This allows integration between the applications, for example via context menus that start other PV-related applications based on the current selection. Given the high number of monitored quantities, phoebusgen [98] has been developed. It allows to use a Python script to generate the Phoebus XML file, allowing to use loops and variables to generate multiple widgets and screens, associated to different PVs, at once.

The interplay between EPICS and Phoebus is schematically shown in Fig. 5.4. They both interact with the common network so that Phoebus has access to the PVs created in the different EPICS IOCs. The GUIs and Web GUIs can be accessed and operated by the users and the relevant information stored.

5.3 Mu2e Calorimeter DCS

The Mu2e DCS systems are currently under development. Accesses to the machines, details of data-handling and expected requirements for the DCS systems of the Mu2e detectors are being continuously improved and optimised. The slow control software for the accelerator beam and the muon beamline, the DAQ health status (like the run

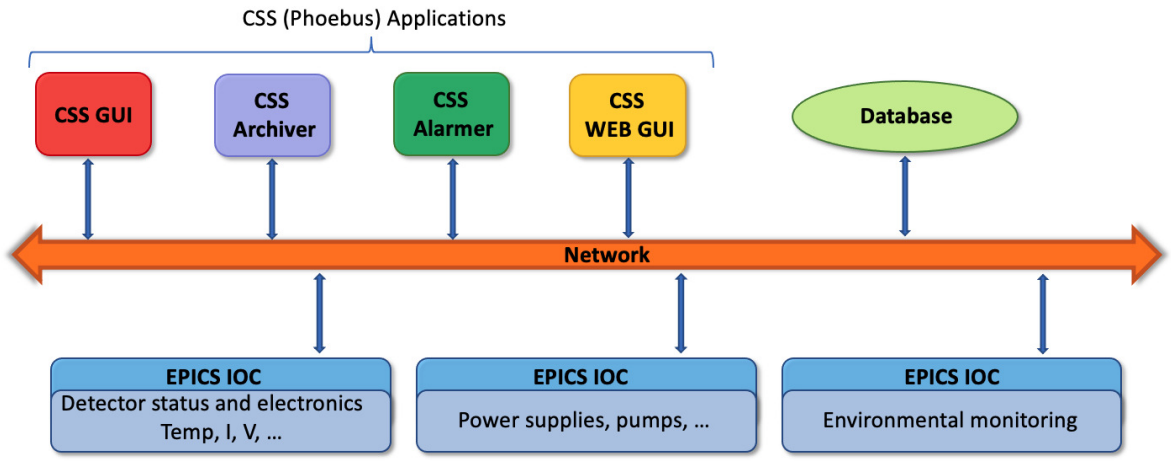

Figure 5.4: EPICS and Phoebus interaction with the Network system.

state, number, event rate) and the tracker HV power supplies monitoring in current and voltage is in a well advanced state.

For the specific case of the calorimeter, it is very important the interaction with the calorimeter calibration system. So far, the plan for the slow control of the calorimeter requires:

- DCS monitor of the power supplies voltage and current, allowing HV setting only by expert personnel.
- Temperature monitoring of the calorimeter SiPMs and of the calorimeter external surfaces with temperature sensors.
- Radiation hardness monitoring at the calorimeter surfaces with RADFET sensors.
- DQM of dead channels, occupancy and resolutions of the calorimeter detector hardware.
- Continuous in-situ calibration with Laser and MIPs and weekly calibrations with the source.

For the DAQ, the calorimeter will then use: $\sim$ 3100 ROC channels in 140 ROCs, 28 DTCs and 16 DAQ servers (since 1 Server can host $0 \div 2$ DTCs and 1 DTC can host $0 \div 6$ ROCs).

5.3.1 Power supplies and labeling scheme

The Mu2e calorimeter has filled out two racks 48 U size in the Mu2e DAQ room with a total of 20 HV modules and 20 LV modules per rack. The modules have been mounted

on the racks in specific crates, alternating LV and HV supplies, and leaving open spaces among crates to increase the air flow and heat diffusion.

The power supplies offer a remote analogue control, 10 mV resolution and an accuracy of ±(0.05%+10 mV) on the LV value (model CPX400SP by Aim-TTi [99]) and ±(0.05%+ 50 mV) on the HV value (model PLH250-P by Aim-TTi [100]). A picture of the PS faces and some PS in the Mu2e DAQ room are shown in Fig. 5.5. Typically, for these PS models it is guaranteed a delay < 25 ms between receiving the command terminator for a step voltage change at the instrument and the output voltage beginning to change. The

Figure 5.5: Left: LV Power Supply CPX400SP. Centre: HV Power Supply PLH250-P. Right: Eight PS mounted in the rack at the Mu2e DAQ room.

correct wiring of the PS to the DAQ boards and ultimately to the SiPMs is important because it guarantees, together with the ROUs design, a redundant readout per each calorimeter crystal. On each disk 10 crates are mounted on the outer surface. Each create needs two pairs of HV and two of LV PS, since one HV and one LV will power the boards handling the SiPMs on left side of the ROU (side 0) and the other two the SiPMs on the right side (side 1). So, a total of 80 PS (40 HV and 40 LV) are going to be needed by the calorimeter. Each PS, has to be identified unambiguously, in order to be able to act on it if needed. The chosen naming convention of the PS allows to address a specific PS and associate to it the position in space of the units it powers. This is illustrated in Fig. 5.6 and works as follows:

- Disk selection: 0,1
- Crate selection: 0,1,2,3,4
- Phi Angle selection (disk side): 0,1
- SiPM side selection: 0,1

Each disk will result divided into 34 similar pseudo-azimuthal sectors, each one grouping 20 crystals. The naming convention for the PS is then:

$$PS\_\mathrm{d}X\_\mathrm{cr}Y\_\mathrm{phi}Z\_\mathrm{sipm}K \tag{5.1}$$

with $PS = [\mathrm{LV}, \mathrm{HV}]$ and $X = [0, 1]$, $Y = [0, 4]$, $Z = [0, 1]$, $K = [0, 1]$.

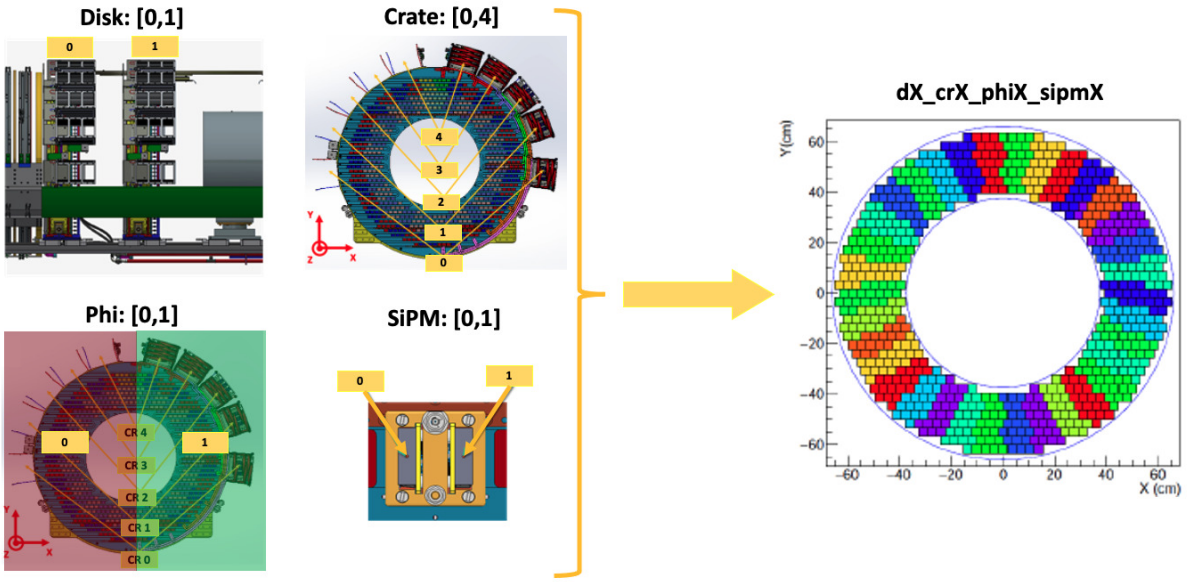

Figure 5.6: Illustration of the naming convention chosen for the Mu2e Calorimeter power supplies. On the right, the sectors resulting from the chosen sub-division of the calorimeter disks ares shown.

5.3.2 Calorimeter DCS test at LNF

A first small-scale prototype of a EPICS IOC has been developed for two PS, one HV and one LV, used at the QC Station (Sect. 4.3). In order to scale-up the IOC, the naming scheme just described in the previous section has been kept, anticipating the use of phoebusgen to easily increase the number of PVs used. This was done for the test performed at SiDet, as described in the next section.

In the IOC, a basic protocol file has been built for each device type, i.e. one for the LV PS and one for the HV. A protocol file describes the communication with a specific device type and allows to define actions on the PS using their native commands sent via TCP/IP with the use of StreamDevice. The built actions allow to read and set the voltage and the current, to turn ON or OFF the PS output and to verify its status.

As previously said, the fundamental instance in an EPICS IOC is a record. These are included in a database (.db) and/or in a template (.tpl) file. These two file types

share same characteristics, but a substitution (.sub) file can be associated to a template file. This contains the explicit record names which can remain then a variable in the tpl file. This is convenient because if there are many devices of the same type with different IP addresses, for instance, only one template is needed and their name can be explicitly written only once in the substitution file. In the specific case of the QC Station, the fictitious position of $(0, 0, 0, 0)$ was chosen for both the LV and HV, such that their names are: LV_0_0_0_0 and HV_0_0_0_0. The name and IP address of each PS have to be written in the executable file which launches the IOC. The name has to be consistent with the one indicated in the tpl and sub files.

For the calorimeter PS DCS, the voltage and the current are the main quantities to monitor. To do so, in the template file, one `ai` record and one `ao` are defined for the voltage: its value is set with the `ao` and read back with the `ai`. Analogous records are built for the current monitoring. The status of the power supply is also read: with a binary output record the device can be turned on and off, while the status can be verified with its `bi` counterpart. A further control on the voltage that the PS is supplying is done with a `calcout` record, which can monitor the difference between the set and read voltage. The duties of each record are set by the fields included in it. The fundamental ones employed in this application are:

- `SCAN`: determines when a record is processed. There are three scanning methods for database records: periodic (occurs on set time intervals), event (occurs on either an I/O interrupt event or a user-defined event) and passive (occurs when the records linked to the passive record are scanned, or when a value is "put" into a passive record through the database access routines).

- `DTYP`: device type field where the name of the device support module appears. For this application it is "stream", i.e. StreamDevice.

- `INP`/`OUT`: these fields contain the address from where device support retrieves the value. It links to the protocol file and the action that the record has to perform, like set the current value in an `OUT` field, or get the value in an `INP` field.

- Alarm status and severity: the alarm status fields allow to set a lower and upper limit on the monitored quantities (`HIHI`, `HIGH`, `LOW`, `LOLO`) and the alarm severity is used to give weight to the current alarm status (`HHSV`, `HSV`, `LSV`, `LLSV`). This is also related to how the monitored PV will appear in the GUI.

At execution of the IOC, an EPICS prompt opens and any messages for the user are printed there. The GUI built for the QC Station PS is shown in Fig. 5.7.

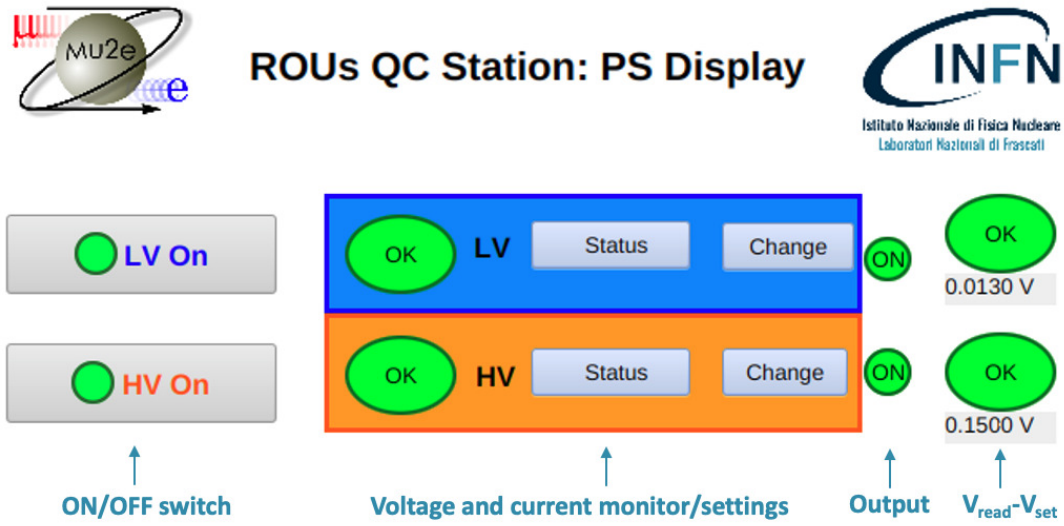

Figure 5.7: Main GUI panel of the QC Station PS DCS. In blue are indicated the meaning of the LEDs and buttons, for clarity.

The first row is dedicated to the LV while the second one to the HV. The GUI buttons and LEDs display the status of the PVs according to the parameters and methods described in their associated records. The "Status" and "Change" buttons open respectively the panels in Fig. 5.8-left and Fig. 5.8-right.

The panels shown are for the LV PS, but for the HV analogous panels have been developed. While the panel on the left simply gives further details about the PS status, the panel on the right has two additional boxes where the user can insert new values for the PS voltage and current limit. This panel is password protected to allow access only to authorised users, as indicated in the requests for the DCS calorimeter. It can also be noticed that the borders of the read V and I boxes are marked in red: this means that an alarm was raised being some of these values outside of the "good acceptance" range. The acceptance ranges for the LV, HV and currents are:

- The HV is set at 200 V and a ± 5 V range is accepted. Outside those values an alarm of increasing severity is raised. The LED and value boxes are initially coloured in orange and then red. To take into consideration colour-blind standards, "warning" is also explicitly written on the LED. A similar monitor on the current limit, by default set at 8.65 mA, is applied.

- The LV is set to 28 V with a ± 1 V tolerance. Any alarm is signaled similarly to what is done for the HV. An analogous monitor on the current limit, initially set to 0.65 A, is also applied.

- The difference $\Delta V = |V_{read} - V_{set}|$ is also monitored, considering that its value in

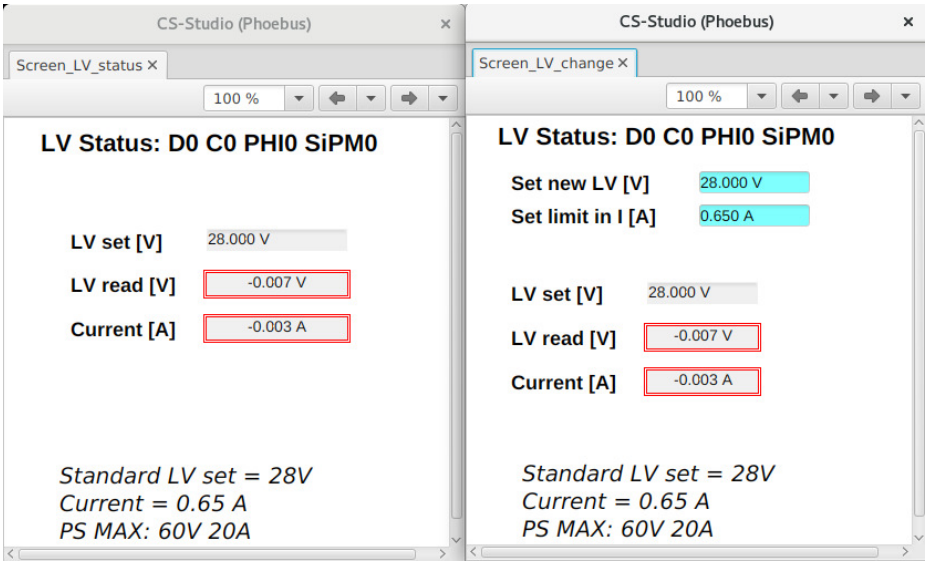

Figure 5.8: "Status" and "Change" panels of the LV PS, taken as example. The name chosen for the PS, written at the top, follows the convention that will be adopted in the final version of the calorimeter DCS.

normal conditions is $\Delta V \lesssim 0.02\,\mathrm{V}$ for the LV and $\Delta V \lesssim 0.2\,\mathrm{V}$ for the HV.

The ones here described are preliminary values and specific settings for the setup of the QC. They can be easily changed when the entire calorimeter DCS will become operational.

5.3.3 Calorimeter DCS test at SiDet

A rack with 10 HV and 10 LV PS is present at SiDet, Fermilab, in the mechanical assembly room. In the top of the rack there is an Ethernet Switch, located to allow a connection via TCP/IP to all the assembled PS. These PS will be the ones used to power each half of the calorimeter disks to carry out a cosmic ray data taking and fully survey the calorimeter and its electronics before moving it to the Mu2e Detector Hall.

A slightly modified version of the EPICS IOC and Phoebus GUI with respect to the QC station have been developed for this task. To build the GUI, phoebusgen has been used so that the Phoebus executable file is obtained directly through a Python script.

The number of PS under consideration can be increased simply changing one parameter, virtually making the produced GUI promptly ready for all the calorimeter power supplies. To connect to the PS, their IP addresses have been set and written into the IOC. The GUI used at SiDet is shown in Fig. 5.9 and a picture of the PS is shown in Fig. 5.10, where the DCS active on the computer can also be seen.

This preliminary test has proved that the DCS for the calorimeter power supplies is

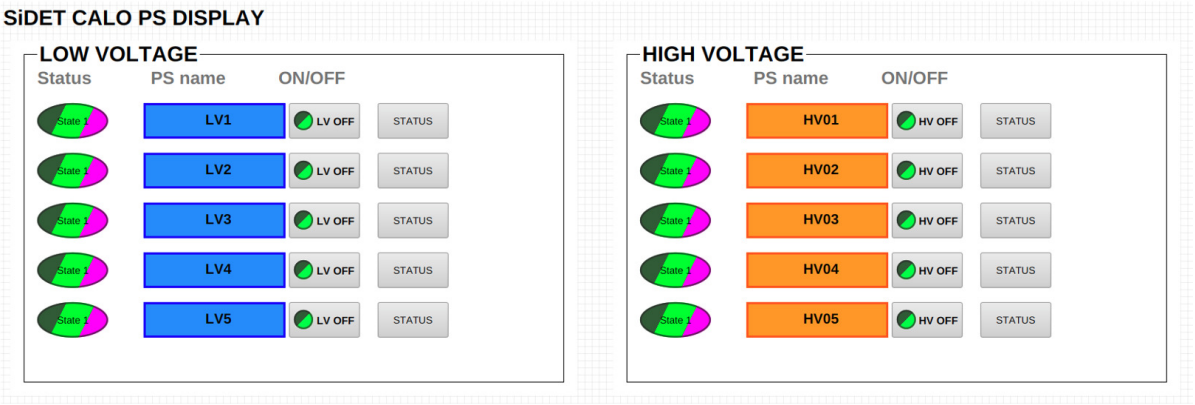

Figure 5.9: Main GUI panel of the DCS for the PS at SiDet, in edit mode.

practically available. The final step consists only in integrating it into the DCS and Mu2e Web network. On the other hand, the EPICS software is available, can communicate with many PS and can be easily scaled-up to be operative on the 80 PS of the Mu2e DAQ room. The Phoebus interface is also operative and available for all the Mu2e calorimeter PS. Following the Mu2e calorimeter DCS requirements, the PS DCS allows to monitor current and voltage parameter, thus allowing full access and parameter setting privileges only to selected experts/users.

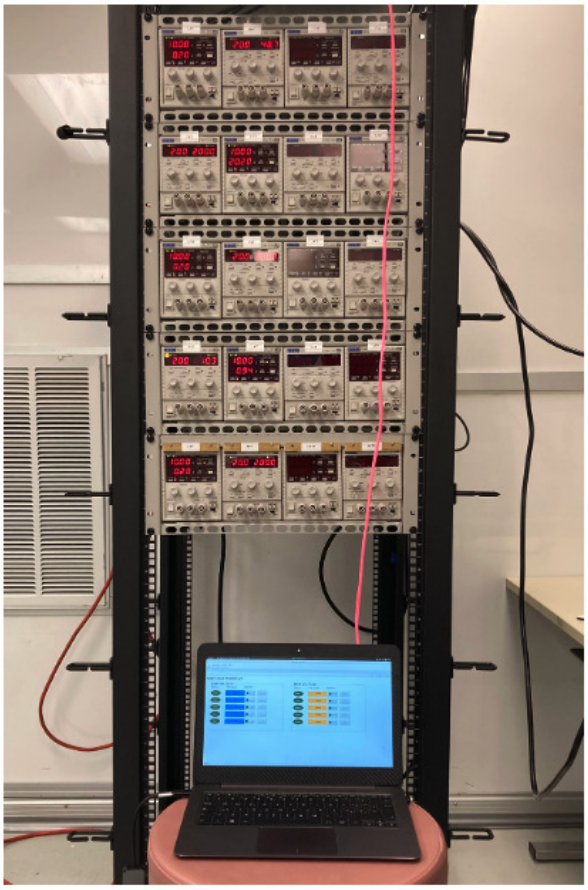

Figure 5.10: Picture of the power supplies at SiDet while the DCS was being tested.

Chapter 6

CAPHRI: using calorimetry as a tool for beam normalization

In order to achieve the Mu2e goal for a precise measurement of $R_{\mu e}$, an accurate knowledge of the normalization factor in the ratio is also needed. The experiment requirement is to measure the stopping rate with an overall accuracy of 10%, both systematical and statistical. In theory, it could be possible to perform an estimate of this number based on a model of muon production and transmission through the solenoids, but the uncertainties associated to it are too high to guarantee the needed 10% accuracy [101]. A direct measurement is surely preferred and the experiment solution is to perform this task with the Stopping Target Monitor detector (STM).

The STM is based on two different and complementary detectors: a High Precision Germanium (HPGe) detector and a $LaBr_3$ crystal detector. Both of them are located at large distance ($> 30\,\mathrm{m}$) from the exit of the Detector Solenoid, observing, along the DS axis, the X-rays emitted during the formation of a muonic atom and γ-rays associated with muon capture, both in the aluminum target. The HPGe is a very precise detector that can disentangle any unexpected line from other sources, but it is too slow to provide fast feedback to follow up in real-time the beam intensity variation expected for each beam injection cycle. The $LaBr_3$ is less precise but it is much faster than the HPGe, however due to background and dose considerations, it can perform a statistically reliable feedback only in few minutes of data taking.

In order to perform a faster and independent measurement of the normalization factor, we have studied and proposed the possibility to carry out such a measurement relying on few high LY crystals placed inside the calorimeter disk. This system has been named CAPHRI (Calorimeter Precise High-Resolution Intensity detector) and it will employ four LYSO crystals that have been already procured and characterised. Both the CAPHRI proposal and the measurement of the LYSO crystals will be described in

the following sections.

6.1 Stopping Target Monitor

As reported in Section 2.5.1, the STM will detect prompt X-rays produced by the orbital transitions of muons captured in the atomic orbit of the target nuclei and γ-rays from muon capture processes. The best choice to detect such photons is relying on High Purity germanium solid-state detectors [102]. Commercially-available Ge detectors, however, have generally to integrate the collected charge, so they are slow in their response and cannot be employed in this context given the very fast emission time of $\mathcal{O}$(ps) from the initial capture. Commercial off-the-shelf detectors can generally manage a rate 10 times smaller with respect to what is needed in Mu2e (10^5 MeV/s). Therefore, the individual X-rays from muon stops at the nominal intensity could not be detected and an event-by-event count cannot be made.

There are also issues posed by the beam-flash background from the Mu2e beam. This is an intense electron component at early times which can produce bremsstrahlung photons in the STM with a rate of 51 MHz/cm^2 and a mean energy of 1.4 MeV [33]. Many of these bremsstrahlung photons are above pair production threshold so that if they hit the HPGe detector, they can produce e^+e^- pairs and cause radiation damage. The radiation damage to an HPGe placed just at the exit of the Detector Solenoid would require annealing usually after $\sim 10^9$ n/cm^2, that corresponds from few hours to few days. Since the annealing process can take more than a day, such a configuration does not match the Mu2e schedule and is therefore not acceptable.

6.1.1 Photons detected by the STM

As muons are captured in excited energy levels of aluminum atoms, they promptly cascade down to lower energy states emitting characteristic X-rays. Captured muons also produce excited nuclei which emit γ-rays with known energies and intensities. There are three categories of events considered for the STM normalization measurement with an aluminum target:

- Prompt X-rays: emitted when the muon comes to rest in the Stopping Target (ST) and is captured into the atomic orbit ("muon stop"). These are emitted within $\mathcal{O}$(ps) from the μ-stop.
  - From $2p \rightarrow 1s$ transition at 347 keV. In 79.8(8)% of muon stops.
  - From $3d \rightarrow 2p$ transition at 66 keV. In 62.5(1.8)% of muon stops.

- Semi-prompt γ-rays: emitted upon nuclear capture of the muon after its stop. These exhibit timing characteristics of the muonic aluminum lifetime ($\tau = 864\,\text{ns}$) since the de-excitation time of $^{26}\text{Mg}^*$ is negligible (476 fs). A 1809 keV γ-ray is emitted in 50% of the cases, following the nuclear chain:

$$\mu^- + {}^{27}_{13}\text{Al} \rightarrow {}^{26}_{12}\text{Mg}^* + \nu_\mu + \text{n} \qquad {}^{26}_{12}\text{Mg}^* \rightarrow {}^{26}_{12}\text{Mg} + \gamma(1809) \tag{6.1}$$

- Delayed γ-rays: at 844 keV from long-lived (9.5 minutes half-life) activated daughters resulting from muon nuclear capture in the Stopping Target:

$$\mu^- + {}^{27}_{13}\text{Al} \rightarrow {}^{27}_{12}\text{Mg} + \nu_\mu \qquad {}^{27}_{12}\text{Mg} \rightarrow {}^{27}_{13}\text{Al} + \gamma(844) + \text{e}^- + \bar{\nu_\text{e}} \tag{6.2}$$

  This occurs in 13% (^{27}Mg production) $\times$ 72% (^{27}Mg β-decay) $\simeq$ 9% of muon captures.

Due to the high intensity and their correspondence to stopped muons, the prompt 347 keV X-rays are ideal candidates for the STM measurement. However, there are many neighbouring peaks, such as the $3p \rightarrow 1s$ and the $4p \rightarrow 1s$ transitions, which require a high precision detector to be resolved. Furthermore, there are the bremsstrahlung photons from the beam flash during the early part of the X-ray distribution which can cause dead time in the detector.

The 1809 keV γ-ray is the so called "golden line" and it has been established from data of the AlCap experiment at PSI [103] that there are no significant contaminant peaks near it [104]. This allows for the use of a lower resolution detector with higher rate capability, for example $LaBr_3$(Ce) or high-LY LYSO crystals. This line has the advantage of being directly proportional to the muon capture rate as a function of time. Since its characteristic time is that of the muonic Al, the measurement window of the Mu2e main detectors can be fully exploited. A different time window for the Mu2e measurement normalization factor would have to be carefully weighted to avoid introducing a systematic uncertainty in its comparison with the signal window.

The 844 keV is appealing because of its time characteristics. The excited ^{27}Mg beta-decays to an excited state of ^{27}Al with a half-life of 9.5 minutes. The excited ^{27}Al in $\sim 35\,\text{ps}$ emits the 844 keV photon that can then be detected. The experiment could use the macro-structure of the beam and use the long "off" period (the 0.8 s when the beam is delivered to NOνA, as described in Section 2.3) to avoid rate problems and to perform a measurement of the delayed photons with a better S/B ratio [105].

These processes are summed up in Fig. 6.1.

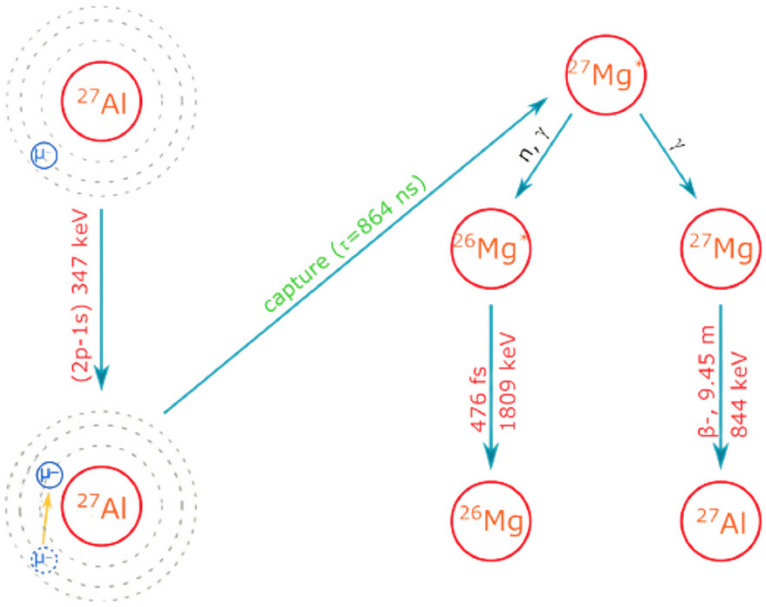

Figure 6.1: Scheme of the decays which produce the X-rays and γ-rays detectable by the STM. The figure does not cover all the existing processes [105].

The AlCap photon spectra

The upcoming experiments probing CLFV with μ^-, in particular COMET and Mu2e, must well understand all the processes occurring when a negative muon is captured in a stopping target. The existing information of these processes is not directly usable by these experiments since they refer to either too high energy ranges or to a different target material (both experiments use aluminum).

To measure the rates and the spectra of particles emitted after nuclear muon capture, members of COMET and Mu2e collaborated on a common experiment, AlCap, whose goals are to perform the measurement of:

1. The emission of heavy charged particles following nuclear muon capture.
2. The neutron yield after muon capture.
3. The muonic X-rays and γ-rays needed for the normalization of the stopping rate in aluminum.

The latest measurement was accomplished using a HPGe crystal and a $LaBr_3(Ce)$ scintillator very similar to those under consideration for Mu2e. The results AlCap obtained for the photon spectra are shown in Fig. 6.2. In Table 6.1, the emission rates for the aforementioned processes measured by AlCap are presented.

AlCap has also successfully measured the possible backgrounds that can manifest as peaks very near to the energy of the interesting lines for the muon to electron conversion

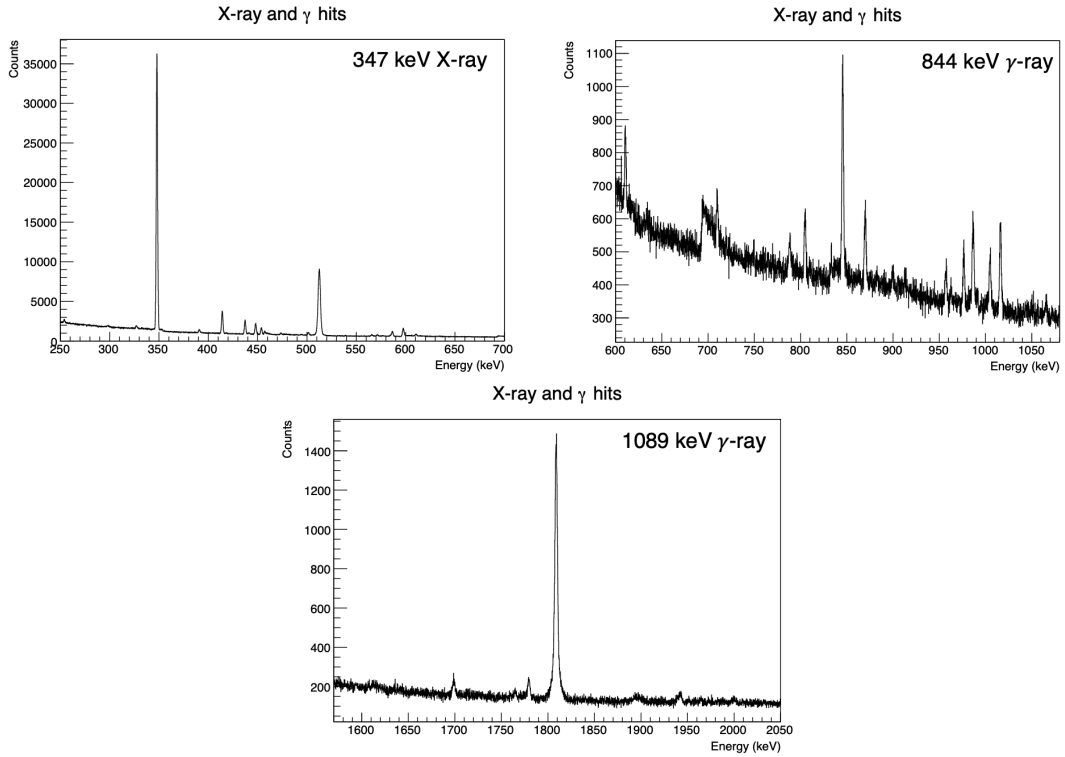

Figure 6.2: Data from the AlCap experiment detailing the prominent 347 keV, 844 keV and 1809 keV peaks [106].

search. These background lines are reported in Table 6.1. Notice that, in proximity of the 1809 keV line, no significant background was found.

Line	Emission rate (% μstops)	Background	Bkg energy
347 keV	79.8%	Pb(μ,ν,...)^{207m}Tl	351 keV
		Natural Pb decay	352 keV
		W(μ) $5g \rightarrow 4f$	351 keV
844 keV	4%	Al(n,n'γ)	844 keV
		Fe(n,n'γ)	847 keV
		Fe(μ, n, ...)^{56}Mn	847 keV
1809 keV	30%	none	/

Table 6.1: Table summing up the AlCap results for the emission rate of the photons the STM will detect and the background lines close in energy [104].

6.1.2 STM design and position within the DS

As explained before two different detectors compose the STM system:

1. A high-purity germanium detector to measure both X-rays and γ-rays, but mainly the 347 keV and 844 keV lines, which require a good energy resolution due to the

presence of nearby contamination. The detector resolution of about 2.2 keV FWHM at 1.33 MeV will be sufficient to resolve each of the signal lines from the neighboring background lines.

2. A large $LaBr_3$ crystal with PMT read-out. This crystal has an energy resolution ~ 10 times poorer compared to the HPGe, but a much higher rate capability. For this reason it is well suitable for measuring the 1.81 MeV line albeit it can provide interesting rate comparisons for the lower energy lines.

At the moment of writing, the final design is under active development to complete the read-out and the shielding.

The STM is located at the most downstream end of the DS area, about 34 m from the Stopping Target, reducing the measuring rate of $1/d^2$, with d the distance from the ST to the detector. A series of collimators and a sweeping magnet are designed to reduce background rates in the HPGe in order to make the radiation damage and acquisition rates more manageable. Travelling downstream, some of the windows and shielding elements that the particles will meet are:

- Polyethylene at the end of the Muon Beam Stop (MBS) where there is a hole centered on the axis of the DS to allow the punch-trough of the photons for the STM.
- A thin mylar vacuum window in the Instrumentation Feed-through Bulkhead (IFB).
- The ~ 91 cm thick concrete DS End-Cap Shield (ECS).
- Stainless steel shields.
- A 1 m long, 500 gauss permanent magnet to sweep away charged. Particles which could otherwise hit the HPGe at high rates.
- A 45 cm long Pb collimator.
- An air gap and the last Pb shielding and collimator just close to the STM detectors.

The HPGe is slightly offset with respect to the DS solenoid axis to allow the installation of a second detector (HPGe or $LaBr_3$). In Fig. 6.3 a rendering of the DS region up to the location of the STM is shown.

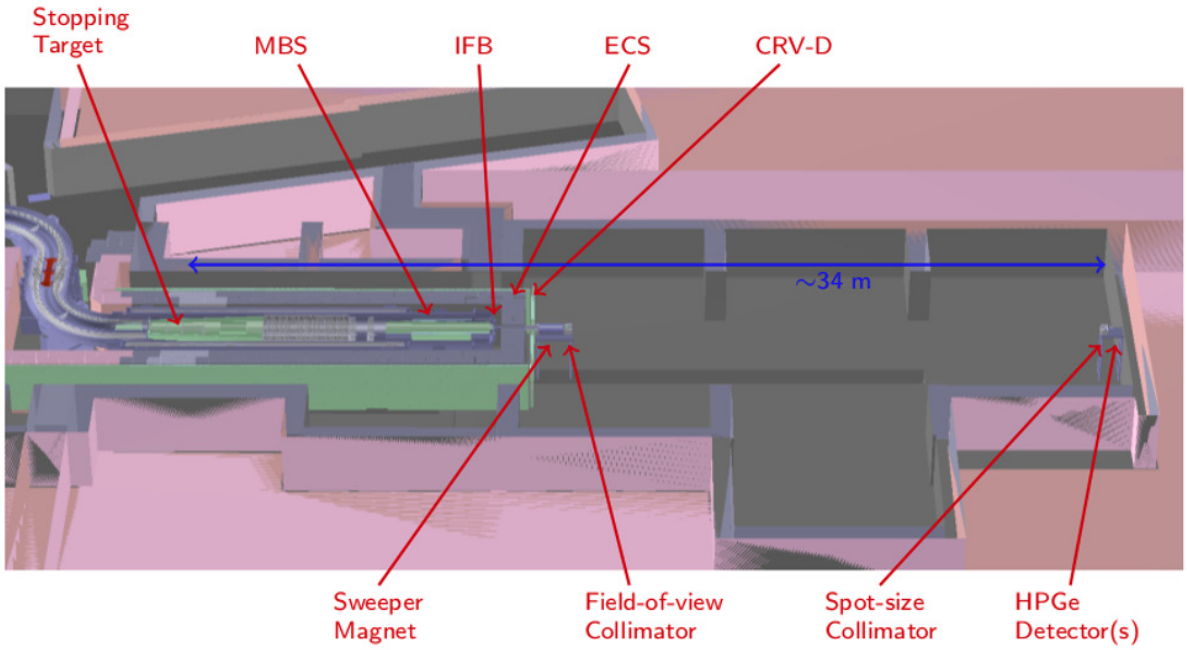

Figure 6.3: Graphical 3D rendering of the top view of the DS and the region where the STM will be placed. The main elements are indicated. CRV-D indicates the CRV downstream side.

6.2 Design and requirements of CAPHRI system

The Mu2e Calorimeter team has proposed the idea to perform an independent and faster measurement of the $R_{\mu e}$ normalization factor using high-LY crystals placed into the upstream calorimeter disk.

The first goals were to evaluate the precision of the measurement that CAPHRI could perform, its dependence on the Proton Bunch Intensity (PBI) and if the PBI variation could be measured with the calorimeter in the same time. Indeed, these questions are relevant for the experiment and are motivated by several considerations:

- The STM will need several minutes to measure the Muon Capture Rate (MCR) with $\mathcal{O}(10\%)$ precision, looking at the 1.8 MeV line. When comparing with CAPHRI final precision, this will be referred to as "golden line". In the following is shown that CAPHRI can provide a high precision measurement on MCR for each injection cycle (1.4 sec).

- The PBI intensity varies inside a spill not in a randomic way, but in a correlated matter showing msec-like structure, as evaluated by simulations carried out by the accelerator team.

- The reconstruction efficiency, like the tracking of the CE or the CRV reconstruction,

shows some dependencies on the PBI. This implies that the PBI has to be evaluated for each pulse in order to provide a correction for the final normalization factor provided by the STM.

There are a lot of parallel efforts that want to use independent information to tackle these same questions, like using the hits in the tracker straws or in the calorimeter to evaluate the PBI variation and timing. These studies do not bring any direct information on the MCR, so another suggestion would be to perform an additional MCR measurement directly from the counting of protons. While these are all viable alternatives, the calorimeter can provide its own contribution to this kind of measurements so that the comparison and correlation among all these studies will improve the knowledge on normalization and reduce the related systematics.

6.2.1 Crystal choice and positioning

The basic idea behind CAPHRI is to use four high LY crystals to measure the 1.8 MeV γ line. The calorimeter pure-CsI crystals do not have a resolution high enough at those energies, so two more performing crystals were taken into consideration: LYSO (from SICCAS) and $LaBr_3$ (from Saint-Gobain). Details about these crystals characteristics have been reported in Appendix A and Appendix B. The positioning of the crystals within the disk was object of many studies and a final decision has not been yet reached at the moment of writing. There are some considerations that allowed to narrow down the possibilities and constrain the crystal dimensions and choices:

- The crystals have to be inserted in the calorimeter Disk0, i.e. the upstream disk, since it is the only one having a good acceptance for photons coming from the Stopping Target.
- It is preferable to place these crystals at high radius to reduce mixed-background contamination coming from the beam;
- Studies of the background led to choose a symmetric configuration in the X and Y directions (the XY plane is the plane of the calorimeter disk face).
- An "up and down" symmetry is preferable since it allows to check the rate difference between background distributions.
- The interference of these crystals with the standard calorimeter operations and reconstructions (e.g. clustering algorithms or cabling) has to be minimised.

- The transversal dimension of the crystals is limited to $34 \times 34\,\mathrm{mm}^2$ to avoid affecting the calorimeter assembly strategy.
- The maximum length available is 20 cm for the LYSO and 7.5 cm for the $LaBr_3$ (for production reasons).
- No coupling grease will be used to put in optical contact the crystals and the sensors in order to keep the same quality and electronics of the CsI crystals read-out.

In Fig. 6.4, two possible configurations of the CAPHRI crystals, satisfying the aforementioned requirements, are shown.

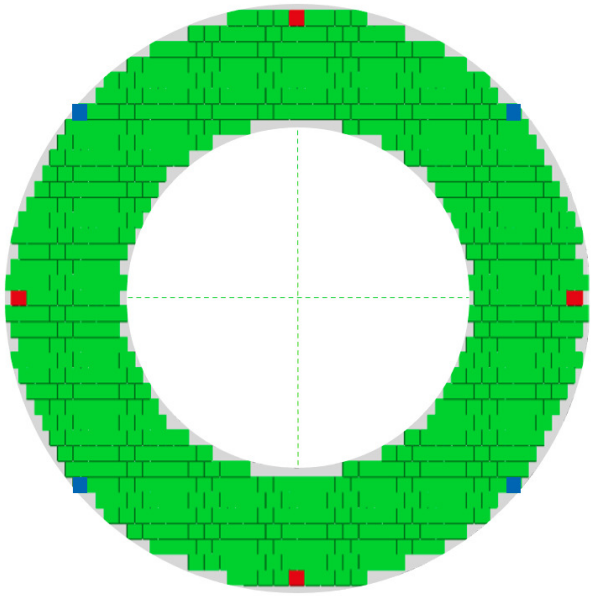

Figure 6.4: Graphical rendering of the calorimeter disk with two possible configurations of the four CAPHRI crystals, indicated in red for one and in blue for another configuration.

Preliminary estimate of the crystal performance

To achieve a more accurate signal simulation of the 1.8 MeV line, some preliminary measurements have been done on one LYSO and one $LaBr_3$ crystal, using a ^{22}Na source to measure the response at 511 keV (see Appendix C for a description of the ^{22}Na decay). The SiPMs used to read-out the signal were operating at their V_{op}, with a gain of 1.7×10^6 and a further factor 2 amplification added by the electronics.

The tested LYSO crystal (from SICCAS, $30 \times 30 \times 130\,\mathrm{mm}^3$) was wrapped with a 3M Enhanced Specular Reflector (ESR) super-reflective foil [107]. The read-out was performed with two Mu2e custom SiPMs coupled to the Mu2e calorimeter front-end boards. The crystal-SiPM coupling was done in air. The tagger for the ^{22}Na source was

a $3 \times 3 \times 20\,\mathrm{mm}^3$ LYSO crystal, read-out with a $3 \times 3\,\mathrm{mm}^2$ standard MPPC. The tagger signal and the mean charge of the read-out SiPMs obtained for the 511 keV photon are shown in Fig. 6.5. The resolution obtained is $\sigma/\mu = 7.7\%$, which is then 6.7% subtracting the noise contribution in quadrature.

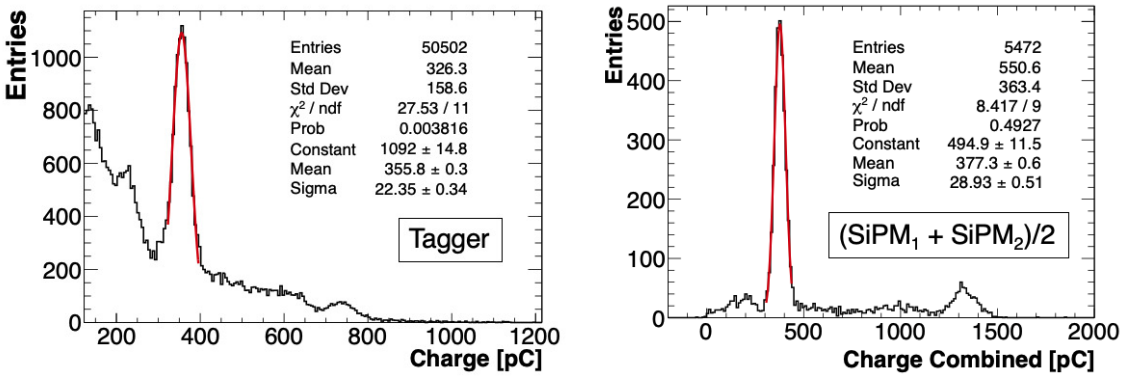

Figure 6.5: Tagger (left) and mean SiPM charge (right) for the 511 keV ^{22}Na photon detected by the LYSO crystal.

The tested $LaBr_3$ (Saint-Gobain) crystal was a cylinder with a diameter of 38 mm and 38 mm long, placed in an aluminum box with a transparent optical window for the coupling to SiPMs. The read-out, the tagger and the general setup were the same as used for the LYSO. The shape of this crystal made it difficult to obtain a perfect coupling and also the data acquisition setup did not allow for a high enough statistics. The obtained charge peak is shown in Fig. 6.6. The final resolution of the combination of the two SiPMs is 3.2%, without the subtraction of the noise contribution.

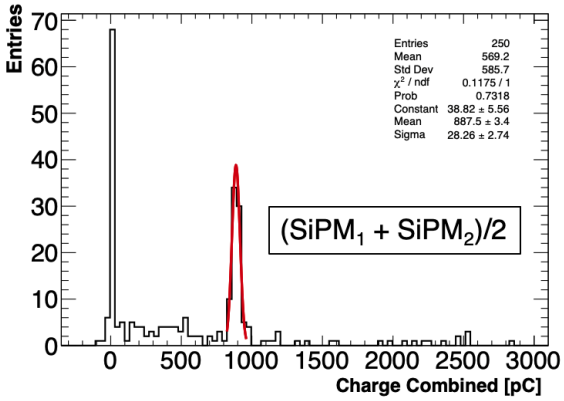

Figure 6.6: Mean SiPM charge for the 511 keV ^{22}Na photon detected by the $LaBr_3$ crystal.

6.2.2 Simulation of CAPHRI signal and background

Two main simulations were carried out in order to evaluate the expected sensitivity and acceptance of CAPHRI and to help perform a downselect on the crystal type. First of all, a preliminary simulation of a single $30 \times 30 \times 75\,\mathrm{mm}^3$ $LaBr_3$ crystal was done assuming the photons generated isotropically within a solid angle cone of 1 degree. The average acceptance between photons coming from the closest and furthest ST foils is 3.7×10^{-7}. A $\sim 3\%$ reduction is obtained when an absorber is added.

A more detailed simulation with Geant-4 was done in order to understand the acceptance changes for the various configurations. 10^7 events at 1.8 MeV were generated from a point-like source from different target foils. For the reconstruction and evaluation of the photo-peaks, an annular ring around the mean radius of the considered crystals of $\pm 25\,\mathrm{mm}$ was used. Four crystal configurations were simulated:

- A $34 \times 34 \times 75\,\mathrm{mm}^3$ $LaBr_3$ crystal (useful also to compare this simulation with the previous one performed).
- A LYSO crystal with the same dimensions as the $LaBr_3$.
- A $34 \times 34 \times 200\,\mathrm{mm}^3$ LYSO crystal to match the CsI dimensions, but isolated in the space.
- A $34 \times 34 \times 200\,\mathrm{mm}^3$ LYSO crystal surrounded by pure CsI crystals.

The crystals positions considered were those shown as the red configuration of Fig. 6.4. The obtained total efficiency for the $LaBr_3$ has an optimal agreement, of few %, with the previous simulation. We first evaluated the efficiency of the photo-peak reconstruction (ϵ(PP)) in the given crystal configuration, i.e. the number of 1.8 MeV photons that were fully reconstructed over the generated ones in the ring. We then calculated the geometrical acceptance of getting a photon from the target in the annular ring area. The total acceptance for the photo-peak (A_{tot}(PP)) is then estimated as the product of these two variables. In Table 6.2, the results of the simulation for the LYSO and the $LaBr_3$ are reported. The final total efficiency is then obtained as the mean of the results for the nearest and furthest foils in the stopping target. In more details, the nearest target position is at 5719 mm from the calorimeter, along the Z direction, while the furthest point is 800 mm further away. The annular region considered is in a region with a radius, from the center of the calorimeter disk, of $587.4 \div 637.4\,\mathrm{mm}$, for which one obtains a geometrical acceptance factor of 4.67×10^{-4} for the nearest, and 3.57×10^{-4} for the furthest target.

Quantity	**$LaBr_3$**	**LYSO**	**LYSO**	**LYSO**	**LYSO**
Crystal length	7 cm	7 cm	20 cm	20 cm	20 cm
Target position	near	near	near	near	far
Total Events	61513	69814	92310	97094	97665
Photo-Peak (PP)	11361	26730	32534	29990	30047
ϵ(PP)	1.13×10^{-3}	2.67×10^{-3}	3.25×10^{-3}	2.99×10^{-3}	3.00×10^{-3}
A_{tot}(PP)	$5.27(0.05) \times 10^{-7}$	$1.24(0.01) \times 10^{-6}$	$1.50(0.01) \times 10^{-6}$	$1.39(0.01) \times 10^{-6}$	$1.07(0.01) \times 10^{-6}$

Table 6.2: Table summing up some results from the CAPHRI simulation. All the data refer to a crystal in the same position among the 4 possible. The near target position is at 5719 mm from the calorimeter, along the Z direction, while the far point is at 6519 mm.

As can be observed, the LYSO performed > 2 times better than the $LaBr_3$. Variations in the performance can be attributed to the different density of the two crystals and the different lengths. Varying the position of the crystals, a change of $1\% \div 2\%$ in the total acceptance can be seen. The effect of the surrounding CsI crystals is not negligible and appears as an acceptance decrease of $\sim 7\%$. A very important result concerns the crystal length, since a 10% improvement is seen when the 20 cm LYSO is considered. In Fig. 6.7-top, the simulated signal of a 10 cm LYSO, surrounded by CsI, for the photons coming from the nearest or furthest foils is shown. The signal for the $LaBr_3$ is also shown in the bottom plot.

To evaluate the signal over background (S/B) for the identification of the 1.8 MeV line, we have used as background 500000 events from the MDC2018 Mu2e data samples, where minimum bias (machine) background events were simulated and fully reconstructed. The event selection was done by requiring at least 2 hits in the CAPHRI crystals, both with an energy deposition $E > 1$ MeV and at a time $t > 500$ ns from the proton pulse arrival. The events were normalised considering that the minimum bias simulation used was equivalent to 1.25 beam-on injection periods. The fit to the background shape around the signal region ($1.5 \div 2.1$ MeV) is well represented by a simple exponential law. To check the detector behaviour for higher intensity/pulse or, equivalently, for a higher number of spills, a Toy MC has been developed. The MC used the fit parameters obtained from the MDC2018 background data to random generate samples of larger statistics. The resulting background for the Toy MC and for MDC2018 are shown in Fig. 6.8-left, while the behaviour of the background shape for the different crystal positions is shown on the right plot.

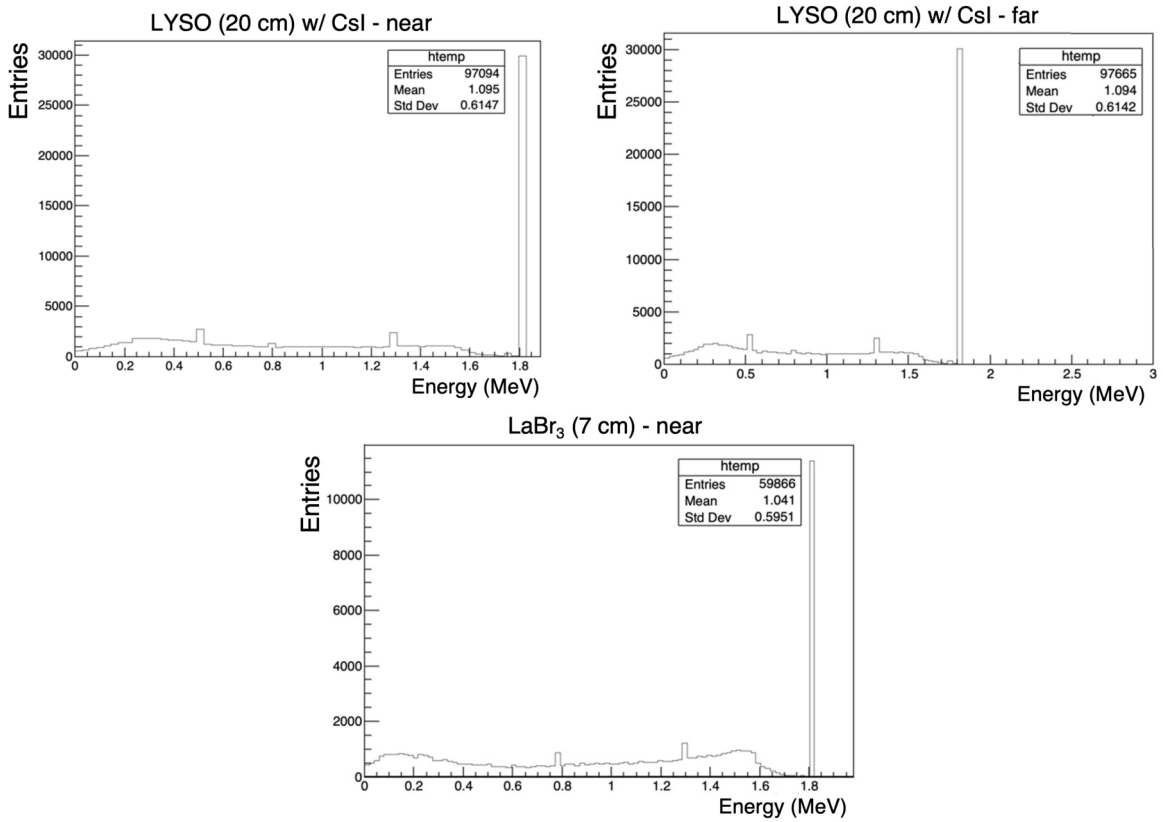

Figure 6.7: Signal peaks for three configurations of CAPHRI.

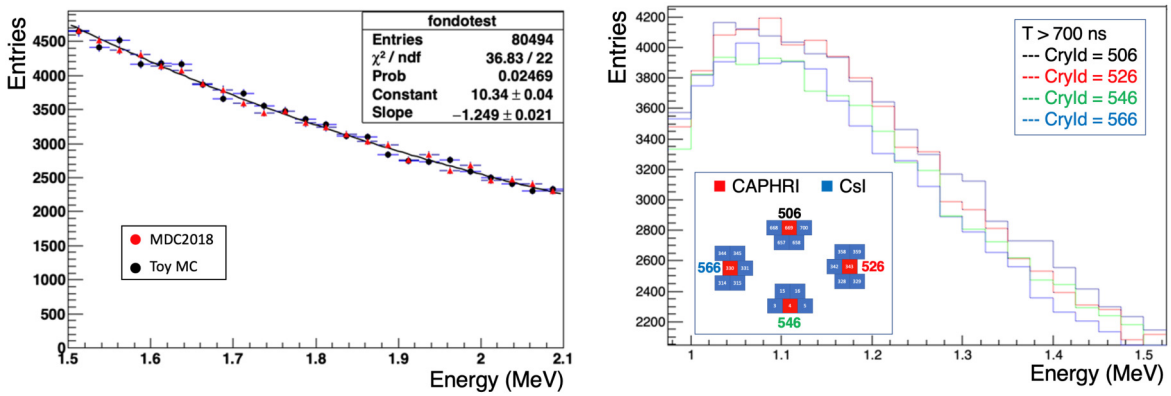

Figure 6.8: Left: Comparison between the Toy MC and the Mu2e simulation of the background data. Right: Difference in the background contribution for the four CAPHRI crystal positions. The considered positions are indicated and correspond to the red configuration of Fig. 6.4.

To complete the S/B determination, the signal sample has been evaluated considering the photo-peak efficiency previously reported, the number of POT used for the background generation and a 50% probability to have the "golden line" generated for each muon capture. The signal shape has been over-imposed to the simulated back-

ground by smearing the 1.8 MeV line with the expected energy resolution, thus yielding the plots of Fig. 6.9. The S/B ratio obtained is of the order of 1/4 in the signal region. In 1.25 beam-on periods, i.e. in a live time of 1.75 seconds, the achieved resolution on the MCR signal counting is of around 3% for the LYSO, and 5% for the $LaBr_3$. Counting rates in $1 \div 2$ ms time window will be very challenging for CAPHRI since the rates will not be enough for a good monitor. A 10 ms integration time still offers a 20% resolution, which is encouraging.

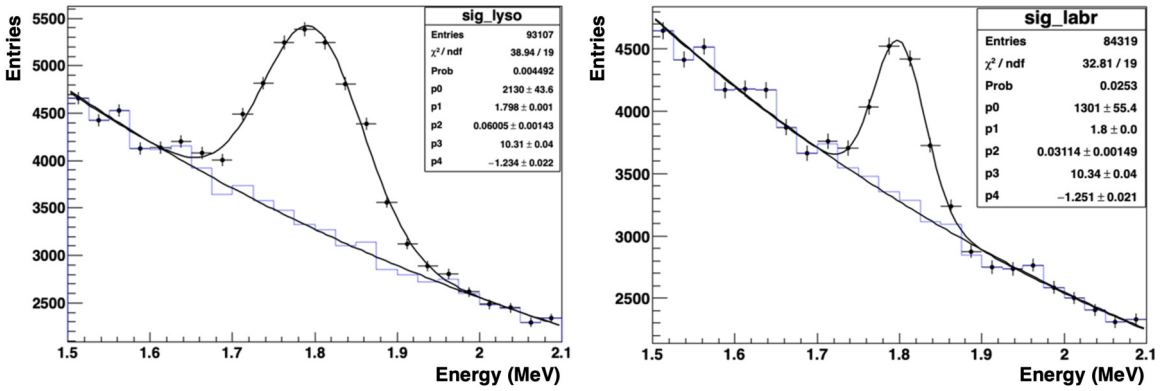

Figure 6.9: Simulated signal and background for CAPHRI LYSO (left) and $LaBr_3$ (right) crystals.

The LYSO crystal has performed better than $LaBr_3$ in the simulations due to its higher density and larger dimensions. Furthermore, LYSO offers less technical challenges due to the high hygroscopicity of the $LaBr_3$. These considerations lead to the choice of LYSO as the crystal for CAPHRI, with SICCAS as basic supplier. Four LYSO crystals, with same length and transversal section of the pure CsI crystals, were procured. This geometry allows using the same calorimeter read-out and avoid any modifications to the crystals stacking scheme.

6.3 LYSO crystals characterisation at Fermilab

The procured LYSO crystals are shown in Fig. 6.10. By-eye inspection of the crystals showed some imperfections or inclusions. One crystal looks to be worse than the others and discussions are on going with the supplier to get a replacement, based also on its performance. The crystals have been wrapped with high reflection efficiency foils (3M ESR) and equipped with the same 3D printed plastic frames used for the CsI crystals.

The wrapped LYSO crystals have then been characterised at SiDet. For each crystal, a multi-position scan with a ^{22}Na source is performed, reading out on both sides of each crystal, one at the time. In the following, the two sides will be referred to as side-a

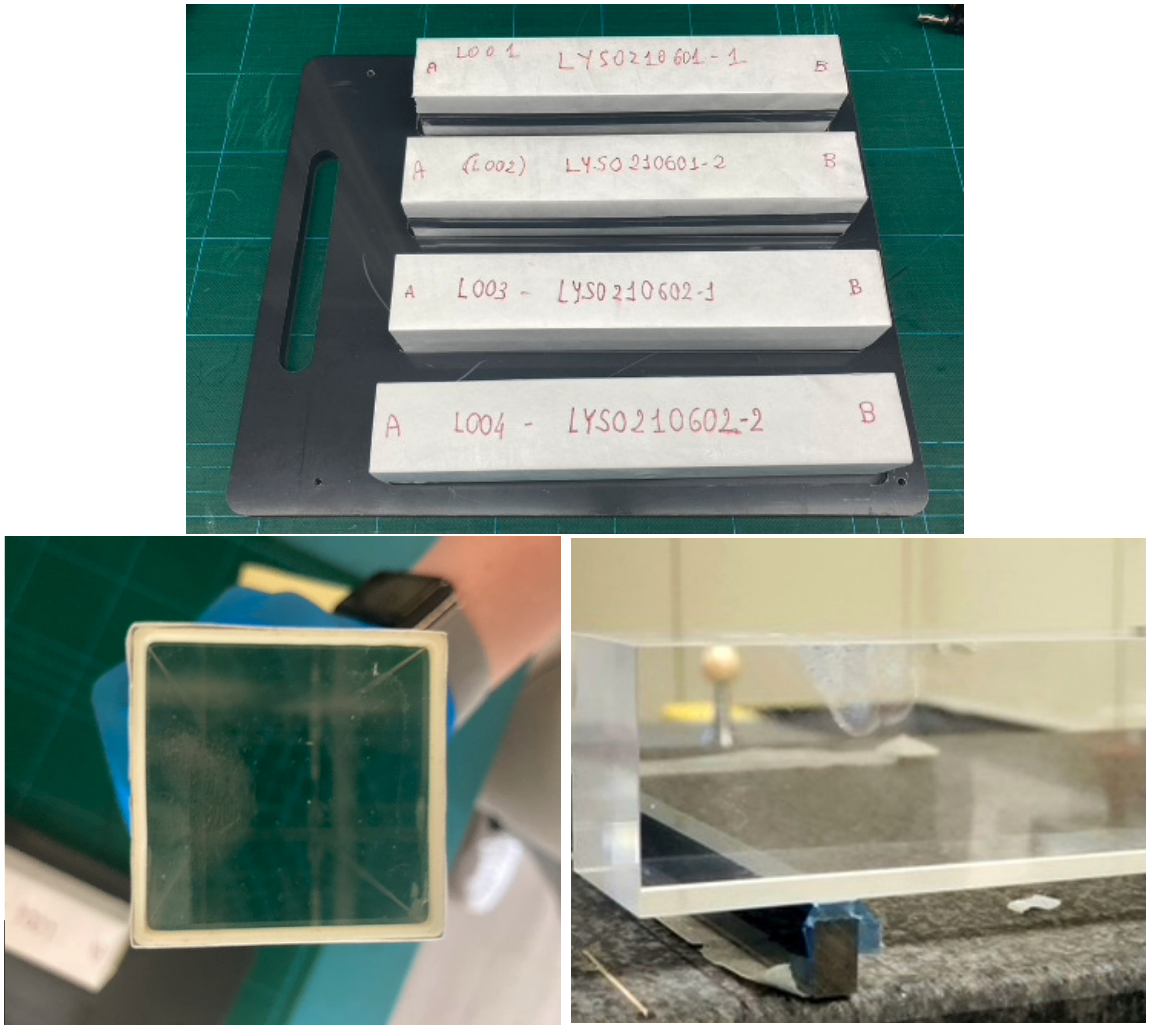

Figure 6.10: Pictures of the CAPHRI LYSO crystals. In the bottom row, the 3D printed plastic frame can be seen on the left, while the crystal before wrapping is shown on the right where also an inclusion can be seen.

and side-b. As a first preliminary measurement of the crystal performance, a large-area PMT was used to read-out the scintillation light. In a second stage, and in order to get a better estimate of the final results, the measurement was repeated reading them out with the Mu2e SiPMs. The achieved results on both configurations are presented in the following subsections.

6.3.1 Measurements with a PMT at the crystal QC Station

A first characterisation of the CAPHRI LYSO crystals has been performed with the crystal QC Station at SiDet (see Section 3.2.1).

Experimental Setup

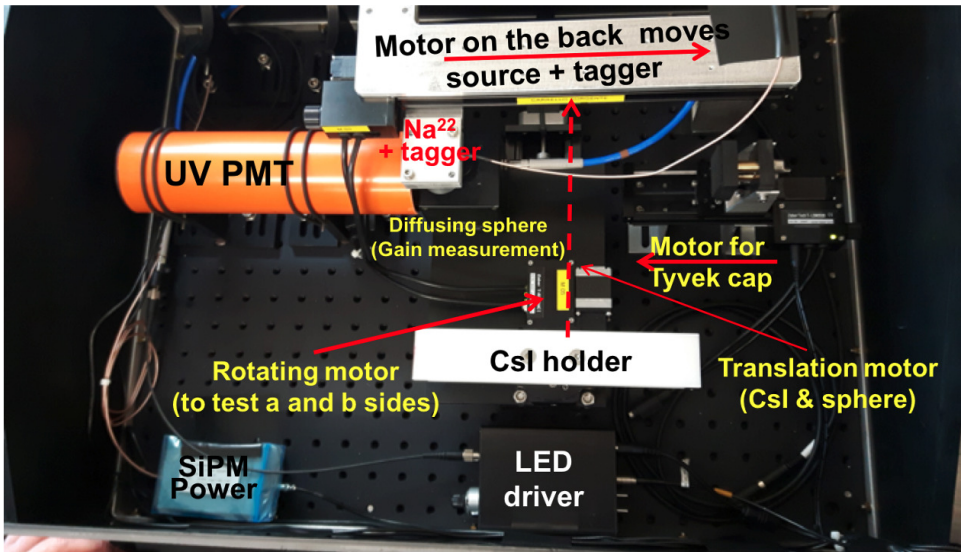

Figure 6.11: Picture of the QC Station of the Mu2e crystals used for the CsI and the 4 CAPHRI LYSO crystals. The main components are indicated.

A picture of the crystal QC station is shown in Fig. 6.11. The crystals were wrapped in Tyvek on all faces except for the read-out one. The read-out was performed with a large-area UV-extended PMT through a 2 mm air gap, without any optical grease nor glue. The PMT gain was measured before the crystal characterisation to allow following its variation over time. This was done with a LED emitting at 350 nm, driven with a CAEN LED driver, fired at 100 Hz. The obtained values for the PMT gain were compatible with 4.6×10^6.

The crystal under test gets inserted in a perfectly-fit holder which can be positioned at the centre of the PMT face. A Tyvek cap is then moved into position to cover the open side of the crystal. The fact that the cap is not fixed allows to use an automated procedure to measure both crystal sides. A ^{22}Na source is positioned on top of the crystal and it is moved at pre-defined positions along its length. The source is placed inside an Al holder which also acts as a collimator. Above the source, a small LYSO crystal ($3 \times 3 \times 10\,\text{mm}^2$) connected to a $3 \times 3\,\text{mm}^2$ SiPM is placed. The SiPM signal is used to tag one of the two ^{22}Na annihilation photons at 511 keV, as well as for triggering. For each read-out side, 8 positions are measured and the entire data-taking phase on one crystal is automated thanks to a LabView controller program. The same program also drives the data analysis in real time, allowing to get a complete result on the crystal in few tens of seconds after the completion of the scan. The total time needed to measure both crystal sides is $\sim$ 20 minutes. The sampling frequency is 250 kHz and the data is acquired for 4 μs after the trigger.

Results of the analysis

In Fig. 6.12 the wave profile of the tagging system (left) and of the LYSO crystal under test (right) is shown. The red vertical lines indicate the integration region used to evaluate the collected charge.

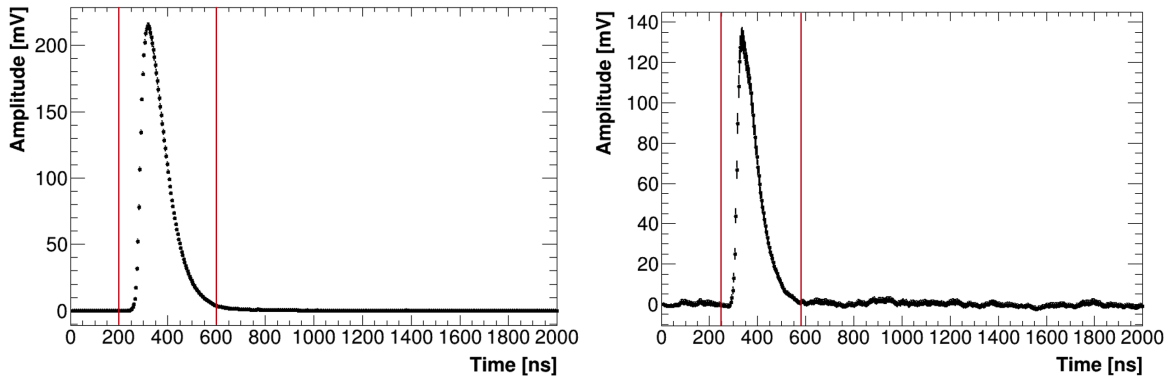

Figure 6.12: Left: Digitized waveform of the LYSO tag system. Right: Digitized waveform produced by the 511 keV photon in the LYSO crystal. The red lines represent the integration range.

An example of the resulting tagger charge distribution is shown in Fig. 6.13-left. The peak is fitted with a Gaussian to extract the distribution standard deviation. This information is used to perform a cut on the selected events in a range $\pm 2\sigma$ around the tagger peak. To exclude accidental coincidences, a cut on the mean time (T_{mean}) is also applied at $\pm 3\sigma$ (Fig. 6.13-right). In Fig. 6.14, an example of the charge collected by the PMT after the two aforementioned cuts, is reported. The spectrum looks very clean and the 511 keV photon lines are clearly visible.

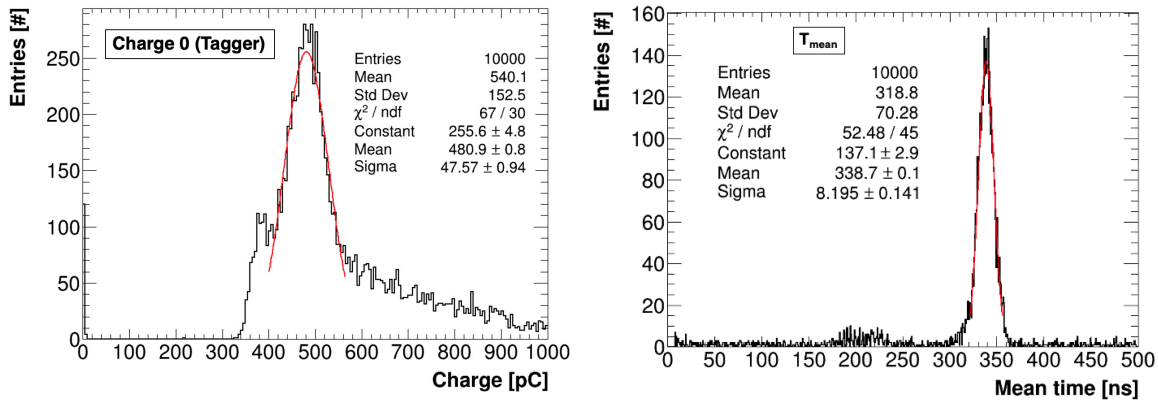

Figure 6.13: Left: charge distribution of the LYSO-tagger system. The fit is a Gaussian function. Right: Time distribution mean value, fitted with a Gaussian function.

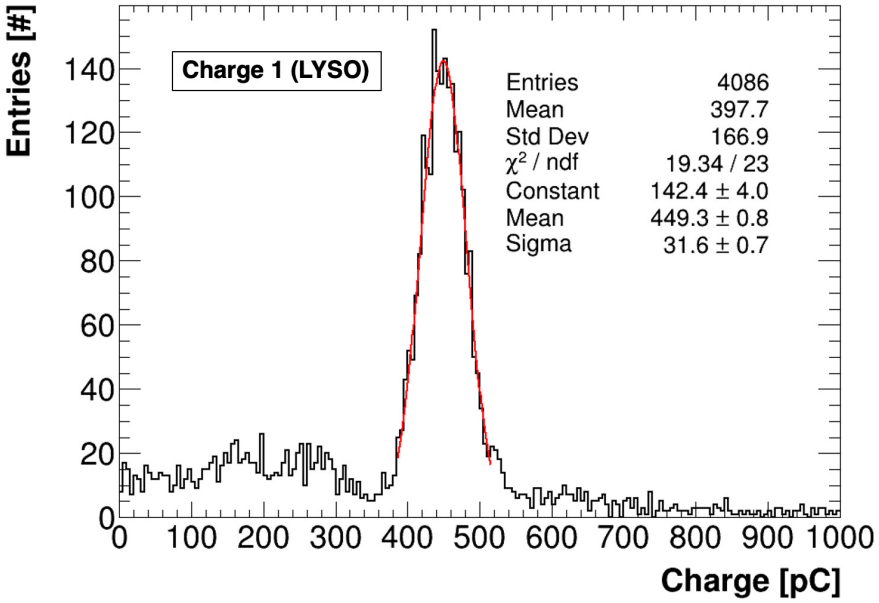

Figure 6.14: Example of the charge collected by the PMT with the cuts applied on time and on the tagger charge peak.

Since the number of photoelectrons follows Poisson statistics, the Light Yield can be calculated with the formula:

$$LY = \frac{\mu_Q}{G_{PMT} \times E_\gamma \times q_e} = \frac{NPE}{MeV}, \tag{6.3}$$

where G_{PMT} is the PMT gain at the operational voltage, E_γ is the energy of the ^{22}Na photon and q_e is the elementary charge of the electron.

The Longitudinal Response Uniformity (LRU) represents the variation of the response along the crystal axis and it is estimated by the RMS of the eight LY values, each one measured at a 2 cm distance from the other. The intrinsic energy resolution of the crystal (σ_Q/Q) at 511 keV is obtained by performing a Gaussian fit to the ^{22}Na photon peak of each charge spectra of the longitudinal scan and averaging the obtained resolutions. The plots in Fig. 6.16 show the LY for every position, while in Fig. 6.17 the resolution is shown. These distributions are very promising, showing a good uniformity along the crystal axes and a good consistency in the overall performance. Some deviations are observed in the measurements done in the last position (position 7) for almost all crystals. This somehow affected the evaluation of the overall crystal resolution, especially for crystal L003. This effect was attributed to a problem of the acquisition setup, further motivating a more dedicated measurement carried out with a readout with Mu2e SiPMs, described in the next section.

In Table 6.3 a summary of the results for the four crystals with PMT readout can be

found.

Crystal	**Side**	**<LY>**	**LRU**	$<\sigma/\mu>$
L0001	a	1116	0.033	7.39(.22)%
L0001	b	1168	0.024	7.16(.22)%
L0002	a	1003	0.024	7.33(.22)%
L0002	b	1004	0.042	7.51(.22)%
L0003	a	935	0.039	8.01(.24)%
L0003	b	960	0.037	8.11(.24)%
L0004	a	1167	0.043	7.25(.22)%
L0004	b	1223	0.029	7.26(.22)%

Table 6.3: Summary table of the LYSO crystal performance. The columns report: the crystal number, the side of the crystal, the mean LY over all positions (expressed in photoelectrons/MeV), the LRU and the average resolution over the 8 positions. Measurements are taken with the PMT.

In order to estimate the noise contribution in the used setup, the signal baseline has been evaluated in a region far from the signal, i.e. $2000 \div 3000$ ns. The observed baseline RMS is ~ 5 mV for all crystals, except L004 for which it is ~ 10 mV. We conclude that the contribution of the system noise, considering that the LYSO peaks correspond to pulse heights of ~ 200 mV, remains of the order of $\sim 2 \div 4\%$ and is therefore negligible on the energy resolution of the crystal. The dominant resolution term is therefore attributed to the stochastic one. Finally, in Fig. 6.15 the FT ratio measured for all crystals is presented. The "fast" contribution has been integrated for a 200 ns window around the signal peak (peak$-$40 ns to peak+160 ns). The "total" value is obtained integrating for 3μs. The obtained result well follows the expected behaviour and is consistent with a LYSO decay time of $\tau \simeq 45$ ns.

From these first measurements, two best performing crystals (L001 and L002) were identified. A decrease with respect to the previously quoted LY of > 2000 photoelectrons per MeV is observed [108]. These losses were due to the wrapping in Tyvek and to the the insertion on the frames that added a contribution to the LY loss of the order of 15%. A study of the LYSO response with different wrapping materials was performed and is reported in Appendix D, where it is clearly indicated that the usage of 3M ESR foils represents the best choice. In order to verify this, we have done a new measurement of the CAPHRI setup with the full Mu2e read-out and with an improved ESR wrapping, as described in the next section.

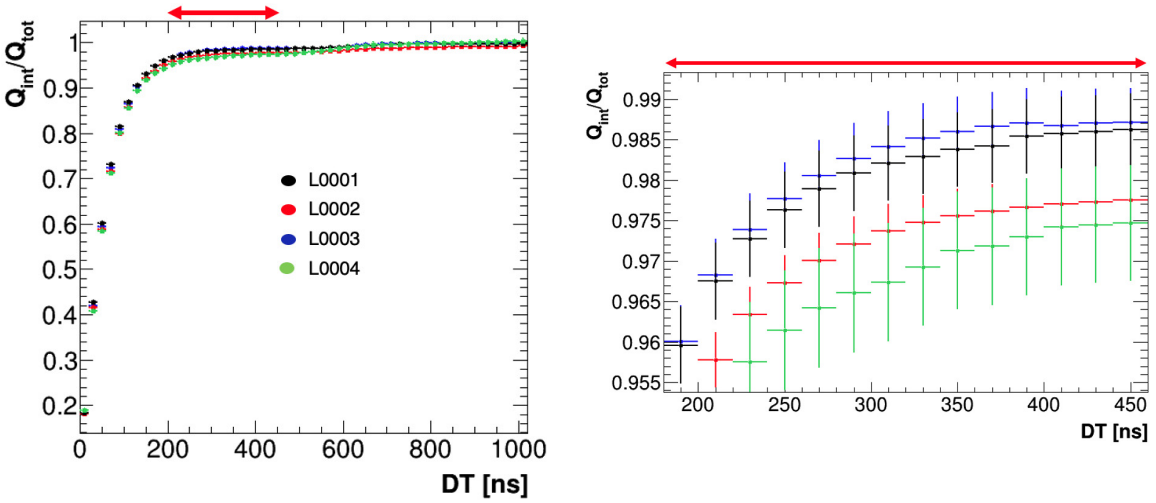

Figure 6.15: Left: Fast over Total ratio as a function of the integration gate. Right: Detail of the region at the end of the fast rise, as indicated by the red arrows.

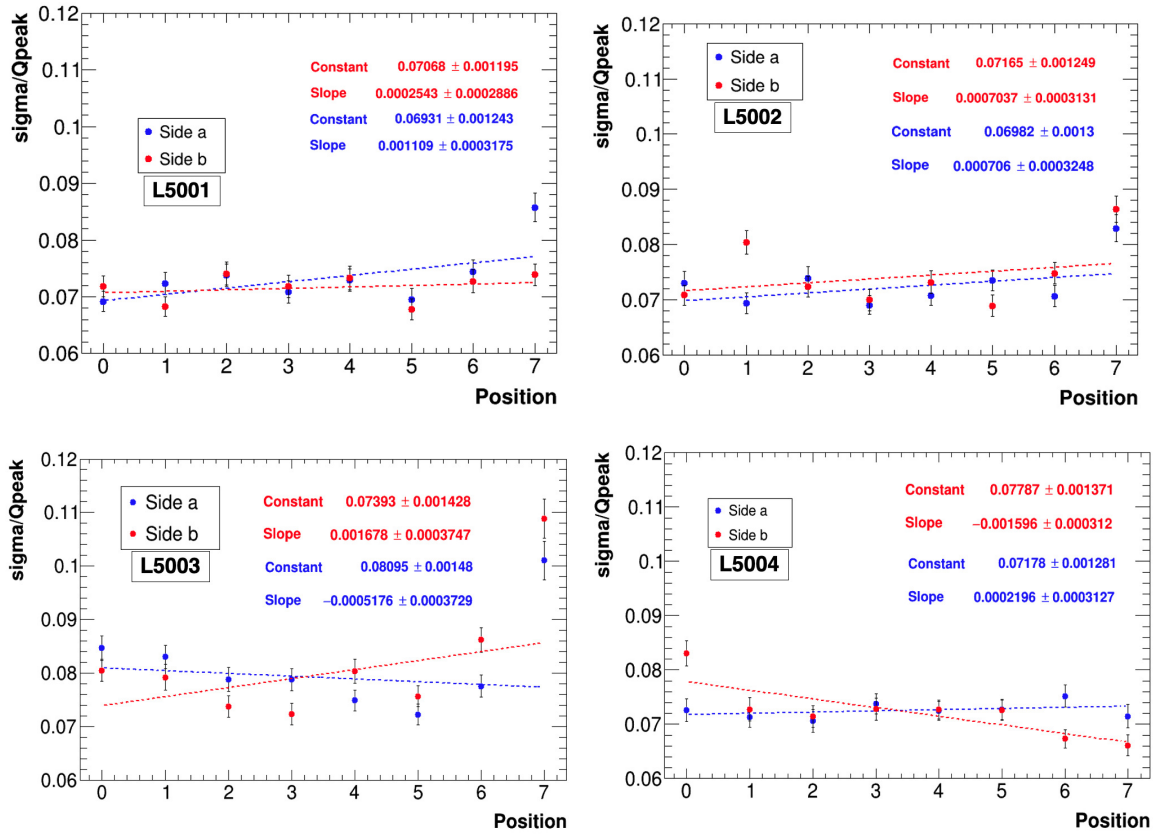

Figure 6.17: Resolution for every position, and both sides, of the four LYSO crystals, as measured with the PMT.

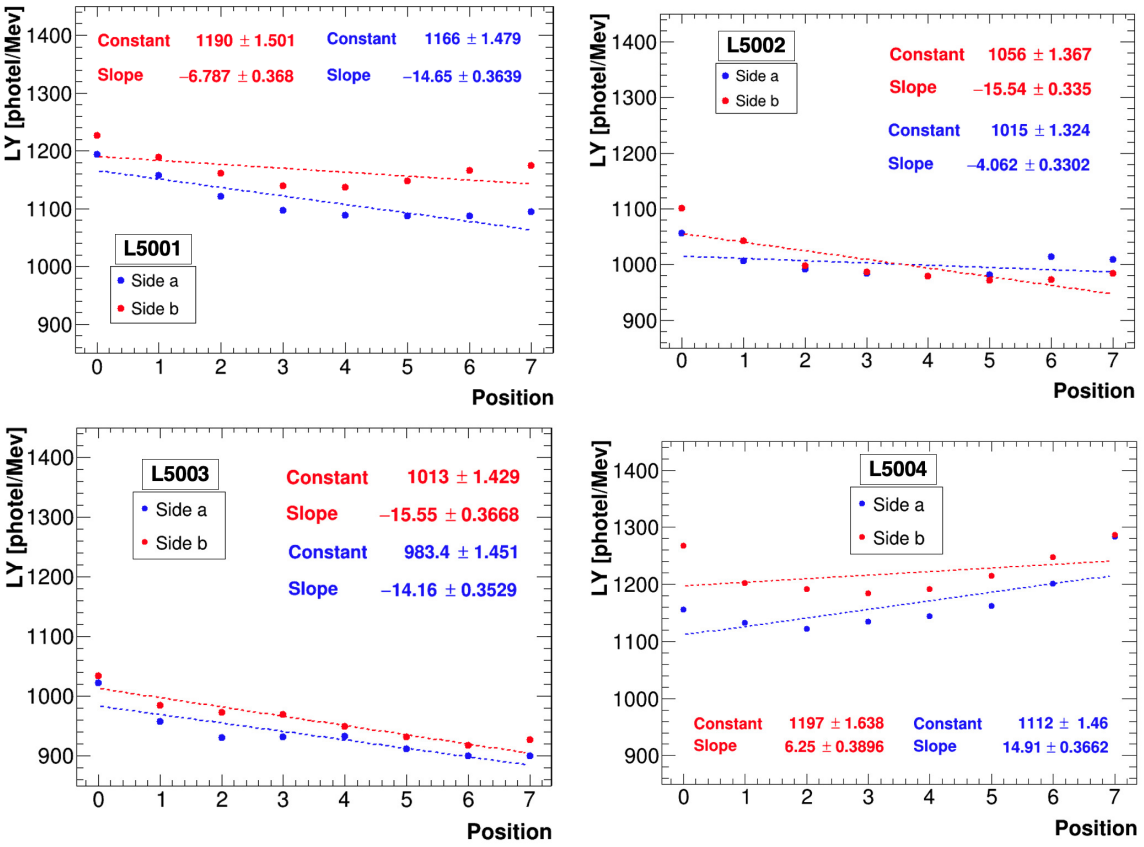

Figure 6.16: Light Yield for every position, and both sides, of the four LYSO crystals, as measured with the PMT.

6.3.2 Measurement with Mu2e SiPMs

The measurement presented in the following has been performed at SiDet as well. The crystals were wrapped in a foil of ESR and a square of ESR was placed onto the face opposite to the read-out to maximise the LY. In the following, the experimental setup and the results obtained are described.

Experimental Setup

The employed setup is shown in Fig. 6.18. The crystals are placed in a light-tight box to ensure darkening and to hold the crystal in position with respect to the Mu2e SiPMs. The tagger, whose signal is used as trigger, is the small LYSO crystal already employed at the crystal QC station. That, is connected to a $3 \times 3\text{mm}^2$ SiPM. The read-out is performed thanks to custom Mu2e electronic boards. In the picture, the ROU is covered by Al foil, used to further shield the SiPMs from light.

As shown on the side of the box holding the crystal, six positions were acquired $(0 \div 5)$ for each side of the crystal (a, b). The first position is at 2.5 cm from the end

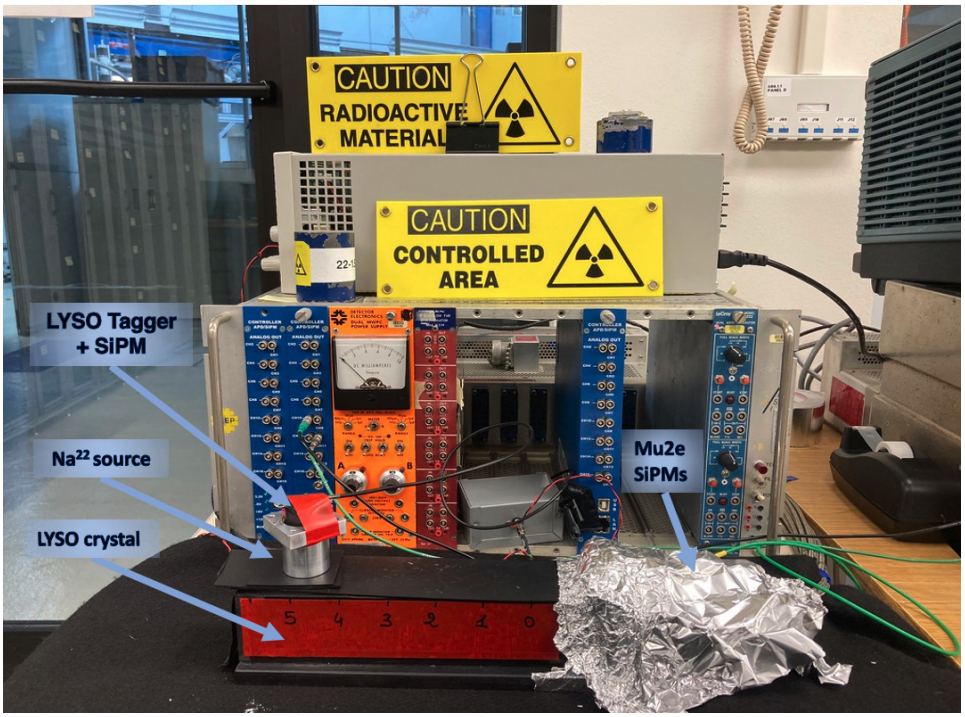

Figure 6.18: Experimental setup at SiDet for the characterisation of the CAPRI LYSO crystals with the Mu2e read-out.

of the crystal, with the other positions spaced of additional 3 cm. The SiPM was placed at $\sim$ 3 mm from the crystal face to mimic the final layout inside the calorimeter disk. Each SiPM was set at its own operational voltage to get a gain of 1.7×10^6. Then, an amplification factor of 4 is added by the available FEE electronics. Data are acquired triggering on the tagger signal, collecting 10^4 events per position for 4 μs after the trigger, with a triggering rate of 250kHz.

Results of the analysis

In Fig. 6.19 the waves for the tagger and for the two Mu2e SiPMs, reading out the crystal, are shown. The red lines indicate the chosen integration range for the charge evaluation.

The charge distributions are shown in Fig. 6.20. On the left, the cumulative tagger charge for all the collected events is shown for one side of one crystal, on the right the SiPM mean charge with a Gaussian fit isalso shown.

Additional cuts used to select the events were based on the SiPMs mean time – subtracting the tagger time – and on the tagger charge, analogously to what done for the PMT based data. Both cuts were asked at 2σ. Furthermore, since now the readout is performed by two independent SiPM units, a time coincidence at 2.5σ on the left and right side of the read-out unit was also required. An example of the distributions of

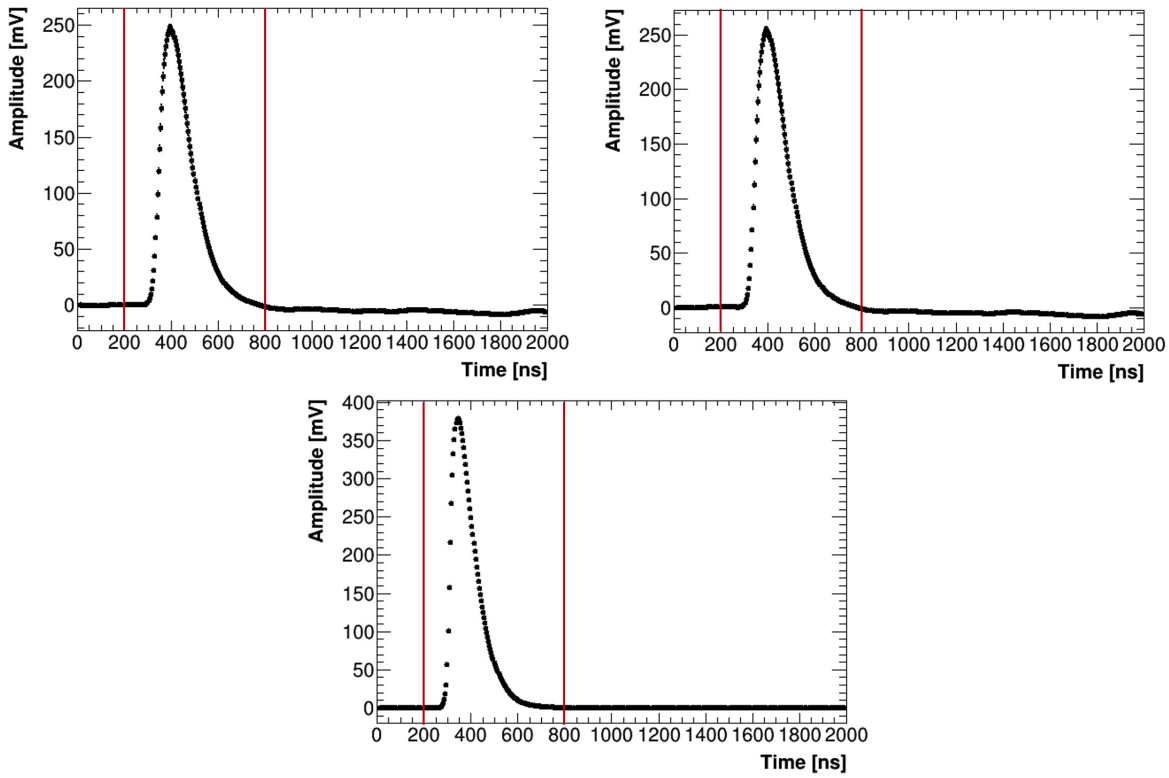

Figure 6.19: Waveforms of the left and right SiPM of the read-out (top left and right respectively) and of the tagger SiPM (bottom).

the time difference and the tagger charge are shown in Fig. 6.21. The distributions of the mean collected charge and resolution can be seen in Fig. 6.22 as a function of the position along the crystal.

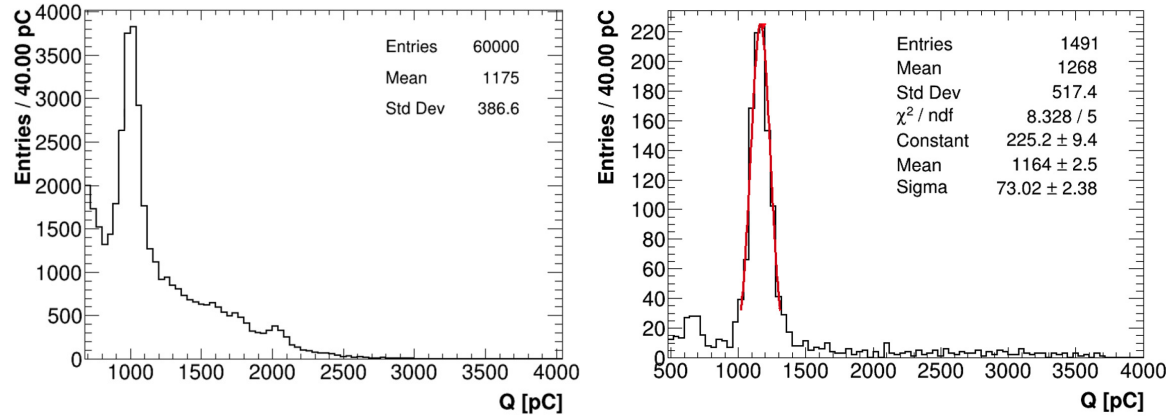

Figure 6.20: Left: Cumulative tagger charge for all the 6 positions on one side on the crystal. Right: Mean charge distribution of the left and right SiPMs with a Gaussian fit.

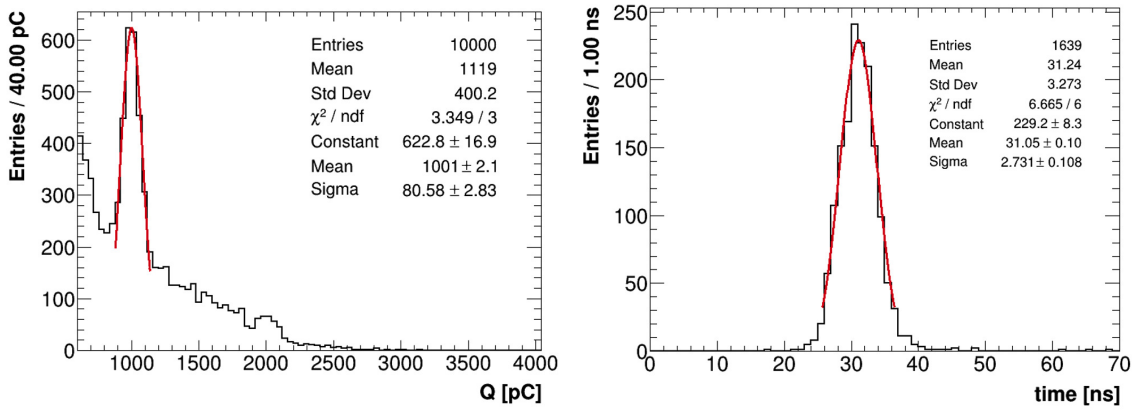

Figure 6.21: Tagger (left) and time difference (right) distributions with Gaussian fits marking the cuts employed in the analysis.

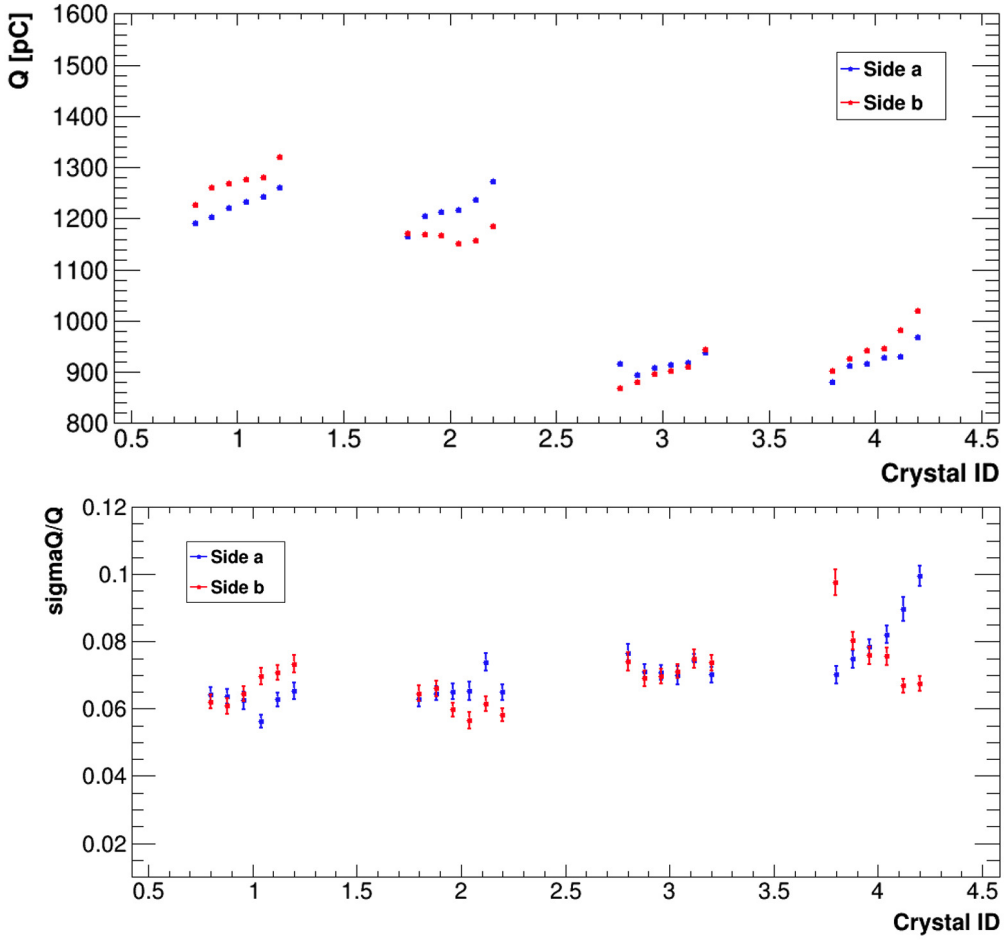

Figure 6.22: Summary of the mean charge (top) and resolution (bottom) for all the crystals and the data for every position and both sides. The x axis indicates the crystal number and the distribution of the points along the crystal length, showing the different positions.

The LY is shown in Fig. 6.23 separately for each crystal. The summary plot at the

bottom allows to better visualise the different response of the crystals. As it can be observed, the LY has improved noticeably with respect to the results obtained with the PMT thanks to the wrapping done with the ESR foil.

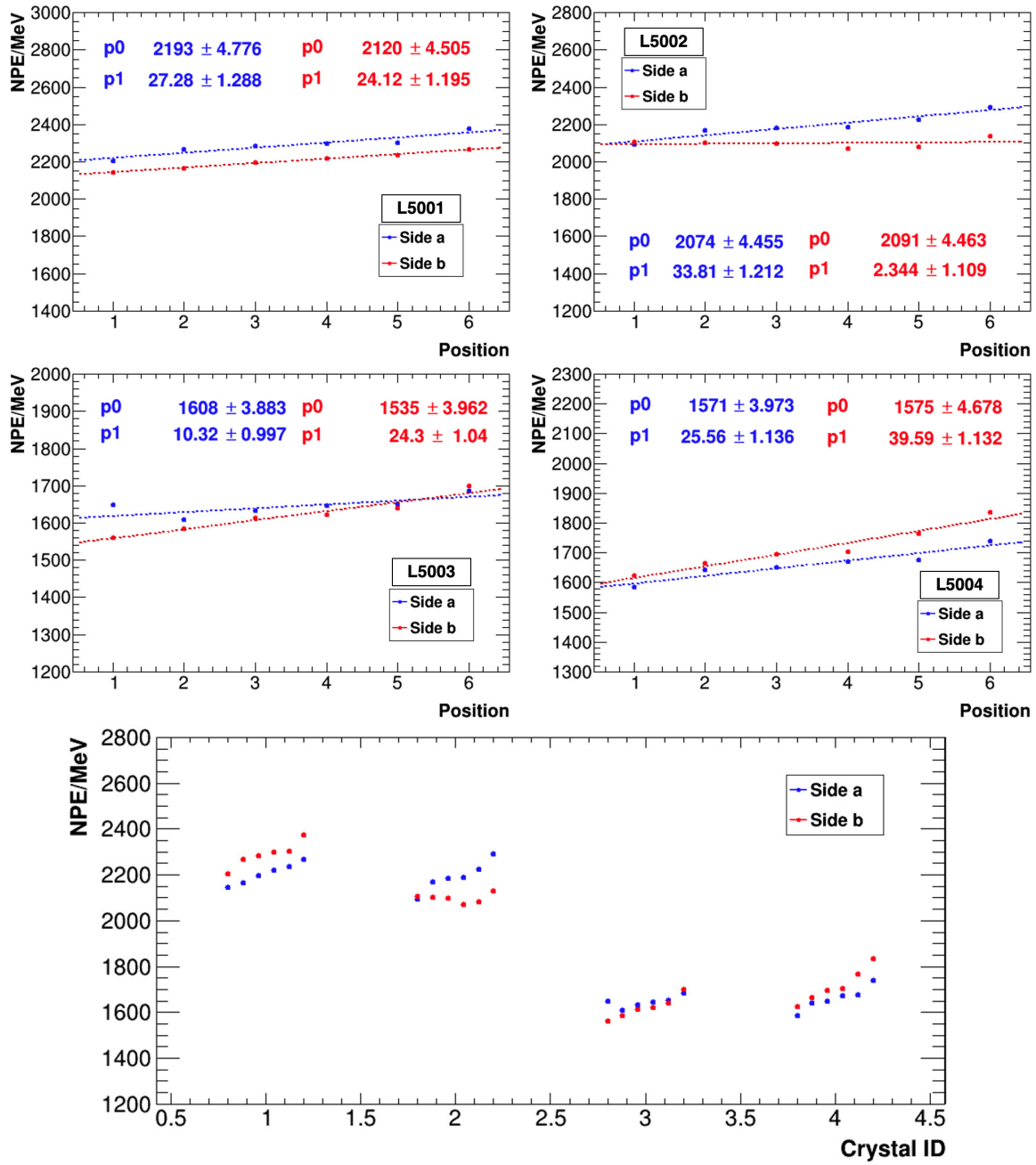

Figure 6.23: Top: Light Yield for every position, and both sides, of the four LYSO crystals, as measured with the SiPM read-out. Bottom: Summary plot which allows to better compare the performance of the different crystals.

The measurements with the Mu2e SiPMs has confirmed that with the LYSO crystals, a resolution of the order of 7% can be obtained. The acquired crystals have a nice

uniformity in their response and the LY results are, as expected, of $\mathcal{O}(2000)$ photoelectrons/MeV. Two of the crystals, L003 and L004, have confirmed to be slightly worse than the others and will be likely returned to SICCAS. A summary result on the LRU can be seen in Fig. 6.24. The results are summed up in Table. 6.4.

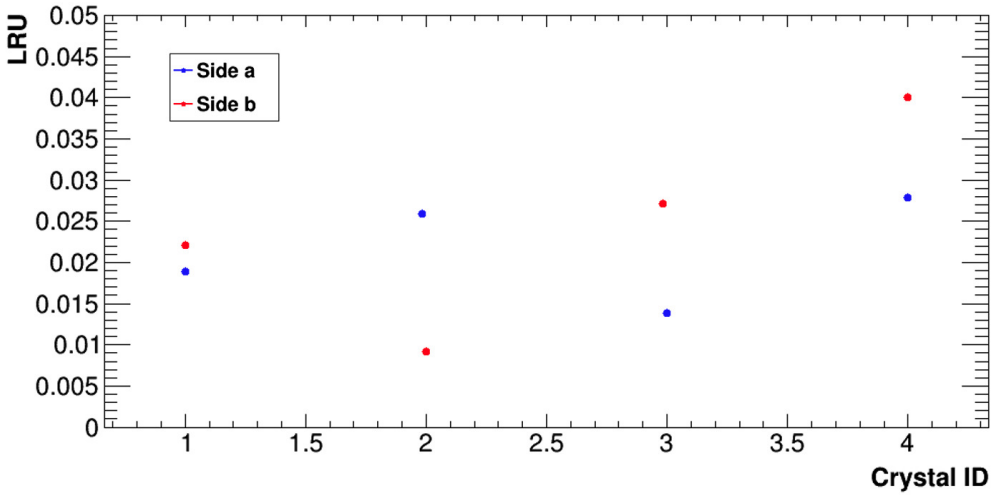

Figure 6.24: Summary of the mean charge (top) and resolution (bottom) for all the crystals and the data for every position and both sides. The x axis indicates the crystal number and the distribution of the points along the crystal length, showing the different positions.

Crystal	**Side**	**<LY>**	**LRU**	$<\sigma/\mu>$
L0001	a	2204	0.019	6.24(.19)%
L0001	b	2288	0.022	6.67(.21)%
L0002	a	2191	0.009	6.60(.20)%
L0002	b	2098	0.042	6.11(.18)%
L0003	a	1646	0.014	7.21(.22)%
L0003	b	1620	0.027	7.20(.22)%
L0004	a	1660	0.028	8.23(.25)%
L0004	b	1714	0.040	7.72(.23)%

Table 6.4: Summary table of the LYSO crystal performance. The columns report: the crystal number, the side of the crystal, the mean LY over all positions (expressed in photoelectrons/MeV), the LRU and the average resolution over the 8 positions. Measurements are taken with the SiPM.

Conclusions

In this work, the Mu2e experiment has been presented along with the theoretical motivations that propel Charged Lepton Flavour Violation (CLFV) searches. Mu2e will employ an intense and pulsed muon beam, generated by proton-tungsten interactions, to improve by four orders of magnitude the current limit on μ^- to e^- conversion in Al muonic atoms. The Mu2e detectors and its state-of-the-art Superconducting Magnetic System are presented, with special focus put on the electromagnetic calorimeter. The calorimeter is made of two annular disks, each one hosting 674 pure CsI crystals. Each crystal is read-out by a Readout Unit (ROU), composed of two custom SiPM matrices, each coupled to an independent front-end electronic board.

In order to ensure that the performance of the ROUs meets the expected requirements, a Quality Control (QC) Station, presented in this work, has been built and operated at the Laboratori Nazionali di Frascati of INFN (LNF). This QC Station allows to measure the SiPM gain, charge and photon detection efficiency in a controlled environment. The signal is obtained thanks to a LED illuminating the sensors through a filter wheel, by which the light intensity can be modulated in a controlled manner. More than 900 ROUs have been tested and the measured gain resulted to have a mean of $(3.541 \pm 0.003) \times 10^6$, with a channel by channel spread of 3% and a measurement reproducibility of $\sim 1.5\%$. The gain dependence on temperature was also evaluated and was found to be consistent with a gain variation of $(-1.60 \pm 0.07)\%/°C$. The ROUs show a very good consistency along production. Shippings to Fermilab of the scanned ROUs are ongoing and thanks to the Station measurements they are assured to have a correct functionality, with their response dependence on HV and temperature well determined.

The Station employs two remotely controlled power supplies. I have personally developed a Slow Control application for their control and monitoring, complying with the requirements and software tool guidelines of the experiment. This software has lately been expanded to control 10 power supplies in the calorimeter assembly room at Fermilab and it is now ready to control and monitor all the 80 power supplies needed for the entire calorimeter.

In order to achieve the Mu2e goal for a precise measurement of the rate of the muon

conversion into an electron, an accurate knowledge of the normalisation factor is also needed. A Stopping Target Monitor system (STM) has been designed by the Mu2e experiment to provide this information with an overall precision of 10%, as dominated by systematical errors. The STM has an intrinsic high precision in solving the X-ray and γ-ray lines related to the muon stopping and capturing processes. However, its evaluation is really slow, moving from 10 to 60 minutes depending upon the process and instruments involved. We proposed to perform a faster and independent measurement by relying on a calorimeter sub-system named CAPHRI (Calorimeter Precise High-Resolution Intensity detector). The goal is to evaluate the normalisation factor by counting the 1.8 MeV photons emitted from muon capture in the target. To do so, CAPHRI will employ four LYSO crystals placed inside the upstream calorimeter disk and readout with the Mu2e calorimeter SiPMs. Simulated performances are promising: this detector is able to get a 3% resolution on the capture rates each second, thus allowing a fast feedback to the machine and a possible offline study of its dependence on the beam intensity. The four LYSO crystals have been procured and I have personally participated to the characterisation of their parameters at Fermilab, exposing them to a ^{22}Na source. Of the four crystals, two show some occlusions and have lower performance than the others, so that they will likely be returned to the seller. The obtained experimental results are however very promising for the final performance of CAPHRI: the mean resolution has been measured to be of the order of 6.5% with more than 2000 photoelectrons per MeV of energy deposited in the crystal, thus confirming the resolution terms used in the detector simulation.

Appendix A

LYSO characteristics

LYSO decay time is of 36 ns, with a maximum emission wavelength at 420 nm. It has a refraction index of ~ 1.8 and a high light yield of ~ 33000 photons/MeV. Its density is of 7.1 g/cm^3.

LYSO contains a naturally occurring radioactive isotope ^{176}Lu, a beta emitter. The decay results in a 3 γ-rays cascade of 307, 202 and 88 keV, where self-absorption of these photons results, in a $1'' \times 1''$ cube, in the spectra shown in Fig. A.1. As can be seen from that plot, the spectrum endpoint of 1 MeV is far from the line CAPHRI looks for at 1.8 MeV.

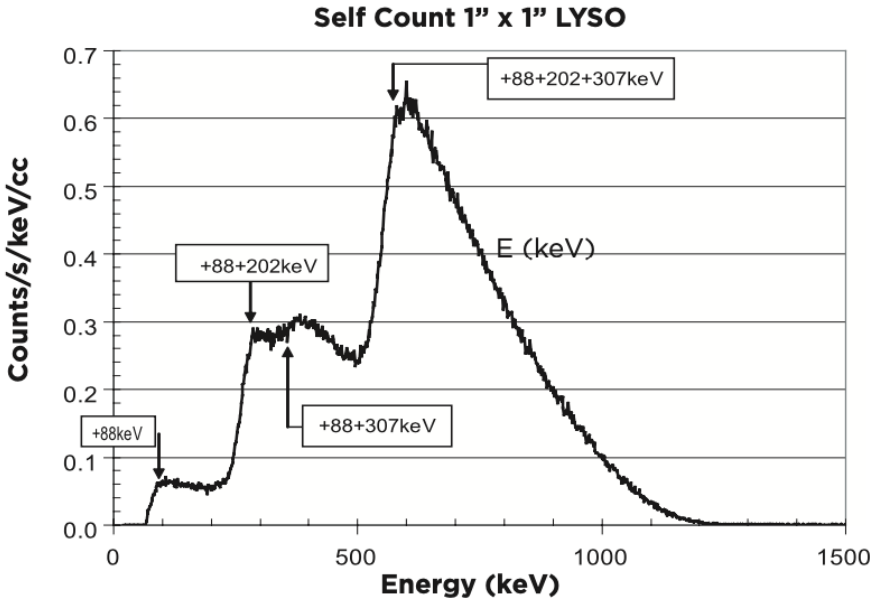

Figure A.1: LYSO spectrum for self-counts on a $1'' \times 1''$ cube [109].

Appendix B

$LaBr_3$ characteristics

$LaBr_3$ decay time is 25 ns, with a maximum emission wavelength of 380 nm. Its refraction index is ~ 2.0 and has a very high photon production yield of 73000 photons/MeV. It has a density of 5.08 g/cm^3. $LaBr_3$ is hygroscopic and must be hermetically packaged in a way that allows the readout with a photosensor, so with a window transparent to its emission wavelength embedded in the casing. The energy resolution for $LaBr_3$ crystals is determined both by their high light output and by their excellent energy linearity. In Fig. B.1-top is shown the non-proportionality $LaBr_3$ compared to NaI(Tl).

Its has its own radiation background since ^{138}La is a naturally occurring radioisotope. In 66.4% of its decays it undergoes electron capture to produce excited ^{138}Ba, which in turn decays by emission of a 1436 keV gamma. A necessary byproduct of electron capture is refilling of the electron shell which results in emission of coincident barium X-rays in the 35 keV region. The remaining decays, 33.6%, proceed by beta emission to ^{138}Ce, which decays by emitting a 789 keV gamma in coincidence with the beta, having an end point energy of 255 keV. The background spectrum is easily measured by self-counting, as shown in Figure B.1-bottom for a 38×38 mm detector counted for about 3 days in a low background chamber. As can be seen from that plot, the spectrum endpoint is far from the line CAPHRI looks for at 1.8 MeV.

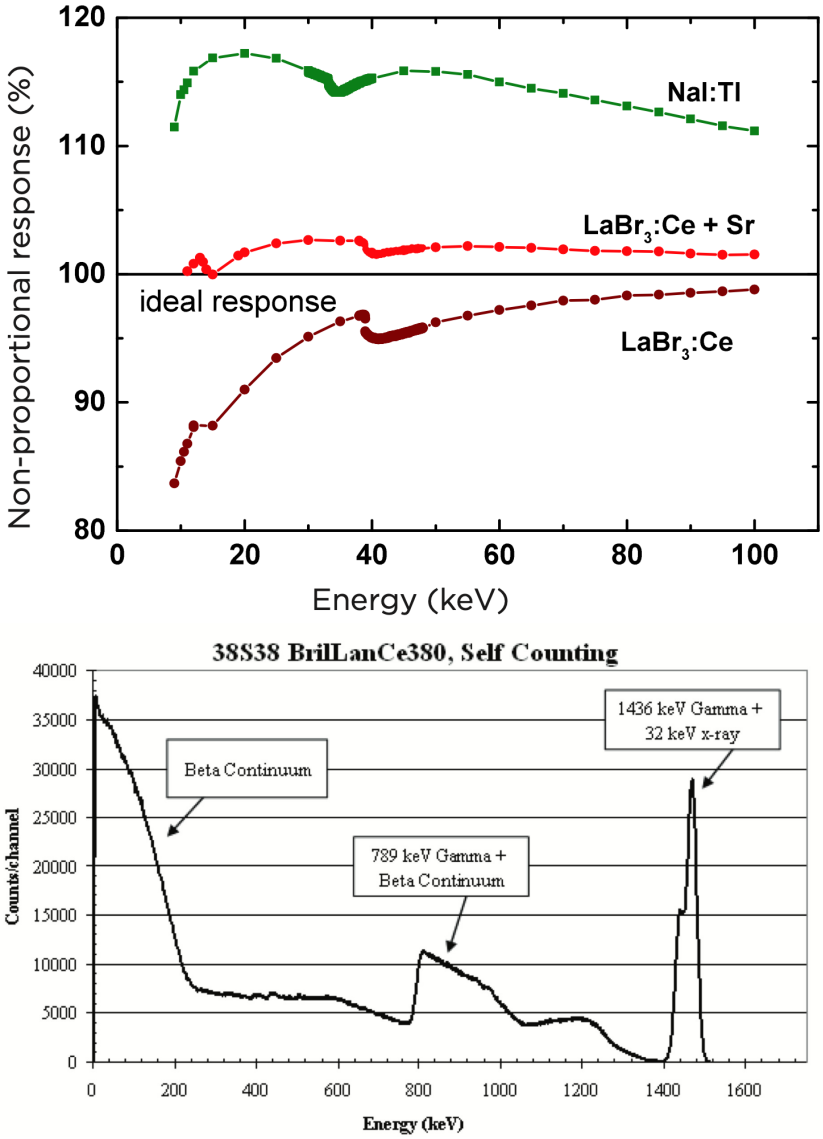

Figure B.1: Top: Non-proportionality of $LaBr_3$ and Enhanced $LaBr_3$ compared to NaI(Tl) [110]. Bottom: Self-counting background spectrum for a $LaBr_3$:Ce detector [111].

Appendix C

^{22}Na decays

For the preliminary tests and also the final measurements with both the PMT and the Mu2e SiPMs, a ^{22}Na source was used. ^{22}Na has a half-life of 2.6 years and decays emitting a positron (β^+ decay) into stable ^{22}Ne. The emitted positrons react with the electrons of the surrounding matter and lead to a characteristic annihilation radiation at 511 keV. Due to momentum conservation, the two photons produced upon e^+e^- annihilation are emitted back-to-back. A very small part (0.06%) of the sodium decays leads directly to the ground state of neon. The rest leads to an excited state, partly via electron capture (9.6%) from the inner atomic shell, but mainly via positron emission. Upon de-excitation, the neon emits a 1275 keV photon. The lifetime of this excited neon is only 3.7 ps. In Fig. C.1 is shown the sodium spectrum and its decay scheme.

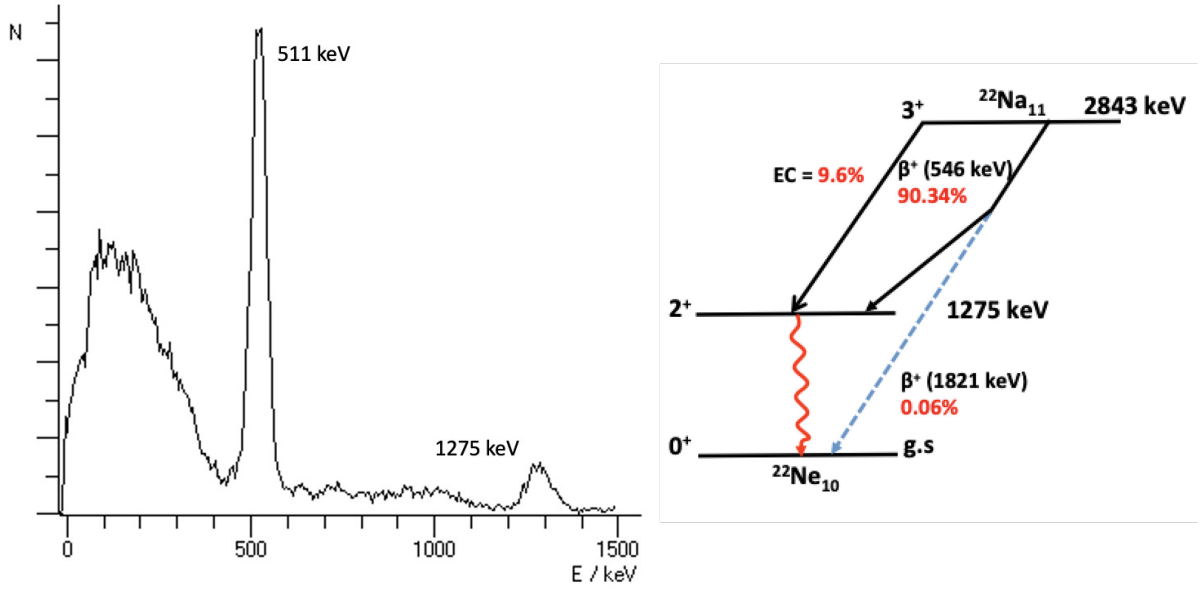

Figure C.1: ^{22}Na spectrum (left) and decay scheme (right).

Appendix D

Optimization of LYSO wrapping material

Members of the Mu2e calorimeter group and collaborators have performed,in 2014, tests on the mean collected charge with different wrappings on LYSO crystals [112]. Their results can be seen in Fig. D.1. The source was ^{22}Na and the readout was performed with a PMT. As can be seen, the collected charge strongly depends on the wrapping. For CAPHRI LYSO crystals, the best option was then ESR, having to exclude the optical grease due to the Mu2e working environment.

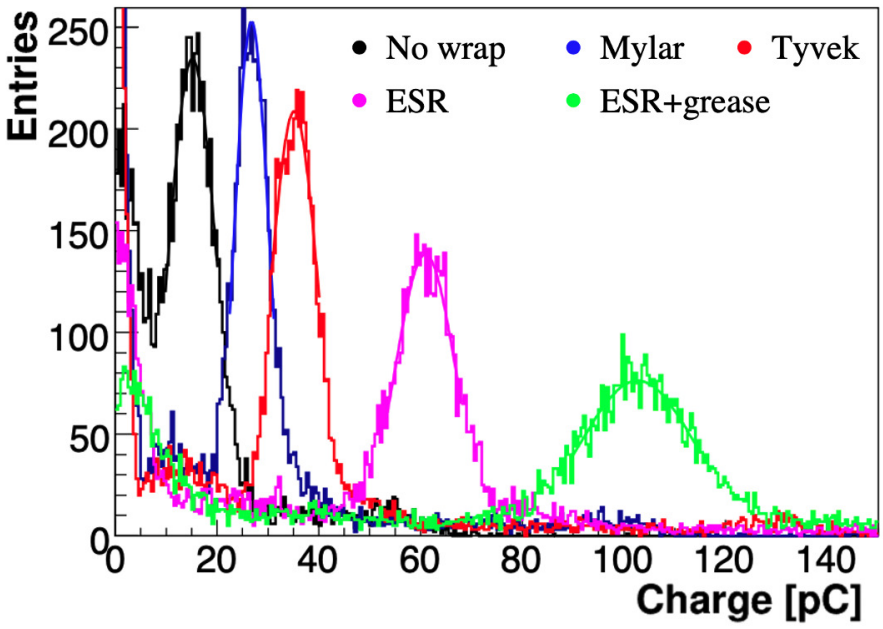

Figure D.1: Charge spectrum for a LYSO crystal with different kinds of wrapping: without any wrap (black), Mylar (blue), Tyvek (red) and ESR (magenta). For all measurements, the source was placed at the same position along the crystal.

Bibliography

[1] D. H. Perkins, *Introduction to High Energy Physics*. Cambridge University Press, 2014.

[2] S. Braibant, G. Giacomelli, and M. Spurio, *Particles and fundamental interactions: An introduction to particle physics*. Springer, 2012.

[3] J. Ellis, "Limits of the Standard Model," *arXiv hep-ph/0211168*, 2002.

[4] A. de Gouvêa and P. Vogel, "Lepton flavor and number conservation, and physics beyond the Standard Model," *Progress in Particle and Nuclear Physics*, vol. 71, pp. 75–92, jul 2013.

[5] Y. Fukuda *et al.*, "Evidence for Oscillation of Atmospheric Neutrinos," *Physical Review Letters*, vol. 81, pp. 1562–1567, aug 1998.

[6] N. Agafonova *et al.*, "Final results on neutrino oscillation parameters from the OPERA experiment in the CNGS beam," *Physical Review D*, vol. 100, sep 2019.

[7] C. Giganti, S. Lavignac, and M. Zito, "Neutrino oscillations: the rise of the PMNS paradigm," *Progress in Particle and Nuclear Physics*, vol. 98, pp. 1–54, jan 2018.

[8] A. de Gouvea, "GeV Seesaw, Accidentally Small Neutrino Masses, and Higgs Decays to Neutrinos," *arXiv:0706.1732*, 2007.

[9] M. Ardu and G. Pezzullo, "Introduction to Charged Lepton Flavor Violation," *Universe*, vol. 8, no. 6, p. 299, 2022.

[10] W. J. Marciano, T. Mori, and J. M. Roney, "Charged lepton flavor violation experiments," *Annual Review of Nuclear and Particle Science*, vol. 58, no. 1, pp. 315–341, 2008.

[11] M. Aiba *et al.*, "Science Case for the new High-Intensity Muon Beams HIMB at PSI," *arXiv:2111.05788*, 2021.

[12] A. De Gouvêa, S. Lola, and K. Tobe, "Lepton-flavor violation in supersymmetric models with trilinear R-parity violation," *Physical Review D*, vol. 63, no. 3, p. 035004, 2001.

[13] M. Aoki, R. Appleby, M. Aslaninejad, R. Barlow, R. Bernstein, C. Bloise, L. Calibbi, F. Cervelli, R. Culbertson, A. L. de Gouvea, *et al.*, "A New Charged Lepton Flavor Violation Program at Fermilab," *arXiv:2203.08278*, 2022.

[14] E. Hincks and B. Pontecorvo, "Search for gamma-radiation in the 2.2-microsecond meson decay process," *Physical Review*, vol. 73, no. 3, p. 257, 1948.

[15] T. Mori, "Final results of the MEG experiment," *arXiv:1606.08168*, 2016.

[16] Y. Bao *et al.*, "Search for the lepton flavour violating decay $\mu^+ \to e^+\gamma$ with the full dataset of the MEG experiment: MEG Collaboration," *The European Physical Journal C-Particles and Fields*, vol. 76, no. 8, pp. 434–434, 2016.

[17] M. Meucci, "MEG II experiment status and prospect," *arXiv:2201.08200*, 2022.

[18] Y. Kuno and Y. Okada, "Muon decay and physics beyond the standard model," *Reviews of Modern Physics*, vol. 73, no. 1, p. 151, 2001.

[19] L. Calibbi, D. Chowdhury, A. Masiero, K. Patel, and S. Vempati, "Status of supersymmetric type-I seesaw in SO(10) inspired models," *Journal of High Energy Physics*, vol. 2012, no. 11, pp. 1–19, 2012.

[20] J. M. Arnold, B. Fornal, and M. B. Wise, "Phenomenology of scalar leptoquarks," *Physical Review D*, vol. 88, no. 3, p. 035009, 2013.

[21] R. Harnik, J. Kopp, and J. Zupan, "Flavor violating Higgs decays," *Journal of High Energy Physics*, vol. 2013, no. 3, pp. 1–34, 2013.

[22] M. Raidal, A. Van Der Schaaf, I. Bigi, M. Mangano, Y. Semertzidis, S. Abel, S. Albino, S. Antusch, E. Arganda, B. Bajc, *et al.*, "Flavor physics of leptons and dipole moments," *The European Physical Journal C*, vol. 57, no. 1, pp. 13–182, 2008.

[23] C.-H. Lee, P. B. Dev, and R. Mohapatra, "Natural TeV-scale left-right seesaw mechanism for neutrinos and experimental tests," *Physical Review D*, vol. 88, no. 9, p. 093010, 2013.

[24] M. Kakizaki, Y. Ogura, and F. Shima, "Lepton flavor violation in the triplet Higgs model," *Physics Letters B*, vol. 566, no. 3-4, pp. 210–216, 2003.

[25] G. t Hooft, "Symmetry breaking through Bell-Jackiw anomalies," *Physical Review Letters*, vol. 37, no. 1, pp. 8–11, 1976.

[26] A. De Gouvêa, W.-C. Huang, J. König, and M. Sen, "Accessible lepton-number-violating models and negligible neutrino masses," *Physical Review D*, vol. 100, no. 7, p. 075033, 2019.

[27] D. Q. Adams, C. Alduino, K. Alfonso, F. T. Avignone, O. Azzolini, *et al.*, "Search for Majorana neutrinos exploiting millikelvin cryogenics with CUORE," *Nature*, vol. 604, no. 7904, pp. 53–58, 2022.

[28] M. Agostini, G. Araujo, A. Bakalyarov, M. Balata, I. Barabanov, L. Baudis, C. Bauer, E. Bellotti, S. Belogurov, A. Bettini, *et al.*, "Final results of GERDA on the search for neutrinoless double-β decay," *Physical review letters*, vol. 125, no. 25, p. 252502, 2020.

[29] Y. Gando, "Neutrinoless double beta decay search with KamLAND-Zen," *PoS, NOW2018*, vol. 68, no. 10, 2018.

[30] G. Wang, C. Nones, A. Cazes, and M. De Jesus, "CUPID: CUORE (Cryogenic underground observatory for rare events) upgrade with particle IDentification," *arXiv:1504.03599*, 2015.

[31] Y. Kuno, "A search for muon-to-electron conversion at J-PARC: The COMET experiment," *Progress of Theoretical and Experimental Physics*, vol. 2013, no. 2, p. 022C01, 2013.

[32] H. Natori, D. Collaboration, *et al.*, "DeeMe experiment-An experimental search for a mu-e conversion reaction at J-PARC MLF," *Nuclear Physics B-Proceedings Supplements*, vol. 248, pp. 52–57, 2014.

[33] L. Bartoszek *et al.*, "Mu2e Technical Design Report," *arXiv:1501.05241*, 2015.

[34] J. Kaulard, C. Dohmen, H. Haan, W. Honecker, D. Junker, G. Otter, M. Starlinger, P. Wintz, J. Hofmann, W. Bertl, *et al.*, "Improved limit on the branching ratio of $\mu^- \to e^+$ conversion on titanium," *Physics Letters B*, vol. 422, no. 1-4, pp. 334–338, 1998.

[35] P. Divari, J. Vergados, T. Kosmas, and L. Skouras, "Exotic muon-to-positron conversion in nuclei: partial transition sum evaluation by using shell model," tech. rep., Joint Institute for Nuclear Research, 2001.

[36] M. Lee and M. MacKenzie, "Muon to positron conversion," *Universe*, vol. 8, no. 4, p. 227, 2022.

[37] J. M. Berryman, A. De Gouvêa, K. J. Kelly, and A. Kobach, "Lepton-number-violating searches for muon to positron conversion," *Physical Review D*, vol. 95, no. 11, p. 115010, 2017.

[38] A. v. d. Schaaf, "SINDRUM II," *Journal of Physics. G, Nuclear and Particle Physics*, vol. 29, no. 8, pp. 1503–1506, 2003.

[39] S. Ahmad, G. Azuelos, M. Blecher, D. Bryman, R. Burnham, E. Clifford, P. Depommier, M. Dixit, K. Gotow, C. Hargrove, *et al.*, "Search for muon-electron and muon-positron conversion," *Physical Review D*, vol. 38, no. 7, p. 2102, 1988.

[40] Sindrum II Collaboration *et al.*, "A search for muon to electron conversion in muonic gold," *Eur. Phys. J. C*, vol. 47, p. 337, 2006.

[41] R. M. Djilkibaev and V. M. Lobashev, "The solenoid muon capture system for the MELC experiment," in *AIP Conference Proceedings*, vol. 372, pp. 53–60, American Institute of Physics, 1996.

[42] J. L. Popp, "The MECO experiment: a search for lepton flavor violation in muonic atoms," *Nuclear Instruments and Methods in Physics Research Section A: Accelerators, Spectrometers, Detectors and Associated Equipment*, vol. 472, no. 3, pp. 354–358, 2001.

[43] A. Czarnecki, X. G. i Tormo, and W. J. Marciano, "Muon decay in orbit: spectrum of high-energy electrons," *Physical Review D*, vol. 84, no. 1, p. 013006, 2011.

[44] T. Suzuki, D. F. Measday, and J. Roalsvig, "Total nuclear capture rates for negative muons," *Physical Review C*, vol. 35, no. 6, p. 2212, 1987.

[45] D. S. Armstrong, A. Serna-Angel, S. Ahmad, G. Azuelos, W. Bertl, M. Blecher, C. Chen, P. Depommier, T. von Egidy, T. Gorringe, *et al.*, "Radiative muon capture on Al, Si, Ca, Mo, Sn, and Pb," *Physical Review C*, vol. 46, no. 3, p. 1094, 1992.

[46] M. MacKenzie and P. Murat, "Mu2e 2020 sensitivity update: RMC background estimate to $\mu^- \to e^-$." Mu2e Internal note, Mu2e-DocDB 36497.

[47] R. H. Bernstein, "The Mu2e Experiment," *Frontiers in Physics*, vol. 7, p. 1, 2019.

[48] G. De Felice, "An updated estimate of the Mu2e experiment sensitivity," *Università di Pisa - Master thesis*, 2020.

[49] S. Striganov, "Pbar Background Studies with MARS." Mu2e Internal note, Mu2e-DocDB 1776-v3.

[50] R. Bernstein, "A New Antiproton Production Model." Mu2e Internal note, Mu2e-DocDB 27801-v10.

[51] D. Ayres, G. Drake, M. Goodman, J. Grudzinski, V. Guarino, R. Talaga, A. Zhao, P. Stamoulis, E. Stiliaris, G. Tzanakos, *et al.*, "The NOνA technical design report," tech. rep., Fermi National Accelerator Lab.(FNAL), Batavia, IL (United States), 2007.

[52] E. Prebys and S. Werkema, "Out-of-Time Beam Extinction in the Mu2e Experiment," tech. rep., Fermi National Accelerator Lab.(FNAL), Batavia, IL (United States), 2015.

[53] P. Murat, "Optimization of TS1/TS3 pbar absorbers." Mu2e Internal note, Mu2e-DocDB 33410.

[54] G. Feinberg, P. Kabir, and S. Weinberg, "Transformation of muons into electrons," *Physical Review Letters*, vol. 3, no. 11, p. 527, 1959.

[55] The Mu2e Collaboration, "Mu2e Proposal." Mu2e Internal document, Mu2e-DocDB 388.

[56] V. Cirigliano, R. Kitano, Y. Okada, and P. Tuzon, "Model discriminating power of $\mu \to e$ conversion in nuclei," *Physical Review D*, vol. 80, no. 1, p. 013002, 2009.

[57] A. Knecht, A. Skawran, and S. M. Vogiatzi, "Study of nuclear properties with muonic atoms," *The European Physical Journal Plus*, vol. 135, no. 10, pp. 1–18, 2020.

[58] M. Lee *et al.*, "The straw-tube tracker for the Mu2e experiment," *Nuclear and particle physics proceedings*, vol. 273, pp. 2530–2532, 2016.

[59] G. Pezzullo, "The Mu2e Tracker," in *39th International Conference on High Energy Physics*, vol. 11, 2018.

[60] M. Srivastav, "Efficiency Analysis of the Layers and the Module." Mu2e Internal note, Mu2e-DocDB 27601.

[61] E. Dukes, R. Ehrlich, S. Boi, and Y. Oksuzian, "The Cosmic Ray Background Estimate in a Staged Mu2e." Mu2e Internal note, Mu2e-DocDB 28266.

[62] A. Gaponenko, "CD3 backgrounds." Mu2e Internal note, Mu2e-DocDB 7464-v13.

[63] P. Murat *et al.*, "SU2020: blessing." Mu2e Internal note, Mu2e-DocDB 39099-v2.

[64] R. Bernstein, D. G. Hitlin, and S. Miscetti, "Calorimeter Requirements Document." Mu2e Internal note, Mu2e-DocDB 864.

[65] S. Baccaro, A. Cemmi, M. Cordelli, E. Diociaiuti, R. Donghia, S. Giovannella, S. Loreti, S. Miscetti, M. Pillon, and I. Sarra, "Radiation hardness test of un-doped CsI crystals and Silicon Photomultipliers for the Mu2e calorimeter," in *Journal of Physics: Conference Series*, vol. 928, p. 012041, IOP Publishing, 2017.

[66] N. Atanov, V. Baranov, J. Budagov, S. Ceravolo, F. Cervelli, F. Colao, M. Cordelli, G. Corradi, E. Dane, Y. Davydov, *et al.*, "The Mu2e calorimeter final technical design report," *arXiv preprint arXiv:1802.06341*, 2018.

[67] G. Pezzullo, J. Budagov, R. Carosi, F. Cervelli, C. Cheng, M. Cordelli, G. Corradi, Y. Davydov, B. Echenard, S. Giovannella, *et al.*, "Progress status for the Mu2e calorimeter system," in *Journal of Physics: Conference Series*, vol. 587, p. 012047, IOP Publishing, 2015.

[68] The Mu2e Project and Collaboration, "Mu2e Conceptual Design Report," tech. rep., Lawrence Berkeley National Lab.(LBNL), Berkeley, CA (United States), 2012.

[69] G. Ren, S. Zhao-Hui, Z. Zi-Chuan, Z. Kan, Y. Fan, L. Huan-Ying, and C. Feng, "Luminescence and Decay Time Properties of Pure CsI Crystals," *Journal of Inorganic Materials*, vol. 32, p. 169, 02 2017.

[70] C. Amsler, D. Grögler, W. Joffrain, D. Lindelöf, M. Marchesotti, P. Niederberger, H. Pruys, C. Regenfus, P. Riedler, and A. Rotondi, "Temperature dependence of pure CsI: scintillation light yield and decay time," *Nuclear Instruments and Methods in Physics Research Section A: Accelerators, Spectrometers, Detectors and Associated Equipment*, vol. 480, no. 2-3, pp. 494–500, 2002.

[71] E. Diociaiuti, "Study of the Mu2e sensitivity to the $\mu^- \to e^+$ conversion process," *Università degli Studi Tor Vergata - PhD thesis*, 2020.

[72] "AmCrys Undoped CsI." http://www.amcrys.com/details.html?cat_id=146&id=4281.

[73] "SICCAS CsI(Tl) Crystal and Array." http://www.siccas.com/scintillatorCesiumIodineCrystals.htm.

[74] "Saint Gobain CsI(Tl) Scintillation Material." https://www.crystals.saint-gobain.com/radiation-detection-scintillators/crystal-scintillators/csi-cesium-iodide.

[75] N. Atanov, V. Baranov, J. Budagov, D. Caiulo, F. Cervelli, F. Colao, M. Cordelli, G. Corradi, Y. I. Davydov, S. Di Falco, *et al.*, "The Mu2e calorimeter: quality assurance of production crystals and SiPMs," *Nuclear Instruments and Methods in Physics Research Section A: Accelerators, Spectrometers, Detectors and Associated Equipment*, vol. 936, pp. 154–155, 2019.

[76] S. Baccaro, A. Cemmi, G. Ferrara, and S. Fiore, "Calliope gamma irradiation facility at ENEA-Casaccia R.C. (Rome)," *ENEA Report, RT//13/ENEA*, 2015.

[77] A. Pietropaolo, F. Andreoli, M. Angelone, U. B. Vetrella, S. Fiore, S. Loreti, G. Pagano, R. Pilotti, and M. Pillon, "The Frascati Neutron Generator: A multipurpose facility for physics and engineering," in *Journal of Physics: Conference Series*, vol. 1021, p. 012004, IOP Publishing, 2018.

[78] R. Donghia, "The Mu2e calorimeter: R&D and calibration strategies," *Università degli Studi Roma Tre - PhD thesis*, 2016.

[79] I. Sarra, E. Diociaiuti, and E. Di Meco, "Test on irradiated SiPMs." Mu2e Internal note, Mu2e-DocDB 40745-v1.

[80] F. Nagy, G. Hegyesi, G. Kalinka, and J. Molnár, "A model based DC analysis of SiPM breakdown voltages," *Nuclear Instruments and Methods in Physics Research Section A: Accelerators, Spectrometers, Detectors and Associated Equipment*, vol. 849, pp. 55–59, 2017.

[81] Hamamatsu, "TSV MPPC array, production flyer 2015.05 KSX-I50080-E- S13361-3050xx-04." https://www.hamamatsu.com/content/dam/hamamatsu-photonics/sites/documents/99_SALES_LIBRARY/ssd/s13361-3050_series_kapd1054e.pdf.

[82] D. Paesani, "Design and characterisation of the CsI Crystal Calorimeter, Cosmic Ray Tagger and SiPM front-end electronics for the Mu2e experiment at Fermilab," *Politecnico di Torino - Master thesis*, 2020.

[83] N. Yahlali, L. Fernandes, K. González, A. Garcia, and A. Soriano, "Imaging with SiPMs in noble-gas detectors," *Journal of Instrumentation*, vol. 8, no. 01, p. C01003, 2013.

[84] G. Gallina, F. Retière, P. Giampa, J. Kroeger, P. Margetak, S. B. Mamahit, A. D. S. Croix, F. Edaltafar, L. Martin, N. Massacret, *et al.*, "Characterization of SiPM avalanche triggering probabilities," *IEEE Transactions on Electron Devices*, vol. 66, no. 10, pp. 4228–4234, 2019.

[85] R. Tschirhart, M. Bowden, K. Biery, R. Rivera, and D. Glenzinski, "Mu2e Trigger and DAQ Requirements." Mu2e Internal note, Mu2e-DocDB 1150.

[86] R. Rivera, "How Slow Controls & Monitoring Works from the TDAQ perspective." Mu2e Internal note, Mu2e-DocDB 31727.

[87] A. Gioiosa, R. Bonventre, S. Donati, E. Flumerfelt, G. Horton-Smith, L. Morescalchi, V. O'Dell, E. Pedreschi, G. Pezzullo, F. Spinella, *et al.*, "Online DAQ and slow control interface for the Mu2e experiment," tech. rep., Fermi National Accelerator Lab.(FNAL), Batavia, IL (United States), 2022.

[88] K. Biery, E. Flumerfelt, J. Freeman, W. Ketchum, G. Lukhanin, A. Lyon, R. Rechenmacher, R. Rivera, L. Uplegger, and M. Votava, "Flexible and scalable data-acquisition using the artdaq toolkit," *arXiv preprint arXiv:1806.07250*, 2018.

[89] K. Biery, C. Green, J. Kowalkowski, M. Paterno, and R. Rechenmacher, "artdaq: An event filtering framework for Fermilab experiments," in *2012 18th IEEE-NPSS Real Time Conference*, pp. 1–8, IEEE, 2012.

[90] C. Green, J. Kowalkowski, M. Paterno, M. Fischler, L. Garren, and Q. Lu, "The art framework," in *Journal of Physics: Conference Series*, vol. 396, p. 022020, IOP Publishing, 2012.

[91] R. Rivera, "Mu2e Detector Control System (DCS) Design and Specification." Mu2e Internal note, Mu2e-DocDB 3965.

[92] "EPICS: Experimental Physics and Industrial Control System." https://epics-controls.org.

[93] "EPICS Channel Access." https://epics-controls.org/resources-and-support/documents/ca/.

[94] "PostgreSQL." https://www.postgresql.org.

[95] "StreamDevice documentation." http://epics.web.psi.ch/software/streamdevice/.

[96] "Asynchronous Driver Support documentation." https://epics-modules.github.io/master/asyn/.

[97] "Phoebus documentation." https://control-system-studio.readthedocs.io/en/latest/intro.html.

[98] "Phoebusgen documentation." https://als-epics.github.io/phoebusgen/.

[99] "Low Voltage Power Supply manual." http://resources.aimtti.com/manuals/CPX400S+SA+SP_Instruction_Manual-Iss9.pdf.

[100] "High Voltage Power Supply manual." https://resources.aimtti.com/manuals/PLH+PLH-P_Instruction_Manual-Iss6.pdf.

[101] J. Miller and R. Bernstein, "WBS 5.06 Muon Stopping Target Monitor." Mu2e Internal note, Mu2e-DocDB 1438.

[102] J. Miller and R. Bernstein, "WBS 5.06 Muon Stopping Target Monitor." Mu2e Internal note, Mu2e-DocDB 4010-v5.

[103] A. Edmonds, J. Quirk, M.-L. Wong, D. Alexander, R. H. Bernstein, A. Daniel, E. Diociaiuti, R. Donghia, E. L. Gillies, E. V. Hungerford, *et al.*, "Measurement of proton, deuteron, triton, and α particle emission after nuclear muon capture on Al, Si, and Ti with the AlCap experiment," *Physical Review C*, vol. 105, p. 035501, 2022.

[104] A. Palladino, J. Quirk, and J. Miller, "Mu2e Stopping-Target Monitor baseline design." Mu2e Internal note, Mu2e-DocDB 6453.

[105] N. Tran, "Status of the Stopping Target Monitor." Mu2e Internal note, Mu2e-DocDB 33563.

[106] J. R. Quirk, "AlCap Photon Spectra." Mu2e Internal note, Mu2e-DocDB 67825-v2.

[107] "3M Enhanced Specular Reflector (ESR)." https://multimedia.3m.com/mws/media/1389248O/application-guide-for-esr.pdf.

[108] R.-Y. Zhu, "Tests of first six LYSO crystals from SIC." Mu2e Internal note, Mu2e-DocDB 3791.

[109] "LYSO Scintillation Material Saint-Gobain Data Sheet." https://www.crystals.saint-gobain.com/sites/hps-mac3-cma-crystals/files/2021-08/LYSO-Material-Data-Sheet.pdf.

[110] "Lanthanum Bromide Saint-Gobain Data Sheet." https://www.crystals.saint-gobain.com/sites/hps-mac3-cma-crystals/files/2021-09/Lanthanum-Material-Data-Sheet.pdf.

[111] "Lanthanum Bromide Scintillators Performance Summary - Saint-Gobain." https://www.crystals.saint-gobain.com/sites/hps-mac3-cma-crystals/files/2021-06/LaBr-Performance-Summary-2021.pdf.

[112] M. Cordelli, S. Giovannella, F. Happacher, M. Martini, S. Miscetti, R. Rosellini, I. Sarra, F. Shi, and V. Stomacia, "Test of the INFN LYSO crystals with ^{22}Na source." Mu2e Internal note, Mu2e-DocDB 4399-v1.